Hydrodynamics, control and numerical modelling of absorbing wavemakers

Andrew Eoghan Maguire

Doctor of Philosophy

The University of Edinburgh

2011

To my parents

Abstract

This research investigates the effects that geometry and control have on the absorption characteristics of active wavemakers and looks at the feasibility of modelling these wavemakers in commercial computational fluid dynamic software. This thesis presents the hydrodynamic coefficients for four different types of wavemakers. The absorption characteristics of these wavemakers are analysed using different combinations of control impedance coefficients. The effect of combining both geometry and control is then investigated. Results, quantifying the absorption characteristics are then presented. It is shown that the amount of absorption for a given paddle differs greatly depending on the choice of control coefficients used to implement complex conjugate control. Increased absorption can be achieved over a broader bandwidth of frequencies when the geometry of the wavemaker is optimised for one specific frequency and the control impedance is optimised for an alternate frequency.

In conjunction to this theoretical study, a numerical investigation is conducted in order to verify and validate two commercial computational fluid dynamic codes' suitability to model the previously discussed absorbing wavemakers. ANSYS CFX and FLOW3D are used to model a physical wavemaker. Both are rigorously verified for discretisation errors and CFX is validated against linear wavemaker theory. Results show good agreement and prediction of the free surface close to the oscillating wavemaker, but problems with wave height attenuation and excessive run times were encountered.

Acknowledgements

I would like to thank Prof. David Ingram for his guidance, support and supervision during this work. On my first day you posed a question, How do you eat an elephant? This approach managed to get me through my Ph.D. as I approached my research one bite at a time.

I am indebted to many colleagues within the Institute for Energy Systems but in particular to Ally Price for all of her comments and tuition on wave energy control theory and to Gareth Gretton for his guidance on CFD. Many thanks to Matthew Topper for his help with the Latex template and David Forehand for helping me with any mathematical problems I encountered and my lunch friends who were always a welcome source of distraction from research. I am also grateful to my brother Diarmuid for his time and effort proof-reading of this thesis.

This thesis is the culmination of many years research, and I am truly lucky that my girlfriend, Mireille, has been here from day one. You have been the most important and best part of my life in Edinburgh. You always ensured that I maintained a healthy balance between work and play and you are the reason why I have enjoyed my studies so much.

Finally I am forever indebted to my parents for their understanding, endless patience and encouragement. I truly appreciate everything that you have done and provided for me. Without your continued support I would not be where I am today. Thank you.

Declaration

I declare that this thesis was composed by myself, that the work contained herein is my own except where explicitly stated otherwise in the text, and that this work has not been submitted for any other degree or professional qualification except as specified.

Eoghan Maguire

Contents

List of Figures

List of Tables

Chapter 1

Introduction

> "Our Problems are man made, therefore they can be solved by man. Man can be as big as he wants. No problem of human destiny is beyond human beings."
>
> J.F. Kennedy

The world today is a very different one to that of Kennedy but, there are still real problems facing society. The spectre of global warming and its dire consequences for future generations is looming large on the horizon. It is only recently that man has been big enough to admit his mistakes. The Intergovernmental Panel on Climate Change has stated that global warming is in all probability a man made problem (Pachauri and Reisinger, 2007). Concluding that most of the observed increase in globally averaged temperatures since the beginning of the 20^{th} century is likely due to the observed increase in anthropogenic greenhouse gas concentrations. Some might not share Kennedy's faith in man's ability, reason and judgement, but for future generations' sakes, I hope man is strong enough and smart enough to correct his mistakes.

Publications highlighting the potential cost of inaction against global warming (Stern, 2006) have added impetus to the debate on low carbon energy production. As a result the European Union (EU) has put in place a renewable energy directive in order to reduce carbon dioxide emissions from electricity production, increase energy security within the EU and reduce members exposure to oil price fluctuations.

The EU directive requires member countries to produce a pre-agreed proportion of energy consumption from renewable sources such that the EU as a whole shall obtain at least 20% of total energy from renewables by 2020 (European Union, 2009). Local governments have even set more ambitious targets; Scotland

aims to meet 80% of its energy needs via renewable energy sources by 2020. The prognosis for renewable energy is positive, and a recent publication has shown that renewable energy production has nearly doubled in the period between 1999 and 2009 (Eurostat, 2011), with an increasing upward trend. Traditionally, renewable energy sources consisted of biomass, hydropower, geothermal energy, wind and solar energy. One major renewable energy resource that has not yet been tapped into is wave energy.

The wave energy resource approaching Western Europe's coastline is considerable. Studies have shown that wave energy fluxes of up to 50-70kW per meter of wave-front approach from the Atlantic Ocean (Mollison *et al.*, 1976), with the British Isles receiving more than anywhere else in Europe. This is an immense resource that is lying on our door step. It could potentially replace large proportions of electricity produced by carbon dioxide emitting coal fired power plants. Security of supply is guaranteed and the price of energy will not be be subject to the vagaries of other nations foreign policies. Understandably, EU members are now starting to investigate whether or not wave power will be able to make a meaningful contribution to the renewable energy mix. The energy potential is huge, but building, operating and maintaining man-made structures at sea is not a trivial matter. In order to address some of these concerns and problems, many researchers have begun looking at the problems facing the industry and putting forward their solutions.

Research on wave energy dates back far longer than many realise, with the first patent in 1799 (Cruz, 2008) however, most recognise the seminal paper by Salter *et al.* (1976) as the instigator for current research on the topic. This publication was at the height of the 1970s oil crisis and it highlighted the opportunity of boundless energy production for nations with an Atlantic facing coastline. For a number of different reasons the early research in wave power did not culminate in any significant full scale devices. This was primarily due to the UK governments decision to pursue large scale centralised generation rated around 2GW but also as a result of wrongly pricing the cost of wave energy (House of Lords, 1988).

Since the mid-1990s there has been a resurgence of interest in wave energy, starting with small scale on-shore oscillating water column devices and progressing to the present day, with several companies testing full-scale devices at the European Marine Energy Centre (EMEC) and elsewhere. The range of different types of wave energy converter is extremely broad, at the time of writing EMEC have

registered over 120 wave power developers, each using a different technology and methods to harness the energy in the waves. The plethora of different devices and technologies is encouraging for the wave energy sector, but it also means that it is more difficult to categorise and assess which devices offer the best solution for harvesting wave energy.

There are two criteria by which all wave energy converters are judged and evaluated. The first is survivability. This is binary, pass or fail. If the device does not survive in extreme waves it should not be considered for production. The other is performance. This process will guide the economics of the business case and determine whether a device is worth manufacturing and deploying.

All of the aforementioned technologies will be designed and evaluated using a combination of theory, experiment and numerical modelling before progressing towards full scale production. The realm of theory can be limited due to simplified assumptions in the physics, needed in order to allow for calculation. Experimental modelling is excellent at providing the characteristic response of the device in real water waves but, these facilities are expensive to run and depending on the scale to be tested, only limited information can be obtained.

Experimental wave tanks also suffer from wave reflections from the solid wall boundaries spoiling the test domain. These reflections also limit the test duration due to a build up of spurious waves. Of the many proposed solutions to deal with these unwanted waves is the use of active absorption in the wavemakers. This is where the wavemakers react to waves impinging upon their surface and move in a manner that absorbs the incoming wave. This is a important research topic and improvements in reflection absorption could be made by borrowing from the advancements made in wave energy converter control.

However, numerical modelling has thus far benefited from the unrelenting adherence of CPU processing power to Moore's law (Moore, 1965). This has resulted in numerical modelling becoming an ever more important tool for the design of wave energy devices. Numerical modelling has allowed designers to obtain diagnostic reports of their designs and arrive at technology readiness levels (Holmes and Nielsen, 2010) at a fraction of the cost of a wave tank. Until recently however, the kind of numerical models used in the wave energy industry were limited to linear waves, where the motions of the devices are small and no wave breaking or over-topping occurs. This is appropriate for low to medium energy sea states and allows numerical models to predict performance of a device based upon a given

resource. But it cannot give any indications of the survivability of the device or how the device will behave in higher energy sea-states.

Significant progress has been made in both computational hardware and numerical modelling methods to offer engineers the possibility of using numerical models that do not make simplistic assumptions about the flow-field. These solvers are refereed to as Navier-Stokes solvers or computational fluid dynamic codes. It is being proposed that these Navier-Stokes solvers could offer the possibility of being used as a 'numerical wave tank', solving for viscosity and accounting for wave breaking and air-entrainment. The incorporation of free surface models into commercial computational fluid dynamic software has made this option more accessible to industrial developers, who make use of these off the shelf codes.

Numerical wave tanks also suffer from unwanted wave reflections, similar to experimental wave tanks. There are specific numerical methods for absorbing these waves in a numerical wave tank and some numerical absorption techniques borrow methods used in experimental wave tanks. Combining both types of absorption methods has proved beneficial (Clément, 1996) and could be improved upon with further study, especially if combined with new wave energy control absorption methods. On top of this, unexplored absorption using new geometric wavemaker profiles could also increase the absorption in these numerical models.

These numerical models are powerful tools, but there is always a danger of users having over confidence in their numerical output. There is all too often a tendency, on the user's behalf, to take the given results for granted without treating them with a healthy does of scepticism and analysing them thoroughly. This can be coupled with unrealistic user expectations. Only if a numerical code has undergone a thorough verification and validation can the end user declare his confidence in the results. With the increasing usage of computational fluid dynamic software, in particular commercial codes by industrial users, there is a need to examine how capable these codes are at accurately predicting the free surface flow field in and around a radiating body.

This thesis describes two of the aforementioned realms, theory and numerical modelling of oscillating bodies in water waves, hoping to achieve physical and numerical convergence between the two. The current literature in both hydrodynamics of wavemakers and numerical generation of waves will be presented and discussed. Then, it hopes to develop the hydrodynamic theory behind absorbing wavemakers and analyse the effects that different control strategies have on levels

of absorption. It is envisaged that this theory of absorbing wavemakers will be incorporated into a commercial Navier-Stokes numerical code. Upon successful verification and validation, this code will then be used to model wave generation and absorption by the wavemakers in a two dimensional flume. Then the possibility of using this numerical model to create a three dimensional analogue to the University of Edinburgh curved tank will be investigated. This is not a trivial task, but if this is achieved, it will be a truly useful design tool for industry and academia.

Chapter 2

Literature review

There are two areas of research that are relevant to the the work being presented in this thesis: research on physical wavemakers and research on numerical wave makers. The literature reporting on the generation of waves using physical wavemakers will be reviewed first, where literature behind wavemaker theory will be discussed. Following on from this, absorption techniques used in physical wave tanks will be presented and will be expanded to report on active absorption methods used for absorbing wavemakers. Then publications regarding numerical wave tanks will be presented and the different methods used to generate waves in a numerical code will be discussed. Finally, the research into numerical absorption of waves will be presented.

2.1 Experimental wave tanks

Engineers use wave tank facilities to assess the design, safety and economic feasibility of ships, coastal structures and wave energy devices. Wavemakers are a central component to such facilities and a general theory for the generation of waves by oscillating solid boundaries was first presented by Havelock (1929). This research was further developed by many subsequent studies (Biesel and Suquet, 1951; Galvin Jr, 1964; Gilbert *et al.*, 1971; Bullock and Murton, 1989; Dean and Dalrymple, 1991; Hughes, 1993; Falnes, 2002; Newman, 2008) into the well established wavemaker theory. This theory describes the generation of propagating waves using an oscillating solid boundary. Subsequently, the theory has been used to describe the radiated waves for a variety of different types of wavemakers such as: pistons, bottom hinged flaps, wedge wavemakers, plunger wavemakers and it has also been used to predict the profile of wavemakers that would have no local, evanescent waves (Naito and Minoura, 1994; Falnes, 2002; Maguire and Ingram,

2011). Wavemaker theory has been validated experimentally using laboratory measurements comparing the stroke displacement of the wavemaker to the far field wave height, showing excellent agreement for small amplitude waves (Ursell *et al.*, 1960). This theory been expanded further into second-order wave maker theory by several authors (Sulisz and Hudspeth, 1993; Schäffer, 1996; Spinneken and Swan, 2009a). Linear wave theory will be used throughout this thesis as the basis for any wave tank discussions.

Experimental wave tanks (EWT) provide an excellent opportunity for engineers to assess their designs and analyse its characteristic response in a controlled environmental setting. Scaled testing provides an opportunity to explore parametric studies at less economic expense than at full scale and also the smaller scale test models allow for handling without cranes. In contrast to the ocean however, the size of EWT facilities are limited and, as such, the boundaries and walls of EWTs cause wave reflections which result in an unrealistic representation of the boundless ocean. This is a major issue in EWTs because, if waves are continuously reflecting off solid boundaries, over a period of time the wave reflections can build and contaminate the test domain thus shortening the test duration. In order to mitigate against these wave reflections, many EWTs have incorporated some form of wave absorption mechanism at the boundaries of the EWT. Wave absorbers can be broadly classified into two different categories: active and passive absorption.

2.1.1 Physical wave absorption

Passive wave absorbers try to damp out any impinging waves on solid boundaries other than the wavemakers and ensure that there are no reflections back into the test domain. The most common form of passive absorption is a beach with constant slope but: transversal bars, horsehair and wire screens are also commonly used (Ouellet and Datta, 1986). In order to achieve good levels of absorption, the slope of the beach must be mild (typically $\leq 1:10$). This constraint puts pressure on size of the EWT as having a beach with a mild slope would consume a large proportion of the test domain or require a very large facility. Also, passive absorption does not account for any waves reflecting from the test device back to the wavemaker. These reflections can be significant, especially in coastal engineering applications.

The other option is to use a dynamic system to actively absorb incoming waves,

commonly referred to as; active absorption, absorbing wavemakers or reflection compensation systems. These wavemakers make some hydrodynamic measurement and move the wavemaker in such a manner that absorbs the incoming wave. In theory, it is possible to absorb regular waves perfectly by tuning the active system over a range of frequencies using active control. Several different techniques have been put into practice to achieve optimal control of wavemaking devices, the main difference is the choice of which quantity to measure and the location of the measurement.

One method employed to absorb incoming waves uses the free surface elevations measured directly on the wavemaker (Bullock and Murton, 1989; Schäffer *et al.*, 1994; Ito *et al.*, 1996; Nohara, 1998; Liu *et al.*, 2003). The advantage of mounting the wave sensors on the wavemaker is that they take measurements using a Lagrangian frame of reference. Lagrangian dynamics are reportedly more linear than and Eulerian reference frame, extending the range of validity of linear wave theory (Woltering and Karl-Friedrich, 1994). The evanescent wave is a standing wave that decays with distance from the wavemaker. If the elevation is measured on the wavemaker front, the evanescent wave needs to be accounted for and this can complicate the procedure.

Another similar approach is to mount the wave gauges at some distance ahead of the wavemaker (Milgram, 1970; Christensen and Frigaard, 1994; Frigaard and Brorsen, 1995; Nanri *et al.*, 2002). Several surface displacement measurements are taken and then the incoming wave field is separated from the desired wave field. The wavemaker is then moved in a manner that cancels out the incoming waves. This system has the advantage of having time to process the measurement before the wave arrives at the wavemaker, allowing for a more stable system. But, this extra distance can allow for errors in wave phase between the incoming wave and absorption signal to be introduced, and can lead to sub-optimal performance and stability issues (Schäffer and Klopman, 2000).

A different active absorption method uses force as the hydrodynamic feedback mechanism. Salter (1981) cites three advantages to this method. Force is an integral quantity measured over the entire wave maker front and using this measurement minimises any slight errors encountered with single point measurements. Force sensors can be entirely free from the chemical and biological vagaries of tank water. Most types of tank probes use either resistive gauges or capacitance gauges. Both of these are susceptible to corrosion, biological growths, oil and dust

residues, all of which require frequent recalibration which is unacceptable for a large array of wave makers. Finally, Salter cites the conservation of energy as another reason to choose force feedback. He states that the advantage of using a force measurement is its ease of combining it with a velocity measurement and therefore fixing the rate of energy given to the water. He argues that it is "better to provide the right amount of energy at each frequency than to try to enforce a sinusoidal form that the waves do not like". Thus, controlling energy bypasses many of the non-linearity problems that arise when generating steep waves.

The method of using Force as the hydrodynamic measurement has been studied by several authors, and is used as the active absorption method by one a prominent wavemaker designer, Edinburgh Designs. Maisondieu and Clément (1993) published their results on a force feedback feedforward control loop for a piston wave absorber. The problem considered was the absorption of water waves by the horizontal motions of a vertical plane in response to the hydrodynamic forces it experiences. Due to the lack of causality (Naito and Nakamura, 1985), optimal absorption cannot be achieved in polychromatic waves. In order to address this, a self adaptive control system for a piston wave absorber has been proposed where an adaptive tuning system is implemented to match the incident wave frequency (Chatry *et al.*, 1998). Further analysis on the simultaneous generation and absorption using force-controlled wavemakers (Spinneken and Swan, 2009b) and a theoretical transfer function for force-controlled wave makers (Spinneken and Swan, 2010) have also been published. Naito (2006) described the theory behind the generation of waves using a plunger wavemaker incorporating a force feedback absorption. The absorption force was implemented using a two coefficient control system; one coefficient proportional to velocity the other proportional to displacement. This form of absorption is analogous to the power take off mechanism used in wave energy converters.

The theory behind the extraction of energy by wave energy converters has been presented several times in the literature and is extensively reviewed by Falnes (2007). It has been shown that optimal control of wave energy, at a specific frequency, can be achieved using reactive control methods (Mei, 1976; Evans, 1981; Nebel, 1992). This can also be referred to as impedance matching or complex conjugate control (Salter *et al.*, 1976). This form of control aims to ensure that the control force is in phase with the excitation force via an imaginary component in the control algorithm. Reactive control can be implemented using a number of

control coefficients, but the majority of absorbing wavemakers and wave energy devices implement the impedance matching using just one real coefficient and one imaginary coefficient, either a mass term (Mei, 1976) or, more commonly, a spring term (Evans, 1981). A recent study has shown both of these methods do obtain optimal results at that specified control frequency, but the characteristic absorption absorption levels differ greatly at frequencies other than the specified control frequency (Price, 2009).

This thesis will present the first order wavemaker theory in Chapter 3 where hydrodynamics of conventional wavemakers will be discussed and for the first time, the hydrodynamic expressions and displacement transfer functions of two non-conventional wavemakers will also be presented. The wavemaker with no evanescent waves will be further analysed with respect to its absorption qualities as opposed to its wavemaking properties. As this wavemaker can obtain zero added mass at certain frequencies, the geometry can be considered as a control handle helping to increase the bandwidth of absorption in conjunction with active absorption techniques.

Chapter 4 investigates the control strategies that can be used with absorbing wavemakers. Drawing upon the theory of wave energy conversion, special attention is paid to the difference that control coefficient selection makes on the capture width and what role the tuning frequency plays. It contrasts the results between using one, two or three control coefficients in an absorbing wavemaker and also explores the influence that wavemaker geometry control has on the absorption characteristics. It looks at absorption levels when both the control system and the geometry can be optimised separately and concurrently.

2.2 Numerical wave modelling

Experimental wave tanks (EWT) have been, and still are, an indispensable tool for any engineer working within coastal and ocean engineering. However, they are expensive facilities in both capital expenditure and operational expenditure terms. There is only a limited number world wide. Extracting specific data measurements that are both accurate and precise can be troublesome. It can be hard to manufacture an appropriate scale model that will give a realistic representation of the full scale device, and, conflicting non-dimensional scaling laws can make estimation of full scale characteristics difficult.

Computers are now capable of providing an analogue to the experimental wave tank: the numerical wave tank (NWT). The NWT can offer large benefits to the design engineer compared to an experimental facility, mainly through cost and space saving, but the NWT also has the advantage of being able to provide a vast array of parametric point measurements all over the test domain. The objectives of using an NWT can fall into two categories: reproduce physical wave tanks as closely as possible or to reproduce real sea conditions as closely as possible (Tanizawa, 2000). For this thesis, the emphasis will be on the reproduction of physical wave tanks in numerical software. If physical and numerical convergence between NWTs and EWTs can be achieved, the synergy that this would provide would result in powerful diagnostic tools for the design engineer.

2.2.1 Numerical wave generation

In order to generate a wave within a NWT there are a number of options available. The wave generation can either be imitative of physical wave tank generation or artificially induced.

For physical wave generation, the waves are created as a result of forced oscillations of a solid boundary. The wavemakers are directly analogous to those used in physical wave tanks and have been implemented numerically, such as piston-type wavemakers (Clément and Mas, 1995; Huang *et al.*, 1998; Tanizawa and Naito, 1999; Duclos *et al.*, 2001; Dong and Huang, 2004; Wang *et al.*, 2007), flap-type wavemakers (Westhuis, 2001; Bonnefoy *et al.*, 2006; Lal and Elangovan, 2008; Silva *et al.*, 2010), and plunger-type wavemakers (Koo and Kim, 2005). This type of implementation of a physical wavemaker in an NWT is relatively straight forward and easy to execute as long at the numerical solver can model moving boundaries or 6 degree of freedom bodies. It also has the benefit of there being a well known analytical solution for a propagating wave in a flume (Ursell *et al.*, 1960).

There are a number of methods that can be employed to implement an artificial numerical wave generation. One such method is to use space-periodic waves, where the propagation is imposed via space-periodic boundary conditions on the tank walls (Kim *et al.*, 1999). This method is limited in application due to the requirement of periodicity.

Another method is to impose a velocity condition on the inflow boundary (Park,

2004; Westphalen *et al.*, 2008, 2009). The velocity potential can be obtained from linear wave theory or a higher-order stokes waves and used to generate a propagating wave. The advantage of using this technique is that there will be no local evanescent wave present. This method can be a little more difficult to implement and some problems with extra mass entering the numerical domain are possible.

Chapter 6 concentrates upon the generation of waves in a NWT using physically realisable methods and does not explore the method of numerical wave generation. This is in order to allow for validation against linear wave theory and also to allow for analysis of physical and numerical convergence.

2.2.2 Numerical wave absorption

Similar to EWTs, NWTs suffer from wave reflections rebounding off the numerical boundaries of the tank and spoiling the test domain. NWTs offer a number of different solutions to absorb unwanted wave reflections, some methods analogous to those used in EWTs and others employ purely numerical solution to deal with the unwanted waves.

One of the simplest methods used to numerically absorb waves is via the implementation of a periodic boundary condition (Longuet-Higgins and Cokelet, 1976). Here the solution is assumed to be periodic in space and the values both vertical boundaries but, as mentioned earlier, this method has limitations due to the periodicity.

Another method commonly used in NWTs is the application of artificial damping to the free surface or the dynamic and kinematic conditions in order to damp out wave propagation, often also referred to as sponge layers (Romate, 1992; Israeli and Orszag, 1981). For this method, a specific region within the test domain is designated as the damping zone. Waves pass through this region, lose energy, reflect off the boundary and again are subjected to energy loss. Sponge layers have been shown to be very effective at absorbing high-frequency waves but, these methods do not perform as well for low-frequency waves (Clément, 1996).

There are several other numerical techniques used to absorb outgoing waves such as: simple far field solutions, differential equations matching the outer solution and Sommerfeld-Orlanski conditions. These methods require that either knowledge of the wave frequency is known *a priori* or, the waves need to be monochromatic. As

this thesis is investigating the physical and numerical generation and absorption of waves, these non-physical absorption methods will not be explored further, reviews by Givoli (1991); Romate (1992); Grilli and Horrillo (1997) cover the topics of absorption by numerical techniques in more detail.

Clément (1996) proposed combining a sponge layer which has good absorption characteristics for high-frequency waves with an absorbing piston, that has good low-frequency absorption characteristics. The Absorbing piston boundary condition in analogous to the physical methods of absorption discussed previously. The piston will move in a manner that cancels out the reflected wave based upon the wave force measured on its surface. The combination of both of these methods provides better absorption characteristics across a broader range of spectral bandwidth than using either in isolation.

The piston geometry used by Clément (1996) has good absorption qualities for low-frequency waves in shallow waters but a bottom hinged flap would be more suited to intermediate and deep-water waves. Chapter 4 will quantify the levels of absorption for both a piston and a bottom hinged flap and also explore using a hyperbolic cosine wavemaker to achieve optimal absorption for a specific wavenumber. Further to this investigation into the effect of geometry on absorption, the influence of control strategy will also be investigated. The results of both studies could more readily be applied to absorption of waves in NWTs than EWTs. These absorption methods of geometry control and improved reactive control could then be used in conjunction with a damping sponge-layer similar to the method proposed by Clément (1996), but with better absorption characteristics than using a piston.

2.2.3 Numerical wave models

There are a multitude of numerical wave models available to be used. Numerical wave models can be classified according to a number of categories based upon what kinds of problems that the models solve.

The most commonly used numerical model for large scale wave motion is the spectral model. This type of model assumes that the sea state is composed of an infinite number of waves whose wave heights are a function of frequency and direction (Pengzhi, 2008). There are a number of different implementations of this type of model (Hasselmann *et al.*, 1988; Tolman, 2009), which are used for

large scale oceanographic models and can be coupled with atmospheric models to predict a global wave climate. Shallow water approximations can be applied to approximate wave-current interaction in the large-scale near shore environment and can be used to estimate local wave energy flux and gradients (Ris *et al.*, 1999). As these models are in the frequency domain, they are phase-averaged and the computational grid can be larger than a wavelength. This results in relatively quick computational times, but the limitations imposed by phase-averaging means that the diffraction of waves around a body or a time domain solution cannot be offered by a spectral model.

The Boussinesq equation models are phase resolving and can be used to model the wave climate near shore and on a smaller spatial scale than the spectral models (Kirby *et al.*, 1998; Madsen *et al.*, 2006; Zhang *et al.*, 2007). These models are depth averaged with the dispersion terms partially representing vertical fluid transport, but they should only seriously be considered for intermediate water depths (Pengzhi, 2008). These models are quick at representing a time domain representation of intermediate water depths and, are used for simulation of water waves in shallow seas and harbours. They are not suitable to calculate wave forces on a radiating body or for use as a NWT.

Potential flow codes obtain Boundary Integral Equations (BIE) from the Laplace equations and they are solved numerically using Boundary Element Methods (BEM) (Tanizawa, 2000). These numerical codes can model non-linear waves in both shallow and deep waters, accounting for linear wave diffraction on oscillating bodies and wave force calculations on structures. As they use non-grid numerical methods they are not as computationally expensive as other grid based methods. Potential flow codes are used extensively for the hydrodynamic analysis of ships, oil platforms and wave energy converters as well as being used to model NWTs. The major drawback with potential flow codes is the assumption of inviscid irrotational flow. This means that complex flow around moving structures cannot be resolved properly, no turbulence or viscous losses can be accounted for and it is not capable of modelling breaking waves.

In order to model accurately an oscillating body and account for viscous and rotational flow, the Navier-Stokes equations need to be solved. Many Navier-Stokes solvers are commonly referred to as Computational Fluid Dynamic (CFD) solvers. The Navier-Stokes equations account for mass, momentum and energy conservation that allows them to accurately describe many types of fluid flow, including

water waves. This type of numerical model is highly versatile, allowing for modelling of breaking waves, air entrainment, fluid-structure-interaction, multi-phase flow to name but a few. The main draw back with using CFD solvers is the computational time. In order to solve a problem using CFD, it would be far more computationally expensive than any of the other numerical wave methods discussed earlier. However, with the advent of high speed, multi-core processing the range of problems that CFD can be used for is expanding. Recent attempts have been made to use CFD to model a NWT (Huang *et al.*, 1998; Kim *et al.*, 2001; Apsley and Hu, 2003; Park, 2004; Dong and Huang, 2004; Wang *et al.*, 2007) but mostly using in-house, bespoke codes. General purpose commercial CFD codes have advanced significantly in the area of free surface flow modelling and now offer the possibility to industry to use CFD in the assessment and appraisal of coastal and ocean engineering applications. Taking into consideration the large benefits that are to be had through solving the full Navier-Stokes equations for fluid flow, Chapter 6 will examine two commercial codes for use as a NWT. Herein, a user's perspective will be adopted, looking at the wavemaking process in particular and examining the fidelity of the waves generated in the CFD code.

2.3 Thesis outline

This thesis will analyse the absorption of waves from both a theoretical and numerical perspective. Chapter 3 will look at the hydrodynamics of wavemakers and use linear wavemaker theory to present analytical hydrodynamic coefficients for conventional wavemakers and for non-conventional wavemakers with varying geometries. Chapter 4 presents and quantifies the absorption characteristics associated with wavemakers under different control schemes. It will then analyse the benefits of combining different wavemaker geometries with various absorption control schemes.

Then this thesis will examine the possibility of implementing the aforementioned theory in a commercial Navier-Stokes solver. Upon review of the literature it is clear that a rigorous verification and validation is needed to be conducted on these codes to assess the fidelity of the propagating wave. Chapter 5 will describe the formal verification process of the numerical codes considered within this thesis. Chapter 6 presents the results of the verification and validation process on two commercial Navier-Stokes solvers, conducted from a users perspective,

concentrating on how well the codes can predict radiating waves from a numerical wavemaker in a numerical wave tank.

Chapter 3

Theory: gravity waves and wavemakers

Real water waves are viscous waves, propagating over uneven surfaces of varying permeability, can be highly non-linear, can be breaking waves with air entrainment and can interact with structures of varying sizes and shapes. Considering this, it is surprising that linear wave theory which assumes irrotational, inviscid flow and infinitesimally small waves can be used to predict the behaviour of real water waves. Remarkably, for large number of situations, water waves can be accurately modelled using potential flow theory. The use of potential flow simplifies the mathematical analysis and is a powerful tool for the design engineer.

This chapter, which closely follows Falnes (2002, Chap. 4 & 5), will present the areas of linear wave theory needed to calculate the hydrodynamic coefficients of wavemakers. The linear wave theory will be used to derive analytical expressions for the added mass and damping of four wavemakers with different shape profiles. Two of the wavemakers are commonly used in hydrodynamic laboratories and their analytical hydrodynamic expressions are well known. The other two wavemakers are different as one will generate waves without any evanescent waves and the other will generate waves without any progressive waves. Their analytical expressions will be presented and graphed for the first time and a transfer function relating the far field wave height to the stroke amplitude will also be presented.

3.1 Boundary Value Problems

If we consider two fundamental fluid dynamic concepts, namely that mass and momentum are conserved, will lead us to the continuity equation,

$$\frac{\partial \rho}{\partial t} + \bigtriangledown \cdot (\rho \vec{v}) = 0, \tag{3.1}$$

and the Navier-Stokes equation

$$\frac{D\vec{v}}{Dt} = \frac{1}{\rho}\nabla p_{tot} + \nu \nabla^2 \vec{v} + \frac{1}{\rho}\vec{f}, \tag{3.2}$$

where $\frac{D}{Dt}$ is the material derivative, $\vec{v}$ is the velocity of the fluid element, ρ is the fluid density, p_{tot} is the the fluid pressure and ν is the kinematic viscosity and $\vec{f}$ is the external force per unit volume, here only gravitational forces $\vec{g}$ will be considered, $\vec{f} = \rho\vec{g}$.

If it is assumed that the fluid is incompressible, then ρ is constant and the continuity equation reduces to

$$\nabla \cdot \vec{v} = 0. \tag{3.3}$$

Considering the fluid to be inviscid and that only a gravitational force exists. Then Eq. 3.2 can be reduced to

$$\frac{\partial \vec{v}}{\partial t} + \vec{v} \cdot \nabla \vec{v} = \frac{1}{\rho}\nabla p_{tot} + \vec{g}. \tag{3.4}$$

Falnes (2002) makes use of the vector identity

$$\vec{v} \times (\nabla \times \vec{v}) \equiv \frac{1}{2}\nabla v^2 - \vec{v} \cdot \nabla \vec{v} \tag{3.5}$$

and takes the curl of Eq. 3.4 to give

$$\frac{\partial}{\partial t}(\nabla \times \vec{v}) = \nabla \times \left(-\frac{1}{2}\nabla v^2 + \vec{v} \times (\nabla \times \vec{v}) - \frac{1}{\rho}\nabla p_{tot} + \vec{g} \right). \tag{3.6}$$

Using the vector identity $\nabla \times \nabla\varphi \equiv 0$ for any scalar function, φ, and recognising that $\vec{g}$ is the gradient of a gravitational potential, gz, thus $\nabla \times \vec{g} = 0$, yields

$$\frac{\partial}{\partial t}(\nabla \times \vec{v}) = \nabla \times [\vec{v} \times (\nabla \times \vec{v})]. \tag{3.7}$$

Assuming that the fluid flow is irrotational initially, $\nabla \times \vec{v} = 0$, then the flow will continue to be irrotational because $(\partial/\partial t)(\nabla \times \vec{v}) = 0$ and

$$\nabla \times \vec{v} \equiv 0. \tag{3.8}$$

Using the vector identity $\nabla \times \nabla\phi \equiv 0$ to give

$$\vec{v} = \nabla\phi, \tag{3.9}$$

where, ϕ is the velocity potential. Inserting this into Eq. 3.4 gives

$$\nabla \left(\frac{\partial \phi}{\partial t} + \frac{v^2}{2} + \frac{p_{tot}}{\rho} + gz \right) = 0. \tag{3.10}$$

Using Eq. 3.5 and that $\vec{g} = -\nabla(gz)$ and integrating gives

$$\frac{\partial \phi}{\partial t} + \frac{v^2}{2} + \frac{p_{tot}}{\rho} + gz = C \tag{3.11}$$

where, C is the integration constant.

For the static case, when the fluid is not in motion, $\vec{v} = 0$ and ϕ is constant, Eq. 3.11 gives

$$p_{tot} = p_{stat} = -\rho g z + \rho C. \tag{3.12}$$

At $z = 0$, on the free surface, the total pressure, p_{tot}, equals the atmospheric pressure, p_{atm}. This gives a solution to the integration constant, $C = p_{atm}/\rho$ and thus,

$$p_{stat} = -\rho g z + p_{atm} \tag{3.13}$$

and as can be seen, this hydrostatic pressure, p_{stat}, increases linearly with distance from the free surface.

Due to the conditions that the flow is in-compressible and irrotational, conservation of mass requires that the Laplace equation

$$\nabla^2 \phi = 0 \tag{3.14}$$

is satisfied throughout the flow field. Solutions to this partial differential equation must satisfy certain boundary conditions. The most interesting boundary conditions to us are the water-air interface at the free surface, and the water-solid

interface where fluid encounters a solid impermeable boundary.

If a solid body is moving through the fluid with a velocity $\vec{u}$ then we have

$$\frac{\partial \phi}{\partial n} = u_n \tag{3.15}$$

where, $\vec{n}$ is the unit normal on the solid boundary. Conversely if the solid surface is not in motion, then

$$\frac{\partial \phi}{\partial n} = 0. \tag{3.16}$$

A follow on from the solid-body boundary condition, is that on the bottom of the domain, there is no flow normal to the sea floor, thus giving the bottom boundary condition,

$$\frac{\partial \phi}{\partial z} = 0 \quad \text{at } z = -h. \tag{3.17}$$

The free surface boundary is located at $z = \eta(x, y, t)$, where η is the displacement of the free surface about the horizontal plane, $z = 0$. A defining characteristic of a free surface is that they cannot support variations in pressure (neglecting surface tension) and needs to respond to ensure that the pressure remains uniform across the interface. A dynamic boundary condition is needed to prescribe the pressure distribution on this boundary. This boundary condition can be obtained from the Bernoulli Equation (non-stationary), Eq. 3.11, and assuming that the total pressure equals atmospheric pressure, $p_{tot} = p_{atm}$ at $z = \eta$, then

$$\left[\frac{\partial \phi}{\partial t} + \frac{v^2}{2}\right]_{z=\eta} + g\eta = C - \frac{p_{atm}}{\rho}. \tag{3.18}$$

The integration constant $C = p_{atm}/\rho$, and this results in the right hand side tending to zero. Making use of Eq. 3.5, the free surface boundary condition can be represented as

$$g\eta + \left[\frac{\partial \phi}{\partial t} + \frac{1}{2}\nabla\phi \cdot \nabla\phi\right]_{z=\eta} = 0. \tag{3.19}$$

If we assume that the higher order terms are negligible the dynamic boundary condition can be represented as

$$g\eta + \left[\frac{\partial \phi}{\partial t}\right]_{z=\eta} = 0. \tag{3.20}$$

The kinematic free surface boundary condition dictates that a fluid particle on

the interface remains on the interface and is represented as

$$\left[\frac{\partial^2\phi}{\partial t^2} + g\frac{\partial\phi}{\partial z}\right]_{z=0} = 0. \tag{3.21}$$

The velocity potential $\phi = \phi(x, y, z, t)$ is a mathematical scalar function whose gradient is equal to the velocity of the fluid, therefore the fluid velocity can be represented as

$$\vec{v} = \vec{v}(x, y, z, t,) = \nabla\phi. \tag{3.22}$$

The velocity potential also allows us to derive the hydrodynamic pressure from the dynamic part of Eq. 3.11

$$p = p(x, y, z, t,) = -\rho(\frac{\partial\phi}{\partial t} + \frac{v^2}{2}) \approx -\rho\frac{\partial\phi}{\partial t} \tag{3.23}$$

where the second order terms have been neglected.

The free-surface elevation at the water-air interface can now be obtained from

$$\eta = \eta(x, y, z, t) = -\frac{1}{g}\left[\frac{\partial\phi}{\partial t}\right]_{z=0} \tag{3.24}$$

3.2 Harmonic Waves

When dealing with waves, it is often useful to work in the frequency domain rather than the time domain. The frequency domain makes use of linear waves and the superposition principle. The frequency domain simplifies the system of equations making them easier to solve, but care should be taken when reverting back to the time domain. This section will present a solution that satisfies the Laplace equation assuming a horizontal sea bed and a free surface with constant pressure at the air-water interface for a body with periodic motions of $2\pi/\omega$.

When considering harmonic waves in deep water with sinusoidal time variation, we can write

$$\phi = \phi(x, y, z, t) = \Re\left\{\hat{\phi}(x, y, z)e^{i\omega t}\right\} \tag{3.25}$$

where $\hat{\phi}$ is the complex amplitude of the velocity potential. Similarly the parmeters of velocity, pressure and free-surface can be defined using complex amplitudes.

Now, in terms of complex amplitudes, the equations describing the physical flow quantities, Eqs. 3.22-3.24, are given as

$$\hat{\vec{v}} = \nabla\hat{\phi}, \tag{3.26}$$

$$\hat{p} = -i\omega\rho\hat{\phi}, \tag{3.27}$$

$$\hat{\eta} = -\frac{i\omega}{g}\left[\hat{\phi}\right]_{z=0} \tag{3.28}$$

and the homogeneous boundary conditions that will be used to satisfy the Laplace equation, state that on the sea bed, $z = -h$, there is no flow normal to it and that pressure is constant on the water-air interface, $z = 0$,

$$\left[\frac{\partial\hat{\phi}}{\partial z}\right]_{z=-h} = 0, \tag{3.29}$$

$$\left[-\omega^2\hat{\phi} + g\frac{\partial\hat{\phi}}{\partial z}\right]_{z=0} = 0. \tag{3.30}$$

Separation of variables is a method of solving ordinary and partial differential equations. It allows us to rewrite an equation so that each of two variables occurs on a different side of the equation. Again, following Falnes (2002) and using this method, we seek a solution in the form of

$$\hat{\phi}(x, y, z) = H(x, y)Z(z). \tag{3.31}$$

Substituting into the Laplace Equation, Eq. 3.26, and dividing by $\hat{\phi}$ we have

$$-\frac{1}{Z}\frac{d^2Z}{dz^2} = \frac{1}{H}\left[\frac{\partial^2 H}{\partial x^2} + \frac{\partial^2 H}{\partial y^2}\right] \equiv \frac{1}{H}\nabla_H^2 H \tag{3.32}$$

The term on the left hand side depends on z alone, while the right hand side depends on x and y. If we were to hold the left-hand term, z, the second term could conceivably vary, thus resulting in a non-zero sum. This is obviously not possible. The only way that this equation can exist is if each term is equal to the same constant, say $-k^2$, except for a sign change thus we have

$$\frac{d^2Z(z)}{dz^2} = k^2Z(z) \tag{3.33}$$

$$\nabla_H^2 H(x, y) = -k^2 H(x, y). \tag{3.34}$$

It can be seen that Eq. 3.33 has a solution of the form

$$Z(z) = c_+ e^{kz} + c_- e^{-kz}, \tag{3.35}$$

where, c_+ and c_- are integration constants. As we have two new integration constants when solving the two dimensional Helmholtz Equation, Eq. 3.34, for H, we may choose Z(0) = 1, giving $c_+ + c_- = 1$. Using this and Eq. 3.35 gives

$$c_+ e^{-kh} = (1 - c_+)e^{kh}, \tag{3.36}$$

$$c_+ = \frac{e^{kh}}{e^{-kh} + e^{kh}}. \tag{3.37}$$

Similarly, a solution for c_- can be obtained as

$$c_- = \frac{e^{-kh}}{e^{-kh} + e^{kh}}. \tag{3.38}$$

It now follows from Eq. 3.35 that

$$Z(z) = \frac{e^{k(z+h)} - e^{k(z+h)}}{e^{kh} + e^{-kh}} = \frac{\cosh(kz + kh)}{\cosh(kh)} = e(kz), \tag{3.39}$$

thus giving the following particular solution to the Laplace solution:

$$\hat{\phi} = H(x, y)e(kz) \tag{3.40}$$

In order to satisfy the homogeneous free-surface boundary condition, Eq. 3.30, we require

$$\omega^2 = \omega^2 e(0) = g\left[\frac{de(kz)}{dz}\right]_{z=0} = gk\frac{\sinh(kh)}{\cosh(kh)} = gk\tanh(kh), \tag{3.41}$$

where this expression is the well known dispersion equation, describing the manner in which polychromatic waves separate or disperse due to the different wave speeds of the various frequency components.

Rearranging this equation, the dispersion relationship can be expressed as

$$\frac{\omega^2 h}{g\,kh} = \tanh(kh). \tag{3.42}$$

It can be easily observed from Figure 3.1 that there is only one real positive

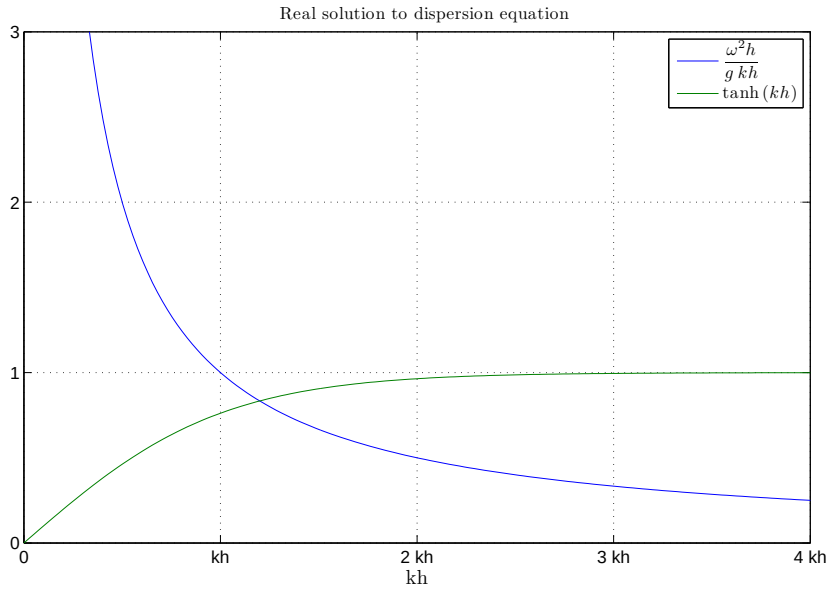

Figure 3.1: Graphical solution to real part of the dispersion equation showing the single positive root. Here $\omega^2 h/g = 1$.

solution, represented by the intersection of the two graphs. There is also a corresponding negative solution with the same absolute value, meaning that there is only one positive value for the separation constant k^2 in Eq. 3.33 and Eq. 3.34.

Therefore we can replace k^2 by λ_n and $\hat{\phi}(x, y, z) = Z(z)H(x, y)$ by

$$\hat{\phi}_n(x, y, z) = Z_n(z)H_n(x, y) \tag{3.43}$$

and re-write the boundary conditions, Eq. 3.33 and Eq. 3.34 as

$$Z_n''(z) = \lambda_n Z_n(z), \tag{3.44}$$

$$\nabla_H^2 H(x, y) = -\lambda_n H(x, y). \tag{3.45}$$

Here λ_n is the eigenvalue and Z_n is the corresponding eigenfunction and the subscript n is to label all of the possible solutions for $n \geq 0$.

It has been shown that there is only one positive eigenvalue, k^2, to the dispersion equation, Eq. 3.42,

$$\lambda = k^2 \equiv \lambda_0 \tag{3.46}$$

and therefore it follows that all other eigenvalues must be negative

$$\lambda_n = -m_n^2 \tag{3.47}$$

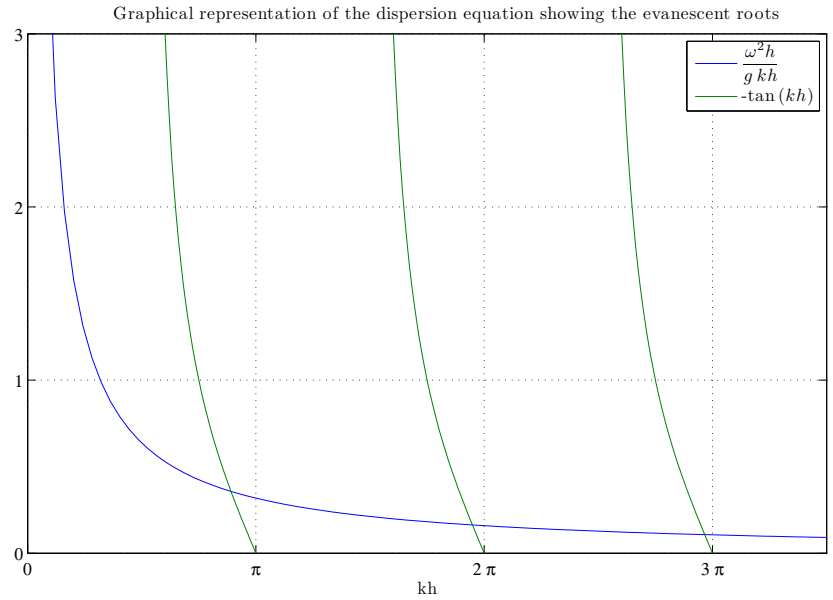

Figure 3.2: Graphical solution for the evanescent solutions to the dispersion equation up to $k_n h = k_3 h$. Again, for this graph $\omega^2 h/g = 1$

for $n \geq 1$.

To obtain the negative eigenvalues, we replace k by $-im_n$ in the dispersion equation to obtain,

$$\omega^2 = -im_n g \tanh(-im_n h) = -m_n g \tan(m_n h). \tag{3.48}$$

As is seen in Figure 3.2, there are an infinite amount of real positive solutions for m_n and the solutions lie in the interval

$$(n-1)\frac{\pi}{h} < m_n < \frac{n}{h} \quad \text{for } n = 1, 2, 3... \tag{3.49}$$

Thus the set of eigenvalues are

$$\{\lambda_0, \lambda_1, \lambda_2, \ldots, \lambda_n, \ldots\} = \left\{k^2, -m_1^2, -m_2^2, \ldots, -m_n^2, \ldots\right\}. \tag{3.50}$$

If the eigenfunctions are normalised such that

$$\int_{-h}^{0} |Z_n(z)| dz = 1, \tag{3.51}$$

Falnes (2002) sets

$$Z_n(z) = h {N_n}^{-1/2} \cos(m_n(z+h)) \tag{3.52}$$

where $N_n^{-1/2}$ is an arbitrary integration constant.

This constant can be obtained by using Eq. 3.51

$$1 = (hN_n)^{-1} \int_{-h}^{0} \cos^2(m_n(z+h))dz \tag{3.53}$$

$$N_n = \frac{1}{h} \int_{-h}^{0} \cos^2(m_n(z+h))dz \tag{3.54}$$

$$= \frac{1}{2}\left(1 + \frac{sin(2m_n h)}{2m_n h}\right). \tag{3.55}$$

For the case where $n = 0$, $m_0 = ik$ and

$$Z_0(z) = h{N_0}^{-1/2} \cosh(k(z+h)) \tag{3.56}$$

$$N_0 = \frac{1}{2}\left(1 + \frac{sinh(2kh)}{2kh}\right). \tag{3.57}$$

In order to obtain a solution to the Helmholtz equation, Eq. 3.44, we set $\partial/\partial y = 0$ and use Eq. 3.47 which yields a solution

$$H_n(x) = a_n e^{-m_n x} + b_n e^{m_n x}, \tag{3.58}$$

where, a_n and b_n are integration constants. Now, from Eq. 3.43 the complex amplitude of the velocity potential can be expressed as

$$\hat{\phi}(x,z) = \left(a_n e^{-m_n x} + b_n e^{m_n}\right) Z_n(z). \tag{3.59}$$

This represents one particular solution that satisfies Eq. 3.29 and Eq. 3.30. For the full set of solutions, linear superposition can be used to give the complex amplitude of the velocity potential

$$\hat{\phi}(x,z) = \sum_{n=0}^{\infty} \left(a_n e^{-m_n x} + b_n e^{m_n}\right) Z_n(z). \tag{3.60}$$

3.2.1 Radiation from an oscillating body

If a rigid body oscillates in water, radiated waves will be generated and in turn there will be a hydrodynamic force acting on the body, commonly referred to as the radiation force. This section will use the theory described in Section 3.2 and discuses the interaction between an oscillating body and water waves. It will look at the hydrodynamic force acting on a body and will show how to derive the radiation impedance matrix for an oscillating body.

Modes of Oscillatory motion

A rigid body oscillating in water, in three dimensions has 6 modes of motion; surge (1), sway (2), heave (3), roll (4), pitch (5) and yaw (6). This motion will radiate a wave with a velocity potential, $\hat{\phi}_r$, which will be a linear combination of the radiated waves caused by each of the six oscillation modes,

$$\hat{\phi}_r = \sum_{j=1}^{6} \varphi_j \hat{u}_j, \tag{3.61}$$

where subscript j represents the mode of oscillation. Falnes (2002, sect 5.1.1) uses $\varphi_j = \varphi_j(x, y, z)$ as a complex coefficient of proportionality and shows that the coefficient φ_j must satisfy;

$$\frac{\partial \varphi_j}{\partial n} = n_j \quad \text{on } S \tag{3.62}$$

where S is the wetted surface of the oscillating body, Figuire 3.3. And φ must satisfy the same homogeneous boundary conditions as ϕ_r, namely the Laplace equation, Eq. 3.14, bottom boundary condition, Eq. 3.29, and free surface boundary condition, Eq. 3.30.

3.2.2 Hydrodynamic force on a rigid body

The hydrodynamic force acting on a body can be obtained by integrating the pressure over the surface area of the wetted surface. Recalling that the pressure, $\hat{p} = -i\omega\rho\hat{\phi}$, then the force acting in surge can be represented as

$$F_1 = -\int\int_S p n_1 dS \tag{3.63}$$

$$\hat{F}_1 = i\omega\rho \int\int_S \hat{\phi} n_1 dS, \tag{3.64}$$

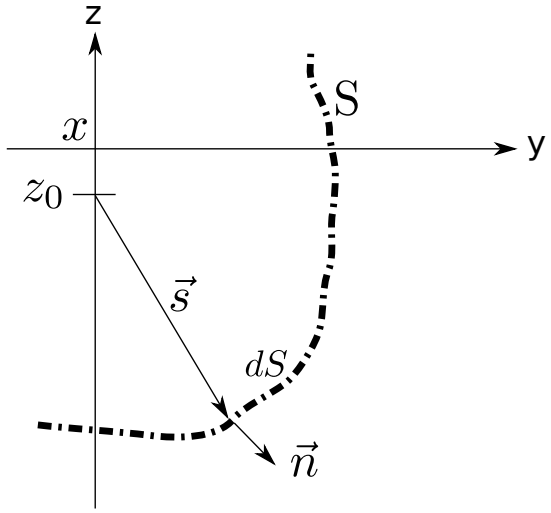

Figure 3.3: A surface element of a rigid body oscillating in water where the vector $\vec{s}$ gives the position of a point on the wet surface S and $\vec{n}$ is the unit normal vector

where $F_1 \equiv F_x$ and similar expressions can be obtained for heave, F_2 and sway. F_3.

The next three components of force: $F_4,\ F_5,\ F_6$, are moment forces about the three respective axes, $x,\ y,\ z$. The complex amplitude of the force moment can be expressed as

$$\hat{M}_x = i\omega\rho \int\int_S \hat{\phi} n_4 dS, \tag{3.65}$$

again similar expressions can be obtained for pitch, M_y and yaw, M_z[1].

Thus for an arbitrary velocity potential, $\hat{\phi}$, the complex force can be represented as

$$\hat{F}_j = i\omega\rho \int\int_S \hat{\phi} n_j dS \quad \text{for} \quad j = 1, 2, .., 6. \tag{3.66}$$

For a body floating on water, a hydrodynamic force can arise from various sources. The most obvious force is when a water wave impinges upon the body. If the body is fixed, this force is referred to as the excitation force, F_e. There will be a resulting force arising from the interactions between the incident wave and the fixed body, this is referred to as diffracted wave. The diffraction force is often neglected in engineering analysis and in particular if the immersed body is small compared to the wavelength of the incident wave.

1. It should be noted that $(n_1, n_2, n_3) \equiv (n_x, n_y, n_z) = \vec{n}$ and $(n_4, n_5, n_6) = \vec{s} \times \vec{n}$

If a body is free to oscillate in water, a wave will be radiated away from the body, thus giving rise to a radiation force. The radiated wave associated with a velocity potential, $\hat{\phi}_r$ is given by

$$\hat{\phi}_r = \varphi_j \hat{u}_j. \tag{3.67}$$

Thus from Eq. 3.66, the j' component of the radiation force is given as

$$\hat{F}_{r,j'} = i\omega\rho \int\int_S \varphi_j \hat{u}_j n_{j'} dS. \tag{3.68}$$

Now we will introduce an element called the radiation impedance matrix,

$$Z_{j'j} = -i\omega\rho \int\int_S \varphi_j n'_j dS \tag{3.69}$$

or, recalling Eq. 3.62 gives,

$$Z_{j'j} = -i\omega\rho \int\int_S \varphi_j \frac{\partial \varphi_{ji}}{\partial n} dS \tag{3.70}$$

and re-write the radiation force as

$$\hat{F}_{r,j'} = -Z_{j'j}\hat{u}_j. \tag{3.71}$$

The impedance is a measure of how much a structure resists motion when subjected to a given force. The subscripts on the impedance matrix, $Z_{j'j}$, refer to the j' component of the reaction force due to the wave radiated from mode j which is oscillation with a unit amplitude of $\hat{u}_{j'} = 1$.

As can be seen from Eq. 3.70, the impedance matrix is composed of both real and imaginary components. As ω is real, the impedance matrix is often split into its real and imaginary components;

$$Z_{j'j} = R_{j'j} + iX_{j'j} = R_{j'j} + i\omega m_{j'j} \tag{3.72}$$

where, R is referred to as the resistance, X is the reactance and m is the added mass.

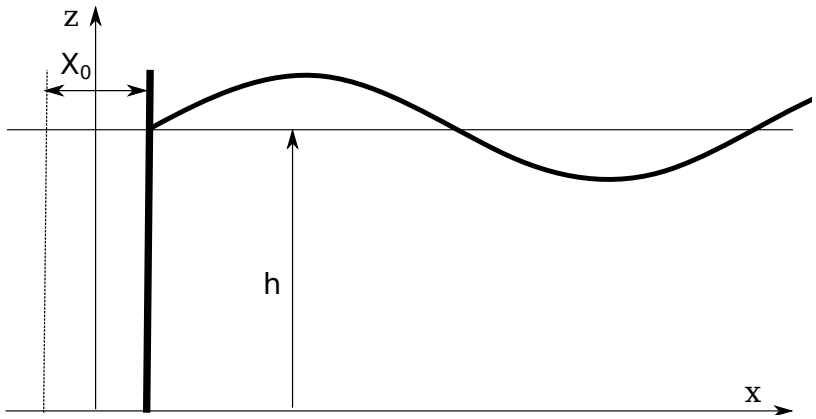

Figure 3.4: Definition plot of wavemaker showing a wavemaker able to oscillate in surge, in water depth, h.

3.3 Wavemaker hydrodynamics

A wavemaker generates progressive waves via the oscillation of a rigid body. In many hydrodynamic laboratories this rigid body takes the form of either a piston or a bottom-hinged flap. If we assume that the wavemaker is two-dimensional, in a channel of constant water depth h, where Cartesian coordinates, x, y, z are used with $z = 0$ at the still water level and the positive z:axis directed upwards, the resulting velocity potential will take the form of Eq. 3.61. If we limit the oscillations to surge, $j = 1$, the inhomogeneous boundary condition, Eq. 3.62, is given as

$$\frac{\partial \varphi_1}{\partial x} = c(z) \quad \text{for } x = 0, \tag{3.73}$$

where, $c(z)$ is a function that defines the shape profile of the wavemaker.

The other relevant boundary conditions are the Laplace equation, Eq. 3.26, bottom boundary condition, Eq. 3.29, and the free-surface boundary condition, Eq. 3.30. As has been show, the solution to this boundary-value problem has been given by Eq. 3.60, and if the oscillation is just limited to surge, we can write the following solution,

$$\varphi_1 = c_0 Z_0(z) e^{ikx} + \sum_{n=1}^{\infty} c_n Z_n(z) e^{m_n x} = \sum_{n=0}^{\infty} X_n(x) Z_n(z) \tag{3.74}$$

where,

$$X_n(x) = c_n e^{m_n x}. \tag{3.75}$$

Here, m_n is the solution to the dispersion relationship, Eq. 3.42, and as has been

shown, Eq. 3.48, it is convenient to allow $m_0 = ik$.

The unknown constants, c_n, in Eq. 3.74 can be obtained if we use the boundary condition on the wavemaker, Eq. 3.73, at $x = 0$,

$$c(z) = \left[\frac{\partial \varphi_1}{\partial x}\right]_{x=0} = \sum_{n=0}^{\infty} X_n'(0) Z_n(z), \tag{3.76}$$

where, $X_n'(0)$ is used to represent $\frac{dX_n}{dx}|_{x=0}$, as X_n is purely a function of x. Multiplying by the complex conjugate, $Z_m^*(z)$, and integrating from $z = -h$ to $z = 0$, using the orthogonality condition yields

$$\int_{-h}^{0} c(z) Z_m^*(z) dz = \sum_{n=0}^{\infty} X_n'(0) \int_{-h}^{0} Z_m^*(z) Z_n(z) dz = X_m'(0) h. \tag{3.77}$$

That is

$$X_n'(0) = \frac{1}{h} \int_{-h}^{0} c(z) Z_n^*(z) dz. \tag{3.78}$$

Combining Eq. 3.78 and Eq. 3.75 yields

$$X_0'(0) = ikc_0, \tag{3.79}$$

$$X_n'(0) = m_n c_n, \tag{3.80}$$

thus giving the two coefficients

$$c_0 = \frac{1}{ikh} \int_{-h}^{0} c(z) Z_0^* dz, \tag{3.81}$$

$$c_n = \frac{1}{m_n h} \int_{-h}^{0} c(z) Z_n^* dz. \tag{3.82}$$

The free surface elevation of the radiated wave, from Eq. 3.28, can now be expressed as

$$\eta = \frac{i\omega}{-g} \left[\hat{\phi}_r\right]_{z=0} \tag{3.83}$$

$$= \frac{i\omega}{-g} \hat{u}_1 \sum_{n=0}^{\infty} c_n Z_n(0) e^{-m_n x}. \tag{3.84}$$

This expression represents both the progressive wave, $n = 0$ and the evanescent wave solutions, $n \geq 1$. The evanescent waves arise due to the mismatch between

the solid wavemaker and the velocity motion beneath a progressive first order wave. It can be seen from this expression that the evanescent waves decay exponentially with distance from $x = 0$ and at a distance of $x \gg h$, their contribution to the surface elevation becomes negligible.

The radiation impedance of a wavemaker, in a channel of width d, can be obtained from Eq. 3.70, where the term $R_{j'j}$ is the radiation resistance matrix and $X_{j'j}$ is the radiation reactance matrix. Care should be taken not to confuse the orthogonal set of eigenfunctions $Z_n(z)$ with the impedance $Z_{j'j}$,

$$Z_{11} = i\omega\rho d \int_{-h}^{0} \left[\varphi \frac{\partial \varphi_1^*}{\partial x} dz \right]_{x=0} \tag{3.85}$$

$$Z_{j'j} = R_{j'j} + iX_{j'j}. \tag{3.86}$$

$$\tag{3.87}$$

As the paddle motion is limited to one degree of motion, the subscripts relating to surge will be dropped hereafter. Thus the impedance for a wavemaker in surge is

$$\begin{aligned} Z(\omega) &= i\omega\rho d \int_{-h}^{0} \left[c_0 Z_0(z) + \sum_{n=1}^{\infty} c_n Z_n(z) \right] c^*(z) dz \\ &= \omega k \rho h d |c_0|^2 + i\omega\rho h d \sum_{n=1}^{\infty} m_n |c_n|^2. \end{aligned} \tag{3.88}$$

The radiation resistance, $R(\omega)$, is the real part of Eq. 3.88 and is commonly referred to as the hydrodynamic damping,

$$R(\omega) = \mathrm{Re}\left\{Z(\omega)\right\} = \omega k \rho h d |c_0|^2, \tag{3.89}$$

and the added mass, $m(\omega)$, is a product of the imaginary part of Eq. 3.88,

$$m(\omega) = \frac{1}{\omega} \mathrm{Im}\left\{Z\right\} = \rho h d \sum_{n=1}^{\infty} m_n |c_n|^2. \tag{3.90}$$

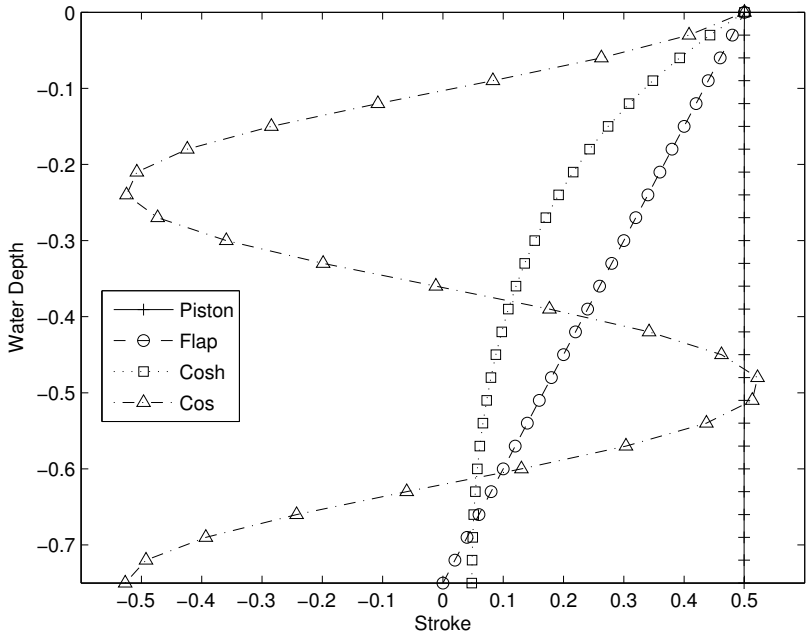

Figure 3.5: The four wavemaker surface profiles. The surface profile for the hyperbolic cosine wavemaker is chosen at a wavenumber of k_{0s}, the profile for the cosine wavemaker is plotted for k_{3s}, both at a fixed frequency of $\omega_s = 2\pi$

3.3.1 Hydrodynamic coefficients for different wavemaker geometries

The added mass and damping coefficients of a wavemaker are dependant on its surface profile, $c(z)$. Changes in the wavemaker's surface profile will result in very different hydrodynamic characteristics. This section presents the analytic expressions for added mass and damping for four different wavemaker types; a piston, a bottom hinged flap, a hyperbolic cosine shaped paddle, and a cosine shaped paddle, Figure 3.5. The piston and bottom hinged flap paddles are similar to those found in many hydrodynamic laboratories around the world. The other two wavemakers have been discussed in theory by Naito (2006) and Falnes (2002). They proposed that, if the paddle profile is chosen, such that it matches the wave field velocity profile of the waves, the evanescent contributions in Eq. 3.84 will be zero. The situation where a wave paddle does not generate any progressive waves and only a standing wave persists is also discussed. This is achieved by choosing a surface profile that results in no real part to the free surface expression, Eq. 3.84.

Derivation of hydrodynamic coefficients for a bottom hinged flap

Following Falnes' theory outlined in Section 3.3, the hydrodynamic coefficients for a bottom hinged flap, $c(z) = 1 + z/h$, can be derived. Using Eq. 3.81 and inserting the orthogonality condition, Eq. 3.52, yields

$$\begin{aligned} c_0 &= -\frac{1}{ikh} N_0^{-1/2} \int_{-h}^{0} (1 + z/h) \cosh(k(z+h)) dz \\ &= -\frac{1}{ikh} N_0^{-1/2} \frac{1 + kh \sinh(kh) - \cosh(kh)}{k^2 h} \\ &= \frac{i\,(1 + kh \sinh(kh) - \cosh(kh))}{k^3 h^2} \left(\frac{1}{2} + \frac{1}{4} \frac{\sinh(2kh)}{kh} \right)^{-1/2}. \end{aligned} \tag{3.91}$$

Thus, from Eq. 3.89 the damping for a bottom hinged paddle is

$$R(\omega) = 4 \, \frac{\omega \, \rho \, (1 + \sinh(kh)\, kh - \cosh(kh))^2}{k^4 h^2 \, (2\, kh + \sinh(2\, kh))}. \tag{3.92}$$

Similarly, combining Eq. 3.52 with Eq. 3.82 gives

$$\begin{aligned} c_n &= -\frac{1}{m_n h} N_n^{-1/2} \int_{-h}^{0} (1 + z/h) \cos(m_n(z+h)) dz \\ &= \frac{1}{m_n h} N_n^{-1/2} \frac{-1 + \cos(m_n\, h) + m_n\, h \sin(m_n\, h)}{{m_n}^2 h} \\ &= \frac{(-1 + \cos(m_n h) + m_n h \sin(m_n\, h))}{{m_n}^3 h^2} \left(\frac{1}{2} + \frac{1}{4} \frac{\sin(2 m_n h)}{m_n h} \right)^{-1/2} \end{aligned} \tag{3.93}$$

and the resulting added mass, Eq. 3.90, is

$$m(\omega) = 4\, \rho \sum_{n=1}^{\infty} \frac{(-1 + \cos(m_n h) + \sin(m_n h)\, m_n h)^2}{{m_n}^4 h^2 \, (2\, m_n h + \sin(2\, m_n h))}. \tag{3.94}$$

Both of these coefficients for added mass and damping are in agreement with Newman (2008) who presented these expressions but did not present the full derivation.

Derivation of hydrodynamic coefficients for a piston

For a piston wavemaker, $c(z) = \frac{S_0}{2}$ (where S_0 is the normalised stroke length). As $c(z)$ is not dependant on the water depth, z, a sinusoidal motion will result in the entire wave board moving in unison. Following the derivation shown in Section 3.3.1, gives the hydrodynamic coefficients of added mass and damping as,

$$m(\omega) = 4 \sum_{n=1}^{\infty} \frac{\rho \left(1 - (\cos(m_n h))^2\right)}{{m_n}^2 \left(2\, m_n h + \sin(2\, m_n h)\right)}, \tag{3.95}$$

and

$$R(\omega) = 4 \frac{\omega\, \rho \left((\cosh(kh))^2 - 1\right)}{k^2 \left(2\, kh + \sinh(2\, kh)\right)}. \tag{3.96}$$

Derivation of hydrodynamic coefficients for a hyperbolic cosine wavemaker

For there to be no evanescent waves, there should be no added mass. This can be achieved if the paddle profile, $c(z)$, matches that of the wave velocity profile

$$c(z) = \frac{\cosh(k_s(z+h))}{\cosh(k_s h)}. \tag{3.97}$$

Here, k_s is a fixed coefficient wavenumber at a frequency of ω_s that satisfies the real part to Eq. 3.42: $k_s = k(\omega_s)$, and the subscript s denoted a fixed coefficient (i.e. not dependant on frequency). Using this expression results in $c_n = 0$ for $n \geq 1$, ensuring only real solutions and hence no evanescent contributions to the free surface, Eq. 3.84.

The expressions for added mass and damping of a wavemaker with no evanescent waves, after some algebra, can be obtained as

$$m(\omega) = \sum_{n=1}^{\infty} \rho\, e^{-c} \left(\frac{(k_s e^c - k_s e^{b+c} - k_s e^b + k_s - i m_n + i m_n e^{b+c} - i e^b m_n + i m_n e^c)^2}{(2\, m_n h - i \sinh(c)) \left(e^b + 1\right)^2 \left({k_s}^2 + {m_n}^2\right)^2} \right) \tag{3.98}$$

and

$$R(\omega) = \omega\, \rho \left(\frac{(k e^{-i(b+ia)} - k + e^a k - k e^{-ib} - e^{-ib} k_s + k_s + e^a k_s - k_s e^{-i(b+ia)})^2}{4\,(a + \sinh(a)) \left(\cos\left(\frac{b}{2}\right)\right)^2 \left({k_s}^2 - k^2\right)^2} \right) e^{i(b+ia)} \tag{3.99}$$

where $a = 2kh$, $b = 2ik_s h$ and $c = 2im_n h$.

It should be noted that the wave number, $m_n = m_n(\omega)$, in Eq. 3.98 is frequency dependant and the wavemaker has no added mass at only one chosen frequency, ω_s. This type of wavemaker will herein be referred to as a hyperbolic cosine wavemaker, $\cosh(\omega_s)$, where ω_s designates the frequency at which the added mass tends to zero. Here, values of $\omega_s = \pi$, 2π and 3π will be considered, resulting in three different wavemaker geometries. The added mass for the wavemakers can be seen in Figures 3.6a, 3.6c, and 3.6e, and it is clear that the added mass, $m(\omega)$, tends to zero at the chosen design frequency, ω_s. All graphs presented within this paper are evaluated for a water depth of $h = 0.75$[m] and a width of $d = 0.5$[m].

Derivation of hydrodynamic coefficients for a cosine wavemaker

The other special case is when a paddle can move in such a way that no progressive wave is radiated, only a standing evanescent wave persists. This would be very difficult to achieve in a physical wavemaker, but could more easily be achieved in a numerical code, or as proposed by Naito (2006), using segmented wavemakers. For there to be no progressive wave, the wavemaker needs to move in a manner that results in the real part of Eq. 3.84 being zero. This is achieved when the wavemaker profile is

$$c(z) = \frac{\cos(m_{3s}(z+h))}{\cos(m_{3s}h)}. \tag{3.100}$$

This form of wavemaker will be referred to as a cosine wavemaker. Here, m_{3s} is the third solution from the infinite sequence of imaginary solutions to the dispersion relationship, Eq. 3.42, at a fixed frequency of ω_s, $m_{3s} = m_3(\omega_s)$. The third mode ($n = 3$) is chosen arbitrarily and any value of $n \geq 1$ would be equally valid. The larger the value of n, the more oscillations in the wavemaker's surface through the water column. The resultant shape using $n = 3$ can be seen in Figure 3.5. The operation of this kind of wavemaker would result in the top and bottom of the paddle oscillating out of phase with each other.

The choice of such a wavemaker profile results in the real part of Eq. 3.84 becoming zero leaving only a standing wave.

The corresponding expressions for added mass and damping for such a wavemaker are

$$m(\omega) = 4\rho \sum_{n=1}^{\infty} \frac{(-m_{3s}\sin(m_{3s}h)\cos(m_nh) + m_n\cos(m_{3s}h)\sin(m_nh))^2}{(2\,m_nh + \sin(2\,m_nh))\left(\cos(m_{3s}h)\right)^2\left(-{m_{3s}}^2 + {m_n}^2\right)^2} \tag{3.101}$$

and

$$R(\omega) = \omega\rho \left(\frac{(-ke^{a+b} + ke^{b} - ke^{a} + k - im_{3s} + im_{3s}e^{b} - im_{3s}e^{a} + ik_{3s}e^{a+b})^2 e^{-a-b}}{4\left(a + \sinh\left(a\right)\right)\left(\cosh\left(\frac{b}{2}\right)\right)^2 \left(k^2 + {m_{3s}}^2\right)^2} \right) \tag{3.102}$$

where $a = 2kh$ and $b = 2im_{3s}h$.

Obviously, a wavemaker operating in a manner that does not create any progressive waves would have little practical value. The hydrodynamic coefficients have been derived out of academic curiosity and to show that it is possible to have a paddle that will have zero damping and no progressive waves.

Figures 3.6b, 3.6d and 3.6f show that such a wavemaker has zero damping at the design frequency of ω_s, but only at this frequency, at all other frequencies the damping is non-zero.

3.4 Wave Generation

When generating waves in a flume or tank, it is important to be able to control both the frequency and the amplitude of the test waves. The frequency of the monochromatic test waves is relatively simple as it is the same as the frequency of oscillation as the wavemaker. The more complicated parameter is the displacement amplitude of the waveboard. One simple concept used is that of Galvin (1964), who reasoned that the volume of water displaced by the wavemaker should be equal to the volume of water in the crest of the propagating wave, Figuire 3.7. For a piston type wavemaker this results in

$$X_0 h = \int_0^{\frac{\lambda}{2}} \frac{H}{2} \sin(kx) dx \tag{3.103}$$

$$= \frac{HL}{2\pi} \tag{3.104}$$

$$= \frac{H}{k} \tag{3.105}$$

and thus the ratio of stroke displacement, S, to far wave height, H is

$$\left(\frac{H}{X_0}\right)_{piston} = kh. \tag{3.106}$$

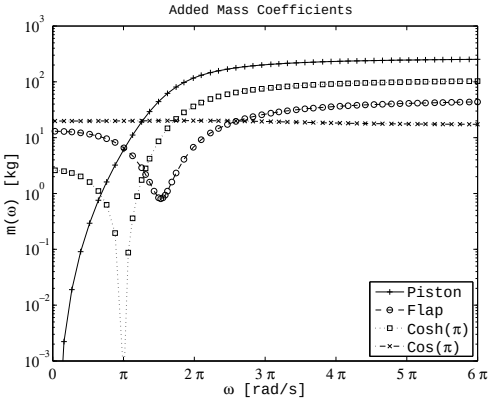

(a) Added mass with $\omega_s = \pi$

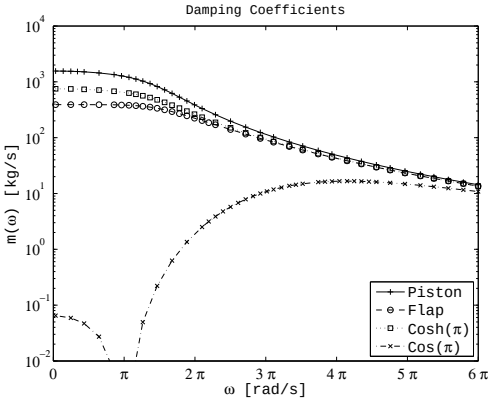

(b) Damping with $\omega_s = \pi$

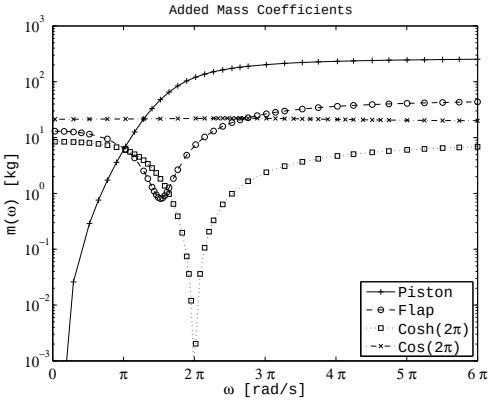

(c) Added mass with $\omega_s = 2\pi$

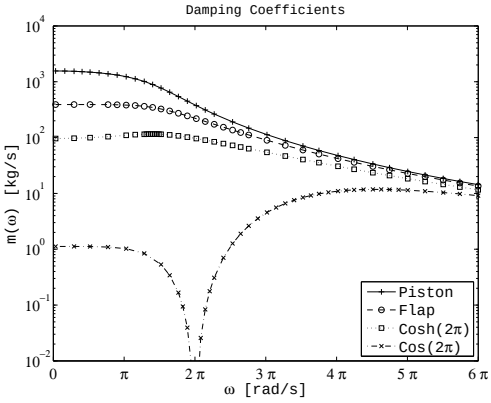

(d) Damping with $\omega_s = 2\pi$

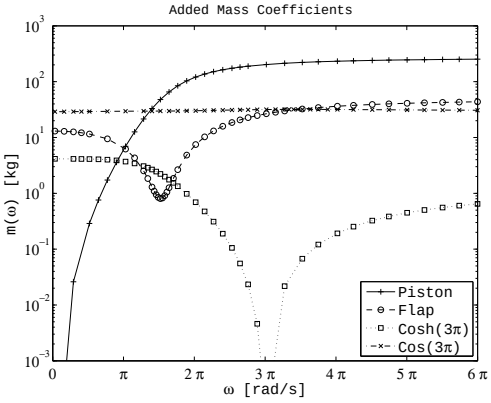

(e) Added mass with $\omega_s = 3\pi$

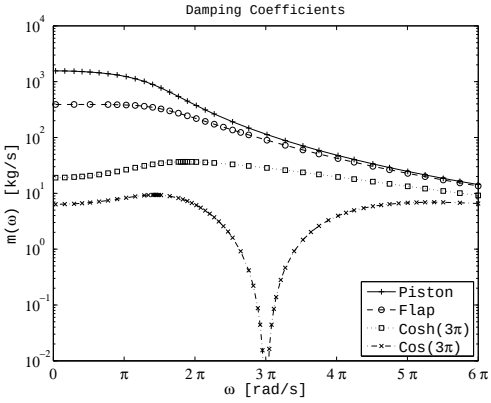

(f) Damping with $\omega_s = 3\pi$

Figure 3.6: Hydrodynamic coefficients for the four different shaped wavemakers; Piston, Bottom hinged flap, $\cosh(\omega_s)$, $\cos(\omega_s)$. Figures 3.6a and 3.6b are for paddles with $\omega_s = \pi$, figures 3.6c and 3.6d with $\omega_s = 2\pi$, and figures 3.6e and 3.6f with $\omega_s = 3\pi$.

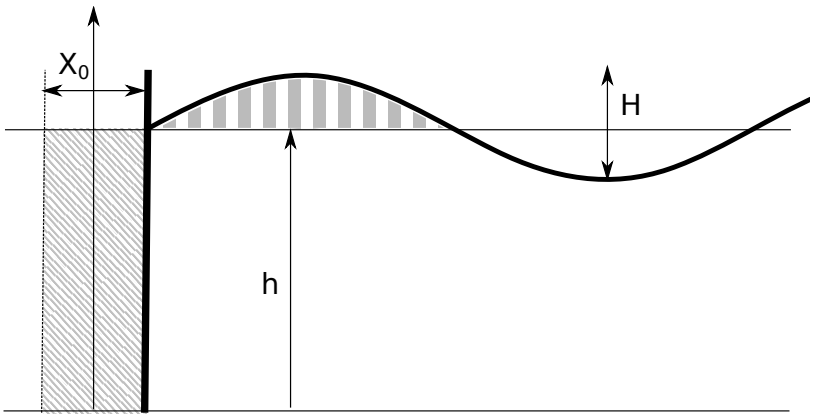

Figure 3.7: Simplified shallow water piston-type wavemaker theory where the volume of water displaced equals the volume of water displaced (Dean and Dalrymple, 1991)

Or following a similar methodology, for a bottom hinged flap,

$$\left(\frac{H}{X_0}\right)_{flap} = \frac{kh}{2}. \tag{3.107}$$

This is a simplified representation of the physical process and a better value for the ratio of wave height to stroke ratio can be obtained from Eq. 3.84. This equation relates the far-field wave height to the complex stroke amplitude of the wavemaker. When referring to wave height, we should be more specific and state that, what we are primarily concerned with is the far-field wave height. This means that we are not interested in the evanescent wave contribution and so the far-field wave is for distances of $x \gg 2h$.

At large distances from the wave board, the free surface, Eq. 3.84, can be given as

$$\hat{\eta}_r = \frac{i\omega}{-g}\hat{u}c_0 Z_0(0)e^{ik_0 x} \tag{3.108}$$

where the evanescent contributions have been neglected. As we are assuming linear first order waves, this can be represented as

$$\hat{\eta}_r = \frac{H}{2}e^{ik_0 x}. \tag{3.109}$$

Equating Eq. 3.108 and Eq. 3.109 will give a relationship between the wave height and the velocity of the wavemaker.

Noting that $\hat{u} = i\omega\hat{x} = i\omega x_0 e^{i\varphi}$, recalling the dispersion relationship is given as

$$\frac{\omega^2}{gk} = \tanh(kh) = \frac{\sinh(kh)}{\cosh(kh)} \tag{3.110}$$

and after some algebra, an expression relating the far field wave wave height, H, to the stroke displacement, x_0, can be obtained.

For a piston wavemaker, this ratio takes the form of,

$$\frac{H}{X_0} = 4\,\frac{(\cosh(kh))^2 - 1}{2\,kh + \sinh(2\,kh)}. \tag{3.111}$$

and for a bottom hinged flap the ratio of far-field wave height to stroke displacement is

$$\frac{H}{X_0} = 4\,\frac{(1 + \sinh(kh)\,kh - \cosh(kh))\sinh(kh)}{kh\,(2\,kh + \sinh(2\,kh))}. \tag{3.112}$$

The algebra for a hyperbolic cosine wave is a little more involved, but remembering that k_s sets the shape of the wavemaker, the ratio is expressed as

$$\frac{H}{X_0} = -\frac{\left(k_s\,\mathrm{e}^{2\,(k_s+k)h} + \mathrm{e}^{2\,k_s\,h}k - k\mathrm{e}^{2\,(k_s+k)h} - k_s + k - \mathrm{e}^{2\,kh}k_s - \mathrm{e}^{2\,kh}k + \mathrm{e}^{2\,k_s\,h}k_s\right)\mathrm{e}^{-(k_s+k)h}k\sinh(kh)}{\left(-{k_s}^2 + k^2\right)(2\,kh + \sinh(2\,kh))\cosh(k_s\,h)}. \tag{3.113}$$

Figure 3.8 shows the wave height to stroke ratio for the three different shaped wavemakers. All three cases give the same limit as $kh \to \infty$ because then, only the upper part of the wavemaker is useful for the generation of a propogating wave. Under shallow water conditions, when $kh < 1$, the piston produces twice as much water displacement and as a result twice as large a propogating wave as a flap. This is very similar to the relationship that proposed by Galvin (1964). It can also be seen from Figure 3.8 that the $\cosh(2\pi)$ wavemaker would require larger displacements for a given wave height compared to a piston and a bottom hinged flap as it displaced less water.

3.5 Chapter Conclusions

This Chapter has presented the theory needed to derive the analytical hydrodynamic coefficients of wavemakers. Analytical expressions for added mass and damping for four different types of wavemaker were presented: a piston, a bottom-hinged flap, a hyperbolic cosine and a cosine wavemaker. It was clearly shown that

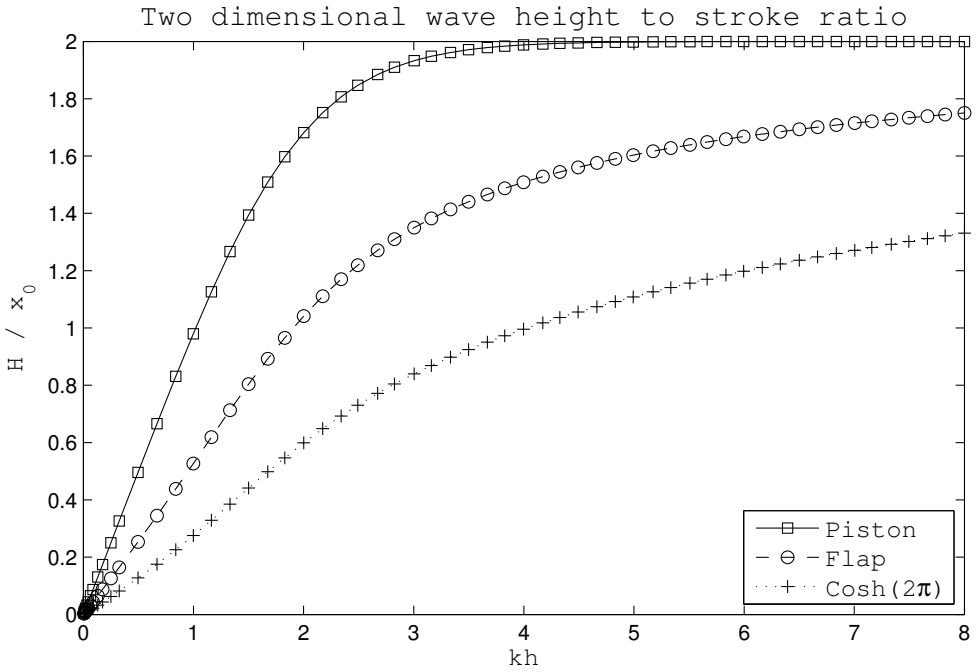

Figure 3.8: Graphical representation showing the wave height to stroke ratio as a function of relative depth for a piston, bottom hinged flap and a hyperbolic cosine, $\cosh(2\pi)$ type wavemakers.

a wavemaker with a hyperbolic cosine profile will have zero added mass at one chosen frequency and that a cosine shaped wavemaker will have zero damping at one specific frequency. The transfer function relating stroke amplitude to far-field wave height was then presented for three different wavemakers. The analytical expressions for hydrodynamic coefficients will prove useful for the analysis of power absorption in the following Chapter.

Chapter 4

Wave absorption by an oscillating body

In this section the absorption of water waves impinging upon a rigid body are discussed. The basic theory behind wave energy absorption will be presented. The different types of real and reactive control will be derived theoretically and expressions comparing absorbed power against theoretically maximum power will be presented. The control theory in this Chapter will follow the work presented by Price (2009) and apply it to the hydrodynamic theory on wavemamkers presented in Chapter 3.

Due to the complexities involved, this chapter will look at linear, small amplitude waves, where it is assumed that the wave height and steepness are sufficiently small for linear wave theory to be valid. In addition, body motions are assumed to be sufficiently small so that linear dynamics can be used, thus allowing the boundary conditions to be applied on the equilibrium position of the body and not the instantaneous position. When presenting power absorption ratios across a broadband of frequencies, these graphs will be considering discretised monochromatic waves.

4.1 Absorption by constructive and destructive interference

One of the great paradoxes in the wave energy sector is, that "*a good wave absorber, must be a good wavemaker*" (Falnes and Budal, 1978). By definition, the absorption of energy from an in-coming wave must result in a reduction of wave energy passing the wave energy converter (WEC). This energy extraction can

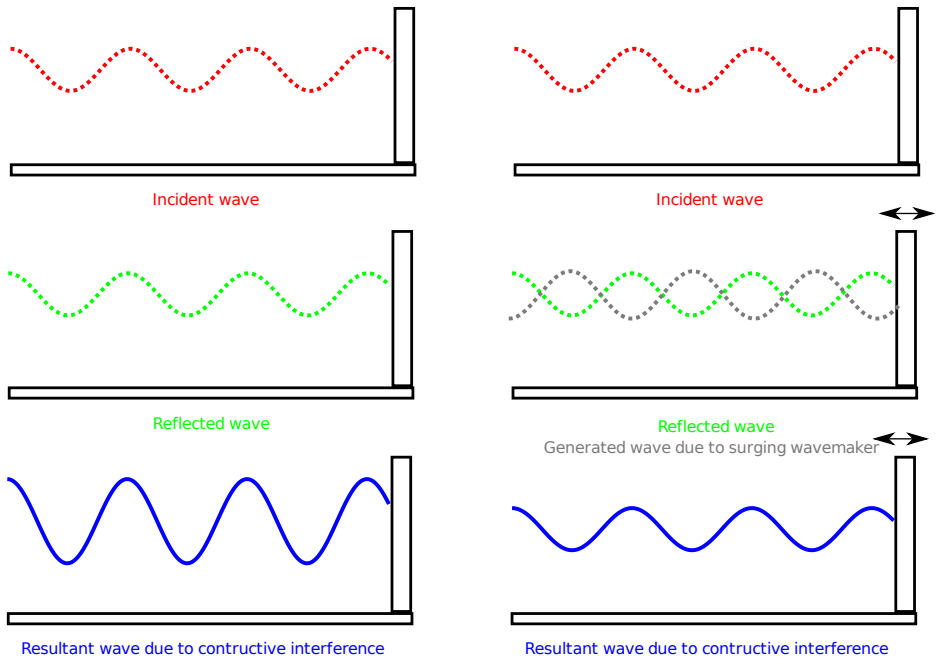

(a) Wave field with a solid wall

(b) Wave field with an absorbing wavemaker

Figure 4.1: Wave absorption via constructive and destructive interference. (a) shows how an incoming wave interacts with a solid wall, where a reflected wave is generated. These then combine constructively which results in a standing wave. (b) shows how the wave field changes with an oscillating wall boundary. The incident wave is absorbed by the wavemaker because the reflected wave is cancelled by the generated wave

best be explained via the process of constructive and destructive interference between the incoming wave and the radiated wave. Figure 4.1a shows how an incoming wave impinging on a solid wall will create a standing wave due to constructive interference. Figure 4.1b shows the wave field when the wall is replaced by a oscillating wavemaker. The wavemaker radiates a wave of equal amplitude to the reflected wave, but 180° out of phase. This results in destructive interference between the radiated wave and the reflected wave and full absorption of the incoming wave field. This is a counter intuitive paradigm, but it is clear that you must radiate a wave if you hope to absorb a wave. How much of this energy that the WEC can absorb is dependent upon what control strategy employed. This topic will be discussed further in Section 4.3.

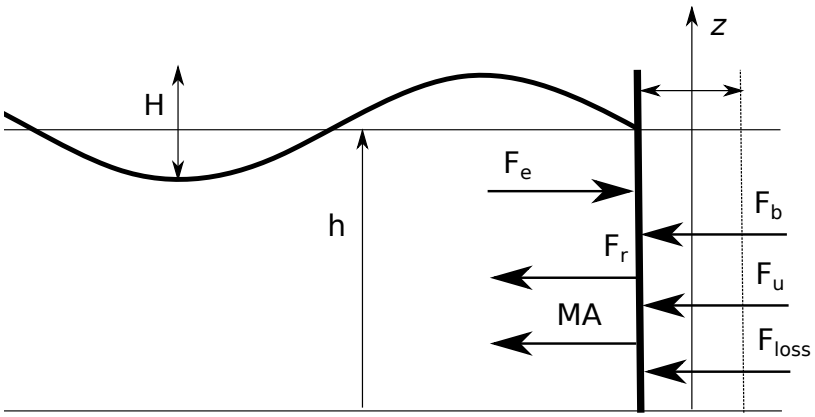

Figure 4.2: Free body diagram showing the forces acting on an absorbing wave maker in surge

4.2 Wave energy converter dynamics

In order to derive a general equation of motion, one needs to start with Newton's second law of motion, $\sum F = ma$. For a wave energy absorber shown in Figure 4.2, Newton's second law, in the frequency domain, can be expanded as

$$F_e(\omega) = MA(\omega) + F_r(\omega) + F_b(\omega) + F_{loss}(\omega) + F_u(\omega), \tag{4.1}$$

where, $F_e(\omega)$ is the excitation force due to the wave, M is the mass of the body, $A(\omega)$ is acceleration, , F_r is the radiation force, F_b a restoring spring force proportional to displacement, $F_b = cx(\omega)$, F_{loss} represents both viscous and frictional losses and the final term, F_u is the control force which represents the load force for wave energy absorption.

The excitation force, $F_e(\omega)$, is the resultant force experienced by a body if it is held motionless in the presence of incoming waves. If we consider the situation in Figure 4.1a, where an in-coming wave, $\hat{\eta}_0 = Ae^{-ikx}$, interacts with a solid wall and a reflected wave is diffracted: $\hat{\eta}_d = Ae^{ikx}$. The velocity potential can then be represented as

$$\hat{\phi}_0 + \hat{\phi}_d = -\frac{g}{i\omega} e(kz)(\hat{\eta}_0 + \hat{\eta}_d). \tag{4.2}$$

The force per unit with in surge, on a wall from $-h \leq z \leq 0$ can now be obtained from Eq. 3.66 as

$$F_e(\omega) = 2\rho g A \frac{\sinh(kh)}{k\cosh(kh)}. \tag{4.3}$$

If we are to assume zero losses, and represent the forces in terms of the product

of their impedance and velocity, Eq. 4.1 can be represented as

$$F_e(\omega) = i\omega M U(\omega) + Z_r(\omega)U(\omega) + \frac{c}{i\omega}U(\omega) + Z_u(\omega)U(\omega) \tag{4.4}$$

where, Z_r is the radiation impedance and, Z_u is the control impedance. Recalling the radiation impedance from Eq. 3.72 the excitation force can now be re-written as

$$F_e(\omega) = \left(R(\omega) + i\left(\omega[M + m(\omega)] - \frac{c}{\omega}\right)\right)U(\omega) + Z_u(\omega)U(\omega) \tag{4.5}$$

$$= \left(Z_i(\omega) + Z_u(\omega)\right)U(\omega) \tag{4.6}$$

where Z_i is the intrinsic impedance,

$$Z_i(\omega) = R(\omega) + i\left(\omega[M + m(\omega)] - \frac{c}{\omega}\right). \tag{4.7}$$

This can then be rearranged to solve for the velocity,

$$U(\omega) = \frac{F_e(\omega)}{\left(Z_i(\omega) + Z_u(\omega)\right)}. \tag{4.8}$$

4.2.1 Time domain equations of motion

The equations of motion thus far have been modelled using the frequency domain equations. This form of analysis is used predominantly in the wave energy sector and naval architecture as it is quicker and easier than using time domain equations. It is important to highlight that this is however an assumption, based on the fact that the waves are linear and superposition applies. It is also important to appreciate the differences and implications of transferring between the frequency domain and time domain via Fourier transform.

It is not possible to directly apply a Fourier transform on Eq. 4.4, as the added mass term in the radiation impedance, $Z_r(\omega)$, tends to a non zero value at infinity, $m(\infty) = m_\infty$ (Cummins, 1962). In order to facilitate the Fourier transform, the multiplication of the two frequency dependent terms needs to tend towards zero at infinity. This is achieved by isolating the frequency dependent terms:

$$K(\omega) = Z_r(\omega) - i\omega m_\infty \tag{4.9}$$

$$= R(\omega) + i\omega\left(m(\omega) - m_\infty\right) \tag{4.10}$$

Therefore the excitation force in the frequency domain can now be represented as

$$F_e(\omega) = i\omega \left[M + m_\infty\right] U(\omega) + K(\omega)U(\omega) + \frac{c}{i\omega}U(\omega) + F_u(\omega). \tag{4.11}$$

The time domain representation is obtained via a Fourier transform, resulting in

$$f_e(t) = \left[M + m_\infty\right] a(t) + k(t) * u(t) + cx(t) + f_u(t), \tag{4.12}$$

where $k(t) * u(t)$ is the convolution. It has been shown that the radiation force is only affected by velocities at $t \leq 0$ (Wehausen, 1992; Falnes, 1995). Price (2009) presents the excitation force in the time domain as

$$f_e(t) = \left[M + m_\infty\right] a(t) + \int_0^t k(\tau)u(t-\tau)d\tau + cx(t) + f_u(t), \tag{4.13}$$

showing that both instantaneous and past velocities are required to solve the equation.

It is important to understand the implications that the convolution has on the time domain equations, especially when dealing with control of the devices. This will be elaborated on in Section 4.3.1.

4.2.2 Absorbed power

The time averaged power absorbed by the mechanical resistance in the control impedance, Z_u, is given as

$$P_u = \frac{1}{2}\Re[Z_u(\omega)] \left|U(\omega)\right|^2. \tag{4.14}$$

Using Eq. 4.8 this can be re-written as

$$\begin{aligned} P_u &= \frac{1}{2}\mathrm{Re}\left[Z_u(\omega)\right] \frac{|\hat{F}_{e,j}|^2}{|Z_i(\omega) + Z_u(\omega)|^2} \\ &= \frac{R_u(\omega)|F_e(\omega)|^2/2}{\left[R_i(\omega) + R_u(\omega)\right]^2 + \left[X_i(\omega) + X_u(\omega)\right]^2}, \end{aligned} \tag{4.15}$$

The optimal condition to maximise the absorbed power is well known and discussed by Mei (1976); Newman (1976); Evans (1976). The amplitude of the radiated wave needs to be of equal amplitude to the diffracted wave and 180° out of phase. By inspection, Eq. 4.15 is maximised when the control impedance equals

the complex conjugate of the intrinsic impedance,

$$Z_u = Z_i^*(\omega) \equiv Z_{u,OPT}(\omega) \tag{4.16}$$

this satisfies both of these conditions to maximise power absorption.

Setting the control impedance, $Z_u(\omega)$ to the complex conjugate of the intrinsic impedance $Z_i^*(\omega)$, namely setting the variables $R_u(\omega)$ and $X_u(\omega)$ to their optimum values of $R_i(\omega)$ and $-X_i(\omega)$ gives an expression for the maximum power

$$P_{u,max} = \frac{|F_e(\omega)|^2}{8R_i}. \tag{4.17}$$

Combining Eqs. 4.15 and 4.17, results in an expression that yields the ratio between absorbed power and the theoretical maximum power absorption

$$\frac{P_u}{P_{u,max}} = 4\frac{R_u(\omega)R_i(\omega)}{\left(R_i(\omega) + R_u(\omega)\right)^2 + \left(X_i(\omega) + X_u(\omega)\right)^2}. \tag{4.18}$$

4.3 Control implementation

In order to absorb incoming waves, the ability to control the motion of the absorber is paramount. In WECs, the force that extracts the energy from the waves and converts it to electrical power is often referred to as the power take off (PTO). Here the control force, F_U, is analogous to this PTO force referred to in the literature.

The generalised linear control force for a wave absorber can be represented as

$$F_u(\omega) = i\omega m_u(\omega)U(\omega) + R_u(\omega)U(\omega) + \frac{c_u(\omega)}{i\omega}U(\omega). \tag{4.19}$$

Where m_u, R_u and c_u are the mass, damping and spring control coefficients. These are coefficients proportional to acceleration, velocity and displacement respectively.

Here the control impedance can now be written as

$$Z_u = R_u(\omega) + i\left(\omega m_u(\omega) - \frac{c_u(\omega)}{\omega}\right). \tag{4.20}$$

Under a fixed coefficient control system tuned to a fixed frequency of $\omega = \omega_p$ results in the optimal control impedance of

$$Z_{u,OPT}(\omega_p) = R(\omega_p) - i\left(\omega_p\left(M + m(\omega_p)\right) - \frac{c}{\omega_p}\right), \tag{4.21}$$

$$= R_p - i\left(\omega_p\left(M + m_p\right) - \frac{c}{\omega_p}\right). \tag{4.22}$$

Here, R_p and m_p have been introduced to show that these coefficients are no longer frequency dependent and denote fixed coefficients at a frequency of $\omega = \omega_p$.

If this control is to be implemented using a system with three control coefficients, m_u, r_u and c_u the generalised absorbing force is obtained as

$$f_u(t) = m_u(a(t) + b_u u(t) + c_u x(t). \tag{4.23}$$

The impedance matrix in the frequency domain can then be obtained as

$$Z_u(\omega) = r_u + i\left(\omega m_u - \frac{c_u}{\omega}\right). \tag{4.24}$$

If we now compare Eqs. 4.24 and 4.22 and separate out the real and imaginary terms we get,

$$r_u = R_p \tag{4.25}$$

$$-\left[\omega m_u - \frac{c_u}{\omega}\right] = \omega_p\left(M + m_p\right) - \frac{c}{\omega_p}. \tag{4.26}$$

This gives a simple solution for the real control coefficient, r_u, but Eq. 4.26 is an indeterminate equation with two unknowns, m_u and c_u. For this situation, where there is one equation and two unknowns, arbitrarily choosing one of the values will as a result a value for the other which satisfies this equation. Therefore there are any number of solution pairs to this equation. Similar to Price (2009) three possible solutions to Eq. 4.26 will be presented.

The first solution can be seen by inspection and is obtained when $c_u = c$ and in order to satisfy Eq. 4.26, this then results in $m_u = M + m_p$. This is one of the many pairs of solutions that would satisfy Eq. 4.26, but for this specific pair, the mass control coefficient cancels the physical mass and the spring control cancels the spring term. This solution is referred to as mass-spring-damping. The other two situations discussed are the extreme cases when $m_u = 0$ and $c_u = 0$. The

former will be referred to as damping-spring and the latter as mass-damping.

The control impedance coefficients for a mass-spring-damping coefficient system are given as

$$m_u = -[M + m_p], \tag{4.27}$$

$$r_u = R_p, \tag{4.28}$$

$$c_u = -c. \tag{4.29}$$

Resulting in a frequency domain representation of the ideal control force at a tuned frequency of ω_p

$$F_u(\omega) = -i\omega[M + m_p]U(\omega) + R_pU(\omega) + \frac{c}{i\omega}U(\omega), \tag{4.30}$$

and the resulting control impedance as

$$Z_u = R_p - i\left(\omega\left[M + m_p\right] + \frac{c}{\omega}\right). \tag{4.31}$$

Inserting Z_u into Eq. 4.18 will give an expression for the ratio of absorbed power to maximum power as

$$\frac{P_u}{P_{u,max}} = \frac{4R_pR(\omega)}{(R_p + R(\omega))^2 + (\omega(m(\omega) - m_p))^2}. \tag{4.32}$$

This expression shows that the physical mass, M, and spring, c, have been cancelled out by the control reactance, X_u. As mentioned before, there are many sets of control reactance pairs, m_u and c_u that could have been used to satisfy Eq. 4.26 but for other pairs, the the control coefficients would not completely cancel out the physical mass and spring terms. This would mean that some of the intrinsic mass would need to be cancelled with the control spring, or conversely some of the intrinsic spring would need to be cancelled with the control mass term (Price, 2009).

Figure 4.3 plots Eq. 4.32 over a range of frequencies showing how P_u/P_{max} varies with choice of control frequency, ω_p for each of the wavemaker profiles. It is clear that optimal absorption is achieved at the chosen control frequency $\omega_p = \pi, 2\pi, 3\pi$, Figures 4.3a, 4.3b and 4.3c respectively. It can be seen that there are differences in absorption levels at frequencies of $\omega \neq \omega_p$ between each of the different shaped wavemakers. The hyperbolic cosine shaped wavemaker achieves the highest levels

of absorption over the broadest range of frequencies. It is also shown that the absorption characteristics for each specific wavemaker change based upon the selection of ω_p.

Integrating Eq. 4.32 over the range of frequencies typical to a $1/100^{\text{th}}$ wave tank (0.5 and 1.75 [Hz]) and normalising gives,

$$\xi = \frac{5}{2\pi} \int_{\pi}^{\frac{7\pi}{2}} \frac{P_u}{P_{u,max}} d(\omega), \tag{4.33}$$

where, ξ is a measure of the effectiveness of the wavemaker in absorbing discretised monochromatic waves of different frequencies to the tuned frequency, ω_p. This gives a quantitative appreciation of how well the device absorbs incoming waves in the frequency range of interest, namely that of a typical hydrodynamic wave flume. Graphically it is the sum of the discretised values of P_u/P_{max} shown in Figure 4.3 divided by the interval range, $\omega = \pi \rightarrow 3.5\pi$. Table 4.2 shows values of ξ for an absorbing wavemaker using a mass-damper-spring control system. Table 4.1 shows that good absorption of incoming waves can be achieved using this type of control system. It is important to appreciate that in the control system in a laboratory or in a WEC can only be tuned to one specific frequency at a time. If the incoming waves are monochromatic, then the wave absorber can be tuned to the frequency of the incoming wave train and full absorption could be achieved. This is not the case if the incoming waves are polychromatic. Optimal absorption can only be achieved at one frequency in the spectrum, as the absorption coefficients are fixed. Generally, the peak energy frequency of the incoming waves is chosen as the tuning frequency. Table 4.1 shows the levels of absorption expected from a wave absorber, tuned to a frequency of ω_p, in discretised monochromatic seas in a range of $\omega = \pi \rightarrow 3.5\pi$.

4.3.1 Time domain representation of control

As highlighted in Section 4.2.1, care needs to be taken when transferring between the time domain and frequency domain via Fourier transforms.

Taking the general control force frequency domain equation, Eq. 4.19, and treating it in a similar manner to Eq. 4.11, namely separating out the frequency independent and dependent terms, the optimal control force (Price, 2009) can be

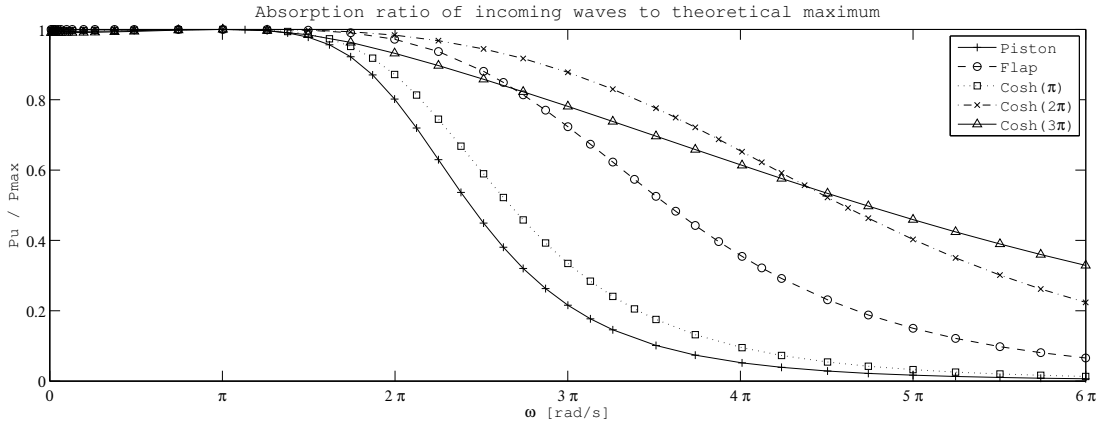

(a) mass-spring-damper tuned to π

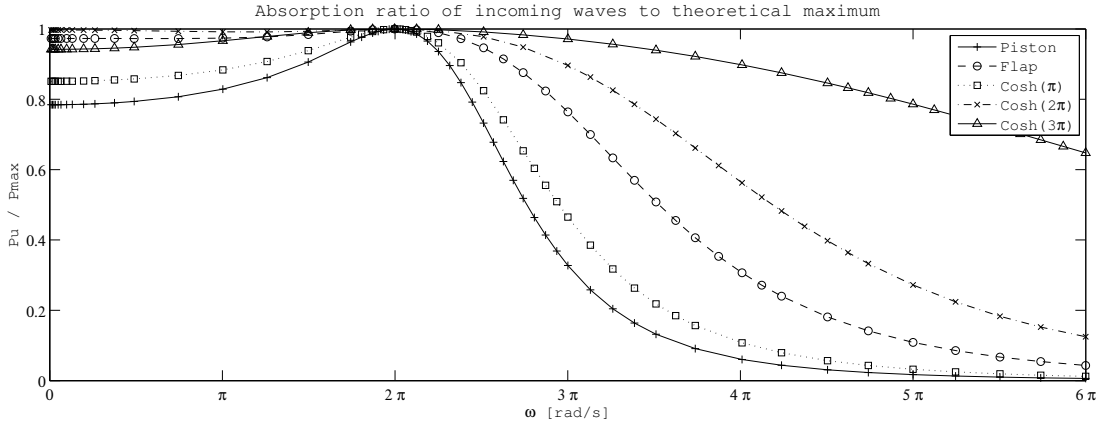

(b) mass-spring-damper tuned to 2π

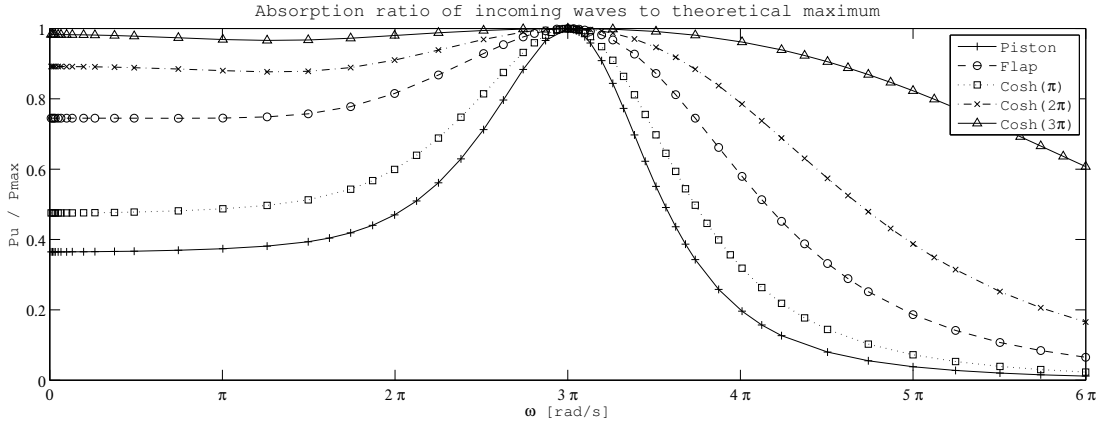

(c) mass-spring-damper tuned to 3π

Figure 4.3: Absorption characteristics using a mass-damper-spring control system. Here, (a) shows how each of the wavemakers absorb incoming waves, under discretised monochromatic waves, using a mass-damper-spring control system tuned to a frequency of $\omega_p = \pi$, (b) is for when $\omega_p = 2\pi$ and (c) is for when $\omega_p = 3\pi$

Table 4.1: Absorption efficiency, ξ, for a paddle controlled using mass-spring-damper coefficients

	Tuning frequency ω_p		
	π	2π	3π
Piston	0.602	0.695	0.617
Flap	0.872	0.892	0.866
$\cosh(\pi)$	0.677	0.761	0.712
$\cosh(2\pi)$	0.941	0.951	0.936
$\cosh(3\pi)$	0.883	0.982	0.985

represented as

$$F_u(\omega) = -i\omega[M + m_\infty]U(\omega) + K^*(\omega)U(\omega) - \frac{c}{i\omega}U(\omega) \tag{4.34}$$

where, $K^*(\omega)$ is the complex conjugate of the frequency dependent radiation impedance, $K(\omega)$. It has been shown that the time domain control force must be real, $K^*(\omega) = K(-\omega)$, therefore the inverse Fourier transform, $\mathscr{F}^{-1}\{K^*(\omega)\} = k(-t)$ (Smith, 1997) and this results in the time domain equation of:

$$f_u(t) = -[M + m_\infty]a(t) + k(-t) * u(t) - cx(t). \tag{4.35}$$

The difference between Eq. 4.12 and Eq. 4.35 is that the convolution is now time reversed. The previous convolution was shown to be dependent on instantaneous and past measurements and $k(t)$ is referred to as the memory kernel. Now, the convolution is represented as the time reversed memory kernel, $k(-t)$, and therefore it is anti-causal and future knowledge is required. It is referred to as the premonition term (Price, 2009). The ideal control force in the time domain can be represented as (Naito and Nakamura, 1985):

$$f_u(t) = -[M + m_\infty]a(t) + \int_0^\infty k(\tau)u(t + \tau)d\tau - cx(t) \tag{4.36}$$

This equation highlights that future knowledge of the velocity is required in order to be able to achieve optimal control. Herein this thesis, analysis will be conducted using discretised monochromatic waves. In monochromatic waves future knowledge is implicitly available as all future waves will be of the same frequency and as such, optimal absorption can be achieved at one specific chosen frequency. There is no memory effect for monochromatic waves. The rest of this thesis will proceed

in the frequency domain, conscious of the findings just presented.

4.3.2 Damper-spring control

As discussed in Section 4.3 there are two extreme situations that present a solution to Eq. 4.26. The first to be discussed here is when $m_u = 0$, thus leaving a damper-spring control scheme. The following will present the derivation of absorption efficiency for a spring-damping control scheme with fixed control coefficients of r_u and c_u.

The control force that uses a spring-damper coefficients in the time domain can be represented as

$$f_u(t) = r_u u(t) + c_u x(t), \tag{4.37}$$

and thus the impedance in the frequency domain can be obtained as

$$Z_u(\omega) = r_u + \frac{c_u}{i\omega}. \tag{4.38}$$

Optimising Eq. 4.38 at a single frequency, ω_p, results in

$$Z_u(\omega_p) = r_u - \frac{ic_u}{\omega_p}. \tag{4.39}$$

Now we can compare the optimal impedance, Eq. 4.22 and the impedance with spring-damping control, Eq. 4.39, and this results in the following control coefficients,

$$r_u = R_p, \tag{4.40}$$

$$c_u = \left(\omega_p^2(M + m_p) - c\right), \tag{4.41}$$

which are in agreement those control coefficients presented by Naito (2006), attributed to Bessho (1973) (in Japanese) but the derivation was not shown.

Substituting these back into Eq. 4.38, gives the tuned control impedance at ω_p, for a spring-damping system, over the full range of frequencies

$$Z_u(\omega) = R_p - \frac{i}{\omega}\left[\omega_p^2\left(M + m_p\right) - c\right]. \tag{4.42}$$

Using radiation resistance and reactance matrices from Eq. 4.7 and Eq. 4.42 and substituting into the power ratio, Eq. 4.18, yields a power absorption ratio for a

Table 4.2: Absorption efficiency, ξ, for a mass-less paddle controlled using spring-damper coefficients

	Tuning frequency ω_p		
	π	2π	3π
Piston	0.628	0.652	0.312
Flap	0.876	0.904	0.775
$\cosh(\pi)$	0.699	0.735	0.430
$\cosh(2\pi)$	0.967	0.951	0.899
$\cosh(3\pi)$	0.990	0.991	0.986

spring-damper controlled system,

$$\frac{P_u}{P_{u,max}} = \frac{4R_pR(\omega)}{\left(R_p + R(\omega)\right)^2 + \left(\omega(M + m(\omega)) - \frac{\omega_p^2}{\omega}(M + m_p)\right)^2}. \tag{4.43}$$

Figure 4.4 plots Eq. 4.43 over a range of frequencies showing the differences in absorption levels for the different absorbing-wavemaker shapes. Similar to the mass-spring-damper control scheme, theoretically, maximum absorption is achievable at the chosen tuned frequency, ω_p. At this one frequency the damper-spring scheme will achieve the same levels of absorption as the mass-damper-spring or mass-damper schemes. It is away from this frequency at $\omega \neq \omega_p$ that the absorption characteristics differ greatly between the schemes. Compared to the mass-damper-spring control scheme, the damper-spring scheme does not achieve such high levels of absorption at the lower frequencies. This is due to the fact that the intrinsic mass term, M, is not completely cancelled by the control reactance and remains in Eq. 4.43.

Table 4.2 shows the absorbing wavemakers' efficiency, Eq. 4.33, using damper-spring control coefficients, where the wavemaker has zero mass. Construction of a mass-less paddle is physically impossible, but this could be implemented in a numerical code. This could provide an absorbing boundary condition to deal with wave reflections in a numerical wave tank. As can be seen from Table 4.2 very high levels of absorption, over the chosen integral range, could be achieved in conjunction with a $\cosh(3\pi)$ shaped wavemaker.

If the paddle has a finite mass, M, the absorption efficiency will decrease due to the second term in the denominator of Eq. 4.43. Table 4.3 shows ξ for a paddle with a mass of 1kg. It can be seen that introduction of mass decreases the absorption

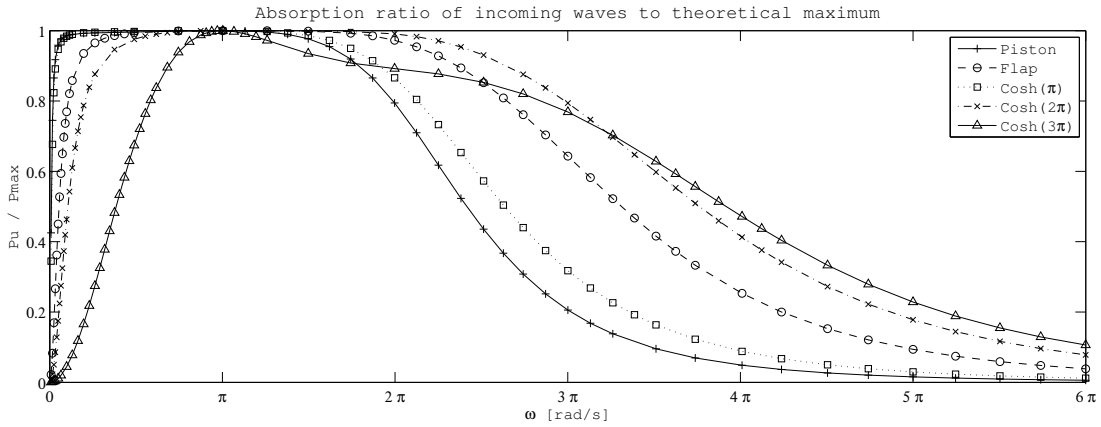

(a) spring-damper tuned to π

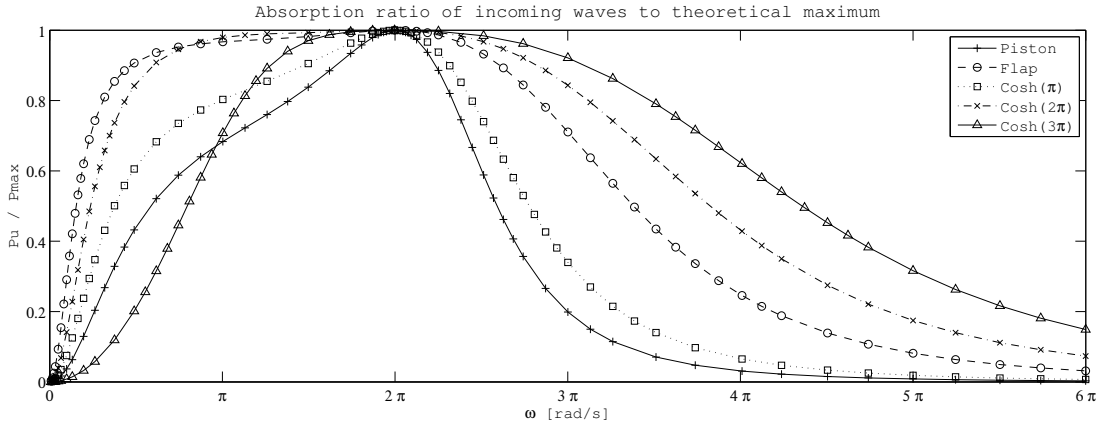

(b) Damper-spring tuned to 2π

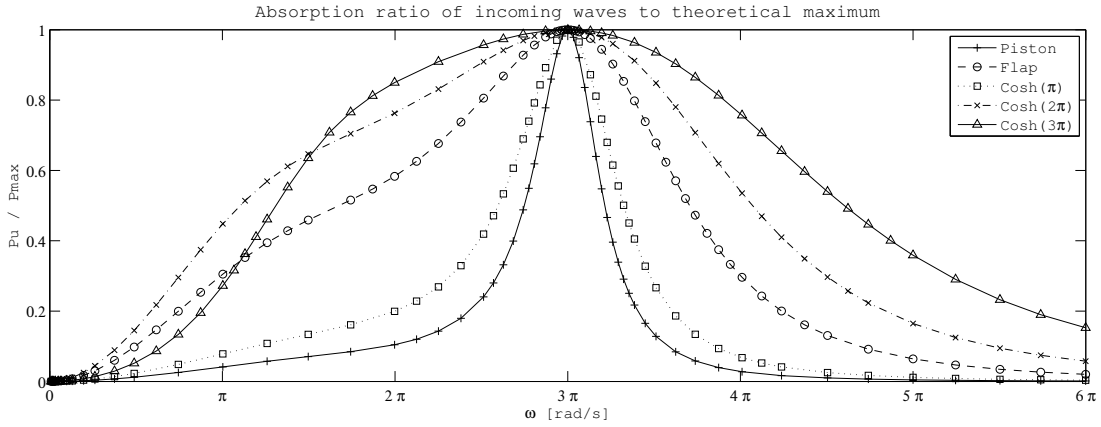

(c) Damper-spring tuned to 3π

Figure 4.4: Absorption characteristics using a damper-spring control system. Here, (a) shows how each of the wavemakers absorb incoming waves, under discretised monochromatic waves, using a mass-damper-spring control system tuned to a frequency of $\omega_p = \pi$, (b) is for when $\omega_p = 2\pi$ and (c) is for when $\omega_p = 3\pi$

Table 4.3: Absorption efficiency, ξ, for a paddle controlled using spring-damper coefficients

	Tuning frequency ω_p		
	π	2π	3π
Piston	0.591	0.603	0.266
Flap	0.826	0.859	0.647
$\cosh(\pi)$	0.662	0.690	0.372
$\cosh(2\pi)$	0.875	0.904	0.736
$\cosh(3\pi)$	0.709	0.852	0.680

characteristics of the wavemaker at lower frequencies.

4.3.3 Mass-damper control

This section presents the absorption efficiency of a wavemaker using the other extreme solution to Eq. 4.26, where, $c_u = 0$. This is referred to as a mass-damper control scheme. In the time domain, the control force is represented as

$$f_u(t) = m_u a(t) + r_u u(t). \tag{4.44}$$

The control impedance in the frequency domain is represented as

$$Z_u(\omega) = r_u + i\omega m_u. \tag{4.45}$$

Optimising Eq. 4.45 at one single frequency, ω_p, results in

$$Z_u(\omega_p) = r_u + i\omega_p m_u. \tag{4.46}$$

Comparing this to the optimal impedance, Eq. 4.22 and the impedance with spring-damping control, Eq. 4.46, results in the following control coefficients (Price, 2009),

$$r_u = R_p, \tag{4.47}$$

$$m_u = -\left((M + m_p) - c/\omega_p^2\right), \tag{4.48}$$

Substituting these back into Eq. 4.45, gives the tuned control impedance at ω_p,

Table 4.4: Absorption efficiency, ξ, for a paddle controlled using mass-damper coefficients

	Tuning frequency ω_p		
	π	2π	3π
Piston	0.585	0.689	0.609
Flap	0.815	0.879	0.856
$\cosh(\pi)$	0.646	0.751	0.700
$\cosh(2\pi)$	0.830	0.932	0.921
$\cosh(3\pi)$	0.545	0.971	0.971

for a spring-damping system, over the full range of frequencies

$$Z_u(\omega) = R_p - i\omega\left((M + m_p) - \frac{c}{\omega_p^2}\right) \tag{4.49}$$

Using radiation resistance and reactance matrices from Eq. 4.7 and Eq. 4.49 and substituting into the power ratio Eq. 4.18, yields a power absorption ratio for a spring-damper controlled system,

$$\frac{P_u}{P_{u,max}} = \frac{4\omega^2 R_p R(\omega)}{\omega^2(R_p + R(\omega))^2 + \left(\omega^2(m(\omega) - m_p) - c\left(1 - \frac{\omega^2}{\omega_p^2}\right)\right)^2}. \tag{4.50}$$

Here can be seen that the physical mass has been cancelled out but but the added mass and the intrinsic spring persist. Figure 4.5 shows that implementation of complex conjugate control at the one tuned frequency, ω_p, will result in optimal control for all of the wavemakers at that specific frequency, $\omega = \omega_p$. Again, at this frequency, the absorption characteristics are identical to that of mass-damper-spring and damper-spring schemes, but away from this frequency the absorption characteristics will differ to a system using both of these other control schemes.

The differing absorption characteristics at frequencies of $\omega \neq \omega_p$ results in different values of ξ over the chosen definite integral. This can be clearly seen in Table 4.4. The spring coefficient was chosen as $c = 20\text{N/m}$, based on the flap type wavemakers used at the University of Edinburgh.

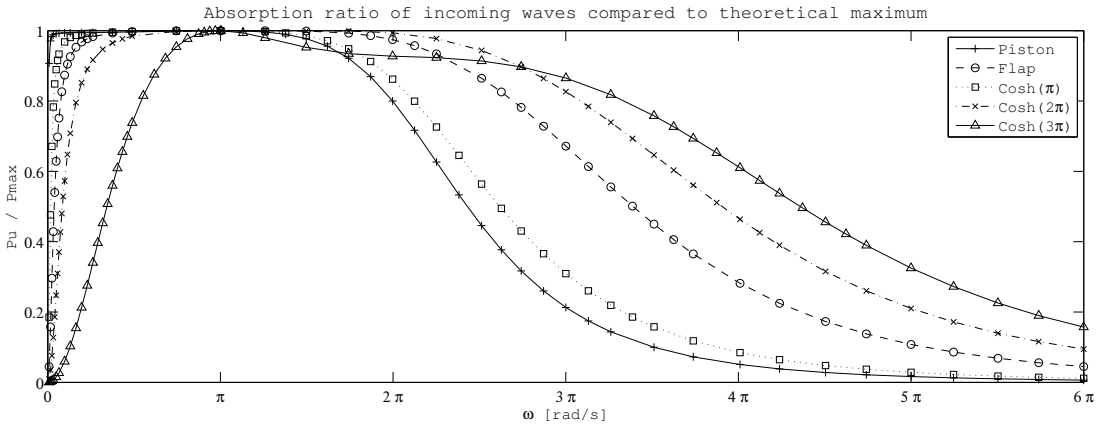

(a) mass-damper tuned to π

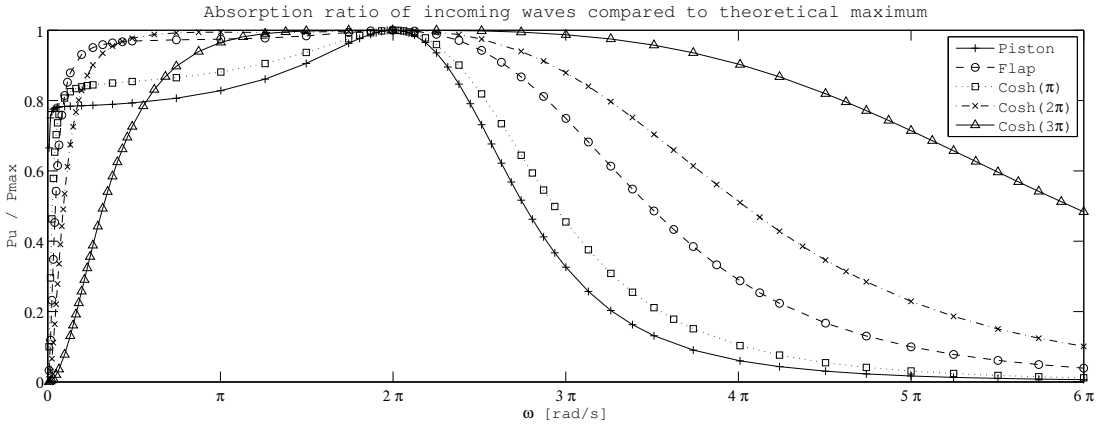

(b) mass-damper tuned to 2π

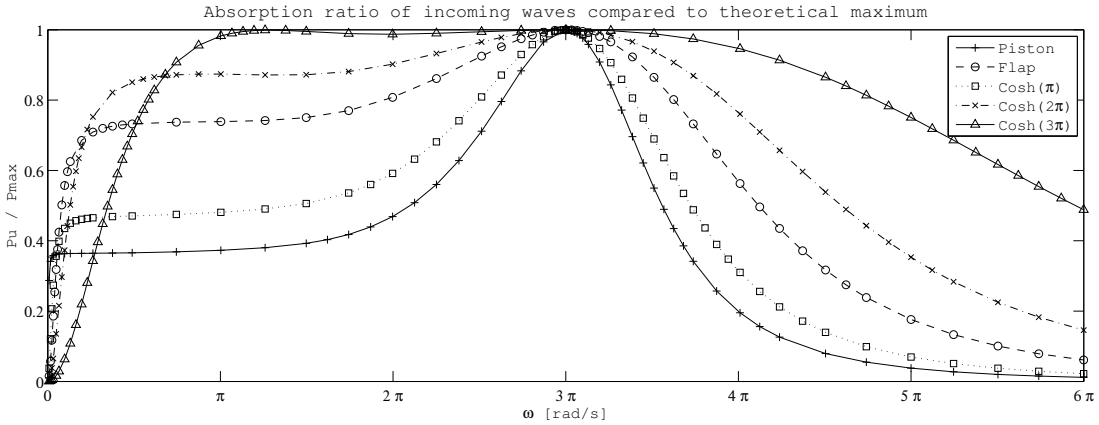

(c) mass-damper tuned to 3π

Figure 4.5: Absorption characteristics using a mass-damper control system. Here, (a) shows how each of the wavemakers absorb incoming waves, under discretised monochromatic waves, using a mass-damper-spring control system tuned to a frequency of $\omega_p = \pi$, (b) is for when $\omega_p = 2\pi$ and (c) is for when $\omega_p = 3\pi$

4.3.4 Damper control

This section presents the derivation of optimal control choice of a purely damping control system and analyses the sensitivity to tuning frequency.

The time domain control force using just a damper scheme is represented as

$$f_u(t) = r_u u(t), \tag{4.51}$$

where the impedance in the frequency domain is

$$Z_u(\omega) = r_u. \tag{4.52}$$

As the control impedance in this situation is purely real, complex conjugate control cannot implemented as there is no reactive component to cancel the complex term in the intrinsic reactance.

Optimising Eq. 4.52 at one single frequency, ω_p, results in

$$Z_u(\omega_p) = r_u. \tag{4.53}$$

Comparing this to the optimal impedance, Eq. 4.22 and the impedance with spring-damping control, Eq. 4.53, results in the optimal setting for damping, tuned to a frequency of ω_p

$$r_u = |Z_{u,OPT}| = \sqrt{R_p^2 + \left(\omega_p \left[M + m_p\right] - \frac{c}{\omega_p}\right)}. \tag{4.54}$$

Again, making use of the radiation resistance and reactance matrices from Eq. 4.7 and Eq. 4.52, then substituting into the power ratio Eq. 4.18, yields a power absorption ratio for a purely real controlled system,

$$\frac{P_u}{P_{u,max}} = \frac{4R(\omega)\sqrt{R_p^2 + \left(\omega_p \left(M + m_p\right) - \frac{c}{\omega_p}\right)}}{\left(R(\omega) + \sqrt{R_p^2 + \left(\omega_p \left(M + m_p\right) - \frac{c}{\omega_p}\right)}\right)^2 + \left(\omega(M + m(\omega)) - \frac{c}{\omega}\right)^2}. \tag{4.55}$$

Absorption of incoming waves using just real control, via a damper, is less complex

Table 4.5: Absorption efficiency, ξ, for a paddle controlled using just a damping coefficient

	Tuning frequency ω_p		
	π	2π	3π
Piston	0.593	0.588	0.577
Flap	0.828	0.843	0.842
$\cosh(\pi)$	0.665	0.664	0.667
$\cosh(2\pi)$	0.881	0.885	0.884
$\cosh(3\pi)$	0.770	0.808	0.795

and easier to implement than using reactive control. For this reason many WECs use only a real PTO in their devices and therefore it is important to appreciate the affect that control choice will have on absorption levels across a broad bandwidth of frequencies when tuned to one frequency.

Figure 4.6 show the absorption levels for the different wavemaker geometries when tuned to frequencies of $\omega_p = \pi,\ 2\pi,\ 3\pi$. The biggest difference between using control scheme with just a real component to one that uses both real and reactive components is that full absorption at the tuned frequency is not possible. This is because there is no reactive term in the control impedance to cancel out the intrinsic reactance of the wavemaker.

Table 4.5 shows how using a control strategy based upon damping alone affects the power absorption. An interesting result here is that for all wavemaker shapes, absorption efficiency is relatively insensitive to changes in tuning frequency. This suggests that the choice of control frequency, ω_p, is not a major contributor to absorption efficiency for these wavemakers between the chosen integral limits. The bottom hinged flap performs favourably compared to the three hyperbolic cosine shaped paddles, this could be due to there being a local minimum in the intrinsic reactance (added mass) of this paddle at a frequency of 1.7π $[rad/s]$, Figure 3.6a, resulting in the real part of the power absorption equation Eq. 4.18 dominating over the imaginary part.

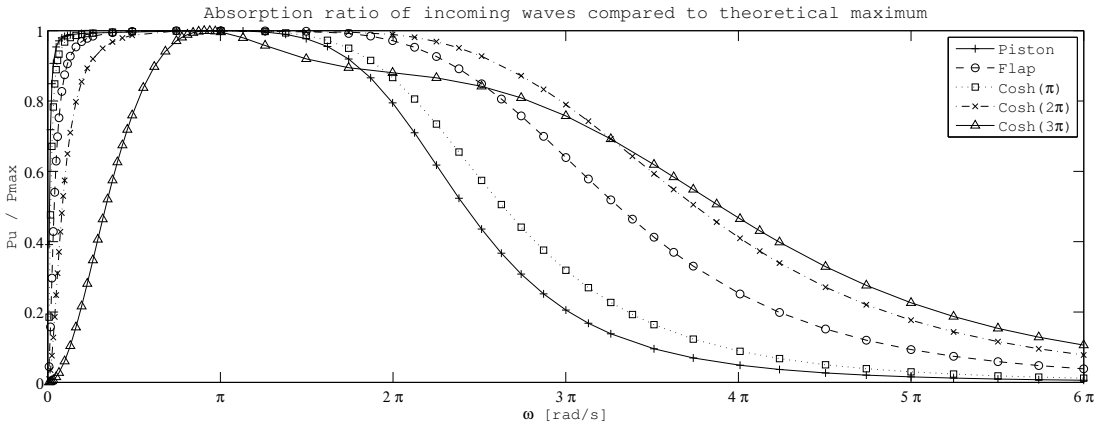

(a) damper tuned to π

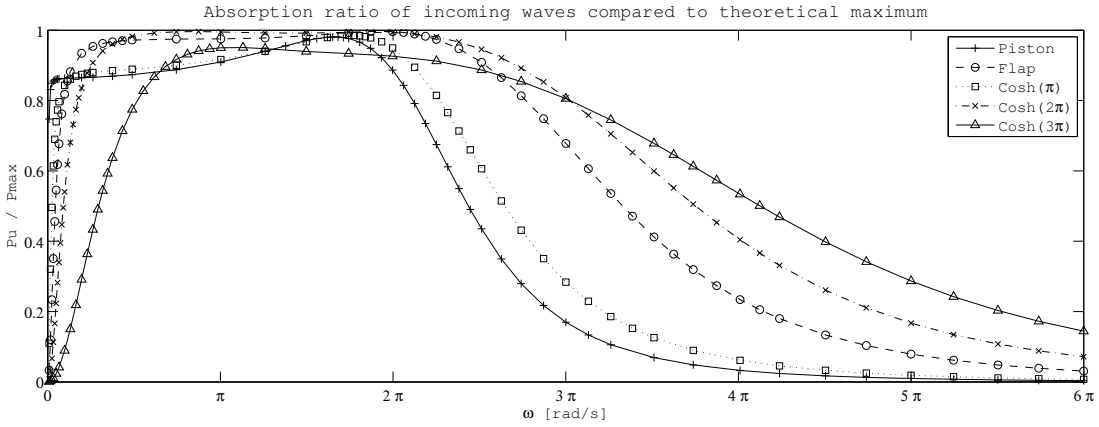

(b) damper tuned to 2π

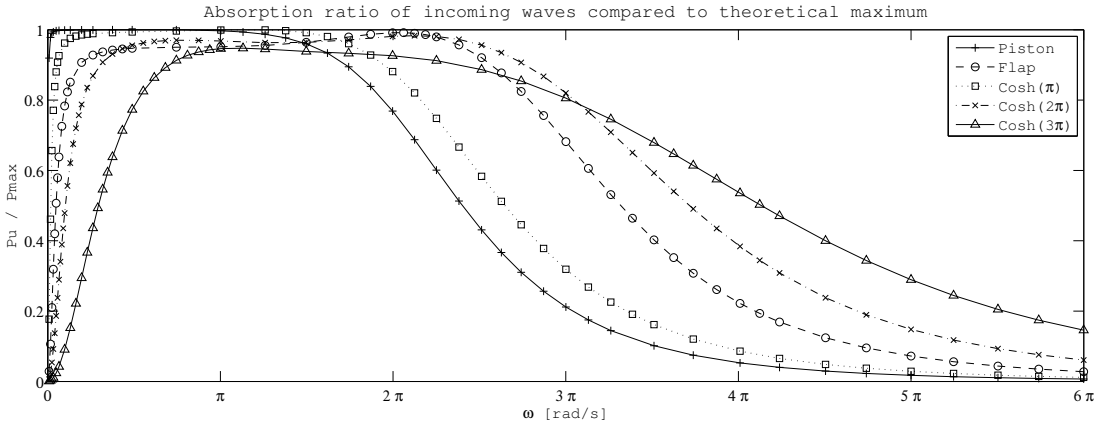

(c) damper tuned to 3π

Figure 4.6: Absorption characteristics using a damper control system. Here, (a) shows how each of the wavemakers absorb incoming waves, under discretised monochromatic waves, using a mass-damper-spring control system tuned to a frequency of $\omega_p = \pi$, (b) is for when $\omega_p = 2\pi$ and (c) is for when $\omega_p = 3\pi$

4.3.5 Effect of control

In wave energy research, it has been long known that optimum absorption of incoming monochromatic waves can be achieved if the power take off (PTO) coefficients of the wave energy absorber are chosen such to achieve impedance matching. Mei (1976) showed that this could be implemented using two control coefficients; one proportional to acceleration and the other proportional to velocity. Evans (1981) arrived at the same results using a velocity-proportional damping force and a displacement-proportional spring force. Using either a mass-damping or a spring-damping approach will yield the same optimum absorption of incoming waves at that one specific tuned frequency, ω_p. Price (2009) showed that, for a point absorber acting in heave, both of these approaches differ when absorbing incoming monochromatic waves of a frequency $\omega \neq \omega_p$. Figure 4.7 confirms that this is also true for absorbing devices acting in surge.

Figure 4.7 shows the absorption levels of four different wavemakers in discretised monochromatic waves using different control strategies, each tuned to $\omega_p = 3\pi$. This allows for comparison of each control scheme for one single absorbing device, highlighting the differences. It is clear that the choice of control affects the absorption levels across the bandwidth of frequencies. The difference between the various control strategies is most evident when considering just one wavemaker shape. For example, for a $\cosh(3\pi)$ paddle, tuned to a frequency of $\omega = 3\pi$, Figure 4.7d, the mass-damper, spring-damper and mass-spring-damper control strategies all achieve the same value of $P_u/P_{max} = 1$. Away from $\omega = 3\pi$, the absorption levels of waves at a frequencies different to that of the tuned frequency, $\omega \neq \omega_p$, differ greatly.

There is a notable difference in absorption levels between the mass-damper and the spring-damper methods of control in Figure 4.7. This can be seen quantitatively comparing the value of ξ in Table 4.3 and Table 4.4, at a tuning frequency of $\omega_p = 3\pi$. Control implemented using mass-damping coefficients out-performs that of spring-damping for every wavemaker shape. Interestingly, upon changing tuning frequency to $\omega_p = \pi$, the situation is reversed and control using spring-damping coefficients display better absorption characteristics than mass-damping.

When only a damping coefficient is used, complex conjugate control is not possible and optimal absorption, $P_u/P_{max} = 1$, at ω_p is unachievable. When only real control is implemented for a piston wavemaker, Figure 4.7a, optimal control is

never achieved, but high levels of absorption are achieved at the lower bandwidth of frequencies. These lower frequencies will have longer wavelengths and once displacement limits are taken into consideration, these high levels of absorption would disappear.

The highest levels of absorption, within the frequencies of interest, were obtained for a $\cosh(3\pi)$ paddle with a mass-spring-damper control strategy tuned to $\omega_p = 3\pi$. Construction of a $\cosh(3\pi)$ wavemaker would be difficult but this shape could be used in a numerical wave tank as an absorbing boundary condition instead of a computationally expensive damping region in the numerical domain. The hyperbolic cosine profile wavemaker exhibits better absorption characteristics and where Clément (1996) coupled a piston and a sponge-layer and an absorbing piston, the hyperbolic cosine wavemaker would result in better numerical absorption.

The role of wavemaker geometry has an important influence on the absorption characteristics. This can be seen contrasting the graphs for the four different shaped wavemakers in Figure 4.7. It can be seen that regardless of control strategy implemented, a $\cosh(3\pi)$ wavemaker displays better absorption characteristics at frequencies of $\omega \neq \omega_p$, thus yielding much broader graphs, Figure 4.7d. This highlights the importance of considering both the geometry of the device and the control strategy implemented.

4.4 Chapter conclusions

This chapter has shown that the absorption of incoming waves is sensitive to the shape of the absorbing wavemaker, the control strategy used to implement the absorption and also the choice of tuning frequency in the control strategy.

The absorption levels for three different wavemakers were presented using a combination of different control strategies. The different control strategies considered were; mass-spring-damping, spring-damping, mass-damping and damping. It was shown that the best absorption, at frequencies between π rad/s and 3.5π rad/s, was achieved with a hyperbolic cosine, $\cosh(\omega_s)$, wavemaker with control coefficients tuned to a frequency of $\omega_p = 3\pi$ using a mass-spring-damper control system.

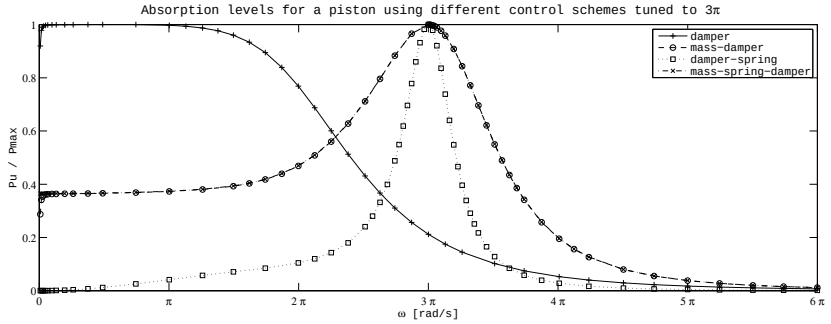

(a) Piston

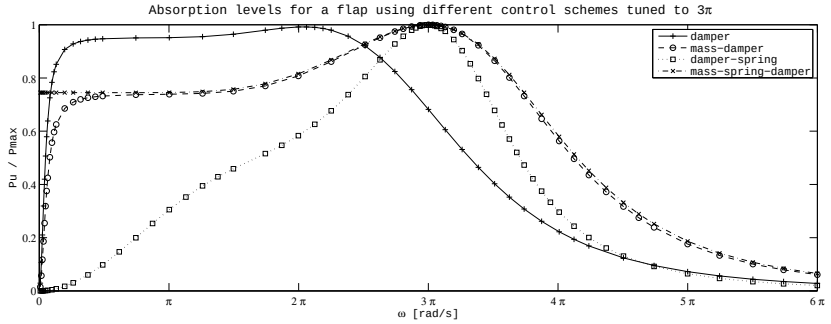

(b) Flap

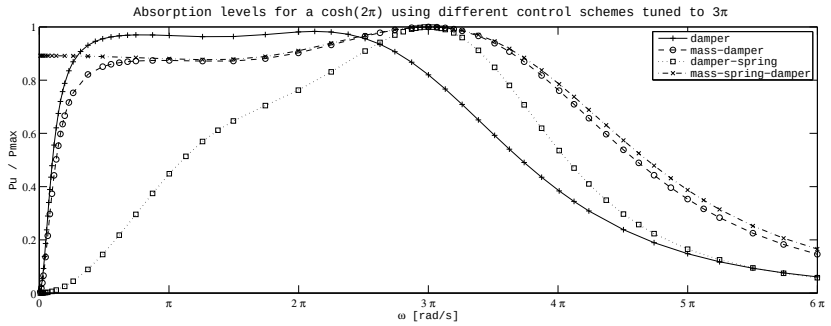

(c) Cosh(2π)

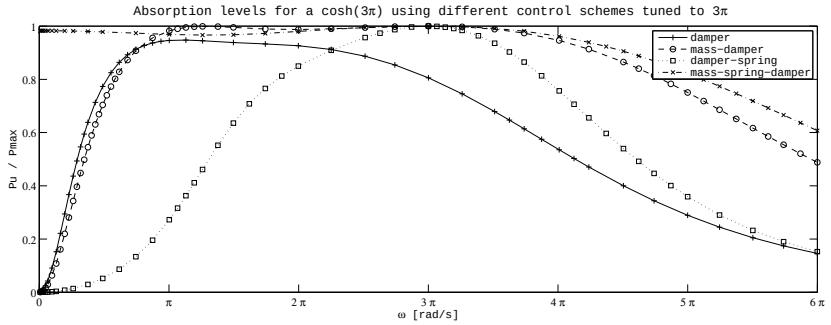

(d) Cosh(3π)

Figure 4.7: Absorption characteristics by wavemaker tuned to $\omega_p = 3\pi$

The author is not suggesting building a $\cosh(\omega_s)$ shaped wavemaker as it would prove difficult. This shaped absorbing wavemaker, however, could be used as a numerical boundary condition to deal with unwanted wave reflections in numerical wave tanks, offering an alternative to other methods that can be computationally intensive and the potential for improved results, especially if coupled with a numerical beach in a similar manner to Clément (1996).

For wave absorbers acting in surge, it has been shown that there are differences between using mass-damping, damping-spring and mass-spring-damping coefficients to implement complex conjugate control. All achieve optimal absorption of $P_u/P_{max} = 1$, at the chosen frequency of ω_p but, absorption levels differ at frequencies other than the tuned frequency. This highlights the importance in choosing what control strategy to choose and include in any wave absorbing device. All of the reactive control options are sensitive to the choice of tuning frequency ω_p adding another variable for consideration. This could have relevance to any surging wave energy converter that makes use of reactive control.

Furthermore, if the absorption of incoming waves is implemented using real control, there is little discernible difference in the absorption efficiency, ξ, upon changing the tuning frequency, ω_p, for all wavemaker shapes. A control strategy using just a real control coefficients is insensitive to the tuning frequency. Better returns on absorption levels could be gained if design efforts concentrated on the shape optimisation as opposed to power-take-off optimisation.

The levels of wave energy absorption by a device is intrinsically linked to the control of the device. The control of wave absorbing devices is implicitly linked to its hydrodynamics, vis-à-vis the geometry of the device. These results have shown that the levels of absorption can differ depending on the choice of control frequency and increased levels of absorption can be achieved if the geometry and control strategy are considered and optimised concurrently.

There are limitations to this study. Displacement limits have not been considered and the amount of absorption reported in Figure 4.7 would be an over estimation at the lower range of frequencies. The response times of the paddles was also neglected, this would have resulted in an over estimation of absorption at higher frequencies. The definite integrals chosen for absorption efficiency, ξ, were based upon frequency limits in the $1/100^{th}$ scale tank at Edinburgh, so the concerns over displacement limits and motion response should be diminished.

Another consideration is that for the absorption efficiency, ξ, it is implicitly assumed that all frequencies occurs in equal amounts. This is not the case and more tailored results could be achieved if the absorption efficiency is weighted against the wave spectrum in the flume. As there are large differences between each wave spectra in a flume, an assumption would have to be made as to the spectral shape etc. Instead of doing so, the method of integration without weighting is used. It is thought that if spectral information was available, the geometry and the absorption coefficients could be chosen in concurrence and best results would be seen for the hyperbolic cosine wavemakers.

Chapter 5

Quality assurance of CFD simulations

Computational fluid dynamics (CFD) is a very powerful tool. It can be used to predict fluid flow characteristics accurately and precisely. CFD can model single phase flow, multi-phase flow, free surface flow, fluid-structure-interactions, thermal flow, sediment transport to name but a few and the range of applications for CFD is continually growing. Originally, CFD solvers were only accessible to those who were fluent and adept in computer programming languages, therefore CFD was only primarily used by experienced users and academics. The advent of commercial CFD codes with their user friendly GUIs opened the world of CFD to all engineers and scientists. Undergraduate engineers can, at the click of a button, analyse the fluid flow over a backward facing step, or predict the aerodynamic drag force acting on high speed trains. Aeronautical engineers used CFD extensively in the design of the new Airbus A380, resulting huge economic savings as they avoided costly large scale wind tunnel testing. Now, engineers and developers in the wave energy sector are looking to CFD to solve some of their more complex problems, that the potential flow codes cannot model accurately.

The rise of commercial CFD codes has been proved an invaluable design tool for the engineer, but it has also fraught with danger if used incorrectly. CFD software can be applied to many complex fluid flow problems, but the danger is that it always gives an answer, correct or otherwise. While this has always been the case, when CFD codes were written using a relatively inaccessible computer programming language, the more discerning users and academics could spot potential misuse issues and rectify them. Their good engineering judgement was based upon experience obtained via trial and error, with the emphasis on the latter. New users to CFD, without a strong understanding of how the CFD solver or methods work, will be presented results (invariably with colourful pictures)

and could potentially take them as fact with out critically analysing them.

Due to the dramatic rise in CFD usage, several well known journals, such as the ASME Journal of Fluids Engineering and all AIAA journals have enforced mandatory use of more formal methods for evaluating errors and presenting quantified bounds on uncertainty in order to increase the credibility of computational results.

This chapter briefly discusses the underlying concepts behind CFD, making reference to free surface modelling. A far more detailed analysis, than the present author could give, discussing CFD, numerical methods and its wide ranging applications can be found in the countless amount of books on the topic. Much of the understanding and theory presented in this chapter was obtained from undergraduate and postgraduate books such as; Anderson (1995); Ferziger and Perić (2002); Versteeg and Malalasekera (2007) and the user manuals from the codes that will be used in Chapter 6, ANSYS CFX and FLOW3D.

As opposed to the theory behind CFD, the emphasis for the majority of this chapter focus on quality assurance and on errors in CFD; how they arise and how to quantify the them. The topics of verification and validation of numerical results have been around for quite some time, but only recently have started to gather pace and acceptance amongst the academic community. This discussions in this chapter will follow Roache (1998), to which a similar approach has been adopted by more recent authors (Oberkampf and Roy, 2010).

5.1 Fluid dynamics and CFD

For most of the twentieth century naval hydrodynamics, and more recently wave energy hydrodynamics has been limited to the two realms of theory and physical experiments. Both of these methods of fluid flow analysis are limited through scope, cost and size of facility. The advent of high speed digital computing has brought with it a new dimension for analysing fluid flows, that of numerical modelling.

CFD is one specific type of numerical modelling that can be used to analyse fluid flow problems. At the core of CFD are the Navier-Stokes equations which define any single-phase fluid flow. These are a very powerful set of equations that describe the motion of fluid substances very accurately over a wide range of

applications from; ocean currents, pipe flow, flow around airfoils, weather models and star motion in a galaxy to name but a few. However, a general solution to the Navier-Stokes equations have thus far eluded mathematicians and physicists and as a result, CFD modellers obtain approximate solutions to these equations using various numeric methods.

In the the marine energy sector, indeed the wider coastal engineering sector, many researchers have opted for a simplified version of the Navier-Stokes equations. In a lot of studies, the fluid being modelled is assumed to be irrotational and inviscid, thus reducing the Navier-Stokes to a potential flow problem governed by the Laplace equation. Potential flow problems are a lot quicker to solve, relatively robust and produce adequate solutions for a range applications. The assumption that the flow is inviscid and irrotational is overly simplistic and means that viscous loses cannot be modelled and there certain limitations regarding what kind of fluid flow can be properly represented. CFD is not limited by these assumptions and can model the underlying physics of the problem more closely than a potential flow solver. It also allows for the possibility to model types of fluid flow that potential flow simply isn't capable of modelling, such as breaking waves.

The largest draw back to using CFD solvers is computational time. Solving the Navier-Stokes equations accurately can prove excessively time consuming. While CFD might offer a huge range of data within its results, experimental scale models might produce the desired results quicker and cheaper. In order for CFD to be of real use to the design engineer, it needs to be less expensive than physical testing and operate on similar time scales. The progress being made with multi-processor computing has meant that CFD now offers a practical design tool for the engineer to be used in conjunction with the experimental facilities.

5.1.1 Fluid equations of motion

All CFD codes, bespoke, commercial or otherwise are based upon the same fundamental governing equations of fluid dynamics. The basic equations of fluid flow are three conservation laws:

1. Mass is conserved (Continuity equation)
2. Momentum is conserved (Newton's second law)
3. Energy is conserved (First law of thermodynamics)

Continuity equation

The continuity equation ensures that mass is conserved and states that any mass entering a system is equal to that rate of mass that leaves the system. For a compressible fluid the differential form is:

$$\frac{\partial \rho}{\partial t} + \nabla \cdot (\rho \mathbf{u}) = 0 \tag{5.1}$$

where, ρ is the fluid density and $\mathbf{u}$ the flow velocity.

Momentum equation

Newton's second law is a fundamental law of physics that states that the net force on a fluid element is equal to the mass times acceleration of the element $F = ma$. For a fluid system, this can be compactly represented as (Gretton, 2009):

$$\rho \frac{D\mathbf{u}}{Dt} = \nabla \cdot \tau_{ij}. \tag{5.2}$$

The first term on the left hand side is the material derivative and τ is the stress tensor which is composed of the pressure and viscous terms,

$$\tau_{ij} = -p\delta_{ij} + \tau_{ij}^{\mathrm{v}} \tag{5.3}$$

where, p is the pressure, δ_{ij} represents the Kronecker delta function and τ_{ij}^{v} represents the viscous forces, which is composed of both normal and shear forces.

Substituting Eq. 5.3 into Eq. 5.2 gives:

$$\rho \frac{D\mathbf{u}}{Dt} = -\nabla p + \nabla \cdot \tau_{ij}^{\mathrm{v}}. \tag{5.4}$$

Assuming that the fluid is Newtonian, i.e. viscous stresses are linearly related to strain rates, gives an expression for the viscous forces:

$$\tau_{ij} = -p\delta_{ij} + \mu \left(\frac{\partial u_i}{\partial x_j} + \frac{\partial u_j}{\partial x_i} \right) + \delta_{ij} \lambda \nabla \cdot \mathbf{u} \tag{5.5}$$

where λ is the bulk viscosity and μ is the ordinary coefficient of viscosity.

Substituting Eq. 5.5 into Eq. 5.2 results in the familiar Navier-Stokes equations

for a compressible viscous flow

$$\rho\frac{D\mathbf{u}}{Dt} = -\nabla p + \frac{\partial}{\partial x_j}\left[\mu\left(\frac{\partial u_i}{\partial x_j} + \frac{\partial u_j}{\partial x_i}\right) + \delta_{ij}\lambda\nabla\cdot\mathbf{u}\right]. \tag{5.6}$$

If the flow is assumed to have both constant density and viscosity, a simpler representation is arrived at:

$$\rho\frac{D\mathbf{u}}{Dt} = -\nabla p + \mu\nabla^2\mathbf{u}. \tag{5.7}$$

Energy equation

The third fundamental equation governing the laws of fluids is the conservation of energy. The conservation of energy is more commonly known through the first law of thermodynamics; energy can be transformed, but not created or destroyed. For a fluid this is represented as

$$\rho\frac{De}{Dt} = \nabla\cdot(k\nabla T) - p\nabla\cdot u + \tau^{\mathrm{v}}_{ij}\frac{\partial u_i}{\partial x_j} \tag{5.8}$$

where, e is the internal energy, p is the pressure, T is the temperature and k is the thermal conductivity.

Equations of state

At present there are five coupled equations with seven unknowns, resulting in an indeterminate set of equations. In order to obtain closure, two more equations are required. The ideal gas laws are used to provide to two extra equations in order to solve the set of equations governing fluid motion

$$p = \rho RT \tag{5.9}$$

and the assumption of constant specific heat (at a constant pressure) gives

$$h = c_p T. \tag{5.10}$$

5.1.2 Discretisation methods

The fluid flow being solved for by CFD codes takes place over a continuous region or continuum. Within this continuum the fluid equations of motion, the Navier-Stokes equations, apply. But computers can not solve the continuous governing partial differential equations. Instead the continuum is broken up, or discretised in to finite temporal and spatial portions. There are a number of different techniques to discretise the governing equations, but the objective of all is the same; to turn a calculus problem into and algebraic problem. There are different methods used to discretise the spatial volumes such as: finite volume, finite difference and finite element. The mesh or grid upon which the equations are discretised can be structured, unstructured and there are also different methods used to discretise the inviscid terms such as central schemes, flux vector splitting, flux-difference splitting, upwinding, ENO, WENO. The fact that a continuous set of equations are solved as a discretised solution means that errors will invariably be introduced. These discretisation errors will be discussed in more detail in Section 5.3.

5.1.3 Free surface modelling

The free surface is of particular interest to engineers using CFD to analyse hydrodynamic flows. In the marine environment, the free surface represents the interface between the water and the air. This can be either simply defined where there is a sharp change at the interface, such as still water, or more complex if we consider breaking water waves with air entrainment.

The main difficulty in dealing with free surfaces is that the position and shape of the free surface is not known, other than at the initial time; its location at later times has to be determined as part of the solution.

The free surface boundary conditions have been briefly discussed in Section 3.1. To recap, the kinematic condition requires that there is no flux through the sharp boundary separating the two fluids. The dynamic condition states that the free surface does not support any pressure differences across the interface and that the forces acting on the fluid at the interface remain in equilibrium. In many engineering scale applications, normal stresses and surface tension effects can be neglected.

Implementation of these boundary conditions is not that simple. As mentioned, the position of the free surface is unknown *a priori* and must be computed as part

of the solution. Therefore only one of the boundary conditions can be implemented at the free surface and the other has to be used to locate the interface. This has to be done iteratively, making it a computationally intensive task (Ferziger and Peric, 1999).

There are many different methods employed in CFD to resolve the free surface but most of these can be categorised according to two groups; interface tracking and interface capturing.

The first is interface tracking, where a sharp interface is maintained by following its motion. The mesh is adapted to the position of the free surface at each time step. Therefore, one of the boundaries is, by default, the free surface where the boundary conditions can be applied.

The other option is interface capturing. These methods can be implemented on a predetermined fixed grid. There are three main techniques in this category, Marker-and-cell, Volume of fluid and level set techniques.

Marker-and-cell

The marker-and-cell (MAC) method, proposed by (Harlow, 1965), introduces massless tracer particles at the free surface and are tracked throughout the calculation. While this method can cope with non-linearities, it is computationally expensive, especially in three dimensions.

Volume of fluid

The volume of fluid (VOF) approach was first introduced by Hirt and Nichols (1981). The VOF method consists of three ingredients; a scheme to locate the surface, an algorithm to track the surface as a sharp interface moving through a computational grid and a means of applying boundary conditions at the surface. Two fluid phases are considered to make up one single fluid across the grid. Each grid volume is assigned a fluid fraction function equal to 1.0 in the fluid and 0.0 outside the fluid, i.e. air void, Figure 5.1. The free surface is then identified by the region of rapid change of this volume fraction. This approach, or similar, is adopted by many commercial CFD codes such as, ANSYS-CFX, cd-adapco STAR-CCM+ and FLOW3D. Codes that employ this method to resolve the free surface generally differ in the way that the shape of the interface is approximated; via simple line interface calculation (SLIC), piecewise linear interface calculation

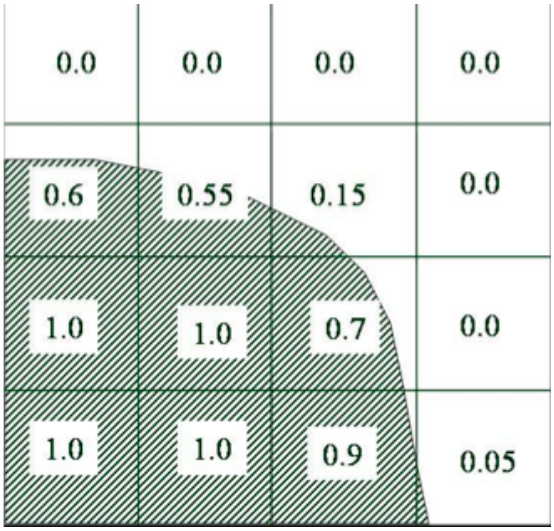

Figure 5.1: Typical values of the Volume of Fluid near the free surface (Barkhudarov, 2004).

(PLIC) and least squares methods, but the underlying concept is the same. This approach is more efficient than the MAC scheme and can be applied to complex free surfaces and breaking waves (Ferziger and Peric, 1999).

Level set method

Another class of interface-capturing methods is based upon the level set technique presented by Osher and Sethian (1988). Level set methods are conceptually simple. Here the level set function is initially defined in each cell as the distance from the free surface, positive in one direction, negative in the other. This function, which is zero on the free surface is tracked because it smoothly changes across the interface. Level set methods are relatively easy to implement and accurate under certain conditions. Issues arise with this method where there is high vorticity or where the interface is significantly deformed and in these flow regimes level set methods can suffer from loss of mass/volume.

Other methods for tracking the free surface include Lattice Boltzmann method, Front-tracking methods and shock-capturing methods.

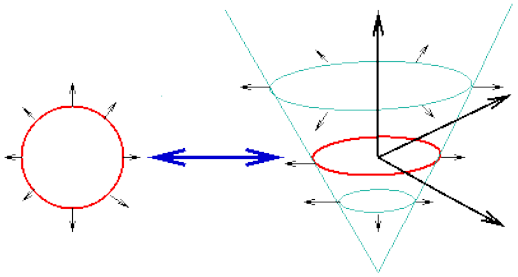

Figure 5.2: The level set function. Here the red front is the zero level set as it represents the collection of points that are at height zero

5.2 General errors and uncertainty in CFD

> "*We know, there are known knowns; there are things we know we know. We also know there are known unknowns; that is to say we know there are some things we do not know. But there are also unknown unknowns, the ones we don't know we don't know*" - D. Rumsfeld

Computational fluid dynamics covers a very wide scope of fluid flow processes. The majority of these flows are governed and well described by the Navier-Stokes equations. As discussed previously, obtaining a direct analytical solution for anything other than the most simple of cases is not possible. To obtain a solution, these governing continuous equations need to be replaced with a discrete representation and numerical solutions to these approximate equations can be obtained using a computer. This discretisation process introduces errors compared to the solution of the continuous set of equations. Further errors are introduced if the chosen governing equations don't adequately represent the fluid flow of interest. A prime example of this is in turbulence modelling when performing a viscous flow simulation. In addition to errors introduced while obtaining a numerical solution, errors can also be introduced by the user either by incorrectly defining the problem or analysis and interpretation of the results.

This subject of errors in CFD has been discussed by several authors and a best practice guide, by the European Research Community on Flow, Turbulence and Combustion (ERCOFTAC, 2002) classify errors and uncertainty under seven different sources;

- Model error and uncertainty
- Discretisation or numerical error
- Iteration or convergence error
- Round-off error

- Application uncertainties
- User errors
- Code errors

The following subsections will discuss some of these errors, or known unknowns, in more detail and discus how to quantify the error bounds associated with them where possible. This will breed confidence in any results presented using a numerical model.

5.2.1 Model error and uncertainties

The AIAA (1998) make the semantic distinction between error and uncertainty. They present the following definitions:

> *Uncertainty*: A potential deficiency in any phase or activity of the modelling process that is due to the lack of knowledge.
>
> *Error*: A recognisable deficiency in any phase or activity of modelling and simulation that is not due to lack of knowledge.

Here the key difference between the two is the *lack of knowledge*.

Modelling errors and uncertainty arise due to solving the wrong equations. They are defined as being the difference between the real flow and the exact solution of the model equations. The most recognised error of this form are as a result of turbulence modelling assumptions. For turbulence modelling it is well known that unrealistic results will be obtained if the incorrect turbulence model is chosen. The fact that there are so many different turbulent models used and recommended for different flow conditions is testament to this.

5.2.2 Discretisation or numerical error

Discretisation errors arise because we are obtaining a discrete numerical approximation to the continuous equations we are trying to solve. They are defined as the difference between the exact solution of the modelled equations and the numerical solution on a mesh of finite grid points. It is due to the fact that finite differences are used to represent exact derivatives. The greater the number of grid points, the lower this error. As the number of grid points is increased the discretisation error will tend to zero at a rate determined by the order of the numerical method used.

5.2.3 Iteration or convergence error

These are errors that arise due to the difference between a fully converged solution on a finite number of grid points and a solution that is not fully converged (MARNET, 2002). If the iterative process was allowed to continue indefinitely, these errors would be zero. Realistically this is not possible as modellers have time constraints and convergence limits are set to tolerances on accuracies. It is a pragmatic balance between these time constraints and solution accuracy requirements.

5.2.4 Round-off error

Also referred to as computer round-off error. Computers only have a limited number of digits available for storing a given value, typically numbers are stored with 16, 32 or 64 bits. Round-off error is the difference between the calculated approximation of a number and its exact mathematical value.

5.2.5 Application uncertainties

Errors can arise due to the problem being complex and an exact definition of the problem is not possible. These uncertainties include, but are not limited to, geometry definition, boundary conditions or whether the flow is steady/unsteady.

5.2.6 User errors

User errors can be introduced at any stage where the user has to interact with the code, geometry generation, meshing, pre-processing or post-processing. These arise due to mistakes or carelessness by the user and it is hoped that these errors will reduce in line with the level of experience of the user.

5.2.7 Code errors

Code errors are often referred to as programming errors or “bugs”. These are unintentional programming errors in the implementation of models or compiler errors on the computer hardware. Often, these can be difficult to find. The primary method of detection is through verification and validation of the code.

5.3 Verification and Validation

Clearly, there is a large variety of error and uncertainty associated with any numerical analysis, CFD in particular. Unless the errors and uncertainty can be quantified and error bounds placed upon the results, CFD should be treated with the utmost of scepticism. This raises a very important question, how can you effectively determine the magnitude of the error or the bound of the uncertainty? This question has been on-going for nearly 100 years, ever since Richardson (1910) published his paper on h^2 extrapolation, now more commonly referred to as Richardson Extrapolation. With the recent advancement in computing power, there has been an increase in the amount of research conducted using numerical models. The research community and journal editors are more keen than ever to ensure that error bounds are placed upon these numerical results, as an experimentalist does physical tests. But still, no consensus has been reached on the methods of performing this analysis (Freitas, 2002).

Many authors propose that a numerical code should be subjected to two phases of analysis in assessing the quality of a CFD model, verification and validation (Aeschliman *et al.*, 1995; Roache, 1998; AIAA, 1998; Ferziger and Peric, 1999; Freitas, 2002; MARNET, 2002; Celik *et al.*, 2008; Oberkampf and Roy, 2010). In everyday parlance, both of these nouns are synonyms, but in the field of numerical modelling they are quite different. The broadly agreed definitions of these terms are (AIAA, 1998)

> *Verification*: The process of determining that a model implementation accurately represents the developer's conceptual description of the model and the solution to the model.
>
> *Validation*: The process of determining the degree to which a model is an accurate representation of the real world from the perspective of the intended uses of the model.

These have been succinctly put by Blottner (1989) as:

> *Verification*: Solving the equations right.
>
> *Validation*: Solving the right equations.

Verification and validation is often referred to in shorthand as V&V.

5.3.1 Verification

Verification is only concerned with mathematics, it is not an endorsement of the physical or mathematical model. Its aim is to identify and quantify the errors in the model implementation and the solution. Verification of codes can be broken down into two smaller subsets; verification of codes and verification of calculations. Roache (2004) suggests that the commonly used shorthand V&V is defective because it suggests that this process only involves two not three subjects and a more complete shorthand of V2V should be used, to recognise more accurately the extra verification distinction.

Verification of codes

Verification of codes is concerned with whether or not the model is correctly coded. The objective of verifying the code is to find and remove any coding errors, bugs or code misuse. Roache (2004) uses the example of a code that uses a perverse mathematical method to trajectory of a projectile to demonstrate this. If a numerical code is used to calculate the trajectory of a projectile or satellite using an inverse-*cube* law, and this is stated in the code's documentation, and as long as there are no coding errors or bugs then this code could pass the level of V2V.

If the source code is available to the end user, the method of manufactured solutions (MMS) is possible to implement to ensure a strong verification of the code (Roache, 2002). If however a commercial CFD code is being used, the source code will invariably be inaccessible to the end user and no verification of codes will be possible. Here a lot of trust is placed with the developers to have previously conducted extensive verification of their code in-house to ensure that no "bugs" exist. As such, more confidence can be had in codes that have been developed over long periods of time, allowing for the verification of codes through usage. ANSYS CFX is a widely used code and has undergone strenuous verification in the past. One such example is published by Bergström and Gebart (1999) who estimated the numerical accuracy of CFDS-Flow3D[1] (AEA Technology, 1994).

---

1. Confusingly, this code is now known as CFX and FLOW3D is a completely different code, both of which will be used in Chapter 6

Verification of calculations

Verification of calculations looks at the errors introduced due to insufficiently resolved spatial and temporal discretisation and insufficient convergence errors. As the partial differential equations in a CFD code do not have an analytical solution, a numerical solution involving discretisation is needed. If the discretisation is sufficiently fine, these errors can be reduced to zero (or at least to a level of round-off error) but this would increase the computational cost of running the simulation. Discretisation will introduce errors, it is up to the the end user to decide what level of accuracy or acceptable error estimate is adequate or needed.

In order to asses the spatial discretisation error in a simulation, a grid convergence study can be conducted. Results from two or more grids of different resolutions are compared and the spatial discretisation is assessed based upon the relative change of a value after grid refinement or coarsening. A more thorough form of verification of calculations will be presented in Section 5.3, where three grids will be used to assess the level of convergence. The observed order of convergence, error bands and grid convergence indices can then be determined.

5.3.2 Validation

Validation is concerned with the error between the numerical model and the physical real world. Here the code is not being validated, but rather the model on which the code is based. It is checking to see if the governing mathematical equations chosen were the correct ones to represent the physical reality. One generally only validates a code for specific applications. However, if a code has been validated for a range of similar cases, one could interpolate between nearby problems and consider the code validated for a range of parameters. Extreme caution should be taken if extrapolating from nearby problems.

If we revert back to the example of a numerical code using an inverse-*cube* law (Roache, 1994), as discussed, this could in theory pass the verification process. It could potentially report a false positive from the validation process if care is not taken to conduct a rigorous validation test. If the validation process compared the numerical results to a small projectile (e.g. a rock being thrown) the numerical model could possibly produce relatively OK results, this is because the model was not stressed enough. If however, this numerical code was used to predict the trajectory of a satellite orbiting the Earth, the inadequacies of the model would

quickly show up and it would fail the validation procedure.

There could be the scenario in which the numerical model is only to be used in calculating the path of a small projectile. It has been validated to a certain percentage for this usage. As long as the problem being modelled is very similar to the validation case, certain degree of confidence can be attached to the results. This highlights the importance of validating numerical results for the specific use wherever possible. Interpolation between previous validation is possible but the end user needs to appreciate that a large caveat should be attached to any extrapolated assumptions of validation.

5.3.3 Qualification

Qualification is another consideration, often ignored in the discussions, that needs to be considered in conjunction with the validation of the numerical code. This is where sound engineering judgement is employed do decide upon what levels of accuracy are needed for the numerical results. On occasion swift results and characteristic information are all that is required to provide rough diagnostic data and this will take precedence over out-right accuracy.

It could be considered that there are three different levels of accuracy required from a CFD calculation,

1. Supply diagnostic information,
2. Provide incremental data,
3. Generate baseline data for the performance model database.

Each of these will have subjective threshold errors when conducting a validation study.

5.3.4 Examining Grid Convergence

Roache (1998) presented a method to examine the spatial convergence of a simulation and a method for determining the formal discretisation error in a CFD simulation[2]. This method calculates a metric referred to as a Grid Convergence Index (GCI) that places an error bound on the obtained results. This method has been adopted by the National Project for Application-orientated Research in

2. Interested readers who cannot obtain the book should consult Roache (1994) and Roache (1997), where this research is outlined in parts

CFD (NPARC), a partnership between NASA and the US Air-Force. This method also sets the criteria and procedure for estimating and reporting of uncertainty in CFD for submission to the Journal of Fluids Engineering (Celik *et al.*, 2008) and all AIAA journals (AIAA, 1998). The research presented in the thesis herein will be following the method outlined by Roache (1998) and the layout proposed by the Journal of Fluids Engineering (Celik *et al.*, 2008).

Richardson Extrapolation

The GCI method is based up on a method for estimating discretisation error first proposed by Richardson (1910), more commonly known as the Richardson Extrapolation (RE), "h^2" method or "iterated extrapolation". RE allows for a higher-order estimate of the continuum value from a series of lower-order discrete values. In essence, it predicts what a measured value will have if the grid spacing was zero. This method has its limitations but it is still recognised as being one of the most reliable predictors of numerical uncertainty (Celik *et al.*, 2008). The discrete solutions for a quantity f are assumed to have a series representation:

$$f = f_{\text{ext}} + g_1 h + g_2 h^2 + g_3 h^3 + \dots \tag{5.11}$$

where, F_{ext} is the exact solution, h is the grid spacing and the functions g_1, g_2 etc. do not depend on any discretisation. For a second order method, $g_1 = 0$.

If two separate discrete solutions f_1 and f_2 are obtained from two different grids, a fine grid with spacing of h_1 and a coarser grid with spacing of h_2, the leading order error terms can be eliminated. The resulting continuum value based upon RE is given as:

$$f_{\text{ext}}^{21} = \frac{h_2^2 f_1 - h_1^2 f_2}{h_2^2 - h_1^2} + \text{H.O.T.} \tag{5.12}$$

where, H.O.T. are higher order terms (Roache, 1998).

Omitting higher order terms and defining the grid refinement ratio $r_{21} = h_2/h_1$ then the RE can be generalised to p^{th} order as

$$f_{\text{ext}}^{21} \cong \frac{r_{21}^p f_1 - f_2}{r_{21}^p - 1} \tag{5.13}$$

$$\cong f_1 + \frac{f_1 - f_2}{r^p - 1} \tag{5.14}$$

The difference between f_1 and f_{ext} could be considered as an error estimate but

careful consideration should be paid to the assumptions and caveats attached to f_{ext}. In Eq. 5.14, the second term on the rhs can be considered as an error estimator of f_1 (NPARC, 2010). Presenting this as an estimated fractional error, E_1, for a fine mesh solution gives, (Roache, 1998)

$$E_1 = \frac{e_a^{21}}{r^p - 1} \tag{5.15}$$

where the approximate relative error, e_a^{21}, is given as,

$$e_a^{21} = \left| \frac{f_2 - f_1}{f_1} \right|. \tag{5.16}$$

The estimated fractional error, E_1 is a good approximation to the discretisation error of the grid solution if that solution is of reasonable accuracy i.e. $E_1 \ll 1$ (Gretton, 2009). This metric is far more useful than the relative error, e_a^{21} as it incorporates both the refinement ratio, r and order, p.

Another metric can also be used with the Richardson extrapolation, the extrapolated relative error of the fine mesh solution, e_{ext}^{21}, comparing the solution on the fine mesh to the Richardson's extrapolated value can be presented as

$$e_{ext}^{21} = \left| \frac{f_1 - f_{\text{ext}}}{f_{\text{ext}}} \right|. \tag{5.17}$$

Grid convergence index for the fine grid solution

Roache (1998) suggests the need for a consistent method for reporting of grid convergence studies to estimate the discretisation errors associated with a calculation. This would allow for comparison between methods that use higher order advection schemes and different grid refinement ratios, r. While the error estimator, E_1 is based upon a rational and consistent theory, it is not a bounded estimate of the error. This value of E_1 does not provide a very good confidence interval, it could be equally over optimistic as conservative. Roache (1998) argues that what engineers and scientists want is a practical level of confidence. They are looking for a set tolerance on the accuracy which may be exceeded, akin to a statisticians 2σ confidence interval.

Most engineers would consider that e_a^{21} would be a reasonable error band, assuming that the solution was indeed in the asymptotic range of convergence. If the

results were obtained using a second-order method with a grid refinement ratio, $p = 2$ and $r = 2$ and the resulting E_1 is only 1/3 of e_a^{21}.

Roache (1998) provides a method for approximately comparing e_a^{21} obtained using any value for p and r to the expected results from a grid doubling using second-order method. The relation is based upon equality of the error estimates. The GCI is defined as being equivalent to the value of e_a^{21} that would produce the same E_1 with $r = 2$ and $p = 2$ as the value of E_1 calculated with the actual values for e_a^{21}, r and p form the grid convergence study. It is expressed as:

$$GCI_{21} = F_s \frac{|e_a^{21}|}{r^p - 1} \tag{5.18}$$

It can be noted that for a grid-doubling with a second-order method, the denominator is equal to 3, in Eq. 5.18 and we obtain $GCI = e_a^{21}$. Thus F_s can be considered as the factor of safety over the Richardson error estimator, E_1.

Choice of F_s

The coefficient value of the factor of safety is an arbitrary number based on rational and objective judgement. Arguably it could be "1" or "3" or any where in between. Roache (1998) recommends that for convergence studies using two-grid solutions a value of $F_s = 3$ should be used, but for studies with a minimum of three grids used to demonstrate the observed order of convergence p on the actual problem a value of $F_s = 1.25$ is recommended as being adequately conservative (Celik *et al.*, 2008; Roache, 1998)[3].

Grid convergence index for the coarse solution - or Achieving the asymptotic range

If there is a choice between a fine grid solution and a coarse grid solution, it would be expected to report the fine grid GCI. However, if a large parametric study is to be carried out, it might be desirable to use the coarser mesh. Then it is needed to quantify the error for this coarser mesh defined as:

$$GCI_{32} = F_s \frac{|e_a^{32}| r^p}{(r^p - 1)}. \tag{5.19}$$

---

3. A more complete discussion on the choice of F_s can be found in Roache (1994) and Roache (1998). Originally Roache recommended a $F_s = 3$ but subsequently decided that $F_s = 1.25$ was more appropriate in certain occasions.

This is useful to check if the solution lies in the asymptotic range of convergence,

$$GCI_{32} = r^p GCI_{21} \tag{5.20}$$

where, the ratio should be close to unity.

Extracting the observed order of convergence

The order of grid convergence is observed as being the difference between the discrete solution and the exact solution,

$$E = f(h) - f_{\text{ext}} = Ch^p + H.O.T. \tag{5.21}$$

where, C is a constant and h is some measure of grid spacing.

In theory, a CFD code that implements a second-order method should observe an second-order of convergence, but the boundary conditions, numerical models and grid stretching will reduce this order so that the observed order of convergence will in fact be lower.

A direct evaluation of the observed order of convergence, p can be extracted from three solutions using a constant grid refinement ratio, $r = r_{12} = r_{23}$, where "1" represents the finest grid.

$$p = \ln \left| \left(\frac{f_3 - f_2}{f_2 - f_1} \right) \right| / \ln r. \tag{5.22}$$

If the refinement ratio is not constant, the order of convergence can be extracted as (Celik *et al.*, 2008):

$$p = \left(\left| \ln \left(\frac{f_3 - f_2}{f_2 - f_1} \right) \right| + q(p) \right) / \ln r_{21} \tag{5.23}$$

$$q(p) = ln \left(\frac{r_{21}^p - s}{r_{32}^p - s} \right) \tag{5.24}$$

$$s = 1 \cdot \text{sgn}(\varepsilon_{32}/\varepsilon_{21}) \tag{5.25}$$

where, $\varepsilon_{32} = f_3 - f_2$ and $\varepsilon_{21} = f_2 - f_1$.

Non-Cartesian or Unstructured grids

If an unstructured mesh is being used it may be difficult to obtain the value of the grid refinement ratio, r. NPARC (2010) show that the effective grid refinement ratio can be obtained as:

$$r_{\text{effective}} = \left(\frac{N_2}{N_1}\right)^{1/D} \tag{5.26}$$

where, N is the number of grid points and D is the dimension of the flow domain.

The Journal of Fluids Engineering suggest a similar approach, showing that for a three-dimensional problem, a representative grid size, h can be obtained as:

$$h = \left[\frac{1}{N}\sum_{i=1}^{N}(\Delta V_i)\right]^{1/3} \tag{5.27}$$

or in two-dimensions as:

$$h = \left[\frac{1}{N}\sum_{i=1}^{N}(\Delta A_i)\right]^{1/2} \tag{5.28}$$

where, ΔV_i is the volume, ΔA_i is the area of the ith cell, and N is the total number of cells used. The effective refinement ratio can then be obtained from $r = h_{\text{coarse}}/h_{\text{fine}}$.

> *The whole problem with the world is that fools and fanatics are always so certain of themselves, but wiser people so full of doubts.* - Bertrand Russell

Chapter 6

Computational fluid dynamic results and discussion

The advantages of using computational fluid dynamic (CFD) commercial codes, that solve for viscous terms and account for wave breaking are highly attractive to the wave energy sector. Studies have been conducted investigating merits of using CFD codes both as numerical wave tanks and for calculating wave loading in extreme waves on wave energy converters, but the studies published have not concentrated on the fidelity of the waves generated and none have conducted a formal grid convergence study on commercial solvers.

Extreme wave loading has been investigated using both commercial and academic codes. Westphalen *et al.* (2008, 2009) compared CD-Adaco's STAR-CCM+ to ANSYS CFX and reported promising results for this application from both commercial solvers. Wave height attenuation, down-wave of the inlet boundary condition, was observed to occur for both solvers, noting that wave amplitudes decreased monotonically down the numerical wave tank. This was reported to be more pronounced for STAR-CCM+ than CFX, but as the waves involved were extreme waves, the height attenuation was not considered to be an issue.

Bhinder *et al.* (2009a) conducted a joint numerical and experimental study on a surging point absorbing wave energy device. Two commercial CFD solvers (CFX and FLOW-3D) were used as the numerical codes. Both underwent a preliminary investigation, examining how well they modelled progressive linear waves. Severe wave height attenuation as the wave travelled down the flume, was reported for CFX. This was attributed to numerical dissipation. FLOW-3D was reported to model progressive linear waves adequately. Wave height attenuation is visible in the published figures, but this was not discussed in the paper. This publication was later followed up with a second paper using FLOW-3D to model the wave

energy device (Bhinder *et al.*, 2009b). Neither publications concentrated in detail on the quality of the waves as more attention was paid to the comparison of numerical forces against experimental measurements.

Wang and Zhao (2010) used FLUENT to model a 2D numerical wave tank. Here, first order, second order and solitary waves are modelled. This paper did not include a large discussion on the results, but it is clear from published figures that wave height attenuation was present. Decreases in wave height measurements down the flume of up to 50% were reported.

Lal and Elangovan (2008) performed a validation study for a flap-type wavemaker using CFX. This publication concluded the the results were in good agreement with wavemaker theory and stated that CFD simulations using CFX can effectively replace physical wavemaking flumes for regular wave generation. These conclusions are in contrast to the results presented where it is clear that there is wave height attenuation within the numerical wave flume which was not discussed. The quality of the waves produces was not analysed in detail and no formal grid convergence study or error bounds were placed on the CFD results. This publication was later followed up with a similar validation study using a plunger type wavemaker, again in CFX (Elangovan, 2010). Wave height attenuation is again clear in the published figures but it is not discussed and the conclusions are that CFX can adequately model plunger type wave makers and the associated radiate waves. Elangovan and Sahoo (2010) published another study on the generation of irregular waves in CFX. The figures presented in this publications were either, in the time domain or frequency domain, so it is difficult to establish if wave height decay was an issue. No thorough in-depth analysis of the results are conducted, yet the publication concluded that it is possible to model irregular waves for a given spectrum.

Silva *et al.* (2010) conducted a validation case comparing CFX and analytical calculations. The numerical output from CFX was compared to first and second order wavemaker theories. Good agreement was reported with errors in the region of $\pm 2.5\%$. The errors increased with progression away from the wavemaker. While no formal grid convergence study was conducted, the informal investigation reported best results for CFX with cell aspect ratios (vertical:horizontal spacing) of $\approx 1:4$ and suggesting the best time step was $\approx T_P/100$, where T_P is the wave period.

Several other studies have used CFD codes to model numerical wave tanks (Huang

et al., 1998; Lin and Liu, 1999; Park, 2004; Wang *et al.*, 2007; Causon *et al.*, 2008; Maguire and Ingram, 2009; Hu *et al.*, 2009; Maguire and Ingram, 2010). None of these studies have conducted a formal grid convergence study and the majority of them are not concerned with the quality of the waves as a they are more interested in the hydrodynamic response of the device being modelled.

There are conflicting reports from the literature regards what commercial CFD solvers can or cannot model. Some studies conclude that commercial CFD solvers are capable of modelling radiated free surface waves from a oscillating body, suggesting that the numerical wave tank could replace the experimental wave tank. Other authors report that wave height attenuation is persistent in commercial codes but it is not an issue for concern. Others report that some commercial codes are not suitable while different ones are suitable.

Wave height attenuation in commercial CFD VOF solvers appears to be an issue, but this is not quantified. There are no studies at present that conduct a formal grid convergence study similar to that mandated by Celik *et al.* (2008). There is a lack of information on what solver options within certain codes are most appropriate, what grid refinement is needs and what time steps result in optimal results.

It is clear that there is a need to quantify formally the capabilities of commercial CFD solvers in order to establish the range of applicability for each code and, arguably more importantly, the limitations of the CFD solvers. There is anecdotal evidence that user expectations are unrealistic when it comes to CFD. It is not always appreciated that commercial CFD codes were designed with specific applications in mind. CFD software companies have ensured that their codes accurately model industries with the potential for greatest financial return. The size of the wave energy market pales in comparison to the oil and gas, offshore, coastal defence and aeronautical industries. As such, the wave energy sector hopes to 'piggy back' of the advancements in free surface modelling due to the impetus of these more lucrative offshore industries. The wave energy industry is concerned with modelling radiated waves from oscillating bodies with a free surface. This is a different problem to that of oil and gas, or ship building where they are more concerned with diffraction forces than radiation forces. Before the wave energy sector can use commercial CFD codes with confidence, the solvers need to be verified and validated for the specific intended use.

This Chapter will perform a formal temporal and spatial verification study on

two commercial CFD codes, concentrating upon free surface modelling capability from oscillating bodies. It will take the most commonly used commercial CFD code reported in wave energy research literature, ANSYS CFX and another code, FLOW-3D which was reported as being the best commercial code for free surface modelling. It will model the monochromatic radiated wave from an oscillating wavemaker in a 2D wave flume and assess the fidelity of the waves produced. A formal temporal and spatial verification procedure, according to Celik *et al.* (2008), will be conducted on both codes. A validation case using CFX and linear wavemaker theory will also be presented and the results and implications will be discussed.

6.1 The numerical wave flume

The dimensions of the numerical flume is chosen to be similar to the physical wave flume at the University of Edinburgh, and indeed many other hydrodynamic laboratories around the world. In modelling the flume, the water depth of the flume was set to 0.8m and the period of oscillation of the wavemaker set to 1s. According to the dispersion relationship, Eq. 3.42, the wavelength can be obtained as

$$\lambda = \frac{g}{2\pi} T^2 \tanh \frac{2\pi h}{\lambda}, \tag{6.1}$$

thus resulting in a wavelength $\approx$ 1.56m. Assuming deep water conditions, the phase speed of the waves, c, is given by $\lambda/T = 1.56$m/s and the group velocity, is half that, $c_g = 0.78$m/s. The overall length of the wave tank was chosen as 15.6m, equating to a non -dimensional tank length of 10λ.

The wave height in the flume is proportional to the stroke amplitude of the wavemaker. For the verification study, a wave height of $H = 8$cm was selected, typical for a flume of these dimensions, and the stroke amplitude of the wavemaker was set according to the ratios described in Section 3.4.

It should be observed that a wave height of 8cm results in waves that operate in the stokes second-order regime, Figure 6.1. This does break some of the underlying assumptions of linear wave theory, upon which the stroke displacement to wave height ratio was based, but linear theory is robust and is still used with physical wavemakers with very good agreement (Ursell *et al.*, 1960). Regardless of the physics of the problem being solved, these results can be analysed for verification

of descretisation errors, as this process is concerned with solving the equations correctly, not with the real world accuracy of the results.

6.2 CFX

This section presents the verification and validation of results from the commercial CFD code ANSYS CFX v12. This is an implicit, coupled, finite volume based solver using the volume of fluid scheme for multiphase flow. The transient solver was selected because the problem being modelled is inherently time varying. Other solver options implemented were homogeneous multiphase, with a second-order transient solver and coupled volume-fraction.

The flow was initialised using a steady state solution of the transient problem at the initial time $t = 0$. This was necessary due to stability issues with the CFX solver, particularly during the initial time steps. For the steady state solution, the flow was initialised with all velocity components set to zero. The pressure field in the water was set according to the hydrostatic pressure and pressure was initialised as uniform in the air. The volume fractions of the water and air were implemented using a step function, within the CFX expression language. The volume fraction below the SWL was set to 1, water, and the volume fraction above the SWL set to 0, air. The steady state solution was run for 100 iterations. Usually, a steady state solution would be run until some residual convergence criteria was met but, the for the steady state, the residuals plateaued at $\approx 1 \times 10^{-4}$ and no further convergence was observed. This could be due to the fact that the boundary conditions were not introducing any mass or momentum into the domain and, therefore the initial conditions were almost an exact solution to begin with and there is no more opportunity for the solution to converge.

The results from the steady state solution were used to set the initial conditions for the transient case. The total time for the transient run was set as 18s. This was chosen to give an appropriate amount of time to analyse the progression of the waves while keeping the computational time to a minimum.

All of the CFX problems were run on machines with Intel core 2 Quad CPU at 2.50GHz processors and 8GB of RAM, unless otherwise specified. The problems were parallelised using local HP MPI and the the mesh was split using the user specified partitioning direction. The best results were found partitioning the

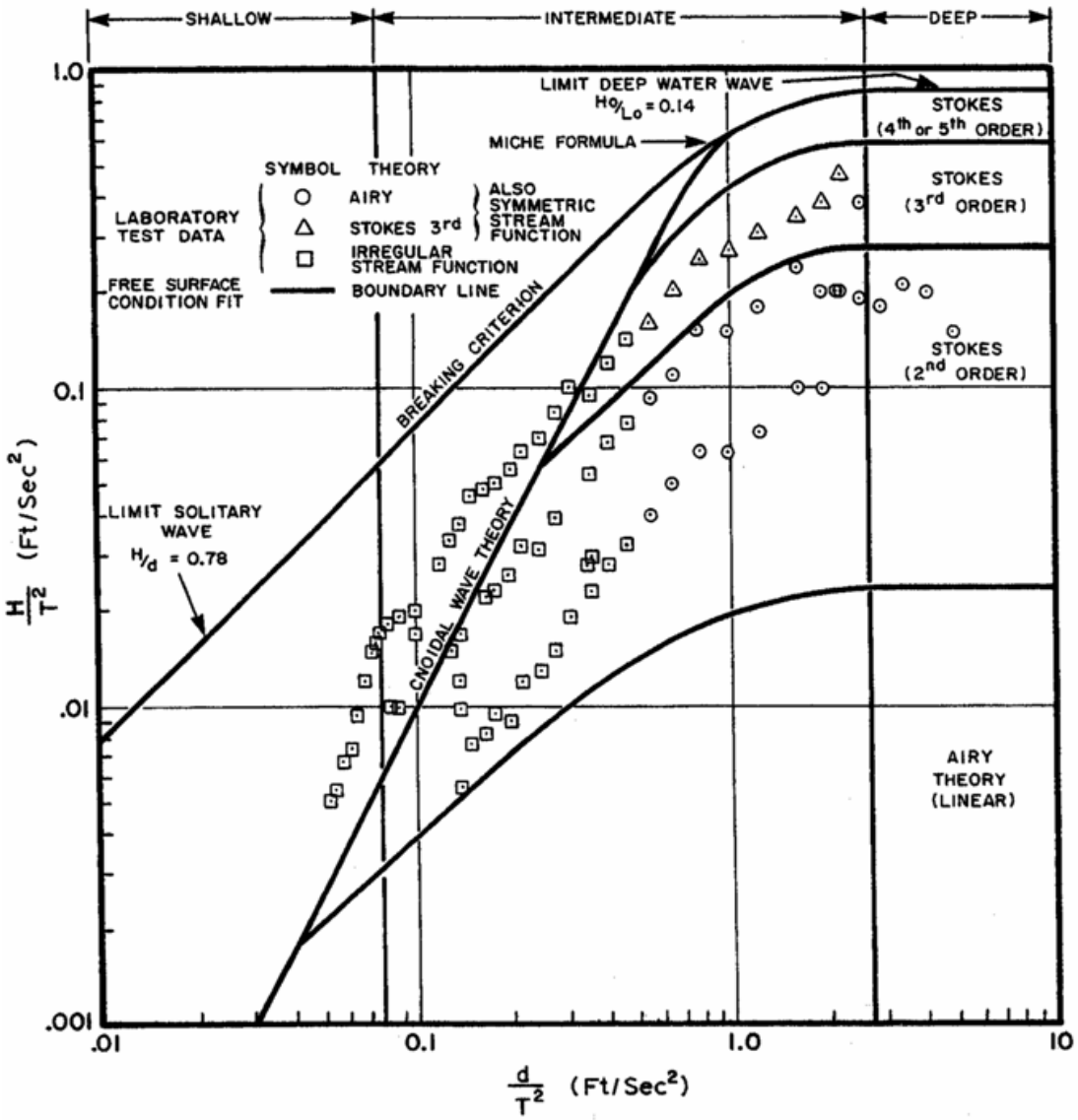

Figure 6.1: Validity ranges of various wave theories (Chakrabarti, 1987).

mesh in the direction of the propagating wave, [1 0 0]. The sovler proved to be more robust using this option, but the computational times were slightly longer compared to the standard MeTiS partitioning option.

6.2.1 Generation of meshes

All meshes for CFX were generated using ICEM, a bespoke meshing programme for ANSYS software. Overall the mesh is 10 wavelengths long (15.6m) in the x-direction and two water depths high, h, in the y-direction (1.5m). This mesh is extruded to a thickness of one cell in the z-direction, as this is a requirement by the CFX solver to model quasi 2D problems. An overview of the coarse mesh is shown in Figure 6.2.

The mesh consists of three distinct regions. The section closest to the wavemaker is a region one wavelength long, where mesh motion in the solver is enabled. This is required in order to implement an oscillating solid boundary, which is needed to replicate a physical wavemaker. Next is a region four wavelengths long, exactly the same as the first region only with mesh motion disabled. This is because the mesh motion is inherently dissipative and could lead to unwanted damping of the progressive waves. The third region is where the node spacing in the x-direction is successively stretched up to a point where the spacing, Δx, is larger than at least half a wavelength. This is to act as a numerical dissipation zone where any waves will be progressively damped out and, thus, avoid any unwanted wave reflections from the far boundary wall. In this region the growth ratio of the cells was ≤ 1.10 as excessively aggressive stretching could lead to numeric reflections. This resulted in a *de-facto* wave flume of five wavelengths long and a five wavelength damping zone.

In order to capture accurately the free surface, a region of refined mesh with decreasing node spacing is required at the interface between the air and water. This region around the still water level (SWL) has a uniform node spacing in in the y-direction. This region, with refined uniform mesh spacing, extends ± 0.05m from the SWL to ensure that the expected wave height of 0.08m would be captured adequately. The region of air above the water is of little interest in this study and, due to the exponential decay of the water partials such dense grid refinement was not necessary at the bottom of the flume. This allows for a mesh with a smaller node count and allowing for quicker solving times. Geometric stretching of node spacing, Δy, is enforced above and below the SWL, Figure 6.3.

Figure 6.2: View of the entire wave flume domain for the coarse mesh. The grid stretching towards of the end of the domain is visible as is the region of mesh refinement around the still water level (SWL).

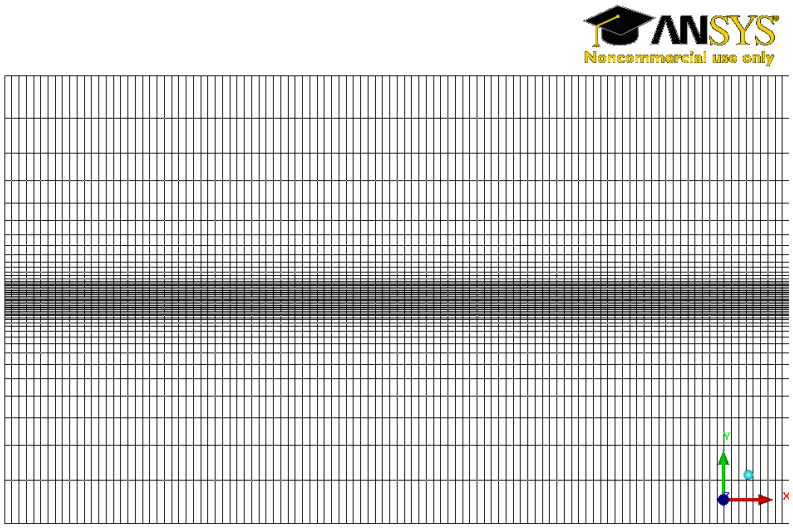

Figure 6.3: Close up of the mesh region beside the wavemaker showing the region of uniform refinement and the grid stretching above and below this region.

6.2.2 Boundary Conditions

The boundary conditions imposed in this problem were: symmetrical boundary conditions on both near and far vertical faces along the length of the flume (with reference to Figure 6.2). No-slip wall conditions were imposed on both the far wall ($x = 15.6$m) and the bottom of the wave flume. The wavemaker was represented using an oscillating wall boundary condition. The wall velocity was set relative to the prescribed mesh motion. The mesh motion was achieved through a specified displacement in the x-direction, implemented via CFX expression language. The displacement was sinusoidal with the amplitude set by Eq. 3.111 for a piston wavemaker,

$$\frac{H}{x_0} = 4\,\frac{(\cosh(kh))^2 - 1}{2\,kh + \sinh(2\,kh)}. \tag{6.2}$$

The amplitude of the sinusoidal displacement was ramped up over 2s. The upper region of the mesh was set as an opening boundary, with entrainment option selected for the mass and momentum option. However, the upper boundary for the region next to the wavemaker was set as a non-slip wall. This is the upper boundary at right angles to the moving paddle where the CFX manual suggests that all open boundaries should be orthogonal to a moving mesh. In the case of a bottom hinged flap, this would not be true as the paddle would be pitching. Therefore this boundary was specified as a wall and not an opening. It extends a distance of one wavelength into the domain and corresponds to the region where

mesh motion is permitted. This would be analogous to a horizontal overhang next to the wavemaker in a physical flume.

The total time for the simulations was selected as 18s. This was to allow for the ramp up period of 2s, the waves to progress to the end of the 5λ tank[1] and then for a wave crest to travel the length of the flume, at the wave phase speed, which takes 5s. Then an arbitrary extra second was included, taking the total transient run time to 18s. As this tank is effectively 10λ in length, and the period of oscillation is $T = 1$, the total run time of 18s will mean result in no wave reflections measured at $x \leq 5\lambda$ within the chosen time duration.

6.2.3 Temporal Discretisation

A temporal discretisation study was conducted in order to analyse the effect of time step selection on the results. The objective of this study was to ensure the selection of an appropriate time step, that yielded accurate results, in the quickest computational time.

If the time step chosen was too large, the CFX solver would perform too many inner loop calculations. This is where the solver iterates through the solution at one single time step in order to achieve convergence of the residuals. Throughout the calculations the inner loop limit was set to ten iterations, thus too high a time step and the solver would reach this limit and move onto the next time step without achieving residual convergence. This results in both suboptimal results due to lack of convergence and increased computational time due to too many inner loop calculations. If the time step was too small, the inner loop iterations would invariably only perform one iteration and move to the next time step with fast residual convergence, but, there would now be an excessive amount of time step calculations and the computation time would be unnecessarily large. Also, the larger the number of time steps could risk the introduction of numerical round off errors.

The time step was chosen with the Courant Friedrichs Lewy (CFL) condition in mind. This number is used as a metric for explicit CFD solvers to analyse the stability of the calculations. While CFX is an implicit solver, and the CFL condition is a limiting factor for explicit schemes, choosing the time step based upon the CFL still has its merits as it is a non-dimensional number based upon

1. ($c_g = \lambda/2T$ thus this equals 10s.)

the time step, grid spacing and the speed at which objects travel through the grid.

For a two dimensional case the CFL number can be calculated as (Apsley and Hu, 2003),

$$\frac{u_x \Delta t}{\Delta x} + \frac{u_y \Delta t}{\Delta y} = CFL \tag{6.3}$$

where, u_x is the maximum expected velocity in the x-direction, u_y is the maximum expected velocity in the y-direction, Δt is the time step and Δx and Δy are the grid spacings in x-direction and y-direction respectively. Generally, when choosing the values of u_x and u_y, the maximum values of velocity are used. Care needs to be taken with deep water waves as the phase velocity of the wave train is twice as fast as the group velocity and, as a result, u_x needs to be set to the phase velocity of the waves, not the maximum particle velocity.

There is some discussion in the literature with regards the choice of stability limit. Some authors suggest using only the maximum value from either the x or y-directions (Hirt and Nichols, 1981), Apsley and Hu (2003) suggests using the aforementioned 2D CFL number, Eq. 6.3 and Thomas (1995) uses both, but suggests that Eq. 6.3 might be more conservative than necessary. For the study herein, the more conservative value method will be used, i.e. Eq. 6.3[2].

Four different relative time steps were investigated during the temporal investigation. The temporal study was conducted on both the coarse and medium meshes. It was advised to keep the calculated CFL number as low as possible, but not lower than one (ANSYS, 2008). This was anecdotal, and needed to be confirmed. The CFL numbers used in this study were: 4.4, 2.2, 1.1 and 0.55. The corresponding time steps for these CFL numbers on the three meshes can be seen in Table 6.1. As time is another physical dimension similar to space, the results from a temporal convergence study can be analysed in a very similar manner to a spatial grid convergence study (Roache, 1998). With four CFL numbers, two convergence studies can be conducted, the first with CFL numbers 4.4, 2.2 and 1.1 and the second with CFL numbers 2.2, 1.1 and 0.55. The corresponding convergence indices can be seen in Table 6.3 and Table 6.4.

The measurement of wave height, H, was chosen as the variable to be used in

2. For reference, the one dimensional CFL numbers would results in, CFL_x: 1.28, 0.64, 0.32, 0.16; and CFL_y: 3.12, 1.56, 0.78, 0.39. It can be seen that the y direction is limiting the time step selection, this is due to the extra refinement needed near the free surface.

Table 6.1: The time steps, in seconds, used to achieve a given CFL number on the three successively finer grids

CFL	Coarse	Medium	Fine
4.4	0.02	0.01	0.005
2.2	0.01	0.005	0.0025
1.1	0.005	0.0025	0.00125
0.55	0.0025	0.00125	0.000625

these convergence studies, but the overall trend was similar for other metrics investigated, such as: wavelength, zero up-crossing point, wave peak, wave trough.

Time step selection

The choice of time step involves balancing accuracy and CPU time. The metrics obtained from this temporal convergence study quantify the error introduced through using a discretised time step and allow for an informed decision to be made as to which time step is appropriate for the relevant end use.

Table 6.3 presents the results using a formal convergence index described in Chapter 5. As discussed, the wave tank is de facto 5λ long and, as a result, four wave heights can be measured using a zero down-crossing measurement. These four wave height measurements are taken using three successively refined time steps; CFL numbers = 1.1, 2.2, 4.4. These are then used to assess how refined the solution is using the finest time step.

Table 6.3 shows good convergence between between CFL numbers of 2.2 and 1.1, reporting actual errors, e_a^{21}, of less that 0.7% and a grid convergence index $\text{GCI}_{\text{fine}}^{21} \approx 0.1\%$. This indicates that good convergence is achieved using a CFL number of 1.1 and reasonable results are also observed when using a larger CFL number of 2.2. Absolute errors between the two time steps were observed as $\varepsilon_{21} \approx 0.0005$m.

Table 6.4 shows the metrics when using CFL numbers of 2.2, 1.1 and 0.55. Here, oscillatory convergence is observed in the wave height measurement between CFL numbers of 1.1 and 0.55.

This suggests that the CFL number of 0.55 is too small and that better, and quicker results would be obtained using a CFL number between $1 - 2$. The exact value is a matter of judgement. The absolute and relative errors between using a

Table 6.2: Total CPU time to run a transient 18 second simulation on the medium mesh using a quad core processor

CFL number	Total CPU time[1]	Wall clock time[2]
4.4	8.621 x10^5 s	2.5 days
2.2	1.651 x10^6 s	4.8 days
1.1	2.021 x10^6 s	5.9 days
0.55	4.135 x10^6 s	11.9 days

[1] Summed CPU time using four core processors
[2] Total wall clock time

Table 6.3: Convergence indices for the temporal convergence study on the medium mesh using CFL numbers of 4.4, 2.2 and 1.1 . The indices are given for four waves, numbered one to four, based upon the zero down crossing of the wave. Subscript index 3 represents the coarsest relative time step and 1 the finest.

	1	2	3	4
f_3 [m]	0.074	0.070	0.068	0.066
f_2 [m]	0.077	0.073	0.074	0.071
f_1 [m]	0.078	0.073	0.074	0.072
ε_{32} [m]	-0.003	-0.003	-0.005	-0.005
ε_{21} [m]	-0.001	0.000	-0.001	0.000
p	2.458	3.000	3.363	3.818
f_{ext}^{21}	0.078	0.073	0.074	0.072
e_a^{21}	0.71%	0.54%	0.70%	0.54%
e_{ext}^{21}	0.16%	0.08%	0.07%	0.04%
GCI_{fine}^{21}	0.2%	0.10%	0.09%	0.05%

CFL number of 1 or 2 can be seen in Table 6.7. If absolute accuracy is paramount, a time step that results in a CFL number of 1.1 should be used. Table 6.2 shows that a halving of CFL number results in roughly a corresponding doubling of CPU solving time. This metric can be used to weigh up the options for the decision making process between accuracy and computational expense.

Qualitatively, the convergence of the time step selection on the coarse mesh can be seen in Figure 6.4 and, on the medium mesh in Figure 6.5. Both showing that there is little discernible difference qualitatively between a CFL number of 1.1 or 2.2.

Table 6.4: Convergence indices for the temporal convergence study on the medium mesh using CFL numbers of 2.2, 1.1 and 0.55 . The indices are given for four waves, numbered one to four, based upon the zero down crossing of the wave. Subscript index 3 represents the coarsest relative time step and 1 the finest.

	1	2	3	4
f_3 [m]	0.077	0.073	0.074	0.071
f_2 [m]	0.078	0.073	0.074	0.072
f_1 [m]	0.077	0.074	0.073	0.074
ε_{32} [m]	-0.001	0.000	-0.001	-0.000
ε_{21} [m]	0.001	-0.001	0.001	-0.002
p	0.689	1.405	1.1335	2.513
f_{ext}^{21}	0.075	0.075	0.072	0.074
e_a^{21}	1.16%	1.42%	1.79%	3.00%
e_{ext}^{21}	1.92%	0.85%	1.19%	0.63%
GCI_{fine}^{21}	2.36%	1.08%	1.47%	0.80%

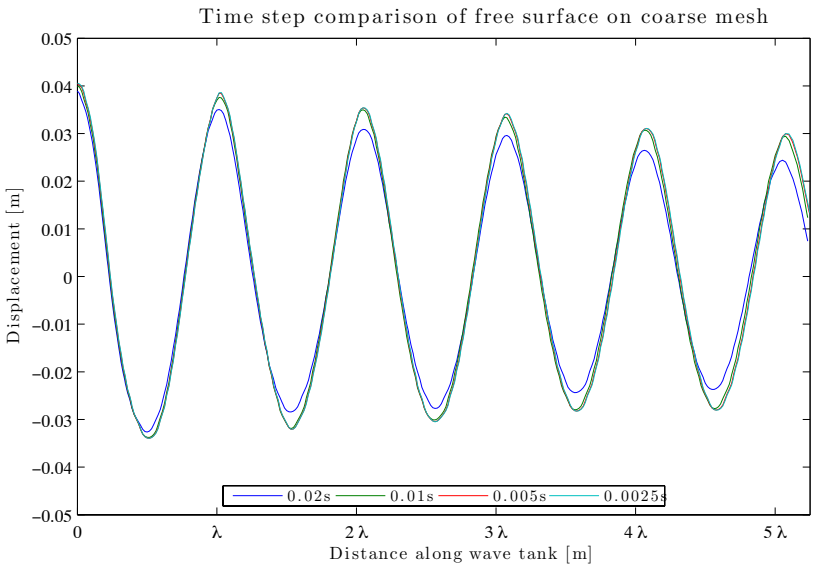

Figure 6.4: Free surface plot showing the water displacement from the SWL at a time of 18s on the coarse mesh. Four time steps were selected, corresponding to CFL numbers of 4.4, 2.2, 1.1 and 0.55 respectively.

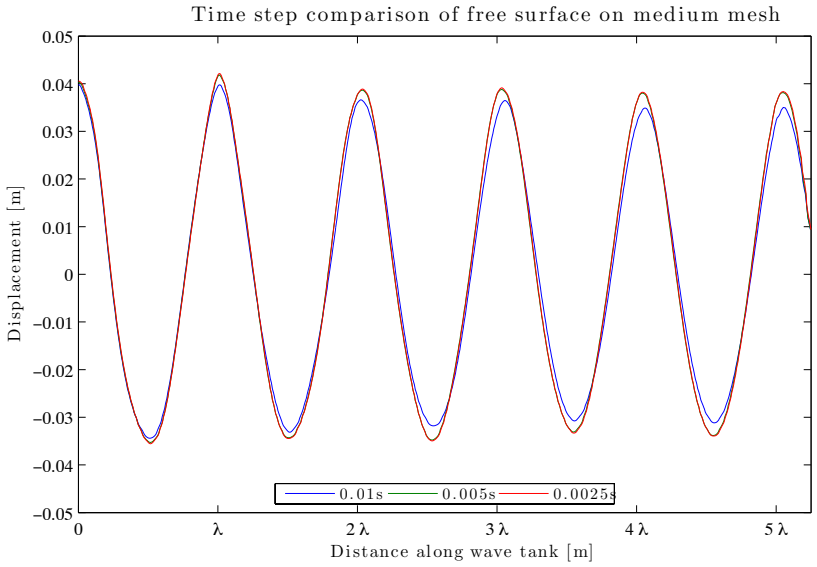

Figure 6.5: Free surface plot showing the water displacement from the SWL at a time of 18s on the medium mesh. Three time steps were selected, corresponding to CFL numbers of 4.4, 2.2, 1.1 respectively.

6.2.4 Spatial discretisation

As discussed in Chapter 5, it is essential that all CFD results undergo a spatial verification process to quantify the errors introduced through solving a set of continuous equations on a discrete grid. The methodology proposed by Roache (1998), and subsequently adopted by NASA (NPARC, 2010) and the Journal of Fluids Engineering (Celik *et al.*, 2008) will be followed herein.

In order to extract the observed order of convergence, at least three different grids with constant refinement ratios are needed. For this verification study, three different scaled meshes were used referred to as: coarse, medium and fine. The coarse mesh has twice the node spacing in both x and y-directions compared to the medium mesh, and similarly, the medium mesh has twice the node spacing in both x and y-directions compared to the fine mesh. Therefore, the refinement ratio was constant at $r = 2$.

The absolute values for medium mesh were chosen based upon a preliminary study detailed in Appendix A. This preliminary study chose initial mesh spacings similar to that used in a publication by Gretton *et al.* (2010), who modelled the fluid flow over a submerged hydrofoil. The preliminary study in Appendix A suggested that the CFX results were more sensitive to the spacing in Δx than Δy. Thus, for the present investigation it was decided to reduce the spacing of

Table 6.5: Grid refinement mesh spacing

	Coarse	Medium	Fine
cells / λ	64	128	256
cells / H	16	32	64
Node Count	37842	142170	552178

Δx compared to Gretton *et al.* (2010).

As the wave flume domain being modelled has an aspect ratio of $\approx 1:10$, and the grid spacing in the x-direction is uniform, any extra refinement to Δx will increase the computational expense proportionally. A pragmatic choice of node spacing for the medium mesh of 128 nodes/λ in the x-direction and 32 nodes/H in the y-direction was decided upon. This specification of node spacing in the y-direction is applicable in the region of refinement around the SWL, as mentioned, away from this uniform region, the node spacing is grown in the y-direction (Figure 6.3). The coarse and fine meshes are coarsened and refined, by a factor of two, versions of the medium mesh.

Table 6.5 lists the relative spacing for each of the three grids. The reason that the total node count between the three meshes does not increase by exactly a factor of four is due to the dissipation region at $x \geq 5\lambda$. In this region, as opposed to doubling the number of nodes in the x-direction for each successive grid, a constant growth ratio was sought. Thus, the relative increase in node count going from the coarse to the medium and the medium to the fine meshes did not result in a quadrupling of nodes. In the region of interest, 5λ out from the wavemaker, the scaling along both the x and y-directions increases by exactly a factor of two and results in a factor of four increase in total node count.

Table 6.6 presents the grid convergence indices, using a CFL number of 2.2 and wave height, H, as the metric of interest. The wave tank is five wavelengths long, allowing for four wave measurements using the zero down-crossing values. The observed levels of grid convergence vary between 1.15% and 4.54% depending on which wave measurement is taken. Relative errors between the medium mesh and fine mesh vary between 2.19% and 5.91%. The Richardson extrapolation error on the fine mesh, detailing the error between the fine mesh and a hypothetical mesh with zero grid spacing, reports errors between 0.19% and 3.50%. Observed orders of convergence give values of $p \approx 1.54$. This order of convergence compares well, considering the second order implemented by the CFX solver, which in theory

Table 6.6: Grid convergence indices for the wave height using a constant CFL number equating to 2.2. The indices are given for four waves, numbered one to four, based upon the zero down crossing of the wave. Subscript index of 3 represents the coarsest relative mesh and 1 the finest.

	1	2	3	4
f_3 [m]	0.071	0.067	0.064	0.059
f_2 [m]	0.077	0.073	0.074	0.071
f_1 [m]	0.079	0.076	0.076	0.076
ε_{32} [m]	-0.006	-0.006	-0.010	-0.012
ε_{21} [m]	-0.002	-0.003	-0.003	-0.004
p	1.753	1.045	1.878	1.483
f_{ext}^{21}	0.080	0.079	0.077	0.078
e_a^{21}	2.19%	3.86%	3.57%	5.91%
e_{ext}^{21}	0.91%	3.50%	1.32%	3.19%
GCI_{fine}^{21}	1.15%	4.54%	1.67%	4.11%

should result in a value of two. It is rarely the case that the observed order of convergence will equal the order of the numeric scheme, as errors are introduced through a number of different sources (Roache, 1998).

Table 6.7 details the same indices, but using a CFL number of 1.1. For this case, the grid convergence indices are not as well behaved compared to a CFL number of 2.2. Here, the observed order of convergence is erratic varying from 0.87 to 3.061. Both the relative errors and the GCI errors are larger using a CFL number of 1.1 compared to 2.2. Analysing this further, and comparing the wave heights on the fine meshes in Tables 6.6 and 6.7, oscillatory convergence in the wave heights is observed. This would suggest that using a CFL of 1.1 on the fine mesh is too small and that more reliable results can be obtained using a CFL of 2.2.

One dimensional refinement

A preliminary study observed that greater improvements in the free surface elevation occurred with refinement of mesh spacing in Δx compared to Δy (Appendix A). The mesh for this preliminary study was based on a publication by Gretton *et al.* (2010), who investigated the wave form behind a submerged hydrofoil. This publication used a medium mesh with 50 nodes/λ in the x-direction and 40 nodes/H in the y-direction. This grid spacing resulted in high aspect ratios

Table 6.7: Grid convergence indices for the wave height using a constant CFL number equating to 1.1. The indices are given for four waves, numbered one to four, based upon the zero down crossing of the wave. Subscript index of 3 represents the coarsest relative mesh and 1 the finest.

	1	2	3	4
f_3 [m]	0.072	0.067	0.065	0.059
f_2 [m]	0.078	0.073	0.074	0.072
f_1 [m]	0.078	0.077	0.075	0.078
ε_{32} [m]	-0.005	-0.006	-0.009	-0.012
ε_{21} [m]	-0.001	-0.003	-0.001	-0.006
p	3.061	0.867	2.994	0.977
f_{ext}^{21}	0.078	0.081	0.075	0.084
e_a^{21}	0.81%	4.23%	1.58%	7.99%
e_{ext}^{21}	0.11%	4.88%	0.23%	7.62%
GCI_{fine}^{21}	0.14%	6.41%	0.28%	10.31%

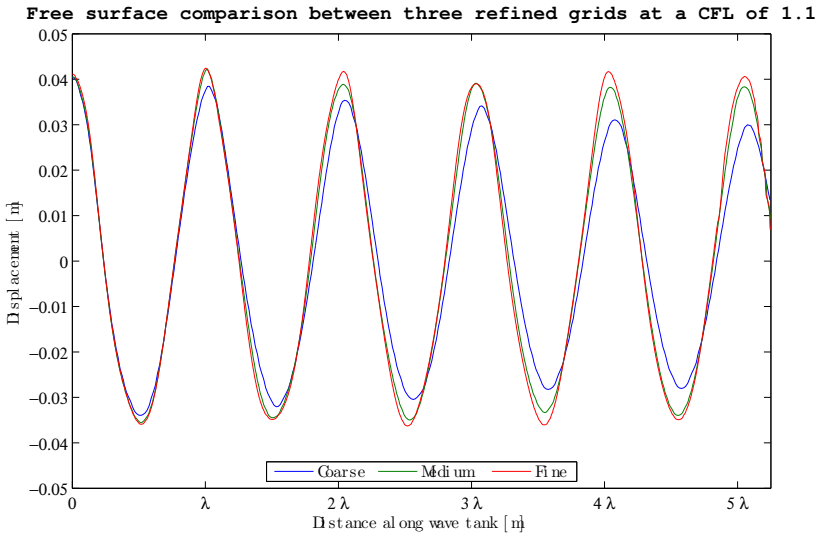

Figure 6.6: Time snap at 18s of the free surface showing wave height elevation on the three different meshes; Coarse, Medium, Fine using a CFL number of 1.1

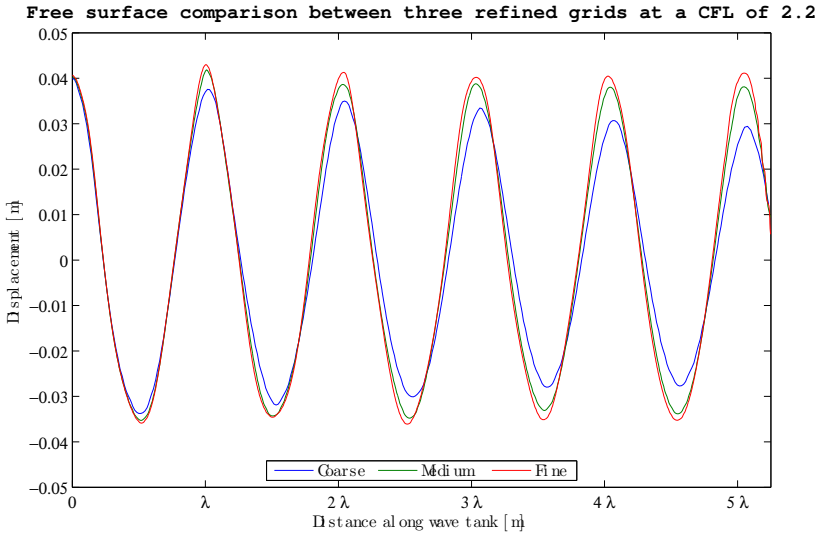

Figure 6.7: Time snap at 18s of the free surface showing wave height elevation on the three different meshes; Coarse, Medium, Fine using a CFL number of 2.2

Table 6.8: Computational times to solve for a NWT lasting 18s on three meshes, each using a CFL number of 1.1

Mesh	Total CPU time[1]	Wall clock time[2]
Coarse	3.492 x10^5 s	1.1 days
Medium	2.021 x10^6 s	5.9 days
Fine	1.684 x10^7 s	48.8 days

[1] Summed CPU time using four cores
[2] Total wall clock time

Table 6.9: Computational times to solve for a NWT lasting 18s on three meshes, each using a CFL number of 2.2

Mesh	Total CPU time[1]	Wall clock time[2]
Coarse	2.266 x10^5 s	0.7 days
Medium	1.651x10^6 s	4.7 days
Fine	1.233 x10^7 s	35.7 days

[1] Summed CPU time using four cores
[2] Total wall clock time

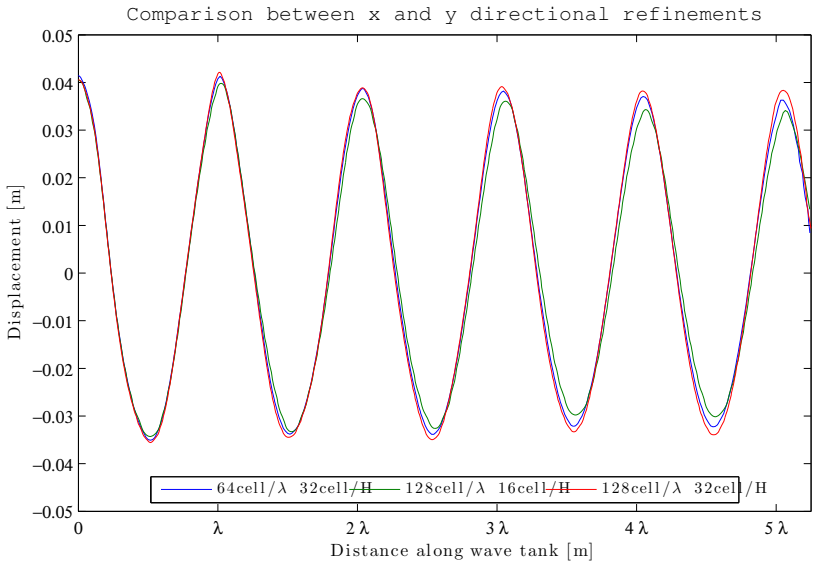

Figure 6.8: Plot showing free surface displacement on the medium mesh with a coarsening in the x-direction and also in the y-direction.

around the SWL, higher than the recommended ratio of 1:3. The preliminary study conducted an investigation in order to assess the sensitivity of the results to one dimensional grid refinement. The results showed that the free surface elevation was more far sensitive to Δx refinement than Δy refinement and nearly all of improvement in the results came from refinement in the x-direction (Figures A.2 and A.1).

Section 6.2.4 used the outcome of the preliminary study (Appendix A) and decreased the aspect ratio, around the SWL, by using 128nodes/λ in the x-direction and 32 nodes/H in the y-direction for the medium mesh. This present section investigates whether or not the same sensitivity to one dimensional refinement is observed for the grids described in Table 6.5.

All numerical options and boundary conditions remained the same as in Section 6.2.4. Only the mesh spacing in either the x-direction or the y-direction was altered at one time. The medium mesh, was coarsened in Δx to give a mesh with 64 nodes/λ in the x-direction and 32 nodes/H in the y-direction and coarsened in Δy to give 128 nodes/λ in the x-direction and 16 nodes/H in the y-direction. The extra meshes used in this one-dimensional are presenting in Table 6.10. The time step was selected in order to maintain a CFL number of 1.1 for each of the respective meshes.

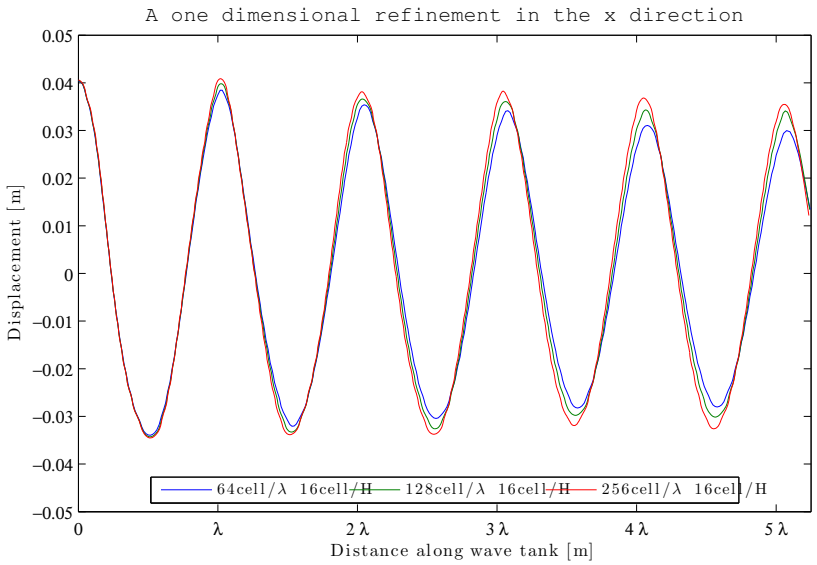

Figure 6.9: Free surface plots showing the effect of effect of one dimensional refinement in the x-direction. Here, a cell density in the y-direction was set to 16 cells per wave height, H.

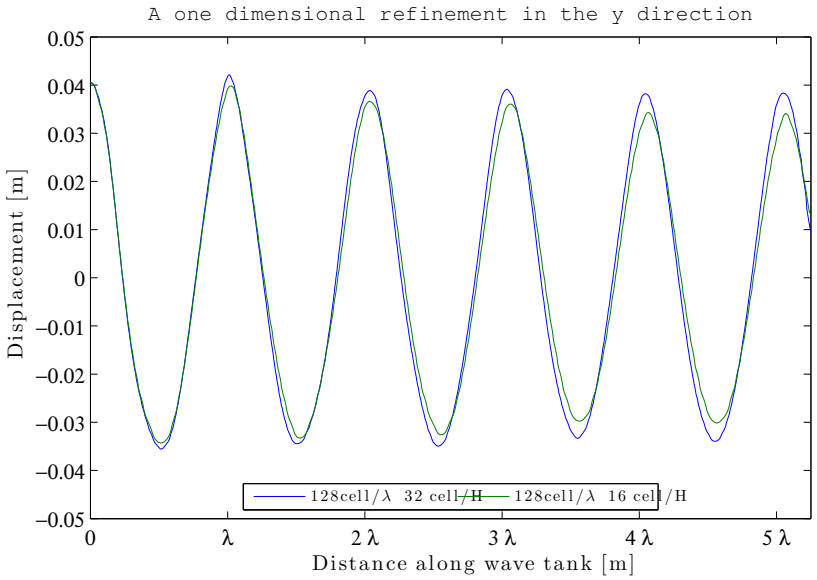

Figure 6.10: Free surface plots showing the effect of effect of one dimensional refinement in the y-direction. Here, a cell density in the x-direction was set to 128 cells per λ.

Table 6.10: Grid spacing node counts used in the one-dimensional refinement study

Nodes / λ	Nodes / H		
	16	32	64
64	37842[a]	74970	-
128	71760	142170[b]	-
256	140660	-	552178[c]

[a] Coarse Mesh
[b] Medium Mesh
[c] Fine Mesh

Table 6.11: Two tables: The left hand table shows the time for running an 18s transient problem with four cores, on the $5\lambda + 5\lambda$ domain. Six different mesh layouts are used, the diagonal being the meshes discussed in Section 6.2.4 the off diagonals being as a result from one dimensional refinement. The right hand table shows the relative change for the average wave height compared to the fine mesh. The average wave height over the four wave heights on the fine mesh = 0.7698m.

	Wall Clock Time			% difference		
	16	32	64	16	32	64
64	1.1 days	5.2 days	-	14.3%	5.8%	-
128	3.7 days	5.9 days	-	10.1%	3.7%	-
256	10.3 days	-	48.8 days	6.4%	-	0%

Table 6.11 compares the computational times each mesh[3], and the corresponding percentage difference compared to the fine mesh. Grid coarsening on the medium mesh in the y-direction reduces the run times from 5.9 days to 3.7 days, but, the results see a change in the error, compared to the fine mesh, from 3.7% to 10.1%. Comparatively, coarsening in the x direction only sees a reduction in computational time of 0.7 days and an increase in error to 5.8%.

Analysis of this table shows that the diagonals of these tables, i.e. the original meshes, seem to exhibit the best balance between run times and accuracy. This suggests that the chosen ratio of cells/λ : cells/H is appropriate.

Uniform mesh spacing

In order to allow for comparison with FLOW3D (Section 6.4) and to ensure that errors would be propagating equally in the x and y-directions, the wavemaker problem was investigated on a mesh with uniform grid spacing through out the domain, except in the numerical dissipation zone where the grid stretching was still imposed.

A mesh consisting of Δx and Δy spacings equal to 2cm, $2/\sqrt{2}$cm and 1cm were used. Qualitatively the results of this investigation can be seen in Figure 6.11. Clearly these results suffer from the wave height attenuation down the flume and some noise exists along the free surface. It was decided not to pursue this avenue of investigation any further.

It can be concluded from this that CFX requires more than 8 cells per wave height in order to adequately resolve the free surface. The computation cost of using more than 8 cells per wave height while preserving the uniform mesh spacing throughout would be excessive [4]. Attempts were made to use a more refined mesh, but solver stability proved to be an issue.

Due to large run times shown in this study, and the poor results observed using a homogeneous grid spacing throughout, the pragmatic approach to mesh design in CFX is to have a small area of refinement around the free surface and then impose a grid stretching away from this area, as presented earlier.

---

3. computational times were wall clock times using four cores and a CFL number of 1.1
4. For reference, the 1cm mesh, on four cores had a run time of 14.4 days

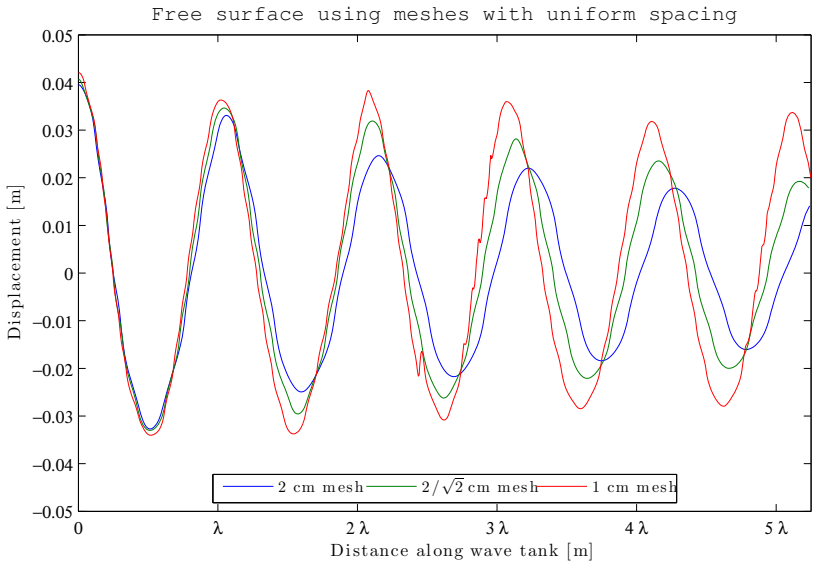

Figure 6.11: The free surface on three different meshes each with a uniform mesh spacing

Wave Height Decay

One persistent observation noticed in all meshes, regardless of time step, was that of wave height decay down the flume. The target wave height, based upon Eq. 3.111, was 8cm. Figures 6.6 and 6.7, and more quantitatively, Tables 6.6 and 6.7 show that the wave heights decrease as the wave train progresses down the wave flume. The wave height attenuation is more severe the coarser the mesh or larger the time step, however, it is present in all meshes and time steps to varying degrees.

Recognising that the use of linear theory and its application to second order waves (Figure 6.1) will result in smaller wave heights and acknowledging that wave heights in physical flumes also decay, the wave height attenuation noticed here is still excessive and while not as severe as reported by Bhinder *et al.* (2009a) (who reported CFX to be totally unusable), wave height decay is still persistent. This will be explored and discussed further during the validation procedure in the following section.

6.2.5 Validation against linear wave theory

As discussed in Section 5.3 a validation case can be conducted using either a physical test case or a well known analytical solution. For many applications in CFD, it is not possible to obtain an analytical solution to the problem being modelled. For this study however, there is scope to compare the CFD results to an analytical solution. Linear wave theory is a well established, studied and understood problem. The theory presented in Chapter 3 can accurately predict the motions of the fluid as long as the waves remain in the linear regime (figure 6.1) and will be used herein as a validation case.

For this section, a validation case will be conducted using linear wave theory and three different wavemaker profiles as discussed in Section 3.4.

The wave parameters chosen for the validation case were; wave height, $H = 0.01$m, wave period, $T = 1.25$s and a water depth, $h = 1.5$m. These wave parameters would generally not be used in a physical wave flume due to their small size at full scale, but they ensured that the validation waves were operating in the linear, deep-water regime and that linear wave theory could be used to validate the numerical results from CFX.

The mesh layout was very similar to that used in Section 6.2.4 and shown in Figure 6.2. There was an area of uniform grid refinement in the y-direction, extending 0.01m above and below the SWL. The grid spacing outside this region was then stretched in the vertical direction, leaving relatively large cells in areas of less importance, i.e. the air void and the bottom of the flume. The wave-flume for this case was again 10 wavelengths long, including a five-wavelength wave dissipation zone.

The predicted wave length for a wave of $T = 1.25$ and $H = 0.01$m operating in deep water conditions results in $\lambda = 2.4375$m, thus the total wave-flume length was 24.375m. Again, this mesh had a grid stretching zone at $x \geq 5\lambda$ resulting in a de facto flume length of 5λ.

The choice of mesh parameters was based upon the verification study presented in Section 6.2.4. It was decided that 200 nodes/λ and 40 nodes/H would yield the best balance between CPU time and result accuracy. Based upon the temporal discretisation study conducted in Section 6.2.3, a time step was chosen in order to achieve a two dimension al CFL number between one and two. A time step of $t = 0.005$s yields a CFL number of 1.75 and based upon the temporal discretisation

study, this is an appropriate CFL number.

The numerical set up and boundary conditions for the validation case were the exact same as for the verification process except for the wavemaker boundary. For the validation case, three different wavemaker profiles, as discussed in Section 3.4, were chosen: a piston, a bottom hinged flap and a hyperbolic cosine wavemaker.

Piston validation

This section presents the validation case for a piston wavemaker, comparing the results of CFX to linear wave theory. The boundary in CFX, representing the wavemaker, is moved horizontally in a sinusoidal motion with the amplitude displacement set according to Eq. 3.111 in order to achieve a wave height, H, of 1cm. As discussed, this combination of wave height, wave period and water depth ensures linear, deep water waves.

The free surface plot comparing the output from CFX to linear wave theory is shown in Figure 6.12. Close to the wavemaker, very good agreement is achieved. The agreement between both the predicted evanescent wave, given in Eq. 3.84 and the CFX output is excellent showing that CFX can very accurately and precisely predict the fluid structure interaction close to a moving body. At distances down the wave flume, the agreement diverges slightly. The CFX solution under predicts the wave height. The further down the flume the worse the wave height attenuation is.

Figure 6.13 shows the progression of the wave for a duration of 5 seconds at 1 second intervals. Close to the wavemaker, at $x = 0$, the contribution of the evanescent wave to the progressive wave can be seen as a standing wave attached to the front of the wavemaker. The exponential decay envelope of the evanescent wave with increasing values of x is also apparent.

Figure 6.14 shows the predicted group velocity and phase velocity superimposed on a time plot showing the progression of the free surface. Not withstanding the wave height attenuation, very good agreement is observed for both the group velocity and the phase velocity of the waves.

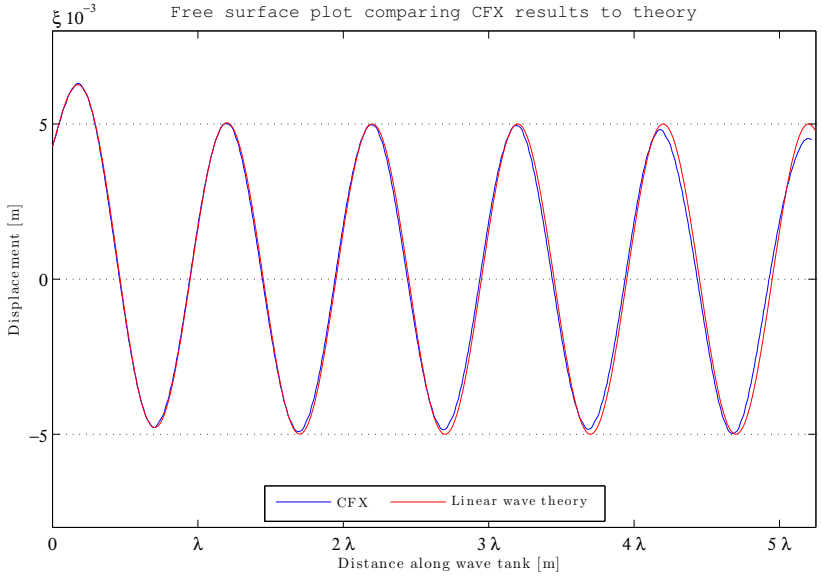

Figure 6.12: Free surface comparison between CFX and Linear wave theory, at 19s, for a piston wavemaker. Close to the wavemaker, the contribution of the evanescent mode is clear. CFX predicts this behaviour accurately. At a distance away from the wave maker, a decrease in wave height is observed and the agreement between CFX and theory diverges slightly.

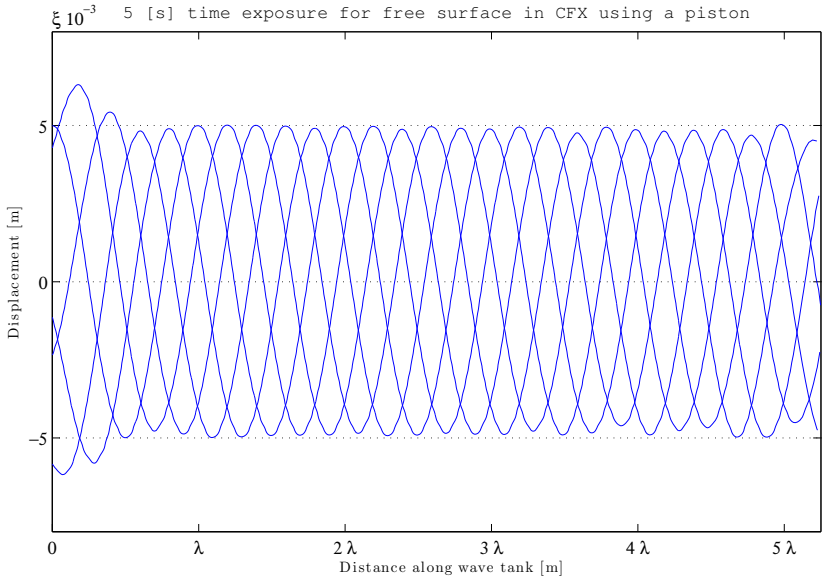

Figure 6.13: A free surface time-lapse over five seconds superimposed onto a single figure for a bottom hinged flap. The evanescent wave contribution near the wavemaker is visible at distances of $x \leq h$.

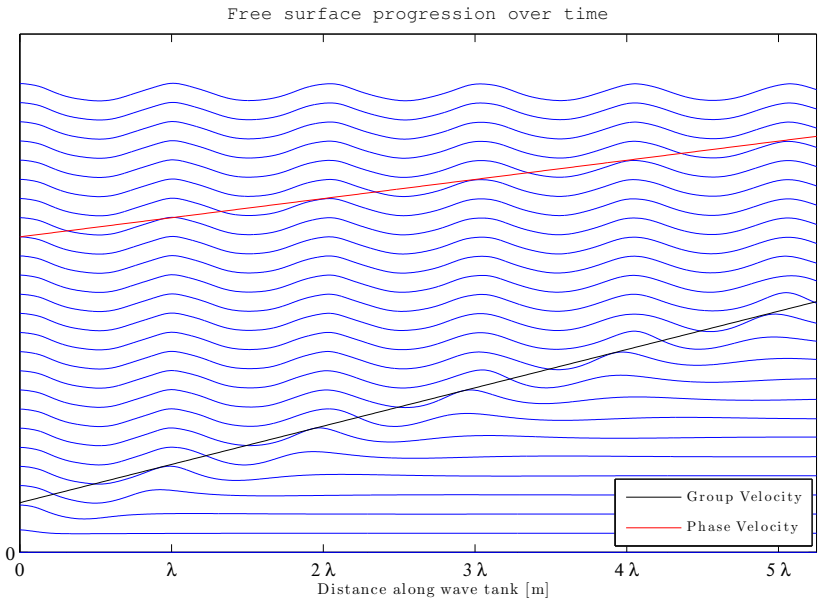

Figure 6.14: Waves generated in CFX by the wave maker at $x = 0$, at a sequence of time steps, t, in intervals of wave period, T. The slopes of the two lines represent the group velocity and the phase velocity.

Bottom hinged flap validation

A bottom hinged flap wavemaker was replicated by setting the displacement amplitude at the free surface according to Eq. 3.112 and imposing a vertical displacement function of $f(y) = 1 + y/h$. Figure 6.15 shows excellent agreement between CFX and linear wave theory close to the wavemaker. Again, the evanescent wave is accurately predicted in CFX. The evanescent wave for a flap is less than that for a piston as the velocity profile a flap wavemaker imposes on the water particles is closer to their natural Airy Orbital paths than that of a vertical piston. Wave height attenuation away from the wavemaker is present again. This is most apparent when looking at Figure 6.16, showing a time lapse of the free surface over 5s at 1s intervals superimposed on one single plot.

Hyperbolic cosine validation

The prospect of having a wavemaker without any added mass or any evanescent wave was discussed by Falnes (2002) and Naito (2006) and presented in detail in Section 3.3.1. Falnes suggested that the wavemaker would be flexible, while Naito proposed that the wavemaker could be composed of many segments in the vertical direction. Neither of these are practically realisable, but CFD allows

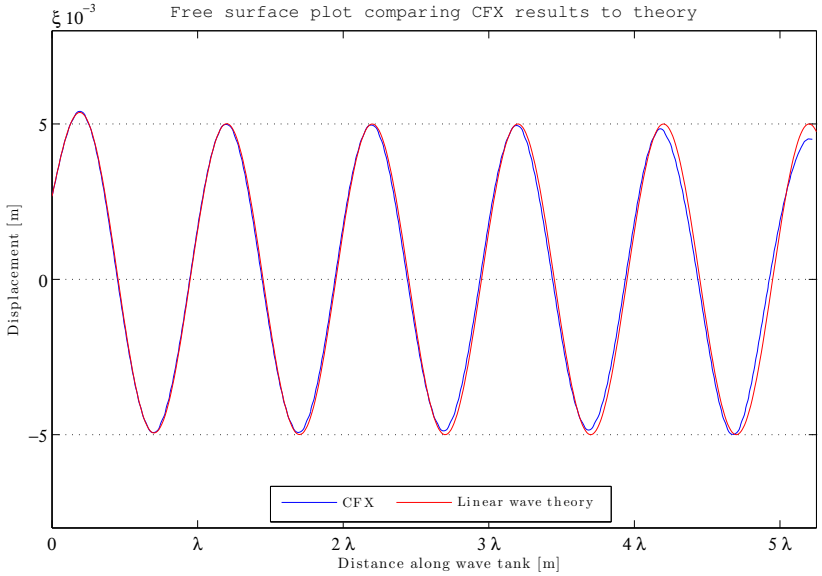

Figure 6.15: Free surface comparison between CFX and Linear wave theory, at 19s, for a bottom hinged flap wavemaker. Close to the wavemaker the contribution of the evanescent mode is clear. CFX predicts this behaviour accurately. At a distance away from the wave maker, a decrease in wave height is observed and the agreement between CFX and theory diverges slightly.

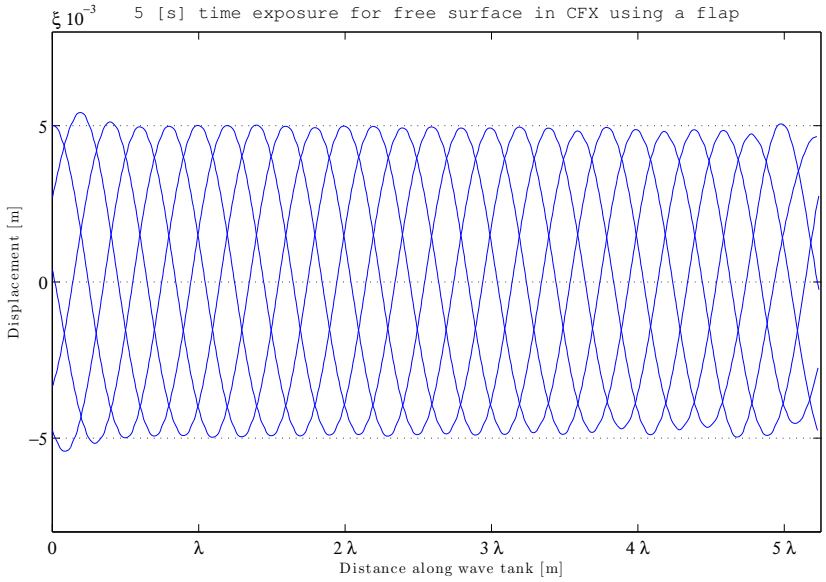

Figure 6.16: A free surface time-lapse over five seconds superimposed onto a single figure for a bottom hinged flap. The evanescent wave contribution near the wavemaker is visible at distances of $x \leq h$.

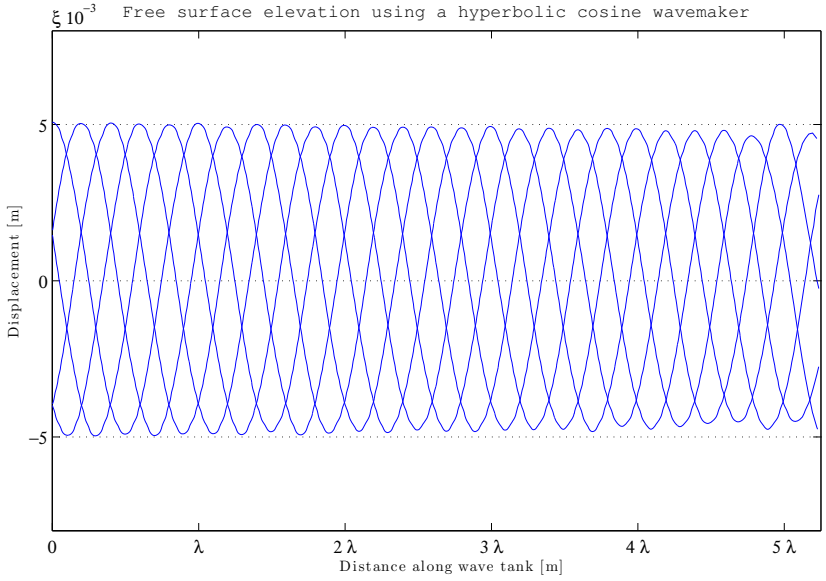

Figure 6.17: Free surface progression over five seconds superimposed onto a single figure. It can be seen that there is no contribution to the free surface from evanescent waves. Close to the wavemaker it can be seen that the wave height is at the target height of 1cm and an envelope of wave height decay down the length of the flume is apparent.

the wavemaker to take any shape or form without the inconvenience of of being limited to physical and technical constraints in order to build such a wavemaker.

The shape profile, $c(z)$ of this wavemaker for this study took the form of

$$c(z) = \frac{\cosh(k_s(z+h))}{\cosh(k_s h)}, \tag{6.4}$$

where k_s is a fixed coefficient wave number at a frequency of $\omega_s = 0.8s$ satisfying the real part of the dispersion relationship, Eq. (3.42). The amplitude of oscillation was chosen according to wave height to stroke amplitude ratio given in Eq. 3.113 and this was subjected to a sinusoidal oscillation at a frequency of 0.8s.

Figure 6.17 shows the free surface over a five second period at one second intervals for a hyperbolic cosine wavemaker. In contrast to both Figures 6.16 and 6.13, no evanescent waves are present near the wavemaker at $x = 0$. The target wave amplitude of 5mm is achieved at distances close to the wavemaker. Again, wave height attenuation is persistent for distances greater than three wavelengths away from the wavemaker.

Table 6.12: Wave metrics for the three validation cases; a piston, a bottom-hinged flap and a hyperbolic cosine.

	1	2	3	4
Piston				
Wave height	0.0099	0.0098	0.0097	0.0095
Wave length[a]	2.4085	2.4277	2.4199	2.4418
Wave length[b]	2.4299	2.4361	2.4320	2.4237
Flap				
Wave height	0.0099	0.0098	0.0098	0.0096
Wave length[a]	2.4284	2.4312	2.4227	2.4384
Wave length[b]	2.5016	2.4288	2.4360	2.4361
Hyperbolic cosine				
Wave height	0.0099	0.0098	0.0097	0.0095
Wave length[a]	2.4292	2.4334	2.4333	2.4292
Wave length[b]	2.4304	2.4264	2.4438	2.4247

[a] Based upon zero up-crossings
[b] Based upon zero down-crossings

6.3 Discussion on CFX results

Sections 6.2.3 and 6.4.4 explored the temporal and spatial discretisation errors associated with a progressive wave radiating away from an oscillating boundary using ANSYS CFX. Section 6.2.5 applied the established optimal time step and grid spacing to problem with an analytical solution. Both of these studies showed up some interesting results.

While conducting the temporal discretisation study in Section 6.2.3 it was found that the best results[5] were obtained when a CFL number between 1.1 - 2.2 is used. Using a time step that corresponds to a CFL number of below 1, (i.e. CFL = 0.55) resulted in increased run time and a deterioration in results. There was little discernible difference, less than 0.71%, in the results between using a CFL number of 1.1 and 2.2. Here the choice could be made between required accuracy and computational time.

The spatial discretisation study highlighted the need for a very fine mesh at the

5. This refers to the best temporal convergence while also taking into consideration the computational expense.

free surface in both vertical and horizontal directions in order for CFX to achieve grid convergence. The formal grid convergence study found that the fine mesh reported convergence indices of the order of $1-4\%$. There could be an argument made that extra refinement should be pursued if smaller errors are needed, but as the run times for the fine mesh with a CFL number of 1.1 were taking nearly 50 days, it was felt that following up with another successively finer grid would be problematic.

The verification procedure for ANSYS CFX was computationally expensive. License availability was limited to eight cores and all of the jobs were broken up into 4 core jobs. Even with eight licences and only one primary user, the verification process was time consuming but necessary. It is disconcerting however, that these excessive run times were for a two dimensional simulation of 18s transient. Without a considerable increase in computing power, modelling a three dimensional wave tank able to test long time durations would be prohibitively time consuming.

The validation case in Section 6.2.5 compared the CFX results to a known analytical solution. Good agreement between the free surface displacement in CFX and linear wavemaker theory was observed, particularly at distances close to the wavemaker. The presence of the evanescent wave was modelled and predicted accurately. There has been discussion in literature on the possibility of constructing a wavemaker that has zero added mass and no evanescent wave, but this was never implemented. CFX has proved that a hyperbolic cosine wavemaker does not have any evanescent waves at a chosen frequency. This is something that practically was impossible to show in a laboratory but CFX confirmed this through CFD.

CFX is capable of accurately predicting the fluid motion close to the moving structure, but throughout the verification and validation process, persistent wave height attenuation was noted as the wave progressed down the flume. Regardless of CFL number or grid resolution, wave height decay was observed. As well as decreasing wave heights, changes in the wavelength of the waves from point to point was also observed. The change in wave length could either be due to energy in the wave transferring from the wave height over to wave length, thus maintaining the same energy levels, or the decreasing wave lengths could be due to over all energy reduction in the domain.

Subsequent discussions with ANSYS, regarding the wave height attenuation problem, have confirmed that in order to maintain a stable interface in the VOF

scheme, ANYSYS introduced a damping term in to the solver to mitigate against high frequency waves that were observed on the free surface. The progressive wave being modelled here is not high frequency, but this damping term could be responsible for the decay in both wave height and length due to energy extraction.

6.4 FLOW3D

This section presents the verification of results from another commercial CFD solver, FLOW3D v9.4. It will attempt to model the same physical problem as CFX, described in Section 6.1, and will follow the same procedure outlined in Section 6.2, using the same spatial discretisation in order to allow for a comparison between results. It should be noted that direct comparisons between different solvers can be hazardous. Each solver was designed with specific applications in mind, and while most claim to be versatile general purpose solvers, each will have its own niche applications. The choice of what solver to use is very much dependant on the end users application and what physics need to be modelled.

FLOW3D is a more specialist code compared to CFX, which is acknowledged as being a more general purpose solver. FLOW3D was developed with free surface applications in mind and it implements a proprietary method of interface tracking and free surface advection referred to as TruVOF®. This method claims that it alleviates the problems associated with the standard VOF advection methods such as over-filling or over-emptying computation cells when volume fluxes are significant in all directions and the time step is close to the local Courant stability limit (Barkhudarov, 2004). TruVOF is a mixed Lagrangian-Eulerian approach and is described in Figure 6.18. Another benefit reported with this method is that it does not need as many cells near the free surface and, therefore, the computational time can be reduced compared to other CFD codes, such as CFX.

FLOW3D is based on the Reynolds Averaged Navier Stokes (RANS) equations. It has both implicit and explicit solver modelling options with first, second and third order advection schemes. FLOW3D incorporates solid body motion via a technique named FAVOR. FAVOR is based upon the concept of area fraction and volume fraction on a rectangular structured mesh (Hirt and Nichols, 1981). It introduces the effects of area fraction and volume fraction into the conservation equations of fluid flow. This method is responsible for the General Moving Object (GMO) in the modelling options which allows six degree of freedom rigid body motion and this is used to implement the wavemaker motion in this study.

FLOW3D has the capability to model only one fluid, water, unlike CFX that models both water and air. The fact that the air is not modelled means that the computational time will be reduced further.

All of the FLOW3D problems, unless otherwise specified, were run on machines

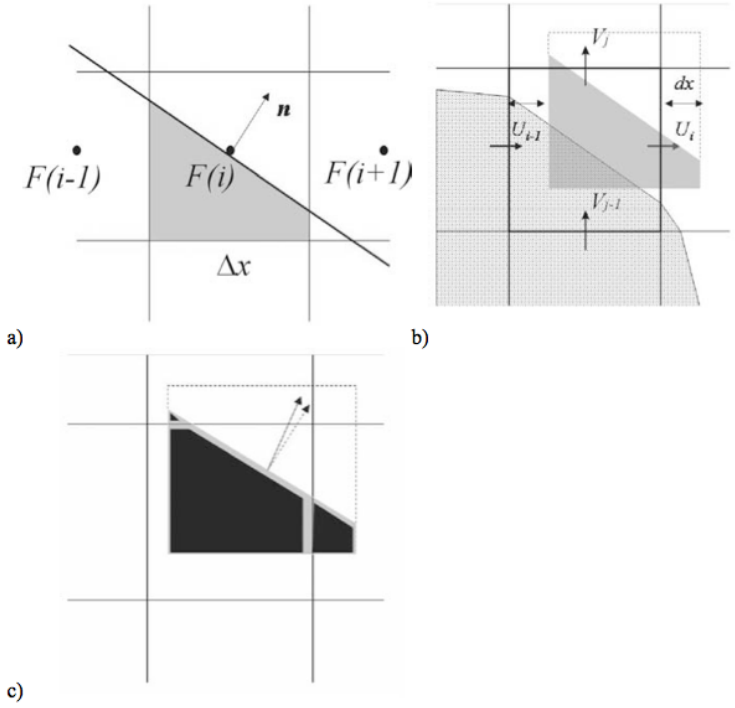

Figure 6.18: Three steps of the Lagrangian interface tracking method: a) piecewise linear interface reconstruction with the normal n b) moving the control volume and c) overlaying the advected volume onto the grid (Barkhudarov, 2004).

with Intel® core™2 Quad CPU at 2.50GHz processors and 8GB of RAM.

6.4.1 Generation of meshes

FLOW3D adopts an integrated mesh generation approach, so all meshes were generated within the FLOW3D user interface. Overall, the mesh length was 14 wavelengths long (21.84m). The increased domain size could be justified due to the relative computational savings in time compared to CFX.

In the vertical direction, the domain is 1m high. As the air flow-field is not solved for in FLOW3D, there is no need to have as high a clearance between the water and the top boundary condition. The grid is extruded one cell thick into the domain, similar to CFX, resulting in the a quasi 2D problem.

Similar to the mesh discussed in Section 6.2.1 for CFX, the FLOW3D mesh also consists of two distinct regions: a region of seven wavelengths immediately in front of the wavemaker and a second region of equal length down-wave to act as a numerical dissipation zone. It should be noted that the numerical dissipation zone

is not entirely necessary for FLOW3D as there is an outflow boundary condition available for selection which can deal effectively with the out going wave, but keeping this region allows for a closer comparison to the CFX meshes and it is considered a conservative approach.

Two different mesh types will be explored with FLOW3D. The first mesh will have an area of cell refinement around the free surface again similar to that used in Section 6.2.4, and it will also explore the effect of using a mesh with uniform mesh spacing, to be discussed in Section 6.4.4.

6.4.2 Boundary conditions

The boundary conditions imposed in the problem were, symmetrical boundary on both the near and far vertical faces of the flume. No-slip wall condition for the floor of the flume and opening for top. The vertical boundary at $x = 21.84$m was set as outflow boundary condition with the option to allow flow enter the domain enabled. Due to the orbital nature of the water particles under wave motion, water at the boundary will need to exit and enter, if the fluid is only permitted to leave the domain, a decrease in the volume of the water is observed.

Numerical options

The wavemaker for FLOW3D was not implemented using a moving boundary condition as in CFX. The GMO option was enabled in the numerical options, allowing the presence of a solid six DOF body to represent the wavemaker. A piston wavemaker was modelled using a rectangular body covering the yz plane at $x = 0$. This was subjected to a sinusoidal displacement with the amplitude set according to Eq. 6.2.

The flow field is initialised using the hydrostatic pressure of the fluid and all velocity components are set to zero. The total time for the transient runs was chosen as 20s. This is 2s longer than the CFX simulations, to allow for the wave flume being an extra 2λ longer, but the simulation times for FLOW3D compared to CFX were found to be drastically shorter and it was decided that the extra transient time could allow for further analysis.

There are six numerical options available for the volume-of-fluid advection, however, only three of these options are of interest to this problem. The first one applicable to this problem is the ‘one fluid, free surface’ option, also referred to

as *ifvof*=4. This is the original VOF advection scheme and 'moves' the fluid in three discrete Eularian steps, x then y then z. The other two methods are the 'unsplit Lagrangian' (*ifvof*=5) and 'split Lagrangian' methods (*ifvof*=6). In the unsplit Lagrangian method the fluid is advected in one single step in x, y and z, whereas in the split version, the fluid is moved in two steps, xy and then in z.

It was found that there was very little difference between the two Lagrangian methods, *ifvof*=5 and *ifvof*=6. Both of these options gave better results when compared to the *ifvof*=4 scheme. The reason that *ifvof*=5 and *ifvof*=6 gave very similar results could be due to the 2D nature of this problem. If modelling a 3D case, the unsplit Lagrangian method, *ifvof*=5, would probably be more suited. This is because water particle motion in gravity waves is characteristically orbital. The extra steps involved in the *ifvof*=4 and *ifvof*=6 might disturb the the conservation of momentum as the free surfaces travel through the mesh diagonally. This is not something that could be investigated further as FLOW3D is a commercial code, and as such a 'black box' tool. For the following problems the split Lagrangian, *ifvof*=6, option was selected for the VOF advection. When modelling a 3D problem differences between *ifvof*=5 and *ifvof*=6 should be investigated and the best chosen accordingly.

There are three momentum advection options available. The most suitable option for this problem wave first order. During preliminary studies, it was found that the higher order schemes, second order, second order monotonically preserving and third order, suffered from instabilities on the free surface and a smooth wave form was not observed. First order momentum advection gave best results.

6.4.3 Temporal discretisation

FLOW3D has inbuilt stability control that adjusts the time step automatically to ensure that the solver remains within the stability limits. There is an option for the user to specify the time step size, but better and more stable results were found leaving the solver set the time step size at each iteration. At times, the solver did report an error message of 'Time step size < dtmin'. This implied that the solver quit because the time step size fell below the minimum time step. The problem occurred for the initial time steps, probably due to the initialised solution not matching up exactly with the physical problem. The solution to avoid this was to increase the maximum amount of iterations in the solver options in order to achieve convergence for the initial time steps.

Table 6.13: Grid spacing and node count for the three initial meshes used in FLOW3D

	Coarse	Medium	Fine
Cells / λ	64	128	256
Cells / H	16	32	64
Cell Count	200,000	400,000	1,600,000

6.4.4 Spatial discretisation

The three meshes chosen for the spatial discretisation study were based upon the meshes used for CFX, presented in Section 6.2.4. Unlike the meshes used in CFX, the spacing in the y-direction was uniform above and below the SWL. The FLOW3D solver crashed when grid spacing was stretched in the vertical direction and, in order to overcome this, the node spacing in the y-direction was kept uniform above and below the SWL. The computational time for FLOW3D was found to be substantially quicker compared to CFX so this extra CPU time was not a cause for concern. As a result, a doubling of the cells in both directions resulted in the cell count increasing by a factor of four. The metrics for the three meshes are shown in Table 6.13.

Similar to Section 6.2.4, a formal grid convergence index study was conducted. The meshes described in Table 6.13, with a refinement ratio of $r = 2$, were used to perform the grid convergence index. These results are presented in Table 6.14. Here the metrics were not as well behaved as for CFX but, as they were point measurements, there is always the possibility for more variance. Further work could be carried out in order to analyse this, possibly using an integral measurement such as force on the wavemaker as the index metric but, it is thought unnecessary for this study as a relatively good idea of the spatial discretisation error can be obtained from wave height measurements.

Figure 6.20 shows the time step size used by the FLOW3D solver. On average the time step size is ≈ 0.004s. Using Eq. 6.3, this corresponds to a CFL number of 1.76. The time step size for the coarse and fine meshes averaged out at ≈ 0.008s and ≈ 0.002s respectively - both corresponding to a CFL number of 1.76 also. This compares closely to the time step size used for the CFX analysis. The outcome of which suggests the use of a CFL number in between 1.1 to 2.2 is appropriate for VOF solvers.

Table 6.14: Grid convergence indices for six wave heights using FLOW3D. Subscript index of 3 represents the coarsest relative mesh and 1 the finest.

	1	2	3	4	5	6
f_3 [m]	0.071	0.068	0.064	0.060	0.056	0.055
f_2 [m]	0.073	0.072	0.069	0.068	0.066	0.064
f_1 [m]	0.076	0.073	0.073	0.071	0.072	0.070
ε_{32} [m]	-0.002	-0.004	-0.005	-0.008	-0.010	-0.009
ε_{21} [m]	-0.003	-0.001	-0.004	-0.003	-0.006	-0.005
p	0.859	2.575	0.501	1.326	0.738	0.381
f_{ext}^{21}	0.079	0.073	0.081	0.074	0.081	0.640
e_a^{21}	4.02%	0.97%	4.84%	4.40%	8.53%	7.95%
e_{ext}^{21}	4.71%	0.19%	10.45%	2.84%	11.33%	12.47%
GCI_{fine}^{21}	6.17%	0.24%	14.58%	3.65%	15.97%	17.80%

Table 6.15: Six wave length comparisons between meshes in FLOW3D using meshes described in Table 6.13.

	1	2	3	4	5	6
Coarse	1.640	1.653	1.631	1.589	1.567	1.583
Medium	1.605	1.624	1.603	1.593	1.575	1.564
Fine	1.597	1.591	1.597	1.572	1.566	1.571

[a] Based upon zero down-crossings

The computational times to obtain these results are given in Table 6.16. These computational times are nearly a factor of 20 shorter than a similar simulation using CFX. It should be noted that this comparison does not take into account that the FLOW3D results are for 2s extra in transient duration, 4λ longer in domain length and uniform cell spacing in the y-direction resulting in high cell counts in the domain.

Table 6.16: Computational time to run 20s on FLOW3D using three different meshes: coarse, medium and fine

Mesh	Total CPU time[1]	Wall clock time[2]
Coarse	1.843 x10^3 s	0.02 days
Medium	5.911x10^4 s	0.17 days
Fine	5.186 x10^5 s	1.77 days

[1] Summed CPU time using four cores
[2] Total wall clock time

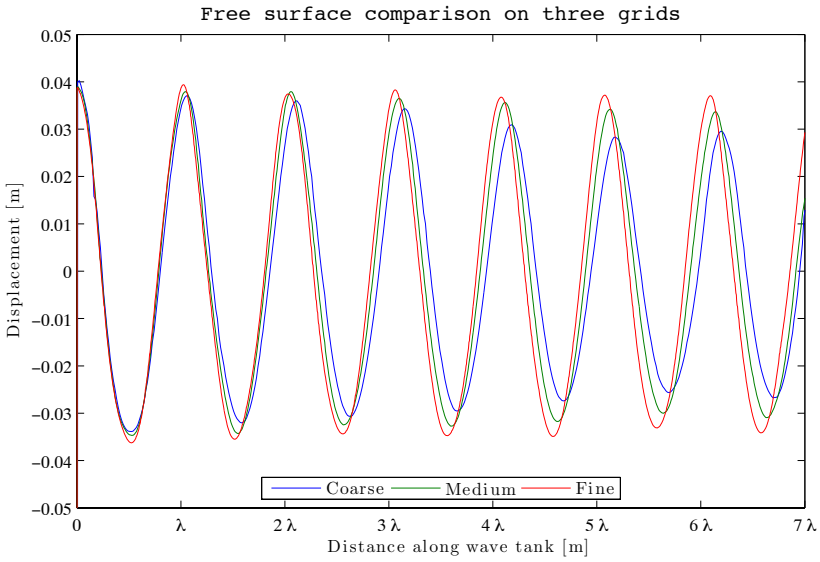

Figure 6.19: Time snap at 18s of the free surface showing wave height elevation on the three different meshes: coarse, medium, fine for FLOW3D

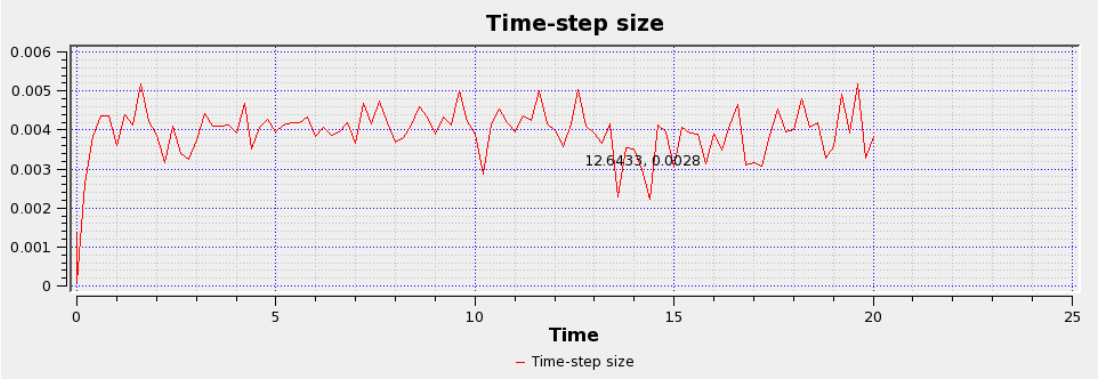

Figure 6.20: The time step size the FLOW3D solver used on the medium mesh. The corresponding time steps for the coarse and fine meshes were roughly double and half respectively

One dimensional refinement

Similar to Section 6.2.4 a one dimensional refinement study was conducted on FLOW3D in order to assess the sensitivity of results to mesh refinement in one dimension. All numerical options and boundary conditions remained the same as in Section 6.4.4, only the (medium) mesh was coarsened in either the x or y-direction at one time. The mesh spacings used are the same as those presented in Table 6.10 for CFX.

Results from the one dimensional refinement study show that FLOW3D is quite sensitive to changes from the original mesh spacing. This would suggest that the initial aspect ratio choice, cells/λ : cells/H, was poor. Table 6.17 presents the results of this study quantitatively. This table presents the computation times on each mesh and then compares the obtained answer to the fine mesh, reporting on the relative error to the fine mesh results.

The medium mesh was coarsened independently in the x-direction and then in the y-direction and the results of both are shown in Figure 6.22. It can be seen that coarsening in the x-direction has a deleterious effect on the results, changing the % error from 5.3% to 36.0%. Conversely and almost counter-intuitively a coarsening in the y-direction resulted in an overall improvement in the results, where the average wave height difference decreased from 5.3% to 2.1% and taking almost one quarter the amount of CPU time, Table 6.17.

The fact that the results improved with a coarsening does not suggest that better results would be achieved upon extra coarsening, but points more to sensitivity in cell aspect ratios around the free surface. This will be explored further in the Section below.

Uniform grid spacing

As a consequence of the results obtained in Section 6.4.4, where it was found that coarsening the grid in the vertical direction gave better results in a quicker time, it was decided to investigate the results of wave propagation on a grid with uniform spacing.

After discussions with FLOW3D user support, a study was conducted investigating the effects of having a mesh with equal spacing in the x and y-directions. It was thought that having a mesh of equal aspect ratio would enable better conservation of momentum using the TruVOF scheme (FLOW3D, 2010).

Table 6.17: Two tables: The left hand table shows the time for running a 20s transient problem with four cores, on the $7\lambda + 7\lambda$ domain in FLOW3D. Six different mesh layouts are used, the diagonal being the meshes discussed in Section 6.2.4. The off diagonals were as a result from one dimensional refinement. The right hand table shows the relative change for the average wave height compared to the fine mesh. The average wave height for the six waves gave a value of 0.0725m.

	Wall Clock Time			% difference		
	16	32	64	16	32	64
64	0.02 days	0.09 days	-	13.7%	36.0%	-
128	0.04 days	0.17 days	-	2.1%	5.3%	-
256	-	-	1.77 days	-	-	0%

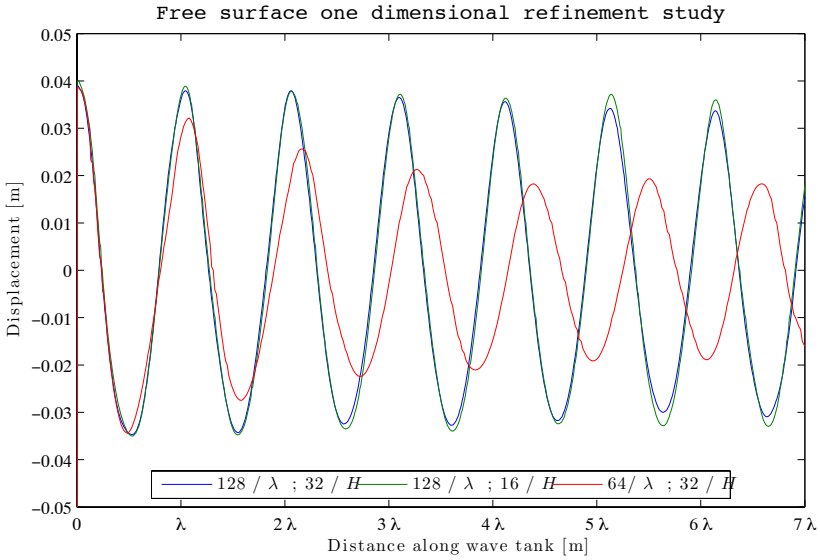

Figure 6.21: Free surface plot examining the effect of one dimensional grid refinement on the wave height elevation.

Table 6.18: Grid refinement mesh spacing for uniform mesh in FLOW3D

	Coarse	Medium	Fine	V. Fine
ΔX,ΔY [m]	0.020	0.010	0.005	0.0025
Cell count	59750	239000	956000	3824000

This study investigates the effect a uniformly spaced mesh has on the propagation of radiated waves. Herein, four different meshes are used, each with square mesh spacing shown in Table 6.18.

Figure 6.22 shows the free surface for the four meshes after twenty seconds. The grid convergence indices based upon the wave height measurements are shown in Table 6.19. The results obtained using wave height as a metric are indicative of other metrics measured but not presented: wave length, zero-crossings, peaks, troughs.

Significant improvements in run times are observed, especially when comparing the run-times of this uniform mesh study to the previous meshing arrangement in Section 6.4.4. The wave heights measured using a uniform mesh with a spacing of 0.02m show comparable wave height measurements from the fine mesh in Section 6.4.4, but the run times are 493 minutes compared to 2549 minutes runtime. The mesh with uniform spacing (0.01m) also yields similar results for the wave heights compared to the fine mesh at almost a tenth of the CPU time.

As mentioned previously, the default automatic time-step selection option was used for all FLOW3D results. The FLOW3D solver imposes several restrictions on the size of the time-step in order to avoid numerical instabilities. The solver will use the largest time step possible without violating these stability limits. The limiting stability code reported by the solver using a uniform mesh was 'fs', relating to gravity waves on the free surface. For the previous mesh in Section 6.4.4 the limiting factor was 'cy', relating to explicit fluid convection in the y-direction. Some brief exploration with different mesh ratios showed that the best results were obtained when the limiting stability factor was set by 'fs' and this predominantly occurred using a mesh with an equal aspect ratio.

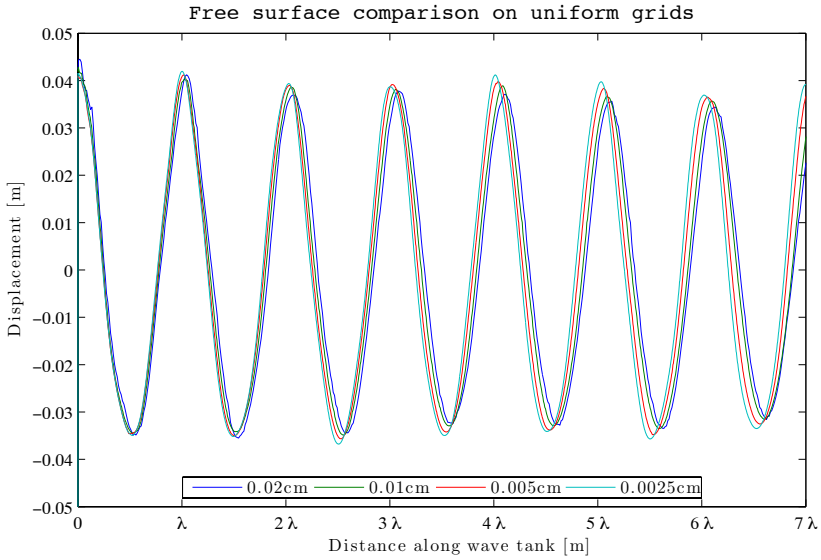

Figure 6.22: Time snap at 20s of the free surface showing wave height elevation on the four different uniform meshes.

Table 6.19: Grid convergence indices for six wave heights using FLOW3D and uniform mesh spacing. For this GCI, the three finest meshes from Table 6.18 are used. Subscript index of 3 represents the coarsest relative mesh and 1 the finest.

	1	2	3	4	5	6
f_3 [m]	0.075	0.073	0.073	0.072	0.070	0.069
f_2 [m]	0.076	0.074	0.075	0.074	0.072	0.071
f_1 [m]	0.077	0.075	0.076	0.076	0.074	0.073
ε_{32} [m]	-0.001	-0.001	-0.002	-0.002	-0.003	-0.002
ε_{21} [m]	-0.001	-0.001	-0.001	-0.002	-0.002	-0.001
p	0.421	1.347	1.411	0.584	0.598	0.653
f_{ext}^{21}	0.080	0.075	0.076	0.079	0.077	0.075
e_a^{21}	1.49%	0.70%	0.88%	2.15%	2.34%	1.83%
e_{ext}^{21}	4.21%	0.45%	0.53%	4.13%	4.36%	3.10%
GCI_{fine}^{21}	5.50%	0.57%	0.67%	5.39%	5.70%	4.00%

Table 6.20: Total CPU time to run 20s transient on FLOW3D using four meshes each with uniform mesh spacing

Mesh	Total CPU time[1]	Wall clock time[2]
0.02m	1.129x10^3 s	0.00 days[a]
0.01m	1.004 x10^4 s	0.03 days
0.005m	1.066 x10^5 s	0.34 days
0.005m	2.577 x10^5 s	3.00 days

[1] Summed CPU time using four cores
[2] Total wall clock time
[a] 4.9 mins

Table 6.21: Wave metrics from the uniform 0.0025cm mesh.

	1	2	3	4	5	6
Wave length[a]	1.580	1.574	1.550	1.567	1.580	1.558
Wave length[b]	1.570	1.553	1.571	1.577	1.555	1.558
Wave height	0.077	0.075	0.076	0.076	0.074	0.073
Wave peak	0.042	0.039	0.039	0.041	0.040	0.037
Wave trough	-0.035	-0.035	-0.037	-0.035	-0.034	-0.036

[a] Based upon zero up-crossings
[b] Based upon zero down-crossings

6.5 Discussion on FLOW3D results

Section 6.4.4 performed a spatial discretisation study on FLOW3D using the mesh configuration that gave the best results in CFX. These results showed poorly-behaved convergence index metrics when compared to results obtained from CFX using the same mesh. The wave height attenuation was also more pronounced in FLOW3D using this mesh compared to CFX. The computational time for FLOW3D was, however, considerably less compared to CFX.

An investigation into a one-dimensional refinement showed that improvements in both computational time and quality of results could be achieved if cells with equal aspect ratios in the x and y-directions were used. Results with grid discretisation errors of $\approx 2-5\%$ could be obtained with computational times in the order of hours rather than weeks.

Upon further investigation it was found that FLOW3D performs best with a mesh of uniform grid spacing throughout. This resulted in the solver stability limit being governed by the free surface term, 'fs'.

In order to conduct a validation study on FLOW3D for a linear wave of $h = 0.01$m and a period or $T = 1.25$s, using the best mesh from the verification procedure, i.e. a mesh with uniform spacing throughout the domain; with roughly 312 cells/λ and 16 cells/H, would require nearly 7.6×10^7 cells. However, with only one license and time resource restraints this was not practical.

The difference in computational times to solve the problems is the most striking difference between FLOW3D and ANSYS CFX. FLOW3D obtained similar results to CFX, but with CPU times an order of magnitude smaller. This would prove advantageous if longer transient run times were required or a three dimensional problem was to be analysed.

FLOW3D seemed to suffer from the problem of wave height attenuation down as the progressive wave travelled down the flume from the oscillating wavemaker. The extent of the attenuation was similar to that noticed in CFX, but the run times were an order of magnitude shorter. Presumably, if the mesh was refined to such an extent that the solver time was comparable to that of CFX (i.e. 48 days), then the wave height decay would be less pronounced than CFX. However, this is just speculative.

6.6 General discussion and conclusions on CFD results

Computational fluid dynamic software has proven to be an invaluable tool in many areas of engineering. It is hoped that CFD codes could offer engineers working in coastal and ocean engineering the possibility of having a numerical wave tank that solved for the viscous terms in the Navier-Stokes equations, thus, allowing for a closer analogue to the real world with less assumptions used in potential flow codes. Indeed, this project was initiated with the same lofty aspirations and aimed to have a numerical wave tank using CFD codes that incorporated absorbing wavemakers similar to those used in the University of Edinburgh.

In order to gain confidence in the capabilities and results provided by the commercial CFD codes a bottom up approach was adopted, where the most simple component of a three dimensional wave tank with absorbing wave makers would be analysed first. Upon satisfactory implementation of the simple problem the next layer of complexity could be added, the problem modelled and again validated. These layers of complexity would be added in a piecewise manner upon successful completion of the validation toll gate. Regrettably the CFD results obtained were not of a quality of precision that would allow progress to a more complex application with appropriate levels of confidence. Not withstanding this, a lot of information was discovered about the limitations and appropriate applications of CFD to the maritime environment.

This Chapter has closely analysed the quality and fidelity of the waves radiated from an oscillating solid boundary. It has performed extensive verification of the results from ANSYS CFX and FLOW3D and conducted a validation of the CFX solution against a well known analytical solution. Undoubtedly CFD is useful for a whole host of problems encountered in the marine environment. This study however, raised some serious concerns that would question the suitability of using commercial CFD codes specifically as numerical wave tanks.

The attenuation of the wave heights as the wave train progresses down the wave flume is one such issue of concern. This wave height decay was observed in both FLOW3D and CFX. It is something that does happen to a certain degree in physical flumes and tanks, albeit to a far lesser extent (Ursell *et al.*, 1960). In physical wave tanks this is circumvented by calibration of the wavemakers in the wave flume. The gain in the wavemaker's controller is adjusted in such a manner

that the desired wave heights are obtained in a certain area of the tank. This could also easily be done for the numerical wave tank too by increasing the stroke amplitude of the wavemaker to counter the wave height decay.

This approach would be fine to measure wave forces on singular objects in a wave flume. In the wave energy sector however, devices are hoped to be deployed in arrays and array interaction effects should be modelled and accounted for in order to assess their importance. If two or more devices are radiating waves, their respective waves will have lost some of their wave height by the time it has travelled to the corresponding oscillating device thus making the analysis difficult, and the results questionable. This becomes more pertinent for wave energy devices, as "in order to absorb a wave, one has to generate a wave". If the numerical code has difficulty generating waves of high fidelity, any results obtained in relation to the absorption characteristics of the device would be suspect.

Another weakness observed while using CFD to model a numerical wave tank is the excessive computational run times. Physical wave tanks can conduct experiments lasting 15 minutes or more and perform multiple variations of the experiments over the course of a day. This allows for a full tank test run of survivability testing and power take off validation to take place over the course of one or two weeks[6]. The fine mesh in CFX took nearly two months to model a transient time of 18s. With the current computational hardware the solver times, it most certainly precludes CFX from being able to run transient times of 900s and questions whether or not CFX could be used to create an analogue to physical wavemakers used in hydrodynamic laboratories. FLOW3D was considerably less computationally expensive compared to CFX and could allow give reasonable result for 2D cases. However, the computational times would spiral quickly if the chosen model was 3D or the transient time increased.

One possible solution to avoid such long run times on the fine mesh would be to use a coarse and medium mesh and perform a Richardson's extrapolation (RE) and assume a second order convergence. Table 6.22 shows the wave heights obtained using the three meshes: coarse, medium and fine. It also conducts a Richardson extrapolation on the wave heights using two combinations: coarse and medium (RE c-m), and again with a medium and fine meshes (RE m-f). It is clearly seen that the errors reported on the fine mesh and the RE c-m calculation

6. Of course this does not account for model construction time which can be considerable depending on the scale of the tests and the quality of the PTO model.

Table 6.22: Wave metrics from the three meshes showing observed wave heights and lengths. And a comparison to the Richardson Extrapolated (RE) values using the coarse-medium meshes and the medium-fine meshes, assuming $p = 2$.

Grid	Wave height [m]	Wave length [m]	%H	%λ
Coarse	0.064	1.613	17.4%	1.6%
Medium	0.074	1.596	4.4%	0.5%
Fine	0.076	1.590	0.9%	0.1%
RE c-m	0.076	1.588	1.1%	0.0%
RE m-f	0.077	1.588	0.0%	0.0%

are similar. The time scales involved however are not. The computational time required to run the coarse mesh compared to the medium mesh is roughly $1/8^{th}$, a factor of four for the spatial discretisation and a factor of two to account for the smaller time step. This approximation is confirmed as a good estimate for the run times by both CFX and FLOW3D. The same time difference is observed when going from the medium mesh to the fine mesh. Thus, the time difference between running two meshes: coarse and medium, is 9/64th the time to run a single fine mesh. This would become even more pronounced if the simulation was three dimensional. Here the computational cost to run a coarse and a medium mesh would be 17/256th the cost of running a fine mesh. This would be of particular use if a parametric study into some aspect of the design was to be conducted as the coarse and medium mesh would allow for far more results at a given computational expense.

ANSYS CFX proved to be very accurate at predicting the fluid velocities and water particle displacements next to the oscillating wavemaker. The validation case in Section 6.2.5 showed that CFX precisely predicts the free surface elevation due to the radiated progressive wave and the standing evanescent wave. This is a very useful result and gives confidence that CFD can predict the fluid forces acting on an oscillating object radiating waves correctly. This suggests that CFD could be a useful tool to be used in conjunction with potential flow codes.

Potential flow codes are appropriate when the waves are of small amplitude, the body motions are small and of course it neglects any viscous energy losses. The small amplitude assumptions break down in the more energetic sea-states and the viscous losses do become important, especially when a wave energy converter is

submerged or re-merges out of the water[7]. CFD codes could provide an empirical relationships or look up tables, that could be included in the potential code that accounts for these viscous losses. This would allow for greater confidence in a potential code's results when modelling more energetic sea states, and also benefiting from the quick run times associated with these numerical solvers.

An issue of concern for any device at sea is that of survivability under extreme conditions. CFD could be used to test a device's survivability characteristics in large deterministic waves. It would provide the wave forces that the device could expect to encounter under specific extreme wave heights, allowing the engineer to design the device accordingly. CFD would not however by suitable for survivability testing using a non-deterministic wave testing approach that uses long run times for a given sea state and relies on statistical probability for certain H_{max} to occur as the computational run times would be excessive.

Commercial CFD software is a powerful design tool and more readily accessible to engineers than bespoke CFD codes. It offers the prospect of knowing all measurable quantities across the whole domain, a large advantage over physical experiments where every measurement needs to be taken independently. With evermore advancements in computer hardware, it will begin to play an even more important role in the design of marine devices. It should be used with caution however, where an appreciation of the limits and validity of the results is paramount. The present failings in the two commercial CFD codes[8], namely the persistent wave height decay and excessive run times, would suggest that they cannot yet provide a realistic option to act as a numerical wave tank. Results from this investigation are positive regarding the fluid-structure-interactions and CFD offers huge potential as a design tool to be used in conjunction with and to compliment theoretical modelling, experimental wave tank work and potential flow code solvers.

---

7. For example a wave energy converter will be constantly submerged by over-topping waves, being subjected to viscous losses as the water rushes over the top of it. Conversely when parts of the device re-emerge at the crest of the wave, viscous losses under the device will also play a part

8. FLUENT and CFX solvers are both owned by ANSYS and their solvers are beginning to converge, so the same wave height attenuation will be in issue with FLUENT also. CD-Adapco's STAR-CCM+ has the same issues with wave height decay, but a more detailed study would be required to quantify this

Chapter 7

Conclusions and further work

This thesis has covered several topics of wave hydrodynamics and numerical modelling, including wavemaker theory, wave absorption, control of wavemakers, verification and validation in a Navier-Stokes solver and the generation of waves in a commercial computational fluid dynamic code. From the outset, the original goal for this project was to incorporate and model hydrodynamic and control theory of wavemakers using a commercial CFD code. It was hoped that physical and numerical convergence would be achieved, allowing the creation of the curved experimental wave tank using a Navier-Stokes solver. This high aspiration was not achieved and the two separate threads of theory and computation were not joined up in the end to give a fully coherent story. This was due to difficulties encountered with the numerical codes.

This project discovered and, more importantly, quantified very serious limitations associated with certain commercial CFD software. Certain shortcomings with these numerical codes became apparent very quickly while attempting to model a simple test case of monochromatic wave generation. It was found that both commercial VOF solvers struggled to model these waves accurately. While very good progress was made in the hydrodynamics and control theory, it could not be implemented as originally envisaged in the CFD codes; as in order to absorb a wave, one must generate a wave. The CFD proved incapable of accurate wave generation.

Not withstanding this, the limitations and applications of commercial CFD codes has been accurately established. These commercial codes are used widely through the industry and the results presented herein will act as an invaluable guide to the discussion and usage of these codes.

This chapter presents a summary of some important findings and original contributions from this thesis, and proposes some recommendations for future work.

7.1 Summary and Conclusions

Using the well established linear wavemaker theory, Chapter 3 presented, for the first time, analytical functions for the hydrodynamic coefficients for two novel wavemaker profiles. It was shown that for a specific frequency, the shape profile of a wavemaker can be chosen such that it either has no added mass or no hydrodynamic damping under oscillation. The existence of such wavemakers has been discussed in the literature, but the analytical expressions of hydrodynamic coefficients have never been derived fully or presented in graphical format. These analytical expressions allowed for easy calculation of the added mass and damping which allowed for quick analysis of absorption characteristics of the wavemakers later in the thesis.

Chapter 4 presented the theory behind the absorption of waves by wave energy converter control systems. This theory was applied to an absorbing wavemaker acting in surge. It was shown that the choice of control strategy and the number of control coefficients used, has a profound effect on the levels of absorption of the wavemaker. All reactive control strategies achieved optimal levels of absorption at the given tuned frequency, but away from the tuned frequency over all levels of absorption differers considerably. Real control systems proved relatively insensitive to the tuning frequency. It argued the need for device developers to consider incorporating reactive control into their devices and also what type of reactive control to implement.

The concept of geometry control was introduced, using wavemakers with geometry chosen to be optimal for one chosen frequency. It was shown that for this chosen frequency an absorbing wavemaker can operate with zero added mass. This reduces the need for reactive power at this geometrically optimal frequency. If the the absorption control system is tuned to achieve complex conjugate control at a frequency other than the frequency where zero added mass occurs, increased levels of absorption over a broad bandwidth are be observed. Thus, two handles of control on absorption are available to the design engineer: geometry and absorption force.

This is particularly applicable in the design of absorbing wavemakers in numerical wave tanks as the shape profiles can readily be altered in a numerical code. If used in conjunction with a numerical sponge layer, it offers the potential for a highly effective numerical absorbing boundary condition. This concept could also

be applied to wave energy converters and highlights the importance of geometry design of the device. If an attenuator or point absorber is geometrically designed to be optimal for a certain wave climate, then increased levels of energy production could be obtained if the absorption control systems were tuned to an alternative frequency to that of the geometry. The chosen frequency does not necessarily need to be the peak frequency of the spectrum. It also argues that increased energy production could be achieved if the geometry and control are considered in the design process concurrently.

Chapter 5 presented the methods associated with a rigorous verification procedure for numerical analysis. These methods of verification appear more frequently in areas where CFD is a more established tool and have yet to be applied to the wave energy sector. Chapter 6 performed a formal verification analysis of wave propagation using an industry standard CFD code, ANSYS CFX and another commercial solver, FLOW3D.

The verification study identified the key numerical parameters that must be specified in order to reduce the errors in the free surface to less than 6% of the correct numerical value. It was shown that CFX and FLOW3D are both sensitive to the spatial discretisation and mesh aspect ratio. The best results using CFX were obtained using an area of grid refinement around the free surface with recommendations of approximately 200 cells per wavelength and 40 cells per wave height. For FLOW3D best results were obtained with a homogeneous uniformly spaced grid with roughly 600 cells per wavelength and 30 per wave height. The time step chosen should result in a CFL number between a value of one to two. The output from these investigations can be readily applied by the industry.

The results from this thesis question the suitability of using commercial CFD codes as a numerical analogue to physical test tanks. The computational run times exceed the physical transient run times by several orders of magnitude. Unless computational run times can be reduced considerably, experimental facilities will always be favoured over CFD options for long duration tests or frequently repeated tests. It should be noted that computational times for CFX were considerably longer compared to FLOW3D and FLOW3D does offer the possibility to model a wave tank in 2D.

Both codes suffered from persistent wave height attenuation of the propagating wave down the numerical wave flume. This is a problem that had not previously been characterised or quantified. In some instances the literature acknowledged

this a being a problem, in other publications it was either missed or ignored. This study has quantified the extent of the wave height attenuation in CFX and FLOW3D which will allow for the industry to make an informed decision on the capabilities and limitations of the two codes.

A validation procedure was conducted, comparing the analytical wavemaker solution from linear wave theory to numerical output from CFX. The agreement close to the wavemaker between the numerical output and theory was almost exact. This shows that CFX is a powerful tool that can accurately predict the velocity flow field around an oscillating body. The good agreement between numerical and theoretical predictions deteriorated with distance down the flume. This again highlights the problems of wave height attenuation within the numerical solution.

The validation was conducted against a piston wavemaker and a bottom hinged flap type wavemaker. For both of these wavemakers, CFX produced results very close to that of linear wavemaker theory, the agreement did diverge with increasing distance from the wavemaker. The free surface displacement generated by a wavemaker with a hyperbolic cosine profile was also presented. This type of wavemaker would prove difficult to physically construct but was more easily implemented in CFX. The numerical results confirmed that indeed it is possible to construct a wavemaker that generates a progressive wave with no evanescent wave present. The hyperbolic cosine wave maker could be used in numerical codes for wave generation as opposed to an open boundary with velocity inlet boundary conditions as there are known issues of volume of fluid entering the domain using this method of wave generation. The hyperbolic cosine wavemaker could also be used in place of piston or flap generated waves in numerical wave flumes. The validation of the hyperbolic cosine as a wavemaker also suggests towards its suitability to be incorporated as a numerical absorbing boundary condition with the correct absorption control.

7.2 Further work

During the course of this research and as a result of certain results presented herein, it is clear that there are a number of points that are worthy of further research. Below are some of the topics that could merit further work.

Implement the absorption theory discussed in Chapter 4 with the hyperbolic co-

sine wavemakers in a potential flow code. There are potential flow codes that have been validated for use as numerical wave tanks and shown excellent agreement. These codes could be used to implement and analyse the theory presented on absorption control of active wavemakers. The theoretical absorption levels using the various combinations of control coefficients could be validated and a hyperbolic cosine wavemaker could also be included in this study.

Investigate the possibility of constructing a hyperbolic cosine wavemaker. While construction a perfect hyperbolic cosine wavemaker would prove difficult, an alternative would be to use a cantilever style wavemaker, fixed to the flume floor. This wavemaker could have physical properties chosen such that when a point load is applied at the exposed tip of the cantilever, the deflection of the beam approximates the profile of a hyperbolic cosine.

Quantify the absorption theory described in Section 4 for polychromatic waves in the time domain. The absorption theory discussed in this thesis has been limited to the realm of discretised monochromatic waves in the frequency domain. Many studies do this in order to reduce the complexity of the analysis, however this is a simplification of the real world physics and it would be important to assess how this assumption affects the absorption levels.

Analyse and quantify the effect of force feedback on absorption. The wavemakers used at the University of Edinburgh use two absorption coefficients in conjunction with a force feedback mechanism. This force feedback measures the force on the wavemaker and compares it to the absorption force. Theoretically, if the incoming waves are at the frequency that the absorption coefficients are optimised for, the measured force on the wavemaker should be insignificant. If the incoming waves are of a different frequency then there will be a mis-match between the absorption force and the measured force on the wavemaker. This will drive an error signal to try to achieve a zero sum force. It would be interesting to quantify the contribution of this force feedback to the absorption characteristics of the wavemaker and contrast this against using different combinations of control coefficients.

Force feedback wavemakers could be compromised if current was introduced into the wave flume and the fluid current impinged upon the wavemaker surface. It would be interesting to quantify this effect and also quantify the effect that this would have on non force feedback wavemakers. The non force feedback wavemakers might provide a better choice, with more stable performance but with slightly less absorption level qualities.

Investigate other CFD solvers that use alternative free surface models to Volume of Fluid. This thesis has shown that wave height attenuation affects two commercial CFD solvers that implement the Volume of Fluid numerical scheme. It seems that this problem is endemic to many commercial CFD solvers that use Volume of Fluid. CFD has the potential to act as a hugely useful tool to the design engineer. Especially if it could be used as a numerical wave tank. The problems of wave height attenuation could be due to the numerical damping introduced into the solver, in order to keep the solution stable. Solvers that do not use the volume of fluid not need to introduce fictitious damping for a stable solution. These solvers could over come the problem of wave height attenuation offer the potential to implement a numerical wave tank using a Navier-Stokes solver, providing large benefits to industrial users.

Appendix A

CFX preliminary temporal and spatial study

This appendix details a preliminary study into spatial and temporal discretisation and different numerical methods, using ANSYS CFX to model a wavemaker and wave propagation in a 2D wave flume. The initial mesh spacings were taken from a study using CFX to analyse a wave train behind a submerged hydrofoil (Gretton *et al.*, 2010). Formal grid convergence analysis, as laid out in Chapter 5 will be followed, and investigations into mesh spacing and other numerical options will be explored to investigate the sensitivity of the results to changes in these parameters.

A.1 Wave generation

An oscillating wall boundary condition was implemented to generate a propagating wave through the test domain. This is analogous to, the well studied, physical wave flume present in many hydrodynamic laboratories around the world. The publication by Havelock (1929) is widely considered as the foundation of wavemaker theory with further work published on the theoretical and practical considerations by Biesel and Suquet (1951), Dean and Dalrymple (1991) and Hughes (1993). Wavemaker theory has allowed experimentalists to obtain an analytic solution to the far field wave elevation for a given wavemaker displacement.

The general first-order solution for a piston wavemaker yields the ratio between the far field wave height and stroke displacement as (Hughes, 1993)

$$\frac{H}{S_o} = \frac{4 \sinh^2 kh}{\sinh 2kh + 2kh} \tag{A.1}$$

where, H is the wave height, S_o is waveboard stroke, h is the water depth and k is the wave number, which in deep water conditions approximates to $\frac{2\pi}{\lambda}$.

$$X = \frac{S_o}{2}\sin(\omega t) \tag{A.2}$$

where ω is the frequency. This was chosen as 1[Hz], thus yielding a wave period of 1[s].

A.2 Numerical Set up

These simulations were carried out using the same solver, ANSYS-CFX, using the same setup as set out by Gretton *et al.* (2010). The main difference is that this run was a transient simulation. The boundary conditions on the bottom, the wavemaker and the back wall were No-Slip, the top boundary was set as an opening, with the static pressure for entrainment option selected and two symmetry conditions on the side walls for a 2-D simulation. Homogeneous multiphase, with second-order transient and coupled volume-fraction solution options were also selected.

A.3 Grid design for wave tank

The grids were constructed using the grid generation package ICEM. This was used to generate a simple rectangular box and populated with a structured mesh. The wave tank geometries were normalised, based upon a $1[Hz]$ wave in deep water thus resulting in a wavelength of $\lambda = 1.56m$. The overall length of the wave tank was 14λ, this was consisted of three regions. The first region closest to the wavemaker wave one wavelength long. This region had mesh motion enabled to capture the movement of the piston wavemaker, analogous to that of a hydrodynamic laboratory. As mesh motion is an inherently diffusive process, this only motion was limited to a distance of one wave length from the piston wavemaker thus having a stationary mesh over most of the domain. A stationary grid of 6λ then made up the area of interest, a 7λ wave tank. The last section is referred to at the 'dissipation' zone, similar to that used with the air-foil. This region had a stretched mesh which allowed the Δx spacing to be equal to that of the wave length, thus filtering out these waves.

Table A.1: Courant numbers and time step selection

Courant No.	Coarse	Medium	Fine
8.8	1/25 [s]	1/50 [s]	1/100 [s]
4.4	1/50 [s]	1/100 [s]	1/200 [s]
2.2	1/100 [s]	1/200 [s]	1/400 [s]
1.1	1/200 [s]	1/400 [s]	1/800 [s]

Table A.2: Grid refinement mesh spacing

	Coarse	Medium	Fine
cells / λ	25	50	100
cells / H	20	40	80

A.4 Temporal Discretization

The time step was chosen with the Courant Friedrichs Lewy condition (CFL condition) in mind. While CFX is a fully implicit solver, and the CFL condition is a limiting factor for explicit schemes, choosing the time step based upon the CFL still has it's merits. For a two dimensional case the Courant number can be obtained as

$$\frac{u_x \Delta t}{\Delta x} + \frac{u_y \Delta t}{\Delta y} = \upsilon \tag{A.3}$$

where u_x is chosen as the maximum velocity that information travels in the X direction. This was chosen as the phase velocity of the wave train, and not the group velocity which is only half the value of phase speed in deep water. u_y is the maximum particle velocity in the Y direction Δt is the time step, and Δ_x and Δ_y are the grid spacings in X and Y respectively.

Four different courant numbers were chosen.

A.5 Spatial Discretization

Following Roache (1998), a formal grid independence study was carried out using three separate grids. Each successive grid adhered to a constant refinement ratio which saw a halving in the node spacing from the coarse to the medium grids, and likewise from the medium to fine grids. This allowed for the calculation of various convergence metrics and for a Richardson extrapolation to be carried out.

A.5.1 One Dimensional Refinement

A uni-directional grid dependence study was conducted to gauge the sensitivity of the results to grid refinement in the Y direction and the X direction. The effect on the free surface can be seen in Figures A.1 and A.2. This compares the uni-directional refinement to the omni-directional refinement. It can be seen that the free surface is far more sensitive to changes in Δx than Δy. This suggests that the initial guesses for mesh spacing (table A.2) over estimated the amount of refinement needed in the vertical direction to capture the free surface accurately. This implies that the initial guesses were overly conservative. More efficient use of computational time could be had with extra Δx refinement.

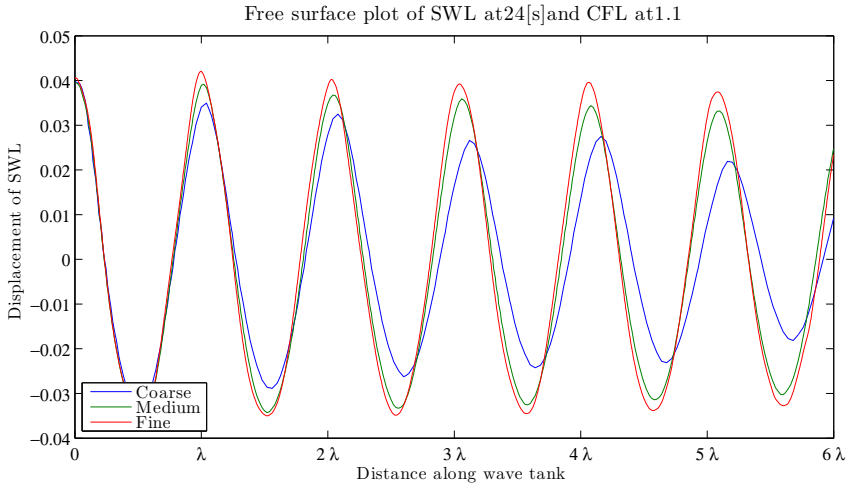

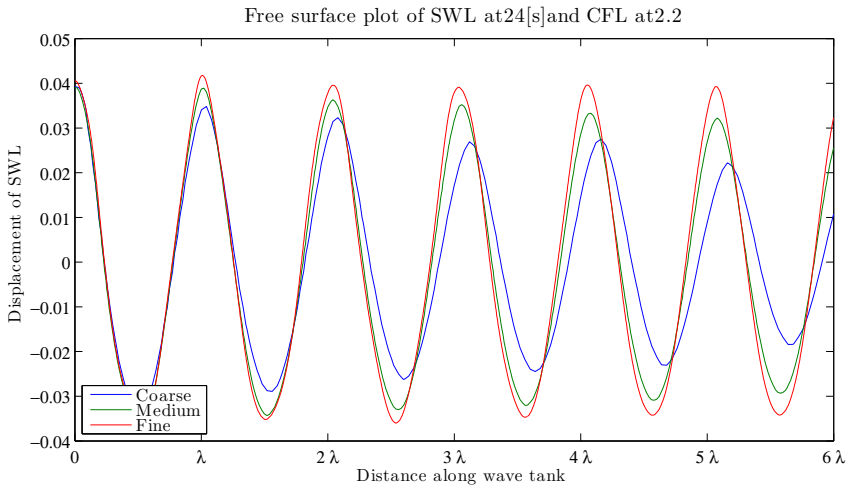

A.6 Spatial Convergence Study

A.7 Temporal Convergence Study

A.8 Y direction grid refinement

A.9 X direction grid refinement

A.10 Convergence criteria sensitivity

A.11 Precision sensitivity analysis

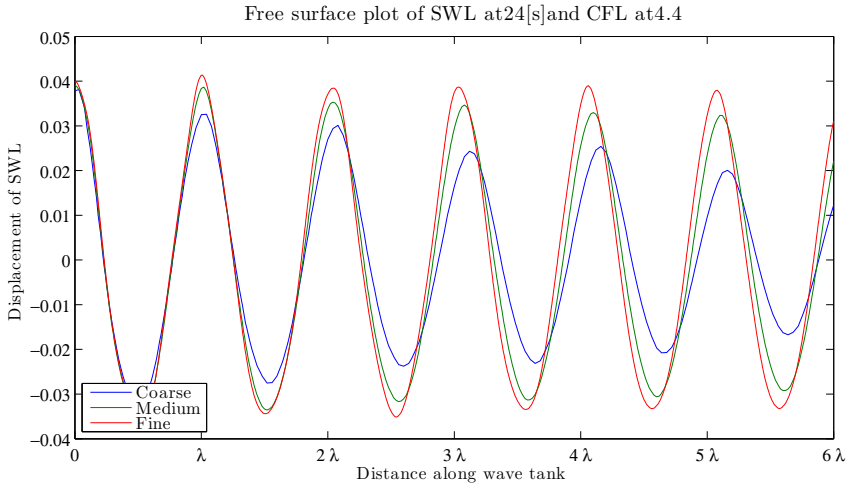
Free surface plot of SWL at24[s]and CFL at4.4
Displacement of SWL
Distance along wave tank
Coarse
Medium
Fine
0.05
0.04
0.03
0.02
0.01
0
−0.01
−0.02
−0.03
−0.04
0
λ
2 λ
3 λ
4 λ
5 λ
6 λ

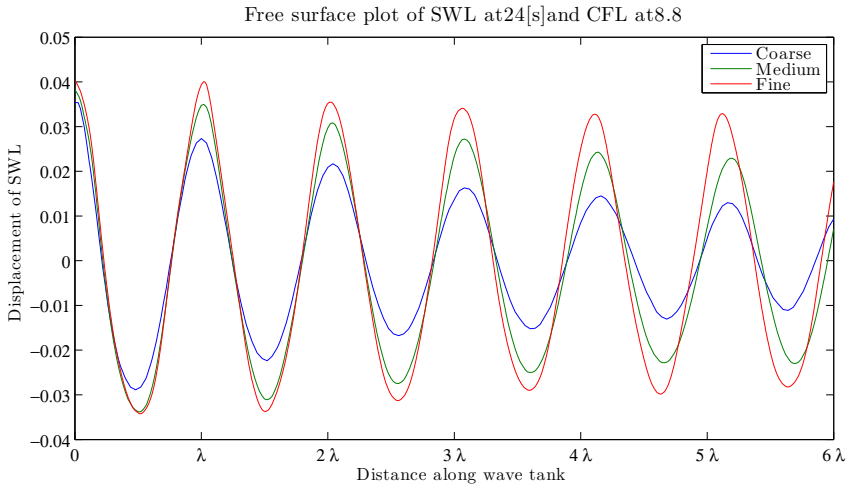
Free surface plot of SWL at24[s]and CFL at8.8
Displacement of SWL
Distance along wave tank
Coarse
Medium
Fine
0.05
0.04
0.03
0.02
0.01
0
−0.01
−0.02
−0.03
−0.04
0
λ
2 λ
3 λ
4 λ
5 λ
6 λ

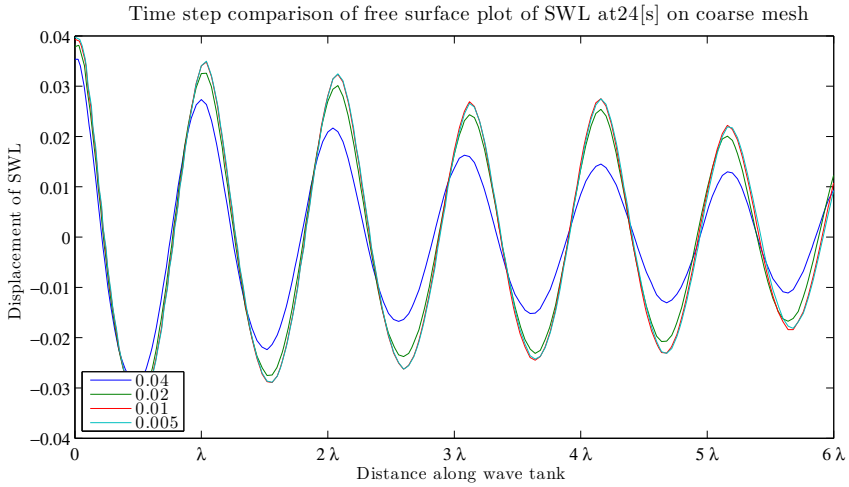
Time step comparison of free surface plot of SWL at24[s] on coarse mesh
Displacement of SWL
Distance along wave tank
0.04
0.02
0.01
0.005
0.04
0.03
0.02
0.01
0
−0.01
−0.02
−0.03
−0.04
0
λ
2 λ
3 λ
4 λ
5 λ
6 λ

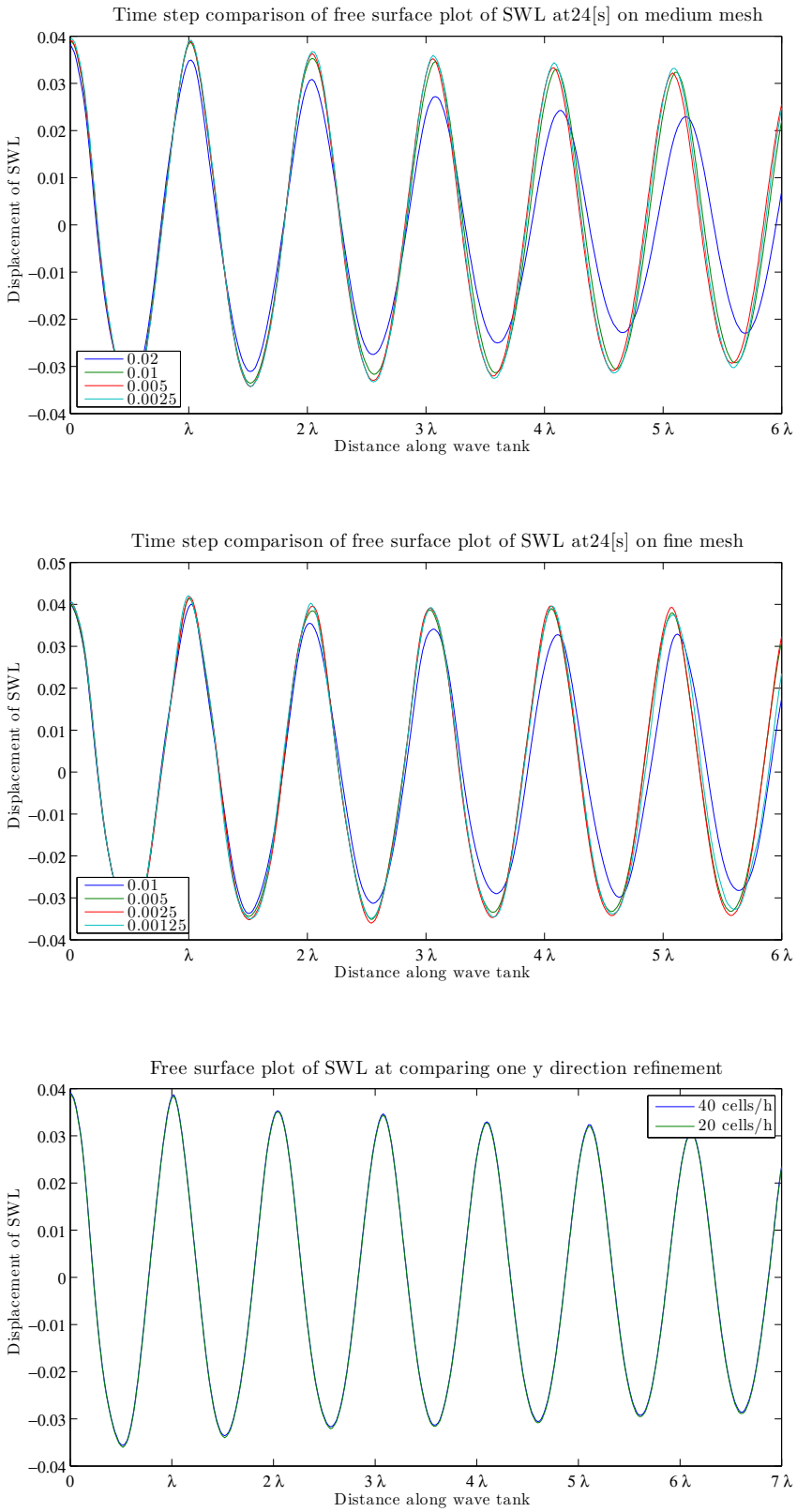

Figure A.1: Free surface comparison looking at y directional refinement.

Table A.3: Grid convergence analysis for the surface elevation. This considers the first six waves, as indicated by the grouping in the table. This values are obtained using a CFL number of 1.1

Value	trough disp.	crest disp.	wave height	zero crossing	wave length
Coarse	−0.034	0.035	0.069	1.221	1.620
	−0.029	0.032	0.061	2.841	1.661
	−0.026	0.027	0.053	4.502	1.597
	−0.024	0.028	0.052	6.098	1.610
	−0.023	0.022	0.045	7.709	1.522
	−0.018	0.020	0.038	9.230	1.542
Medium	−0.036	0.039	0.076	1.211	1.608
	−0.034	0.037	0.071	2.819	1.593
	−0.033	0.036	0.069	4.412	1.589
	−0.033	0.034	0.067	6.001	1.571
	−0.031	0.033	0.065	7.572	1.570
	−0.030	0.032	0.062	9.142	1.559
Fine	−0.037	0.042	0.079	1.198	1.584
	−0.035	0.040	0.075	2.781	1.606
	−0.035	0.039	0.074	4.388	1.577
	−0.035	0.040	0.074	5.965	1.599
	−0.034	0.037	0.071	7.563	1.623
	−0.033	0.038	0.070	9.187	1.575
R	0.114	0.691	0.466	1.338	2.115
	0.137	0.823	0.439	1.752	−0.194
	0.226	0.353	0.298	0.277	1.459
	0.236	0.755	0.471	0.376	−0.701
	0.295	0.381	0.344	0.067	1.112
	0.203	0.487	0.344	−0.503	0.944
p	3.134	0.532	1.102	−0.420	−1.081
	2.870	0.282	1.187	−0.809	–
	2.146	1.504	1.746	1.850	−0.545
	2.086	0.405	1.085	1.413	–
	1.763	1.392	1.538	3.899	−0.153
	2.301	1.038	1.538	–	0.083
Richarson extrapolated	−0.037	0.043	0.080	1.193	1.576
	−0.035	0.041	0.077	2.769	1.611
	−0.035	0.040	0.076	4.379	1.573
	−0.035	0.041	0.076	5.952	1.608
	−0.035	0.039	0.074	7.560	1.641
	−0.034	0.040	0.073	9.201	1.580
GCI_{mc}	0.012	0.300	0.099	−0.041	−0.017
	0.031	0.674	0.134	−0.022	–
	0.077	0.177	0.126	0.010	−0.020
	0.098	0.773	0.253	0.012	–
	0.138	0.261	0.198	0.002	−0.382
	0.127	0.450	0.256	–	0.230
GCI_{fm}	0.001	0.193	0.044	−0.056	−0.036
	0.004	0.506	0.055	−0.040	–
	0.017	0.057	0.035	0.003	−0.030
	0.022	0.507	0.108	0.005	–
	0.038	0.088	0.062	0.000	−0.410
	0.024	0.185	0.078	–	0.215
$\mathrm{GCI}_{mc}/(r^p\mathrm{GCI}_{fm})$	1.008	1.074	1.042	0.989	0.985
	1.022	1.096	1.060	0.987	–
	1.048	1.092	1.071	0.994	0.993
	1.060	1.151	1.107	0.994	–
	1.078	1.129	1.104	0.999	1.034
	1.081	1.185	1.134	–	1.010

[a] An R value $-1 < R < 1$ suggests oscillatory convergence
[b] An R value > 1 suggests divergence

Table A.4: Grid convergence analysis for the surface elevation. This considers the first six waves, as indicated by the grouping in the table. This values are obtained using a CFL number of 2.2

Value	trough disp.	crest disp.	wave height	zero crossing	wave length
Coarse 3	−0.033	0.035	0.068	1.217	1.620
	−0.029	0.032	0.061	2.837	1.656
	−0.026	0.027	0.053	4.494	1.596
	−0.024	0.028	0.052	6.089	1.603
	−0.023	0.022	0.045	7.692	1.525
	−0.018	0.020	0.038	9.217	1.535
Medium 2	−0.036	0.039	0.075	1.207	1.609
	−0.034	0.036	0.071	2.816	1.590
	−0.033	0.035	0.068	4.406	1.582
	−0.032	0.033	0.065	5.988	1.572
	−0.031	0.032	0.063	7.560	1.560
	−0.029	0.031	0.060	9.121	1.555
Fine 1	−0.036	0.042	0.078	1.203	1.593
	−0.035	0.040	0.075	2.797	1.589
	−0.036	0.039	0.075	4.385	1.571
	−0.035	0.040	0.074	5.956	1.581
	−0.034	0.039	0.074	7.537	1.578
	−0.034	0.038	0.072	9.115	1.567
R	0.001	0.702	0.412	0.359	1.401
	0.167	0.816	0.442	0.906	0.020
	0.453	0.469	0.462	0.237	0.823
	0.351	1.089	0.671	0.316	−0.275
	0.428	0.705	0.584	0.179	0.498
	0.447	0.691	0.568	0.059	0.628
p	9.689	0.510	1.279	1.480	−0.487
	2.582	0.294	1.177	0.143	5.639
	1.143	1.093	1.115	2.078	0.281
	1.510	−0.122	0.575	1.664	–
	1.225	0.503	0.777	2.486	1.007
	1.162	0.532	0.817	4.077	0.672
Richardson extrapolated	−0.036	0.043	0.079	1.202	1.588
	−0.036	0.041	0.076	2.790	1.588
	−0.037	0.040	0.077	4.378	1.567
	−0.036	0.042	0.077	5.946	1.583
	−0.035	0.042	0.077	7.529	1.584
	−0.036	0.040	0.076	9.113	1.571
GCI_{mc}	0.000	0.311	0.082	0.006	−0.030
	0.039	0.606	0.132	0.092	0.001
	0.210	0.260	0.236	0.008	0.050
	0.160	−2.675	0.521	0.010	–
	0.237	0.931	0.496	0.005	0.028
	0.376	0.975	0.591	0.001	0.026
GCI_{fm}	0.000	0.204	0.032	0.002	−0.043
	0.006	0.453	0.055	0.084	0.000
	0.087	0.110	0.099	0.002	0.041
	0.052	−2.448	0.308	0.003	–
	0.091	0.539	0.248	0.001	0.014
	0.144	0.543	0.278	0.000	0.016
$\mathrm{GCI}_{mc}/(r^p\mathrm{GCI}_{fm})$	1.000	1.074	1.038	0.997	0.990
	1.026	1.089	1.059	0.993	0.999
	1.092	1.110	1.102	0.995	0.993
	1.083	1.189	1.137	0.995	–
	1.108	1.219	1.165	0.997	1.011
	1.166	1.241	1.204	0.999	1.008

Table A.5: Wave peaks following Y direction grid refinement

	$\lambda 1$	$\lambda 2$	$\lambda 3$	$\lambda 4$	$\lambda 5$	$\lambda 6$
40 cells/h [m]	0.03867	0.03532	0.03466	0.03297	0.03234	0.03080
20 cells/h [m]	0.03842	0.03509	0.03440	0.03275	0.03201	0.03057
Difference [m]	-0.00025	-0.00022	-0.00026	-0.00021	-0.00033	-0.00023
% Change	-0.65%	-0.63%	-0.75%	-0.65%	-1.02%	-0.74%

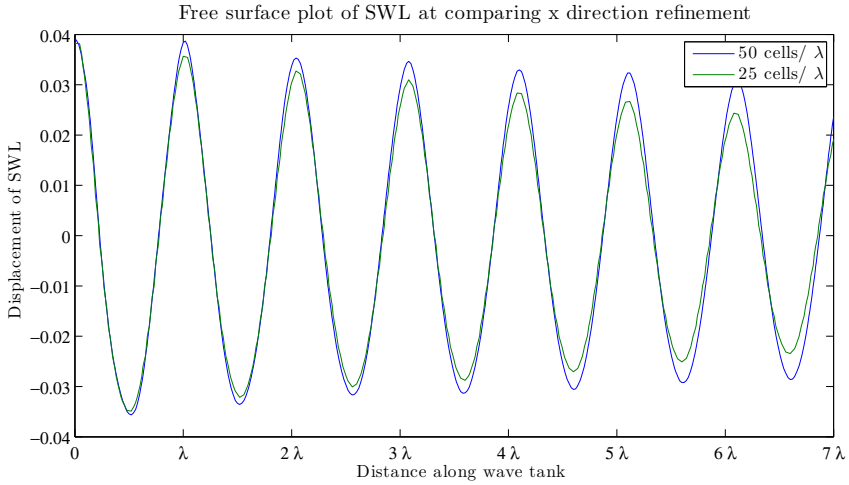

Figure A.2: Free surface comparison looking at x directional refinement.

Table A.6: Wave peaks following X direction grid refinement

	$\lambda 1$	$\lambda 2$	$\lambda 3$	$\lambda 4$	$\lambda 5$	$\lambda 6$
50 cells/h [m]	0.03867	0.03532	0.03466	0.03297	0.03234	0.03080
25 cells/h [m]	0.03566	0.03274	0.03099	0.02836	0.02668	0.02436
Difference [m]	-0.00301	-0.00258	-0.00368	-0.00461	-0.00566	-0.00644
% Change	-7.79%	-7.3%	-10.6%	-13.98%	-17.49%	-20.91%

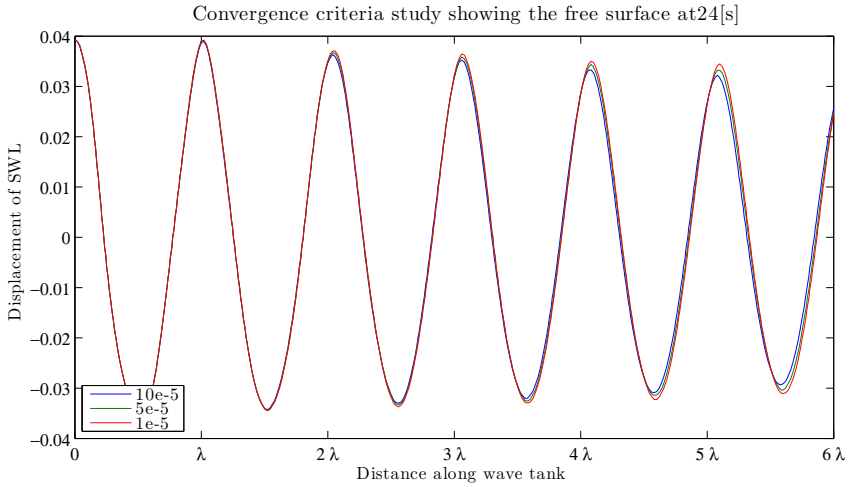

Table A.7: Convergence stopping criteria sensitivity

	$\lambda 1$	$\lambda 2$	$\lambda 3$	$\lambda 4$	$\lambda 5$
Peaks at 10×10^{-5}	0.039	0.036	0.035	0.033	0.032
Peaks at 5×10^{-5}	0.039	0.037	0.036	0.034	0.033
Peaks at 1×10^{-5}	0.039	0.037	0.036	0.035	0.034

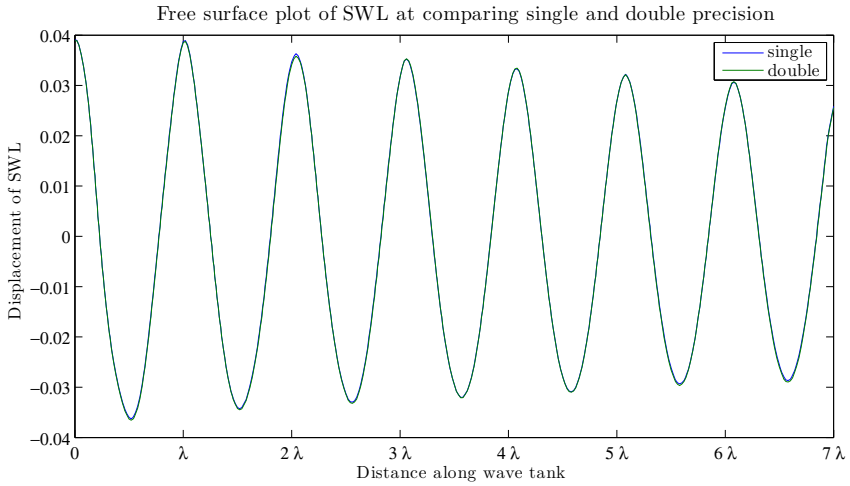

Appendix B

Published papers

B.1 EWTEC, 2009

Maguire, A.E., and D.M. Ingram. Hydrodynamics and absorption efficiencies of wavemakers. In Proceedings of the 8th European Wave and Tidal Energy Conference, 859 - 868. Uppsala, Sweeden, 2009.

Hydrodynamics and absorption efficiencies of wavemakers

A.E. Maguire[1] and D.M. Ingram[2]

[1]Institute for Energy Systems,
Joint Research Institute for Energy ,
The University of Edinburgh,
E-mail: E.Maguire@ed.ac.uk
[2] E-mail: David.Ingram@ed.ac.uk

Abstract

For most of the twentieth century naval hydrodynamics, and more recently, wave energy hydrodynamics have been limited to the realms of theory and physical experiments. Both of these methods of fluid flow analysis are constrained through scope, cost and size of facility. The advent of high speed digital computing has brought with it a new dimension for analysing fluid flows, that of numerical modelling. This paper aims to harness this progress in computing power and established commercial computational fluid dynamics (CFD) codes to create a numerical analogue to the physical test flumes that are in operation in many hydrodynamic labs. Using numerical wavemakers will allow for the use of different shaped wavemakers that would be otherwise impossible to implement in a physical waveflume, these non-conventional shapes will be investigated.

This paper presents the well established wavemaker theory. This is then adapted to obtain the hydrodynamic coefficients of added mass and damping for two novel shaped wavemakers. The different wavemaker geometries are compared on the basis of their theoretical wave absorption efficiencies at various tuned frequencies. Wavemaking simulations using ANSYS CFX are then presented and the results are discussed.

Keywords: Wavemaker, CFD, absorption, added mass, damping.

1 Introduction

A general theory for the generation of waves by oscillating solid boundaries was first prestented by Havelock [1] and is widely considered as the foundation of wavemaker theory. Building upon this knowledge, *Les Appareils Générateurs de Houle en Laboratoire* published by Biésel and Suquet [2] (later to be translated into English [3]) was a huge advancement in laboratory generated waves. It solved the analytical problem for a number of different wavemakers and geometries providing a transfer function relating the wave paddle displacement to the propagating wave amplitude. This linear transfer function has been confirmed through theoretical and experimental comparison [4],[5]. Building on these transfer functions Gilbert *et al.*[6] presented analysis of dimensionless values for the forces and paddle strokes which was used in the construction of the first wave tank at the University of Edinburgh.

A major problem encountered with wave tanks is that of wave re-reflections spoiling the test domain. Passive wave absorbers dealt with impinging waves adequately but problems with re-reflections from the wave makers and test devices persisted. In an attempt to show that it is possible to move a paddle in a manner that absorbs incident waves, Milgram [7] published his paper on "Active water-wave absorbers". Milgram concluded that in the synthesis of a wave-absorbing system four criteria must be met: The complete system must be stable. Drift of the paddle must be prevented by the absorbing system and have zero response at a frequency of zero. To prevent high frequency noise, the absorbing system subfunction should be less than the hydrodynamic system function. And obviously, the reflection coefficient should be less than one for all frequencies. Milgram used surface elevation for the active feedback mechanism. He suggests that the exerted force acting on the paddle would be attractive to operate on but points to physical constraints in his specific flume. There was a short fluid filled space behind the wave paddle. The fluid motion in this small space would complicate calculations through resonance at certain frequencies, thus he concluded that it was not practical to activate the paddle on the basis of measured force. The surface elevation a short distance from the wave paddle was used instead. Milgram conducted experimental work to compare the measured and predicted wave reflection coefficients. Absolute reflection coefficients in the range of 2 % to 11 % were reported for frequencies between 1 to 4 Hz. It should be noted that this active absorber was not used in a combined generation and absorption mode.

Unaware of Milgrams work on wave absorption, Salter [8] proceeded to obtain an active wave maker using force measurement. Salter cited three advantages to this method. Force is an integral quantity measured

over the entire wave maker front and using this measurement minimises any slight errors encountered with single point measurements. Force sensors can be entirely free from the chemical and biological vagaries of tank water. Most types of tank probes use either resistive gauges or capacitance gauges. Both of these are susceptible to corrosion, biological growths, oil and dust residues, all of which require frequent re-calibration which is unacceptable for a large array of wave makers. Finally, Salter cites the conservation of energy as another reason to choose force feedback. He states that the advantage of using a force measurement is its ease in combing it with a velocity measurement and therefore fixing the rate of energy given to the water. He argues that it is "better to provide the right amount of energy at each frequency than to try to enforce a sinusoidal form that the waves do not like". Thus controlling energy bypasses many of the non-linearity problems that arise when generating steep waves.

In numerical wave tanks, many methods exist to try and cope with reflected waves using purely mathematical methods. The periodic boundary condition is where the solution is assumed to be periodic in space, so that the values of the unknowns on one vertical boundary can be to equal those on the other vertical boundary of the domain. Another technique used to simulate infinite outer fields at finite distance is that of artificial damping also referred to as sponge layers. This is the process of applying a dissipative term to the equations near the boundary of the truncated domain. This dissipative term can be added to the free surface boundary condition as well as both the dynamic and kinematic boundary conditions. A novel approach was adopted by Orlanski [9] where he imposed Sommerfeld's condition on the boundary. The main advantage of this approach was that no information on the frequency of the approaching waves was needed. The Sommerfeld-Orlanske is probably the most widely used technique for numerical absorption of waves [10]. As this research hopes to create an numerical analogue to physical paddles, the method for dealing with wave re-reflections will be using a physically realisable method, namely that of force-feedback. For a more in depth discussion on numerical absorption boundary conditions, please consult Romante [10] for a detailed review.

Research from the *Laboratoire de Mécanique de Fluide* at *École Centrale de Nantes* has been published regarding a realisable control strategy for active absorbing wave makers. Maisondieu and Clement [11] were the first to publish their results on a force feedback-feedforward control loop for a piston wave absorber. They considered the problem of absorption of water waves by the horizontal motions of a vertical plane in responce to the hydrodynamic forces it experiences. They are quick to point out that a solution to this in the frequency domain is relatively easy, but upon implementation of an inverse Fourier transform the solution becomes a non-causal impulse response function. In their paper they propose to model the ideal controller by a causal approximation. They compare their new control strategy for two conditions, when one knows the dominant frequency in the incident waves and when one does not.

This publication was quickly followed up with another publication [12] on the same matter, conducting a comparison of time domain control laws for this piston wave absorber. Again this paper concentrated on the derivation of efficient time domain control strategies for the absorption of waves by a vertical paddle. This paper suggests two causal non-ideal approximations of the ideal non-causal controller. This method proved very promising at low frequencies, when one can identify a dominant frequency in the incident wave train *a priori*

Building on this published work Chatry and Clement [13] proposed a self-adaptive control of a piston wave absorber. This paper derived sub-optimal approximations similar to Maisondieu and Clement [11] but as the previous study showed better performance when the incident wave frequency was known, a self-adaptive tuner was developed hoping to maintain the system frequency to the optimal one. It is based on a frequency tracking extended Kalman filter algorithm and a feedforward loop. The efficiency of the controllers was measured by numerical experiments. It was found that this self-adaptive feedforward feedback system performed very well over a broad frequency range.

Newman [14] produced analysis of wave generation and absorption within the framework of linear potential theory. He derives relations that govern the control of the absorbers in an attempt to eliminate reflected waves from the walls of the basin. He sets out the theory behind control of wavemaking and absorbing in two-dimensions and progresses to extend this to the three-dimensional case. This paper encompasses the theoretical framework and analysis of the obtained results. It deals with conditions for optimisation of two-dimensional wavemakers in two and three dimensions. It then investigates the effects of including a floating body in the computational domain. Later in the paper two-dimensional wavemakers are analysed in the time domain.

In a recent paper, Spinneken and Swan [15] discuss causal approaches for controlling active wavemakers. Their technique is based upon infinite impulse response filters and they show that optimisation of this controller results in very good levels of absorption. They compare their results to the techniques of Naito [16] and ECN showing better performance with their control strategy.

2 Hydrodynamic coefficients of a wavemaker in a channel

Following the method used by Falnes [17, sect 5.2.3], let us consider a physical model shown in figure (1). Cartesian coordinates, x, y, z, are used, with $z = 0$ on the still water level and the $+ve\ z axis$ directed upwards. This is a 2D piston, in a water depth, h, that can oscillate in surge. When any body oscillates in water a radiated wave with a velocity potential, ϕ_r is generated. This will be a linear combination of the six modes of oscillation giving

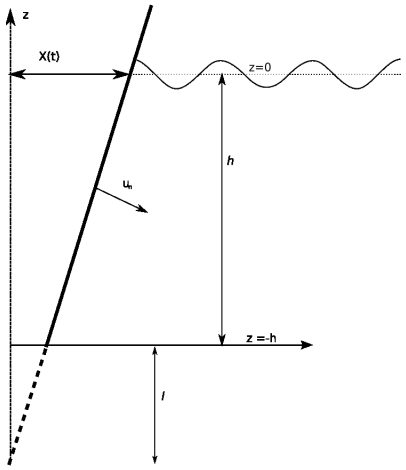

Figure 1: Two-Dimensional Wave Flume Definition Sketch

[17];

$$\hat{\phi}_r = \sum_{j=1}^{6} \varphi_j \hat{u_j} \tag{1}$$

where φ_j is a complex coefficient of proportionality. In the case shown, the piston motion is limited to surge ($j = 1$). If the piston has a complex velocity with complex amplitude $\hat{u}_1 \neq 0$, then according to the inhomogeneous boundary condition

$$\frac{\partial \varphi_1}{\partial x} = c(z) \qquad forx = 0 \tag{2}$$

where $c(z)$ is a function that defines the shape profile of the wavemaker. The general form of $c(z)$ for a two-dimensional wavemaker is

$$c(z) = \left(1 + \frac{z}{h+l}\right) \tag{3}$$

where l is the hinge depth. As $l \to \infty$, c(z) corresponds to the surface profile of a piston ($c(z) = 1$) or as $l \to 0$ the profile is that of a bottom hinged paddle ($c(z) = 1 + \frac{z}{h}$) Following Havelock [1] and Falnes [17] , φ_1 can be represented as

$$\varphi_1 = c_0 Z_0(z) e^{-ik_0 x} + \sum_{n=1}^{\infty} c_n Z_n(z) e^{-k_n x} = \sum_{n=0}^{\infty} X_n(x) Z_n(z) \tag{4}$$

where

$$X_n(x) = c_n e^{k_n x} \tag{5}$$

Here, k_n is the solution to the dispersion relationship for $n \geq 1$ and conveniently letting $k_0 = ik$ [17]

$$\omega^2 = -gik_n \tanh(-ik_n h) \tag{6}$$

Making use of the boundary condition (eqn. 2) gives

$$c(z) = \left[\frac{\partial \varphi_1}{\partial x}\right] = \sum_{n=0}^{\infty} X_n'(0) Z_n(z) \tag{7}$$

As Falnes [17] shows, multiplying by the complex conjugate, $Z_m^*(z)$ and integrating from $z = -h$ to $z = 0$ while using orthogonality condition gives

$$\int_{-h}^{0} c(z) Z_m^*(z) dz = \sum_{n=0}^{\infty} X_n'(0) \int_{-h}^{0} Z_m^*(z) Z_n(z) dz = X_m'(0) h \tag{8}$$

That is,

$$X_n'(0) = \frac{1}{h} \int_{-h}^{0} c(z) Z_n^*(z) dz \tag{9}$$

Combining equation (9) and equation (5) yields

$$X_0'(0) = ik_0 c_0, \qquad X_n'(0) = k_n c_n \tag{10}$$

Thus giving the two coefficients

$$c_0 = \frac{-1}{ik_0 h} \int_{-h}^{0} c(z) Z_0^* dz \tag{11}$$

$$c_n = \frac{-1}{k_n h} \int_{-h}^{0} c(z) Z_n^* dz \tag{12}$$

The orthogonal set of eigenfunctions $Z_n(z)$ are given as [see 17, chap. 4.2]

$$Z_0 = (N_0)^{-1/2} \cosh(k_0(z+h)) \tag{13}$$

$$Z_n = (N_n)^{-1/2} \cos(k_n(z+h)) \tag{14}$$

where

$$N_0 = \frac{1}{2}\left(1 + \frac{\sinh(2k_0 h)}{2k_0 h}\right) \tag{15}$$

$$N_n = \frac{1}{2}\left(1 + \frac{\sin(2k_n h)}{2k_n h}\right) \tag{16}$$

The radiation impedance of the wavemaker in a two-dimensional channel acting in surge is given by Falnes [17]. The term $R_{j'j}$ is the radiation resistance matrix or added damping. $X_{j'j}$ is the radiation reactcance matrix and $m_{j'j}$ is the added mass.

$$\begin{aligned} Z_{j'j} &= R_{j'j} + iX_{j'j} \\ &= R_{j'j} + i\omega m_{j'j} \\ Z_{11} &= i\omega\rho d \int_{-h}^{0} \left[\psi_1 \frac{\partial \varphi_1^*}{\partial x} dz\right]_{x=0} dz \end{aligned} \tag{17}$$

Thus, the impedance per unit width

$$\begin{aligned} \frac{Z_{11}}{d} &= i\omega\rho \int_{-h}^{0} \left[c_0 Z_0(z) + \sum_{n=1}^{\infty} c_n Z_n(z)\right] c^*(z) dz \\ Z_{11}' &= i\omega\rho \left[c_0(-ik_0 h)c_0^* + \sum_{n=1}^{\infty} c_n(k_n h)c_n^*\right] \\ &= \omega k_0 \rho h |c_0|^2 + i\omega\rho h \sum_{n=1}^{\infty} k_n |c_n|^2 \end{aligned} \tag{18}$$

The radiation resistance, R_{11}, or added damping is the real part of eq.18

$$R_{11} = \Re\{Z_{11}\} = \omega k_0 \rho h d |c_0|^2 \tag{19}$$

and the added mass, m_{11}, is the imaginary part of eq.18

$$m_{11} = \Im\{Z_{11}\} = \rho h d \sum_{n=1}^{\infty} k_n |c_n|^2 \tag{20}$$

2.1 Derivation of added mass and damping for a bottom hinged paddle

As can be seen, both the added mass and damping are functions of c_0 and c_n respectively. These parameters are in turn functions of the shape parameter, $c(z)$. Thus for different paddle shapes, the added mass and added damping will vary significantly. The two main shapes of concern, in a physical wavemaker, are that of a piston ($c(z) = 1$) and a bottom hinged flap ($c(z) = 1 + z/h$). The following equations are a derivation of the added mass and damping for the latter, a bottom hinged flap. This derivation was not presented by Falnes [17], but the added mass and damping coefficients agree with those presented by Newman [14] for a bottom hinged flap.

From equation (11) and using equation (13)

$$\begin{aligned} c_0 &= -\frac{1}{ik_0h}N_0^{-1/2}\int_{-h}^{0}(1+z/h)\cosh(k_0(z+h))dz \\ &= -\frac{1}{ik_0h}N_0^{-1/2}\frac{1+k_0h\sinh(k_0h)-\cosh(k_0h)}{{k_0}^2h} \\ &= i\left(1+k_0h\sinh(k_0h)-\cosh(k_0h)\right){k_0}^{-3}h^{-2} \\ &\left(\frac{1}{2}+\frac{1}{4}\frac{\sinh(2k_0h)}{k_0h}\right)^{-1/2} \end{aligned} \tag{21}$$

$$\begin{aligned} R_{11} &= \omega k_0\rho hd|c_0|^2 \\ &= 4\,\frac{\omega\rho\,\left(1+\sinh(k_0h)\,k_0h-\cosh(k_0h)\right)^2}{{k_0}^4h^2\left(2k_0h+\sinh(2k_0h)\right)} \end{aligned} \tag{22}$$

Similarly, from equation (12) and using equation (14)

$$\begin{aligned} c_n &= -\frac{1}{k_nh}N_n^{-1/2}\int_{-h}^{0}(1+z/h)\cos(k_n(z+h))dz \\ &= \frac{1}{k_nh}N_n^{-1/2}\frac{-1+\cos(k_nh)+k_nh\sin(k_nh)}{{k_n}^2h} \\ &= \left(-1+\cos(k_nh)+k_nh\sin(k_nh)\right){k_n}^{-3}h^{-2} \\ &\left(\frac{1}{2}+\frac{1}{4}\frac{\sinh(2k_n)}{k_n}\right)^{-1/2} \end{aligned} \tag{23}$$

$$\begin{aligned} m_{11} &= \omega\rho hd\sum_{n=1}^{\infty}k_n|c_n|^2 \\ &= 4\rho\sum_{n=1}^{\infty}\frac{\left(-1+\cos(k_nh)+\sin(k_nh)\,k_nh\right)^2}{{k_n}^4h^2\left(2k_nh+\sin(2k_nh)\right)} \end{aligned} \tag{24}$$

2.2 Added mass and damping coefficients for different paddle geometries

As shown in section 2.1 the added mass and damping are dependant on the wavemakers geometry. The following results show the added mass (m_{11}) and damping (R_{11}) for four different geometries. The standard piston and bottom hinged geometries that are widely used in many hydrodynamic laboratories around the world. Also included are coefficients for a hyperbolic paddle which matches the boundary condition of the wave velocity profile. This results in a wave maker with no evanescent modes, thus no local waves, at one particular wave frequency. The other is the unique case of a wavemaker with no progressive waves, just a local standing wave. These situations of no progressive waves and no evanescent waves are difficult to achieve in a physical wave flume but could be more easily achieved in a numerical model.

2.2.1 Piston Wavemaker

The unit displacement of a two-dimensional piston-type wave maker is $c(z) = 1$. Under oscillations corresponding to equation (1) this results in the entire boundary moving in unison, as would be expected. Following a the derivation outlined in section 2.1 the following added mass and damping were obtained in a similar manner.

$$m_{11} = 4\sum_{n=1}^{\infty}\frac{\rho\left(1-(\cos(k_nh))^2\right)}{{k_n}^2\left(2k_nh+\sin(2k_nh)\right)} \tag{25}$$

$$R_{11} = 4\,\frac{\omega\rho\left((\cosh(k_0h))^2-1\right)}{{k_0}^2\left(2k_0h+\sinh(2k_0h)\right)} \tag{26}$$

2.2.2 No local waves

For there to be no local or evanescent waves, there should be no added mass. This can be achieved if the paddle velocity matches that of the wave field. This is done by setting the unit displacement to

$$c(z) = \frac{\cosh(k_p(z+h))}{\cosh(k_ph)} \tag{27}$$

It should be noted that the wave number, k_p, is frequency dependant and therefore this wavemaker will have no added mass at only one chosen frequency - the frequency corresponding to the respective wavenumber value, $k_p = k(\omega_p)$. The resulting added mass and damping are

$$\begin{aligned} m_{11} = \sum_{n=1}^{\infty}\rho\,e^{-c}\Bigg(&\frac{\left(k_pe^c-k_pe^{b+c}-k_pe^b+k_p\right.}{\left(2k_nh-i\sinh(c)\right)\left(e^b+1\right)^2} \\ &\left.\frac{-ik_n+ik_ne^{b+c}-ie^bk_n+ik_ne^c)^2}{\left({k_p}^2+{k_n}^2\right)^2}\right) \end{aligned} \tag{28}$$

$$\begin{aligned} R_{11} = \omega\rho\Bigg(&\frac{\left(k_0e^{-i(b+ia)}-k_0+e^ak_0-k_0e^{-ib}\right.}{4\left(a+\sinh(a)\right)\left(\cos(b/2)\right)^2} \\ &\left.\frac{-e^{-ib}k_p+k_p+e^ak_p-k_pe^{-i(b+ia)})^2}{\left({k_p}^2-{k_0}^2\right)^2}\right)e^{i(b+ia)} \end{aligned} \tag{29}$$

where the substitution of $a = 2k_0h$, $b = 2ik_ph$ and $c = 2ik_nh$ have been. As mentioned, for there to be no evanescent waves, the added mass should be zero (at that specific frequency defining the shape $k_p(\omega)$ for $\omega = \pi, 2\pi, 3\pi$, which is the case (figs. 2a,2b,2c)

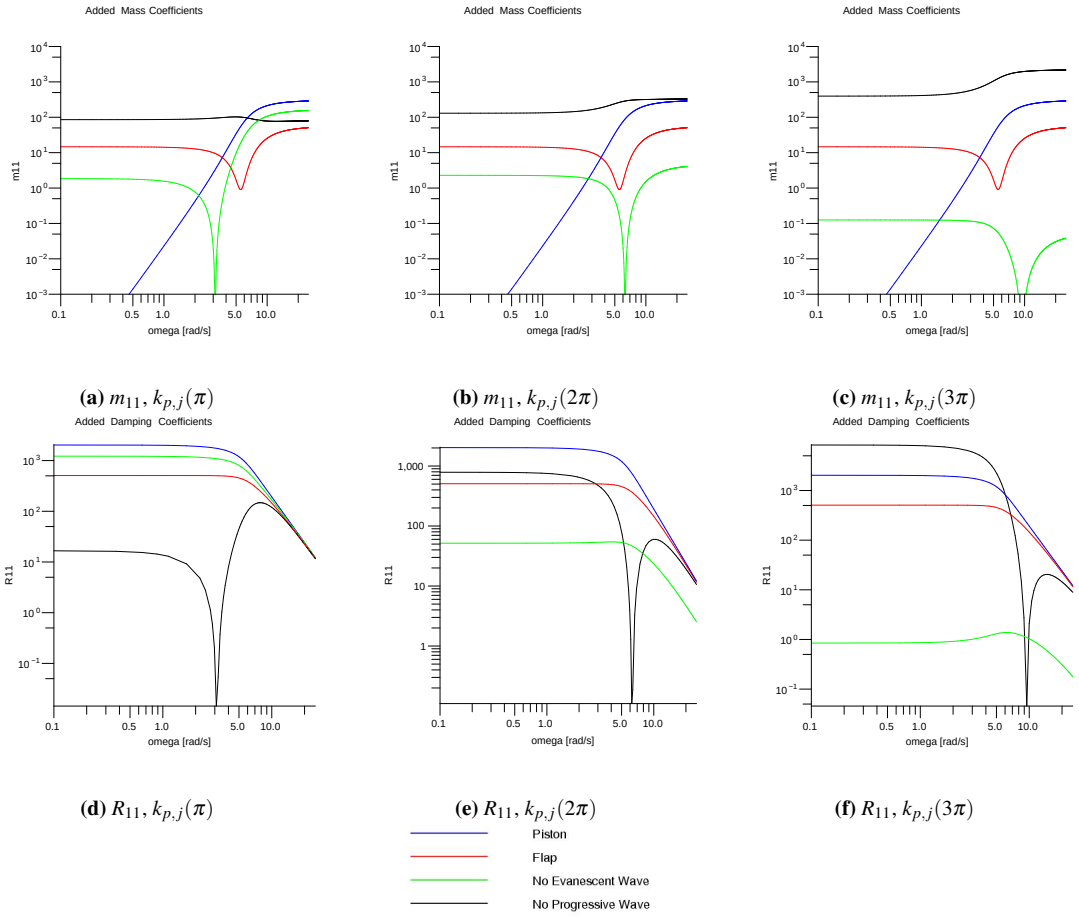

(a) $m_{11}, k_{p,j}(\pi)$ **(b)** $m_{11}, k_{p,j}(2\pi)$ **(c)** $m_{11}, k_{p,j}(3\pi)$

(d) $R_{11}, k_{p,j}(\pi)$ **(e)** $R_{11}, k_{p,j}(2\pi)$ **(f)** $R_{11}, k_{p,j}(3\pi)$

Figure 2: Hydrodynamic coefficients, added mass, top and damping, bottom, for piston, bottom hinged flap, no evanescent waves and no progressive wave wavemakers. The no evanescent and no progressive wavemakers are for three different geometries based on wave numbers $k(\omega_{p,j})$ for $\omega_{p,j} = \pi, 2\pi, 3\pi$

2.2.3 No progressive waves

This is another special case were the paddle will move in such a way that only an evanescent wave will be present. This would be very difficult to achieve in a physical wave maker, but could be more easily achieved in a numerical code. For this to occur, the wavemaker needs to move according to the following $c(z)$ in the case of $n = j$ where j is a single solution to equation (6)

$$c(z) = \frac{\cos(k_j(z+k))}{\cos(k_j h)} \tag{30}$$

Again, the the geometry is dependant on the selection of a wave number at a particular frequency, $k_j = k_j(\omega_j)$. This choice of $c(z)$ results in the upper and lower parts of the vertical wall oscillating out of phase with each other. The number of oscillations between the bottom of the tank and still water lever (SWL) depends on the choice of j. The resulting added mass and damping are given as

$$m_{11} = 4\rho \frac{(-k_j \sin(k_j h)\cos(k_n h)}{(2k_n h + \sin(2k_n h))(\cos(k_j h))^2} \frac{+k_n \cos(k_j h)\sin(k_n h))^2}{\left(-{k_j}^2 + {k_n}^2\right)^2} \tag{31}$$

$$R_{11} = \omega\rho \left(\frac{(-k_0 e^{a+b} + k_0 e^b - k_0 e^a + k_0 - ik_j}{4(a+\sinh(a))\left(\cosh\left(\frac{b}{2}\right)\right)^2} \frac{+ik_j e^b - ik_j e^a + ik_j e^{a+b})^2 e^{-a-b}}{\left({k_0}^2 + {k_j}^2\right)^2} \right) \tag{32}$$

where the substitution of $a = 2k_0 h$ and $b = 2ik_j h$ have been made.

For the three different geometries based upon choice of $k_j(\omega)$ for $\omega = \pi, 2\pi, 3\pi$ it can be seen (figs. 2d,2e,2f) that the damping is zero at these frequencies. For all of these solutions, $j = 1$ resulting in just one oscillation between the tank bottom and SWL increasing the value of j will, in turn, increase the number of oscillations between the SWL and the bottom of the flume.

The non-dimensionalised added mass and damping coefficients for all four shapes are shown in figure (2).

3 Basic Theory of Wave Absorption

3.1 Absorption efficiency

A concept used by Naito [16] and presented further by Spinneken [15] is that of absorption efficiency. Naito [16] presented an absorption coefficient, $C_e(\omega)$ measuring the power absorbed by the external mechanism. The condition of causality was discussed and a power absorp-

tion with fixed coefficients C_{ec} was also presented. This resulted in less than all of the available power being absorbed in irregular waves as the system was only optimised for one frequency.

According to Falnes [17] the intrinsic impedance, Z_i can be represented as

$$Z_i(\omega) = R(\omega) + i\left(\omega\left[M + m(\omega)\right] - \frac{c}{\omega}\right) \tag{33}$$

Where M is the mass of the paddle, c is the spring stiffness, $m(\omega)$ and $R(\omega)$ are added mass and damping, respectively, and where the subscripts for surge have been omitted

Following the same author and many others, the optimum control force occurs when the control impdance, Z_u equals the complex conjugate of the intrinsic impedance

$$Z_u(\omega) = Z_i^*(\omega) = Z_{u,OPT}(\omega) \tag{34}$$

Thus,

$$Z_{u,OPT}(\omega) = R(\omega) - i\left(\omega\left[M + m(\omega)\right] - \frac{c}{\omega}\right) \tag{35}$$

and under a fixed coefficient system tuned to $\omega = \omega_p$,

$$Z_{u,OPT}(\omega_p) = R(\omega_p) - \left(i\left[\omega_p\left(M + m(\omega_p)\right) - \frac{c}{\omega_p}\right]\right) \tag{36}$$

$$= R_p - \left(i\left[\omega_p\left(M + m_p\right) - \frac{c}{\omega_p}\right]\right) \tag{37}$$

where R_p and m_p denotes fixed coefficients at $\omega = \omega_p$

Under a two coefficient (r_u and c_u) control system, the control force in the time domain is represented as

$$f_u(t) = r_u u(t) + c_u x(t) \tag{38}$$

and thus the impedance in the frequency domain is

$$Z_u(\omega) = r_u + \frac{c_u}{i\omega} \tag{39}$$

and optimising equation (39) at a single frequency, ω_p, results in

$$Z_u(\omega_p) = r_u - \frac{ic_u}{\omega_p} \tag{40}$$

Price [18] compared equations (36) and (40) showing control coefficients of

$$r_u = R_p \tag{41}$$

$$c_u = \left(\omega_p^2(M + m_p) - c\right) \tag{42}$$

replacing back into equation (39), [18] presented the tuned control impedance at ω_p, with two control settings, over the full range of frequencies as

$$Z_u(\omega) = R_p - \frac{i}{\omega}\left[\omega_p^2\left(M + m_p\right) - c\right] \tag{43}$$

Falnes [17] shows that the absorbed useful power is given as

$$P_u = \frac{1}{2}\Re\left[Z_u(\omega)\right]\frac{|\hat{F_{e,j}}|^2}{|Z_i(\omega) + Z_u(\omega)|^2}$$

$$= \frac{R_u(\omega)|\hat{F_{e,j}}|^2/2}{\left[R_i(\omega) + R_u(\omega)\right]^2 + \left[X_i(\omega) + X_u(\omega)\right]^2} \tag{44}$$

Setting the control impedance, $Z_u(\omega)$ to the complex conjugate of the intrinsic impedance Z_i^*, namely setting the variables $R_u(\omega)$ and $X_u(\omega)$ to their optimum values of $R_i(\omega)$ and $-X_i(\omega)$ gives an expression for the maximum power

$$P_{u,max} = \frac{|\hat{F}_{e,j}|^2}{8R_i} \tag{45}$$

Combining these equations (eqns 44,45), the absorption coefficient, similar to that of Naito [16] and Spinneken [15], for a fixed coefficient system can be shown as

$$\frac{P_u}{P_{u,max}} = 4\frac{R_u(\omega)R_i(\omega)}{\left(R_i(\omega) + R_u(\omega)\right)^2 + \left(X_i(\omega) + X_u(\omega)\right)^2} \tag{46}$$

Using equations (33,36) the power absorption ratio can be represented as

$$\frac{4\omega^2 R_p R(\omega)}{\omega^2\left[R_p + R(\omega)\right]^2 + \left[(\omega^2 - \omega_p^2)M + \omega m(\omega) - \omega_p^2 m_p\right]^2} \tag{47}$$

3.2 Absorption for different wavemakers

Absorption ratios, $P_u/P_{u,max}$, for different wavemaker shapes (Piston, Bottom hinged Paddle, No Evanescent waves, No Progressive Waves) are shown in figure (3). These figures compare the fraction of waves that can be theoretically absorbed equation (46) by the four different wave makers with different choices of tuning frequency and shape frequency. For the piston and paddle shaped wavemakers, the only handle on control is by setting the tuning frequency ω_p. For the other two types of wave maker - their shape parameter $c(z)$, is a function of wave number and thus frequency dependant. For these wavemakers a second control variable, k_j and k_p is available. Both of these control handles are varied from 0.5 Hz and 1.5 Hz. This range of frequencies is comparable to that of the tank used at Edinburgh University, and most tanks used in small scale hydrodynamic laboratories.

The absorption characteristics for piston and flap wavemakers only varies due to a change in tuning frequency, ω_p. When the shape function is set to $k_{p,j}(\omega) = k_{p,j}(\pi)$ the bottom hinged paddle attains the highest absorption, followed by the hyperbolic paddle with $k_p = k(\pi)$ (eqn.27) and then piston wave maker. The reason for this is setting the shape parameter to $k_{p,j}(\omega) = k_{p,j}(\pi)$, results in a hyperbolic shape in between that of a piston and a flap, thus explaining why the absorption characteristics are in between that of the paddle and flap.

Outwith $k_p(\omega) = k_p(\pi)$,the hyperbolic shaped paddle, with no evanescent waves (eqn.27), has better absorption characteristics than all other paddles regardless of their tuning frequency. This is unsurprising as the hyperbolic profile matches that of the Airy's velocity potential more closely than that of the either the piston or the flap. The big difference is that the hyperbolic shaped paddle has two handles of control. That of the tuning frequency, ω_p similar to the flap and piston, but it also has

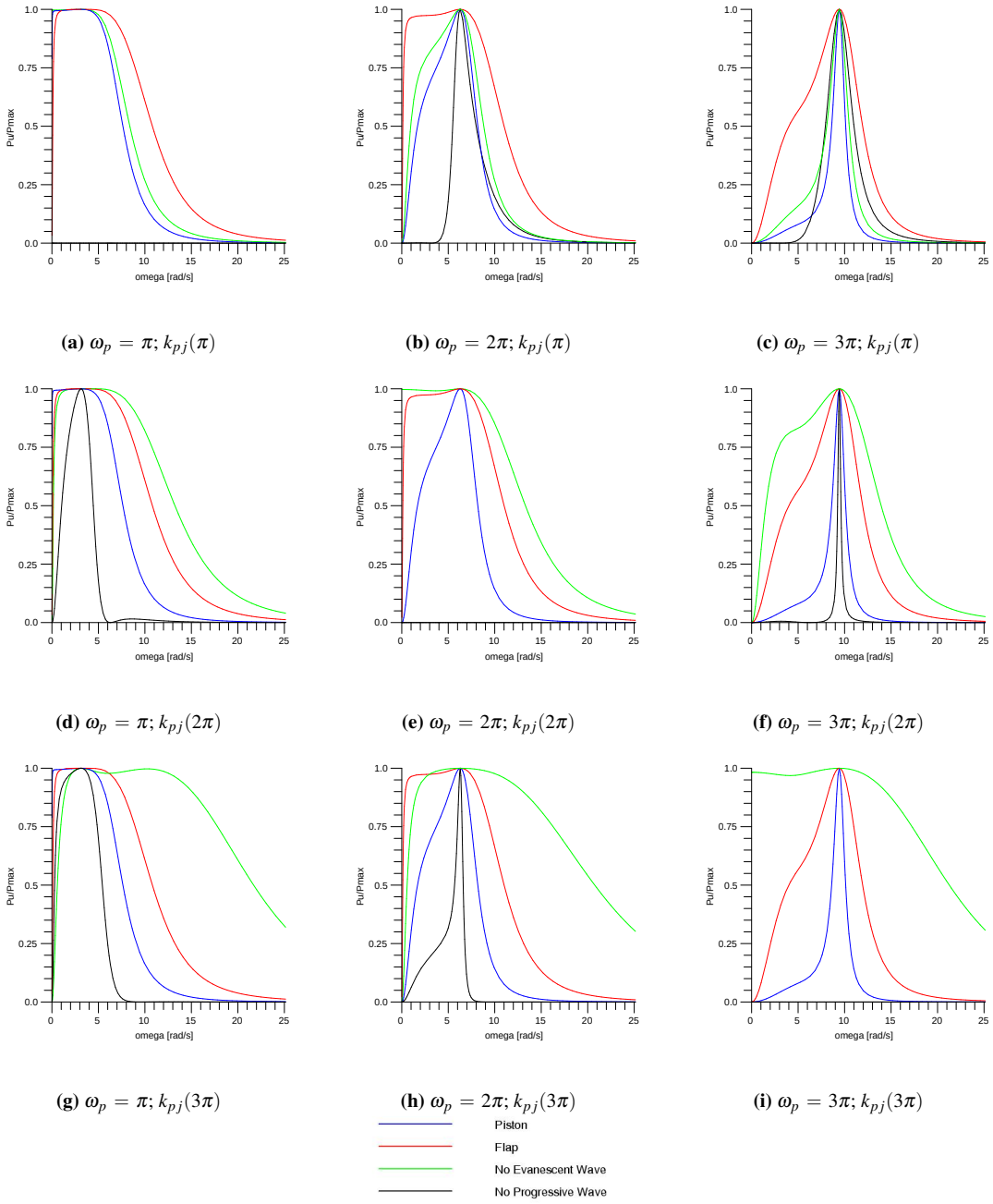

(a) $\omega_p = \pi; k_{pj}(\pi)$ **(b)** $\omega_p = 2\pi; k_{pj}(\pi)$ **(c)** $\omega_p = 3\pi; k_{pj}(\pi)$

(d) $\omega_p = \pi; k_{pj}(2\pi)$ **(e)** $\omega_p = 2\pi; k_{pj}(2\pi)$ **(f)** $\omega_p = 3\pi; k_{pj}(2\pi)$

(g) $\omega_p = \pi; k_{pj}(3\pi)$ **(h)** $\omega_p = 2\pi; k_{pj}(3\pi)$ **(i)** $\omega_p = 3\pi; k_{pj}(3\pi)$

Figure 3: Graphs showing the absorption coefficients ϑ for different tuning frequencies, $\omega_p = \pi,\ 2\pi,\ 3\pi$ (columns) and different geometry shapes $k_{p,j}(\omega)$ for $\omega = \pi,\ 2\pi,\ 3\pi$ (rows)

a geometry control where the shape of the paddle can be designed to minimise the evanescent waves at one specific frequency, thus resulting in two sweet spots of control at ω_p and $k(\omega_p)$. Having these two handles of control, tuning frequency and shape can result in a far wider bandwith of absorption that would otherwise be achieved using either a regular piston or flap wave maker (fig.3).

One of the interesting results occurs for the case where the paddle is controlled in such a manner to have no progressive waves. As can be seen, this paddle can achieve some absorption when $k_j \neq \omega_p$. When the geometry shape, $k_j(\omega)$ is chosen such that $\omega = \omega_j$, as is the case in the diagonal of the $3x3$ matrix in figure (3). Under these conditions the absorption of the *no progressive wave* paddle results in zero absorption. The reasons for this can be attributed to the old addage, *"a good wave absorber is a good wave maker "*. As this wavemaker cannot generate any progressive waves at this frequency, it cannot radiate waves to cause destructive interference, cancelling out the reflected waves thus there is zero wave absorption.

4 CFD simulation of wavemaker

This section describes the methods used to generate waves in a numerical wave tank using ANSYS CFX.

The dimensional values for the geometry of the numerical wave tank (NWT) were chosen such to be comparable to those in Edinburgh's long tank. The length of

Table 1: Dimensions of grids used

	Coarse	Medium	Fine
No. elements Y1	10	20	40
ΔY [m]	0.02	0.01	0.005
No. elements Y2	20	40	40
No. elements X	390	780	1560
ΔX [m]	0.04	0.02	0.01
No. Nodes	38,318	157,762	377,762
No. Elements	18,720	78,000	187,200

the tank is $l = 15.6[m]$ with a water depth of $h = 0.8[m]$. The desired wave has a period of 1 $[s]$ and wave of amplitude 0.08 $[m]$. According to the wave dispersion relationship

$$\lambda = \frac{g}{2\pi} T^2 tanh \frac{2\pi h}{\lambda} \tag{48}$$

the wave length of such a wave is $\approx 1.56[m]$ with $d/\lambda = 0.514$ (deep water conditions). This results in the tank being ten wavelengths long. The phase speed, $c = \frac{\lambda}{T}$, of these waves is $1.56[m/s]$, and the group velocity $c_g = \frac{1}{2}c = 0.78[m/s]$.

Three different grids were used to compare the effects of refinement and to check for convergence, referred to as coarse, medium and fine. The cell dimensions for the initial coarse mesh were based upon the expected free surface elevation and on the phase speed of the wave. The remaining two meshs' dimensions were iterative refinements of the coarse mesh. As the main area of interest is the wave's free surface, extra mesh refinement is used in this region. This area of refinement extended from $\pm 0.1[m]$ around the SWL. The mesh distribution in this area was uniform, the areas above and below this region, extending to the NWT bottom and top opening, have a stretched geometric distribution along a distance of $0.7[m]$ (fig.4). Mesh dimensions for the three different meshes are as follows; For all grids, the domain is split into two regions, one with a distance of a single wavelength, λ from the paddle. This region allows mesh motion. The other region, making up the rest of the mesh is stationary (fig.4). This is was chosen after advice and correspondence with CFX support. It was said that mesh motion, by its very nature is a diffusive process and will lead to unsatisfactory results. Mesh motion is needed in the region near the paddle to facilitate the piston motion. CFX does not have an explicit two-dimensional solver, so When modeling two dimensional simulations it is recommended that the domain is set to one cell thick and symmetry conditions placed on either side. The modelling advice suggests that the thickness of this cell should be comparable to the size of the smallest cell.

The physics for the simulation were held constant. Homogeneous multiphase, with second-order transient and coupled volume-fraction solution were used in the solver control. The only parameter to vary over the three simulation runs was the time step. This was to ensure that the CFL remained constant. In adherence to recommendations by CFX support, the CFL number was

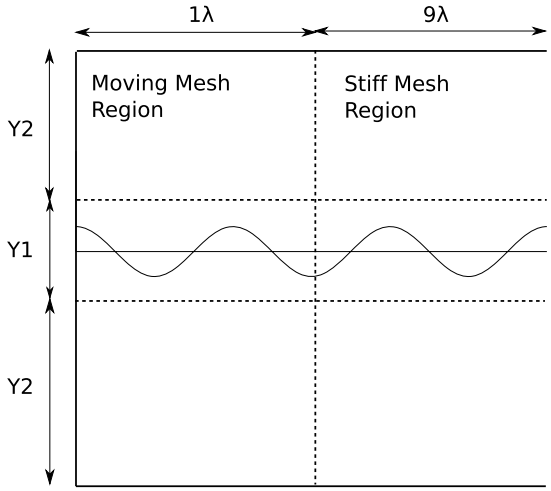

Figure 4: Grid layout corresponding to table 1

Table 2: CFL number

	Coarse	Medium	Fine
Δ t [s]	0.04	0.02	0.01
CFL	1.56	1.56	1.56

maintained between 1-2.

$$CFL = \frac{\Delta t u}{\Delta x} \tag{49}$$

The paddle motion was ramped up over two seconds, as such, the fully developed wave train should have travelled the length of the flume at the group speed, c_g of $0.78[m/s]$ thus taking no less than $22[s]$. This was one of the criteria examined when looking for the suitability of CFX in handling free surface waves. Isosurface plots with the volume fraction = 0.5 at every 1 second time interval are shown in figure (5). It shows how the waves travel down the flume for the three grids. The vertical dotted line is placed at intervals of 1λ $(1.56[m])$.

4.1 Wave making results in CFX

Upon implementation of the aforementioned settings, the coarse mesh (fig. 5a) showed large damping of the progressive waves in the flume. The wave height decreased considerably and this decrease persisted over time. Also, there seemed to be an unexpected increase in the wave length of the generated waves. A wave of period $T = 1[s]$ was expected and under the water depth conditions, a wave length of $1.56[m]$ was anticipated. As can be seen, (fig. 5a) shows the wave crest getting progressively further apart.

The medium mesh (fig. 5b) doesn't show as severe damping of the free surface elevation as the coarse mesh, but there is still some damping persistant. Again, the waves generated seem to be of a longer wave length than expected. This can be seen looking at the distance the wave crest deviated from the vertical lines. These lines are at one wave length $\lambda = 1.56[m]$ intervals.

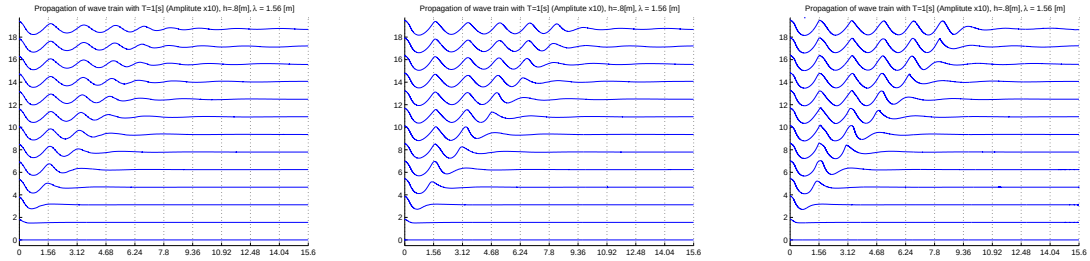

(a) Coarse mesh **(b)** Medium mesh **(c)** Fine mesh

Figure 5: Wave train propagation over time for coarse, medium and fine mesh

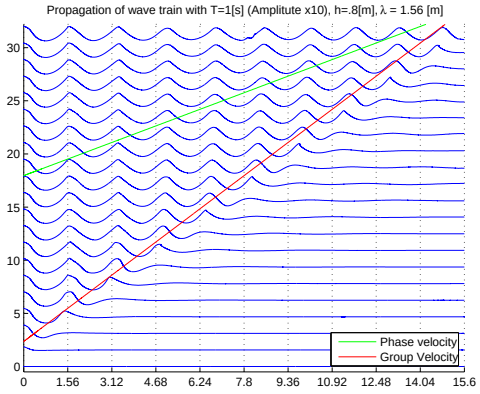

Figure 6: Wave propagation through flume with fine mesh over 20s, with time increasing in the Y+ axis direction. Lines showing both group velocity and phase velocity also shown

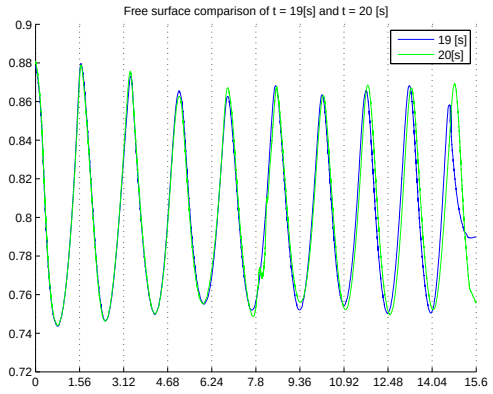

Figure 7: Free surface from fine mesh at 19 [s] and 20 [s]. NB the shift in wave peak from time step 19[s] to 20[s] and also the fact that each peak is no aligned with the predicted wave length position

The last refinement was that of the fine mesh (fig. 5c). This shows a little improvement in capturing the free surface elevation when compared to the medium mesh. Overall, the fine mesh is very similar to the medium mesh results. This suggests that CFX is converging, but not on the expected answer. Upon closer analysis of the free surface from the fine mesh, the damping of the waves is more apparent (fig. 7). The expected wave amplitude of $0.08[m]$ does not materialise. There is a steady decline in wave amplitude which plateaus at 4 wavelengths. There seems to be a shift in wavelength also in these simulations. The wave flume expected to have exactly 10 fully developed waves after 20 [s] this was not the case and there were only 9.5 full waves in the flume.

In order to absorb waves, you must first be able to make accurate and precise waves. This did not prove to be the case in ANSYS CFX. There was persistant damping in the flume and an anomaly where there seemed to be a shift in frequencies that resulted in longer wavelengths in the flume.

Current work includes investigation into other commercial CFD codes and feasibility studies are underway.

5 Conclusions

In conclusion, this paper has presented the fundamental theory behind the wavemaking process. It has presented the hydrodynamic coefficients of added mass and damping for four different paddle shapes. Two of these novel shaped wavemakers have been discussed how the choice of geometry can effect the wave absorption especially in conjunction with tuning frequency. It has shown the there is potential for improved absorption when the both the geometry and the tuning frequency of a wavemaker/absorber can be adjusted. Results from a solid moving boundary in ANSYS CFX were presented and the CFD simulations do not match the expected results.

Acknowledgements

The authors wish to acknowledge funding for this project from the UK Engineering and Physical Sciences Research Council (EPSRC) as part of the Doctoral Training Programme of Phase 2 of SuperGEN MARINE (EP/E040136/1).

Dr Ingram acknowledges the support from Scottish Funding Council of his position within the the Joint Research Institute in Energy with the Heriot-Watt University which is a part of the Edinburgh Research Partnership in Engineering and Mathematics (ERPem).

Comments from A.Price and M.Captieux are greatly appreciated.

References

[1] T. H. Havelock. Forced surface-waves on water. *Philosophical Magazine*, 3:569–576, October 1929.

[2] F. Biésel and F. Suquet. Les appareils generateurs de houle en laboratorie. *La Houille Blanche*, 6, 1951.

[3] F. Biésel and F. Suquet. Laboratory wave generationg apparatus. *St. Antony Falls Hudraulic Report*, (39), March 1954. Translation from La Houille Blance.

[4] F. Ursell, R.G. Dean, and Y.S. Yu. Forced small amplitude water waves: a comparison of theory and experiment. *Journal of Fluid Mechanics*, 7:33–52, 1960.

[5] R. Hudspeth, J. W. Leonard, and M.-C. Chen. Design curves for hinged wavemakers. In *Proceedings of ASCE, Hydraulics Division*, volume 107, pages 553–574, May 1981.

[6] G. Gilbert, D.M. Thompson, and A.J. Brewer. Design curves for regular and random wave generators. *Journal of Hydraulic Research*, 1970.

[7] J. H. Milgram. Active water-waver absorbers. *Journal of Fluid Mechanics*, 43:845–859, 1970.

[8] S. H. Salter. Absorbing wavemakers and wide tanks. In *Proc. Directional Wave Spectra Applications*, pages 182–202. Berkley, California, 1981.

[9] I. Orlansky. A simple boundary condidtion for unbounded hyperbolic flows. *Journal of Computational Physics*, 21:251–269, 1976.

[10] J. E. Romate. Absorbing boundary conditions for free surface waves. *Journal of Computational Physics*, 99:135–145, 1992.

[11] C. Maisondieu and A. Clement. A realizable force feedback-feedforward control loop for a piston wave absorber. In *Eight international workshop on waver waves adn floating devices*, volume 1, pages 79–82, 1993.

[12] A. Clément and C. Maisondieu. Comparison of time domain control laws for a piston wave absorber. In *Proc. European Wave Energy Symposium*, pages 117–122, 1993.

[13] G. Chatry and A. Clément. Self-adaptive control of a pisoton wave absorber. In *Proc. of 8th Int. Offshore Polar Engineering Conference*, volume 1, pages 127–133, 1998.

[14] J. N. Newman. Analysis of wave generators and absorbers in basins. *Submitted for publication - http://www.wamit.com/publications.htm*, 2008.

[15] J. Spinneken and C. Swan. Wave generation and absorption using force-controlled wave machines. In *Proceedings ISOPE, Osaka*, 2009.

[16] S. Naito. Wave generation and absorption in wave basins: Theory and application. *International Journal of Offshore and Polar Engineers*, 16(2):81–89, 2006.

[17] J. Falnes. *Ocean Waves and Oscillation Systems*. Cambridge University Press, 2002.

[18] A. A. E. Price. *New Persipectives on Wave Energy Converter Control*. PhD thesis, The University of Edinburgh, 2009.

B.2 Coastlab, 2010

Maguire, A.E., and D.M. Ingram. Wavemaking in a commercial CFD code. In Proceedings on the Third International Conference of the Application of Physical Modelling to Port and Coastal Protection, 2010.

WAVEMAKING IN A COMMERCIAL CFD CODE

A.E. MAGUIRE (1), D.M. INGRAM (2)
(1) *Institute for Energy Systems, School of Engineering, The University of Edinburgh, The King's Buildings, Edinburgh, EH9 3JK, UK (E.Maguire@ed.ac.uk)*

(2) Institute for Energy Systems, School of Engineering, The University of Edinburgh, The King's Buildings, Edinburgh, EH9 3JK, UK (David.Ingram@ed.ac.uk)

For most of the twentieth century, marine hydrodynamics has been limited to the two realms of theory and physical experiments. These methods of fluid flow analysis are limited through scope, cost and size of facility. The advent of high speed computing has brought with it a new dimension for analyzing fluid flows, that of numerical modelling. Computational Fluid Dynamics (CFD) has the potential to offer an invaluable design tool to marine engineers. One such tool that CFD offers, is the possibility for a numerical wave tank. Physical wave tanks are used in coastal engineering, naval engineering, offshore engineering and marine renewable engineering, but these facilities can be expensive and are limited in size and scale of the testing facility. A numerical wave tank can overcome these problems. But before any confidence can be placed in numerical results from a CFD code, a verification process should be conducted to assess both the coding and the mathematical calculations and the results should also be validated against a physical model or a known analytical solution. In this paper a commercial CFD code (ANSYS CFX) is assessed and verified for its suitability as a numerical wave tank. Both a temporal and spatial convergence study is conducted and the appropriate metrics analyzed. A validation procedure is implemented, comparing the obtained numerical solution to a known analytic solution using linear wave theory.

Keywords: wavemaker; CFD; ANSYS CFX; Verification.

1. Introduction

The methods used for the wave making process in the numerical code are analogous to those used in many hydrodynamic laboratories around the world. An oscillating wall boundary condition was used to generate a propagating wave through the test domain. This solid boundary is moved according to a prescribed displacement according to well known first order wavemaker theory (Havelock 1929, Dean and Dalrymple 1991, Hughes 1993, Maguire and Ingram 2011). The resulting free surface displacement is then used to perform a formal verification of the CFD simulations for both temporal and spatial discritizations (Roache, 1998). The wave parameters chosen for this were based upon typical values used for a hydrodynamic wave flume. The wave parameters chosen were a waveheight (H) of 0.08[m], Period (T) 1 [s] in a water depth (h) of 0.90 [m].

The numerical flume is chosen to be similar in dimension and scope to the physical wave flume at the University of Edinburgh and indeed many other hydrodynamic laboratories. The water depth of the flume was set to 0.75cm and the period of oscillation of the wavemaker set to 1s. According to the dispersion relationship the wavelength can be obtained as

$$\lambda = \frac{g}{2\pi} T^2 \tanh \frac{2\pi h}{\lambda}, \qquad [1]$$

resulting in a wavelength ≈ 1.56m. Assuming deep-water conditions, the phase speed of the waves, c, is given by λ/T = 1.56m/s and the group velocity, $c_g = c/2 = 0.78$ m/s. The overall length of the wavetank was chosen as 15.6m, equating to a non-dimensional tank length of 10λ.

The height of the waves down the flume is dependant upon the stroke amplitude of the wavemaker. Dean and Dalrymple (1991) present the stroke displacement to far-field wave heights for different types of wavemakers. For the verification procedure a wave height of H = 8cm was chosen, typical for a flume of these dimensions. It should be noted that a wave height of 8cm results in waves that operate in the stokes second-order regime. This does break some of the underlying assumptions of linear waves, upon which the stroke displacement to wave height ratio was based, but linear theory is robust and is still used in physical wavemakers with certain caveats applied. Regardless of the physics of the problem being solved, these results can be analysed for verification of descretisation errors.

2. CFX

ANSYS CFX. This is an implicit, coupled, finite volume based solver using the volume of fluid scheme for multiphase flow. The transient solver was used, as the problem being modelled is inherently transient. Other solver options implemented were homogeneous multiphase, with second-order transient solver and coupled volume-fraction.

The flow was initialised with all velocity components set to zero. The pressure field in the water was set according to the hydrostatic pressure field and uniform in the air. The volume fractions of the water and air were implemented using a step function in CFX expression language. The volume fraction below the SWL was set to 1, water, and the volume fraction above the SWL set to 0, air. The total time for the transient run was set as 18s. This was chosen to give an appropriate amount of time to analyse the progression of the waves and in order to keep CPU time down.

3. Mesh Generation

All meshes for CFX were generated using ICEM, a bespoke meshing programme for ANSYS software. Overall the mesh is ten wavelengths long in the x-direction and two water depths, h, in the y-direction and this mesh is extruded one cell thick as this is a requirement by the CFX solver. There is a region of refinement around the free-surface. An overview of the coarse mesh is shown in figure 1.

The mesh consists of three distinct regions. The closest to the wavemaker is a region one wavelength long, where mesh motion is permitted. This is required in order to implement an oscillating solid boundary to replicate a physical wavemaker. Next is a region four wavelengths long, exactly the same as the first region only mesh motion is disabled. This is because the mesh motion is inherently dissipative and could lead to unwanted damping of the progressive waves. The third region is where the node spacing in the x-direction is successively stretched up to a point where the spacing, Δx is larger than at least half a wavelength. This is to act as a numerical dissipation zone where any waves will be progressively damped out and thus avoid any unwanted wave reflections from the far boundary wall. In this region the growth ratio of the cells was ≤ 1.10 as excessively aggressive stretching could lead to numeric reflections. This resulted in a de-facto wave flume of five wavelengths long with a five wavelength damping zone.

The region around the still water level (SWL) has uniform node spacing in Δy. This region extends ± 0.05m from the SWL to ensure that the expected wave height of 0.08m would be encompassed in this region. Both above and below this uniform region in the y-direction a geometric stretching of nodes was enforced. The region of air above the water is of little interest in this study and due to the exponential decay of the water partials such dense grid refinement was not necessary at the bottom of the flume. This allowed for a mesh with a smaller node count and allowing for quicker solving times.

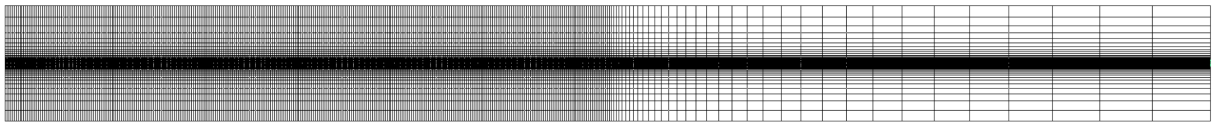

Figure 1. View of the entire wave flume domain for the coarse mesh. The grid stretching towards of the end of the domain is clearly visible as is the region of mesh refinement around the still water level (SWL)

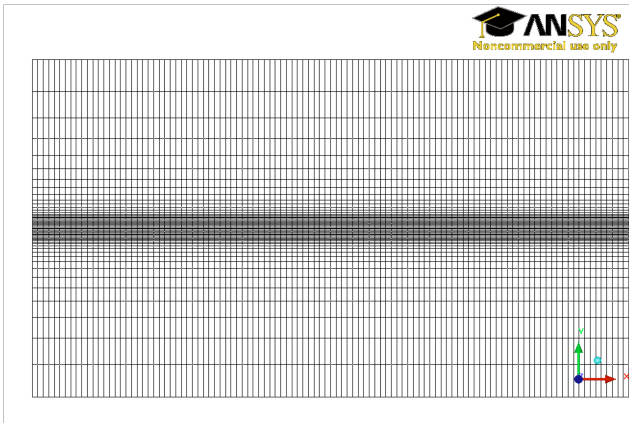

Figure 2. Close up of the motion enabled region of the mesh, showing the uniform Δy spacing around the SWL and the spacing growth towards the top and bottom of the numerical wave flume.

4. Boundary Conditions

The boundary conditions imposed in this problem were; symmetrical boundary conditions implemented on both near and far vertical faces of the flume, (with reference to figure 1). No-slip wall conditions were imposed for both the far wall (x = 15.6m) and for the bottom of the wave flume. The wavemaker was represented using an oscillating wall boundary condition. The wall velocity was relative to the prescribed mesh motion. The mesh motion was achieved through a specified displacement in the x-direction, implemented via CFX expression language. The displacement was sinusoidal where the amplitude was set by Eq (1) for a piston wavemaker,

$$\frac{H}{x_0} = 4\frac{(\cosh(kh))^2 - 1}{2kh + \sinh(2kh)} \qquad [2]$$

and this amplitude was ramped up over 2s. The upper region of the mesh was set as an opening boundary, with entrainment option set for the mass and momentum option. The upper boundary next to the wavemaker was set as a non-slip wall however. This is the boundary next to the moving paddle and CFX suggests that all open boundaries should be orthogonal to a moving mesh. In the case of a bottom-hinged flap, this would not be true so this boundary was specified as a wall and not an opening.
The total time for the simulations was selected as 18s. This was chosen to allow for the ramp up period of 2s, the waves to progress to the end of the five λ tank (cg = λ/2T thus this equals 10s.) and then for a wave crest to travel the length of the flume (at the wave phase speed), which takes 5s, and an arbitrary extra second.

5. Temporal discretisation

A temporal discretisation study was performed to analyse the effect that time step selection had on the results. The objective of this study was to ensure the selection of an appropriate time step that yielded accurate results in the quickest time.
If the time step chosen was too large, the CFX solver would perform too many inner loop calculations. This is where the solver iterates through the solution at one single time step in order to achieve convergence of the residuals. Throughout the calculations the inner loop limit was set to ten iterations, thus too high a time step and the solver would reach this limit and move onto the next time step without achieve residual convergence resulting in both suboptimal results due to lack of convergence and increased CPU solving times due to too many inner loop calculations. If the time step was too small, the inner loop iterations would invariably only perform one iteration and move to the next time step, but there would now be an excessive amount of time step calculations and the computation time would be unnecessarily large.
The time step was chosen with the Courant Friedrichs Lewy (CFL) condition in mind. This number is used as a metric for explicit CFD solvers to analyse the stability of the calculations. While CFX is a fully implicit solver, and the CFL condition is a limiting factor for explicit schemes, choosing the time step based upon the CFL still has it's merits. It was advised to keep the calculated CFL number as low as possible, but not lower than one (ANSYS, 2008). For a two dimensional case the courant number can be calculated as

$$\frac{U_x \Delta t}{\Delta x} + \frac{U_y \Delta t}{\Delta y} = \nu, \qquad [3]$$

where, υ is the CFL number, u_x is the maximum velocity that information travels in the x-direction, u_y is the maximum particle velocity in the y-direction Δt is the time step and Δx and Δy are the grid spacing's in x-direction and y-direction respectively. Generally, when choosing the values of u_x and u_y the maximum values of velocity are used. Care needs to be taken with deep-water waves as the phase velocity of the wave train is twice as fast as the group velocity and as a result u_x needs to be set to the phase velocity of the waves.
When investigating the temporal discretisation four different time steps were selected and analysed on the coarse and medium meshes. The relative CFL numbers used were 4.4, 2.2, 1.1 and 0.55. The corresponding time steps for these CFL numbers on the different meshes can be seen in Table 1.1. The results from a temporal convergence study can be analysed in a very similar manner to a spatial grid convergence study (Roache, 1998) and the corresponding convergence metrics can be seen in tables 1 and 2.
Table 1 shows that good temporal convergence is achieved using either a CFL number of either 2.2 or 1.1. Qualitatively this convergence can be seen in figure 2. Table 2 uses a time step to maintain a CFL number of 2.2, 1.1 and 0.55. It can be seen that there is oscillatory convergence with using a CFL of 0.55. This suggests that this time step is too small and quicker results could be obtained using a larger time step. This is in keeping with advice from ANSYS support.

Table 1: Convergence indices for the temporal convergence study on the medium mesh wave heights using CFL numbers of 4.4, 2.2 and 1.1 . The indices are given for four waves, numbered one to four, based upon the zero down crossing of the wave. Subscript index of 3 represents the coarsest relative time step and 1 the finest.

	1	2	3	4
f_3	0.074	0.070	0.068	0.066
f_2	0.077	0.073	0.074	0.071
f_1	0.078	0.073	0.074	0.072
ε_{32}	-0.003	-0.003	-0.005	-0.005
ε_{21}	-0.001	0.000	-0.001	0.000
p	2.458	3.000	3.363	3.818
f_{ext}^{21}	0.078	0.073	0.074	0.072
e_a^{21}	0.71%	0.54%	0.70%	0.54%
e_{ext}^{21}	0.16%	0.08%	0.07%	0.04%
GCI_{fine}^{21}	0.2%	0.10%	0.09%	0.05%

Table 2: Convergence indices for the temporal convergence study on the medium mesh wave heights using CFL numbers of 2.2, 1.1 and 0.55 . The metrics are given for four waves, numbered one to four, based upon the zero down crossing of the wave. Subscript index of 3 represents the coarsest relative time step and 1 the finest.

	1	2	3	4
f_3	0.077	0.073	0.074	0.071
f_2	0.078	0.073	0.074	0.072
f_1	0.077	0.074	0.073	0.074
ε_{32}	-0.001	0.000	-0.001	-0.000
ε_{21}	0.001	-0.001	0.001	-0.002
p	0.689	1.405	1.1335	2.513
f_{ext}^{21}	0.075	0.075	0.072	0.074
e_a^{21}	1.16%	1.42%	1.79%	3.00%
e_{ext}^{21}	1.92%	0.85%	1.19%	0.63%
GCI_{fine}^{21}	2.36%	1.08%	1.47%	0.80%

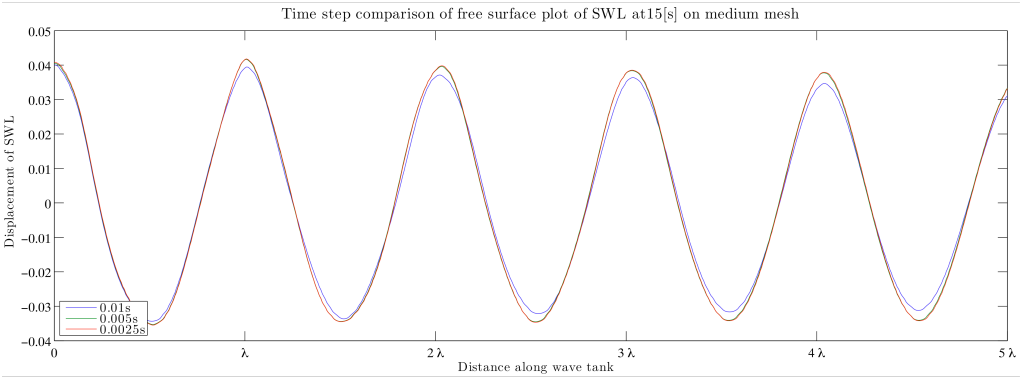

Figure 3. Free surface plot on the medium mesh showing good convergence with time step of 0.005s (CFL=2.2) and 0.0025 (CFL=1.1)

4. Grid convergence index

It is paramount that all CFD process to quantify the errors introduced through discretisation error. The methodology proprosed by Roache (1998) and subsequently adopted by NASA (NPARC, 2010) and the Journal of Fluids Engineering (Celik et al., 2008) will be followed herein.
In order to extract the observed order of convergence, at least three different grids with constant refinement ratios are needed. For this verification study, three different scaled meshes were used; coarse, medium and fine. The coarse mesh has twice the node spacing in both Δx and Δy compared to the medium mesh, similarly, the medium mesh has twice the node spacing in both Δx and Δy compared to the fine mesh.

The absolute values for medium mesh were chosen based upon a preliminary study that suggested that the results were sensitive to the spacing in Δx. However, as the domain being modelled had an aspect ratio of $\approx 1:15$ extra refinement to Δx will become computationally expensive using a structured grid. A pragmatic choice of 128nodes/λ and 32nodes/H was decided upon for the medium mesh. This specification of node spacing in the y-direction is applicable in the region of refinement around the SWL, as mentioned, the node spacing is grown away form this uniform region.

Table 3: Grid refinement mesh spacing

	Coarse	Medium	Fine
cells / λ	64	128	256
cells / H	16	32	64
Node Count	37842	142170	552178

Table 3 lists the relative spacing for each of the three grids used. The reason that the total node count between the three meshes does not increase by exactly a factor of four is due to the dissipation region. In this region, as opposed to doubling the number of nodes in the x-direction for each successive grid, a constant growth ratio was sought. This means that the relative increase in node count going from the coarse to the medium and the medium to the fine meshes did not result in an exact doubling of nodes. In the region 5λ away from the wavemaker (i.e. non-stretched grid), the one-directional scaling is exactly a factor of two different and a factor of 4 in the two-dimensional node count.

Table 4 shows that the observed order of convergence is what would be expected for a second-order scheme and satisfactory convergence is observed and the uncertainty is quantified as being between 1-4%.

Table 4: Grid convergence indices for the wave height using a constant CFL number equating to 2.2. The indices are given for four waves, numbered one to four, based upon the zero down crossing of the wave. Subscript index of 3 represents the coarsest relative mesh and 1 the finest.

	1	2	3	4
f_3	0.071	0.067	0.064	0.059
f_2	0.077	0.073	0.074	0.071
f_1	0.079	0.076	0.076	0.076
ε_{32}	-0.006	-0.006	-0.010	-0.012
ε_{21}	-0.002	-0.003	-0.003	-0.004
p	1.753	1.045	1.878	1.483
f_{ext}^{21}	0.080	0.079	0.077	0.078
e_a^{21}	2.19%	3.86%	3.57%	5.91%
e_{ext}^{21}	0.91%	3.50%	1.32%	3.19%
GCI_{fine}^{21}	1.15%	4.54%	1.67%	4.11%

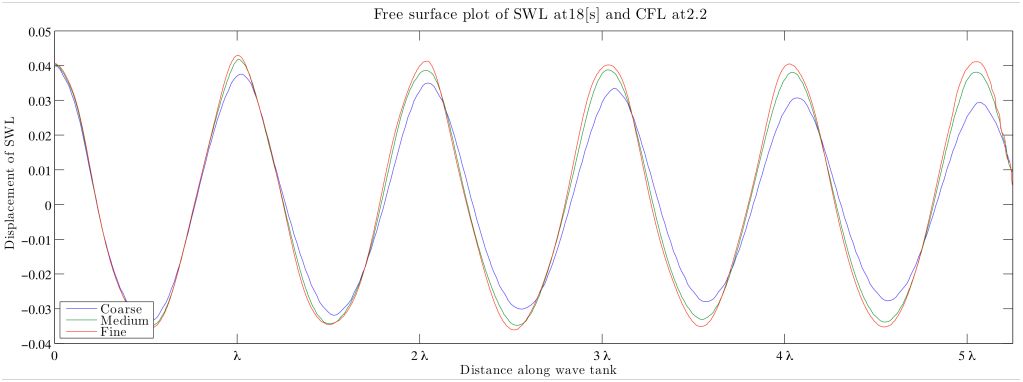

Figure 4. Free surface plot on the three different meshes examining grid convergence.

5. Validation

A Validation process was conducted comparing the numerical output against an analytic solution using linear wave theory. The waves used in the verification section are not strictly linear. In order to allow for a direct comparison between theory and CFD, the CFD needed to model linear waves. In order to achieve this the wave amplitude to be modelled was 0.005m, wave period of 1.25s and a water depth of 1.5m. Based on the temporal and spatial studies, the fine mesh resolution and a time step that produced a CFL number of 2.2 were chosen.

Figure 5 shows an overlay of the numerical result with the analytic solution for a piston wavemaker. Very good agreement is observed close in to the wavemaker (x=0). CFX even predicts the evanescent waves that arise from the mismatch between the wavemaker's velocity profile and the orbital particle velocities of the water. Down wave from the wavemaker however a noticeable and progressive decrease in the wave height can be observed. This wave height attenuation was also present in all of the verification models.

6. Discussion and conclusions.

This paper has presented a formal grid convergence study for the generation of a progressive wave using ANSYS CFX. It primarily concentrated on the disctretisation errors introduced through the use of a finite time step and solving continuous equations on a discrete grid. Temporal convergence is achieved when the CFL number is between 1-2. The level of grid refinement is a matter of judgement. This paper will allow for users to quantify the uncertainty associated with using different relative grid refinements.

One observation, noticed in both the second-order waves and the linear waves, was wave height attenuation occurring down the wave flume. This occurred both using the finest time steps and finest grid. Using Richardson extrapolation in Table 4 shows that with an infinitely fine mesh, the wave height would progressively decrease down the flume. This does occur to some degree in physical flumes as well, but not to the extent as was observed in this study. This is also not the first time that this has been reported in the literature (Bhinder 2009). But this is not necessarily an issue for coastal engineering modellers, a quick solution would be to increase the oscillation amplitude in order to achieve the desired wave height at the desired location. As the validation case shows, CFX can very accurately predict the

fluid flow field and free surface close to a moving object. The wave height attenuation could be more of an issue for the wave energy sector who are looking at the interaction an radiation of waves from several different wave energy converters, their absorption characteristics being highly dependant on the wave radiation properties.

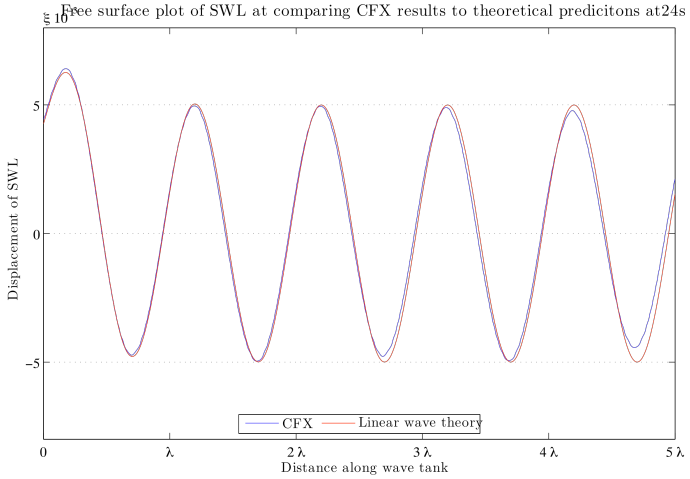

Figure 5. Comparison of CFX and linear wave theory, showing very good agreement near the wavemaker, but a small wave height attenuation was present in CFX results down the flume.

Acknowledgments

The authors wish to acknowledge funding for this project from the UK Engineering and Physical Sciences Research Council (EPSRC) as part of the Doctoral Training Programme of Phase 2 of SuperGen MARINE (EP/E040136/1) and a travel grant from the Royal Academy of Engineering
Prof. Ingram acknowledges the support from the Scottish Funding Council of his position within the Joint Research Institute in Energy with the Heriot-Watt University that is a part of the Edinburgh Research Partnership in Engineering and Mathematics (ERPem).

References

Bhinder, M.A., C.G. Mingham, D.M. Causon, M.T. Rahmati, G.A. Aggidis, and R.V. Chaplin. “A joint numerical and experimental study of a surging point absorbing wave energy converter (WRASPA).” In Proceedings of ASME 28th International Conference on Ocean, Offshore and Arctic Engineering, 1-7, 2009.

Celik, I B, Urmila Ghia, Patrick J. Roache, C. J. Freitas, Hugh Coleman, and Peter E Raad. “Procedure for Estimation and Reporting of Uncertainty Due to Discretization in CFD Applications.” Journal of Fluids Engineering 130, no. 7 (2008): 078001.

Dean, R.G., and R.A. Dalrymple. Water wave mechanics for engineers and scientists. World Scientific Pub Co Inc, 1991.

Havelock, Th. “Forced surface waves on water.” Philosophical Magazine 8, no. 7 (1929): 569-576.

Hughes, S.A. Physical models and laboratory techniques in coastal engineering. World Scientific Pub Co Inc, 1993.

Maguire, A.E., and D.M. Ingram. “On geometric design considerations and control methodologies for absorbing wavemakers.” Coastal Engineering 58, no. 2 (February 2011): 135-142.

Roache, Patrick J. “Verification of codes and calculations.” AIAA Journal 36, no. 5 (1998): 696–702.

B.3 Journal of Coastal Engineering, 2011

Maguire, A.E., and D.M. Ingram. On geometric design considerations and control methodologies for absorbing wavemakers. Coastal Engineering 58, no. 2 (February 2011): 135-142.

Coastal Engineering 58 (2011) 135–142

Contents lists available at ScienceDirect

Coastal Engineering

journal homepage: www.elsevier.com/locate/coastaleng

On geometric design considerations and control methodologies for absorbing wavemakers

A.E. Maguire *, D.M. Ingram

Institute for Energy Systems, Joint Research Institute for Energy, School of Engineering, The University of Edinburgh, Kings Buildings, Mayfield Rd, Edinburgh, EH9 3JL, United Kingdom

ARTICLE INFO

Article history:
Received 3 February 2010
Received in revised form 18 August 2010
Accepted 3 September 2010

Keywords:
Hydrodynamic coefficients
Wavemaker absorption
Geometry control
Wave Energy

ABSTRACT

This paper investigates the effects that geometry and control have on the absorption characteristics of wavemakers. It presents the hydrodynamic coefficients for piston and bottom hinged flap wavemakers and also for two novel wavemaker profiles. Absorption efficiencies are presented for wavemakers using one, two and three control coefficients for reactive control. This is then used to analyse the absorption efficiency of each of the different wavemakers based upon the geometry and the control strategy used. It is shown that the amount of absorption for a given paddle differs greatly depending on the choice of control coefficients used to implement complex conjugate control. Increased absorption can be achieved over a broader bandwith of frequencies when the geometry of the wavemaker is optimised for one specific frequency.

1. Introduction

Engineers use wave tank facilities to assess the design, safety and economic feasibility of ships and wave energy devices. Wavemakers are a central component to such facilities and have been studied extensively (Havelock, 1929; Biesel and Suquet, 1951; Dean and Dalrymple, 1991; Hughes, 1993). A major problem encountered with wave tanks is the contamination of the test domain by wave reflections. Two options can be used to avoid these unwanted waves, passive or active absorption. Passive wave absorbers (e.g. absorbing beaches) damp out the incoming waves and ensure that there are no reflections back into the domain. This form of absorption cannot deal with re-reflections caused by waves impinging upon the test device and tank walls and take up large areas of space. The other option is to use a dynamic system to actively absorb incoming waves. In theory, it is possible to absorb regular waves perfectly by tuning the active system over a range of frequencies using active control. Several different techniques have been put into practice to achieve optimal control of wavemaking devices, the main difference is the choice of which quantity to measure and the location of the measurement.

One method employed to absorb incoming waves uses the free surface elevations in front of the wavemaker. Several surface displacement measurements are taken and then the incoming wave field is separated from the desired wave field. The wavemaker is then moved in a manner that cancels out the incoming waves, (Milgram, 1970; Schäffer et al., 1994; Christensen and Frigaard, 1994).

Another approach adopted is the use of force as the hydrodynamic feedback mechanism. One advantage of this approach is that force is an integral quantity measured over the entire wavemaker front, thus minimising any slight errors encountered with single point measurements (Salter, 1981). Maisondieu and Clément (1993) published their results on a force feedback–feedforward control loop for a piston wave absorber. The problem considered was the absorption of water waves by the horizontal motions of a vertical plane in response to the hydrodynamic forces it experiences. Chatry et al. (1998) proposed a self-adaptive control of a piston wave absorber. Naito (2006) incorporates force feedback and optimal force control based upon a two coefficient system for plunger type wavemakers. Spinneken and Swan (2009b) discuss causal approaches for controlling active wavemakers based upon infinite impulse response filters.

Many of these force controlled absorbing wave makers use established theory for wave energy converters. Optimal control of wave energy devices has been referred to as reactive control (Nebel, 1992), impedance matching or complex conjugate control (Salter et al., 1976). This form of control can be implemented using a number of control coefficients, but the majority of absorbing wavemakers and wave energy devices implement the impedance control using just one imaginary coefficient. Price (2009) investigated the differences between the use of one, two and three control coefficients. It was shown that, in polychromatic seas, the capture width obtained is different for each of the control strategies and this capture width is also influenced by the choice of tuning frequency.

The present paper investigates the differences that control coefficient selection makes to the capture width of absorbing wavemakers when implementing impedance matching. It contrasts the results between using one, two or three control coefficients and also explores the influence that wavemaker geometry has on the absorption characteristics of the wavemaker.

* Corresponding author. Tel.: +44 131 650 8689; fax: +44 131 650 6554.
E-mail addresses: E.Maguire@ed.ac.uk (A.E. Maguire), David.Ingram@ed.ac.uk (D.M. Ingram).

0378-3839/$ – see front matter © 2010 Elsevier B.V. All rights reserved.
doi:10.1016/j.coastaleng.2010.09.002

In the following, Section 2 derives the hydrodynamic coefficients for four different shaped wavemakers, Section 3 explores the effect of control strategy on absorption characteristics and the results and conclusions are drawn up in Section 4.

2. Hydrodynamic coefficients of a wavemaker in a channel

Following the method used by Falnes (2002, sect 5.2.3), a 2D wavemaker in a constant water depth, h, that can oscillate in surge is considered. Cartesian coordinates, x,y,z, are used with $z=0$ at the still water level and the positive z:*axis* directed upwards. This will result in a velocity potential, ϕ_r

$$\hat{\phi}_r = \sum_{j=1}^{6} \varphi_j \hat{u}_j \tag{1}$$

where, φ_j is a complex coefficient of proportionality and the hat denotes complex amplitude. For simplicity, the paddle motion is limited to surge ($j=1$). If the piston has a velocity with complex amplitude $\hat{u}_1 \neq 0$, then according to the inhomogeneous boundary condition

$$\frac{\partial \varphi_1}{\partial x} = c(z) \quad \text{for } x = 0 \tag{2}$$

where, $c(z)$ is a function that defines the shape profile of the wavemaker.

The governing equation to this problem is the Laplace equation

$$\nabla^2 \hat{\varphi} = 0 \quad \text{everywhere,} \tag{3}$$

and the other relevant boundary conditions are the sea-bed boundary condition

$$\frac{\partial \hat{\varphi}}{\partial z} = 0 \quad \text{for } z = -h \tag{4}$$

and the free surface boundary condition

$$-\omega^2 \hat{\varphi} + g\frac{\partial \hat{\varphi}}{\partial z} = 0 \quad \text{for } z = 0. \tag{5}$$

Giving the following solution for φ_1 (Falnes, 2002),

$$\varphi_1 = c_0 Z_0(z) e^{-ik_0 x} + \sum_{n=1}^{\infty} c_n Z_n(z) e^{-k_n x} = \sum_{n=0}^{\infty} X_n(x) Z_n(z) \tag{6}$$

where, Z_n is the nth eigenfunction and

$$X_n(x) = c_n e^{k_n x}. \tag{7}$$

Here, k_n is the solution to the dispersion relationship for $n \geq 0$, letting $k_0 = ik$,

$$\omega^2 = -gik_n \tanh(-ik_n h) \tag{8}$$

where g is the acceleration due to gravity. Application of the boundary condition (2) at the paddle gives

$$c(z) = \left[\frac{\partial \varphi_1}{\partial x}\right]_{x=0} = \sum_{n=0}^{\infty} X_n'(0) Z_n(z) \tag{9}$$

where, $X_n'(0)$ is used to represent $\frac{dX_n}{dx}|_{x=0}$, as X_n is purely a function of x. Multiplying by the complex conjugate, $Z_m^*(z)$ and integrating from $z=-h$ to $z=0$, using the orthogonality condition yields

$$\int_{-h}^{0} c(z) Z_m^*(z) dz = \sum_{n=0}^{\infty} X_n'(0) \int_{-h}^{0} Z_m^*(z) Z_n(z) dz = X_m'(0) h. \tag{10}$$

That is

$$X_n'(0) = \frac{1}{h} \int_{-h}^{0} c(z) Z_n^*(z) dz. \tag{11}$$

Combining Eqs. (11) and (7) yields

$$X_0'(0) = ik_0 c_0, \quad X_n'(0) = k_n c_n, \tag{12}$$

thus giving the two coefficients

$$c_0 = \frac{-1}{ik_0 h} \int_{-h}^{0} c(z) Z_0^* dz, \tag{13}$$

$$c_n = \frac{-1}{k_n h} \int_{-h}^{0} c(z) Z_n^* dz. \tag{14}$$

The free surface elevation of the radiated wave, from Eq. (5), can now be expressed as

$$\eta = \frac{i\omega}{-g} u \sum_{n-0}^{\infty} c_n Z_n(0) e^{k_n x}. \tag{15}$$

Falnes (2002) gives the orthogonal set of eigenfunctions $Z_n(z)$ as

$$Z_0 = (N_0)^{-1/2} \cosh(k_0(z+h)) \tag{16}$$

$$Z_n = (N_n)^{-1/2} \cos(k_n(z+h)) \tag{17}$$

where

$$N_0 = \frac{1}{2}\left(1 + \frac{\sinh(2k_0 h)}{2k_0 h}\right) \tag{18}$$

$$N_n = \frac{1}{2}\left(1 + \frac{\sin(2k_n h)}{2k_n h}\right) \quad \text{for} \geq 1. \tag{19}$$

The radiation impedance of a wavemaker, in a channel of width d, is represented by $Z_{j'j}$. The term $R_{j'j}$ is the radiation resistance matrix. $X_{j'j}$ is the radiation reactance matrix. Care should be taken not to confuse the orthogonal set of eigenfunctions $Z_n(z)$ with the impedance $Z_{j'j}$.

$$\begin{aligned} Z_{j'j} &= R_{j'j} + iX_{j'j} \\ Z_{11} &= i\omega\rho d \int_{-h}^{0} \left[\psi_1 \frac{\partial \varphi_1^*}{\partial x} dz\right]_{x=0} \end{aligned} \tag{20}$$

As the paddle motion is limited to one degree of motion, the subscripts relating to surge will be dropped hereafter. Thus the impedance for a wavemaker in surge is

$$\begin{aligned} Z(\omega) &= i\omega\rho d \int_{-h}^{0} \left[c_0 Z_0(z) + \sum_{n=1}^{\infty} c_n Z_n(z)\right] c^*(z) dz \\ &= \omega k_0 \rho h d |c_0|^2 + i\omega\rho h d \sum_{n=1}^{\infty} k_n |c_n|^2. \end{aligned} \tag{21}$$

The radiation resistance, $R(\omega)$, is the real part of Eq. (21)

$$R(\omega) = \mathrm{Re}\{Z(\omega)\} = \omega k_0 \rho h d |c_0|^2 \tag{22}$$

and the added mass, $m(\omega)$, is a product of the imaginary part of Eq. (21),

$$m(\omega) = \frac{1}{\omega} \mathrm{Im}\{Z\} = \rho h d \sum_{n=1}^{\infty} k_n |c_n|^2. \tag{23}$$

2.1. Added mass and damping coefficients for different paddle geometries

The added mass and damping coefficients of a wavemaker are dependent on its shape profile, $c(z)$. Changes in the wavemaker's shape profile will result in very different hydrodynamic characteristics. This section presents the analytic expressions for added mass and damping for four different wavemaker shapes; a piston, a bottom hinged flap, a hyperbolic cosine shaped paddle, and a cosine shaped paddle (Fig. 1). The piston and bottom hinged flap paddles are similar to those found in many hydrodynamic laboratories around the world. The other two wavemakers have been discussed in theory by Naito (2006) and Falnes (2002). They proposed that, if the paddle profile is chosen, such that it matches the wave field velocity profile of the waves, the evanescent contributions in Eq. (15) will be zero. The situation where a wave paddle does not generate any progressive waves and only a standing wave persists is also discussed. This is achieved by choosing a shape profile that results in no real part to Eq. (15).

2.1.1. Piston wavemaker

For a piston, $c(z)=\frac{S_0}{2}$ (where, S_0 is the normalised stroke length), the added mass and damping are given as

$$m(\omega)=4\sum_{n=1}^{\infty}\frac{\rho\left(1-(\cos(k_nh))^2\right)}{k_n^2(2k_nh+\sin(2k_nh))} \tag{24}$$

and

$$R(\omega)=4\frac{\omega\rho\left((\cosh(k_0h))^2-1\right)}{k_0^2(2k_0h+\sinh(2k_0h))}. \tag{25}$$

2.1.2. Bottom hinged flap

The hydrodynamic coefficients for a bottom hinged flap, $c(z)=1+z/h$, are derived in Appendix A. The added mass for such a wavemaker is

$$m(\omega)=4\rho\sum_{n=1}^{\infty}\frac{(-1+cos(k_nh)+sin(k_nh)k_nh)^2}{k_n^4h^2(2k_nh+sin(2k_nh))}. \tag{26}$$

and the damping is represented as

$$R(\omega)=4\omega\rho\frac{(1+\sinh(k_0h)k_0h-\cosh(k_0h))^2}{k_0^4h^2(2k_0h+\sinh(2k_0h))}. \tag{27}$$

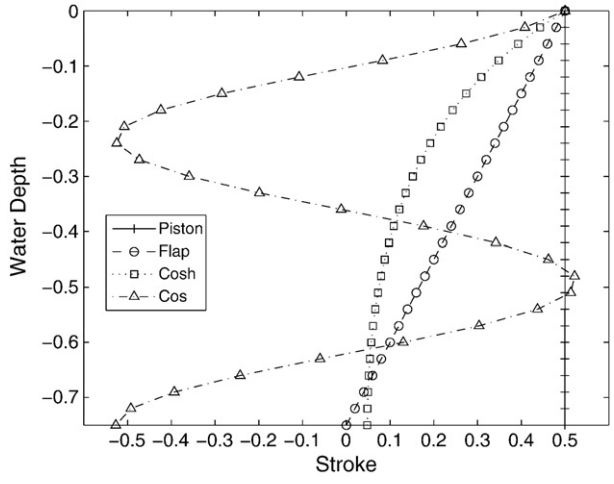

Fig. 1. The four wavemaker shape profiles. The shape profile for the hyperbolic cosine wavemaker is chosen at a wavenumber of k_{0s}, the profile for the cosine wavemaker is plotted for k_{3s}, both at a fixed frequency of $\omega_s=2\pi$.

2.1.3. No evanescent waves

For there to be no evanescent waves, there should be no added mass. This can be achieved if the paddle profile, $c(z)$, matches that of the wave velocity profile

$$c(z)=\frac{\cosh(k_{0s}(z+h))}{\cosh(k_{0s}h)}. \tag{28}$$

Here, k_{0s} is a fixed coefficient wavenumber at a frequency of ω_s that satisfies the real part to Eq. (8); $k_{0s}=k_0(\omega_s)$. Using this expression results in $c_n=0$ for $n\geq 1$ ensuring only real solutions and hence no evanescent contributions to the free surface (Eq. (15)).

The expressions for added mass and damping of a wavemaker with no evanescent waves are

$$m(\omega)=\sum_{n=1}^{\infty}\rho e^{-c}\times\left(\frac{(k_{0s}e^c-k_{0s}e^{b+c}-k_{0s}e^b+k_{0s}}{(2k_nh-i\sinh(c))(e^b+1)^2}\frac{-ik_n+ik_ne^{b+c}-ie^bk_n+ik_ne^c)^2}{(k_{0s}^2+k_n^2)^2}\right) \tag{29}$$

and

$$R(\omega)=\omega\rho\times\left(\frac{(k_0e^{-i(b+ia)}-k_0+e^ak_0-k_0e^{-ib}}{4(a+\sinh(a))(\cos(b/2))^2}\frac{-e^{-ib}k_{0s}+k_{0s}+e^ak_{0s}-k_{0s}e^{-i(b+ia)})^2}{(k_{0s}^2-k_0^2)^2}\right)e^{i(b+ia)} \tag{30}$$

where, $a=2k_0h$, $b=2ik_{0s}h$ and $c=2ik_nh$.

It should be noted that the wave number, $k_n(\omega)$, in Eq. (29) is frequency dependent and the wavemaker has no added mass at only one chosen frequency, ω_s. This type of wavemaker will be referred to as a hyperbolic cosine, $\cosh(\omega_s)$, shaped wavemaker where, ω_s designates the frequency at which the added mass tends to zero. Here, values of $\omega_s=\pi,2\pi$ and 3π will be considered, resulting in three different wavemaker geometries. The added mass for the wavemakers can be seen in Fig. 2a and c, and it is clear that the added mass, m(ω), tends to be zero at the chosen design frequency, ω_s. All graphs presented within this paper are evaluated for a water depth of $h=0.75$[m] and a width of $d=0.5$[m].

2.1.4. No progressive waves

The other special case is when a paddle can move in such a way that no progressive wave is radiated, only a standing evanescent wave persists. This would be very difficult to achieve in a physical wavemaker, but could more easily be achieved in a numerical code, or as discussed by Naito (2006), using segmented wavemakers. For there to be no progressive wave, the wavemaker needs to move in a manner that results in the real part of Eq. (6) being zero. This is achieved when the profile is

$$c(z)=\frac{\cos(k_{3s}(z+h))}{\cos(k_{3s}h)}. \tag{31}$$

This form of wavemaker will be referred to as a cosine wavemaker. Here, k_{3s} is the third solution from the infinite sequence of imaginary solutions to the dispersion relationship (Eq. (8)) at a fixed frequency of ω_s, $k_{3s}=k_3(\omega_s)$. For this paper, the third mode ($n=3$) is chosen arbitrarily and any value of $n\geq 1$ would be equally valid. The larger the value of n, the more oscillations in the wavemaker's surface through the water column. The resultant shape using $n=3$ can be seen in Fig. 1. The operation of this kind of wavemaker would result in the top and bottom of the paddle oscillating out of phase with each other. The choice of such a wavemaker profile results in the real part of Eq. (15) becoming zero leaving only a standing wave.

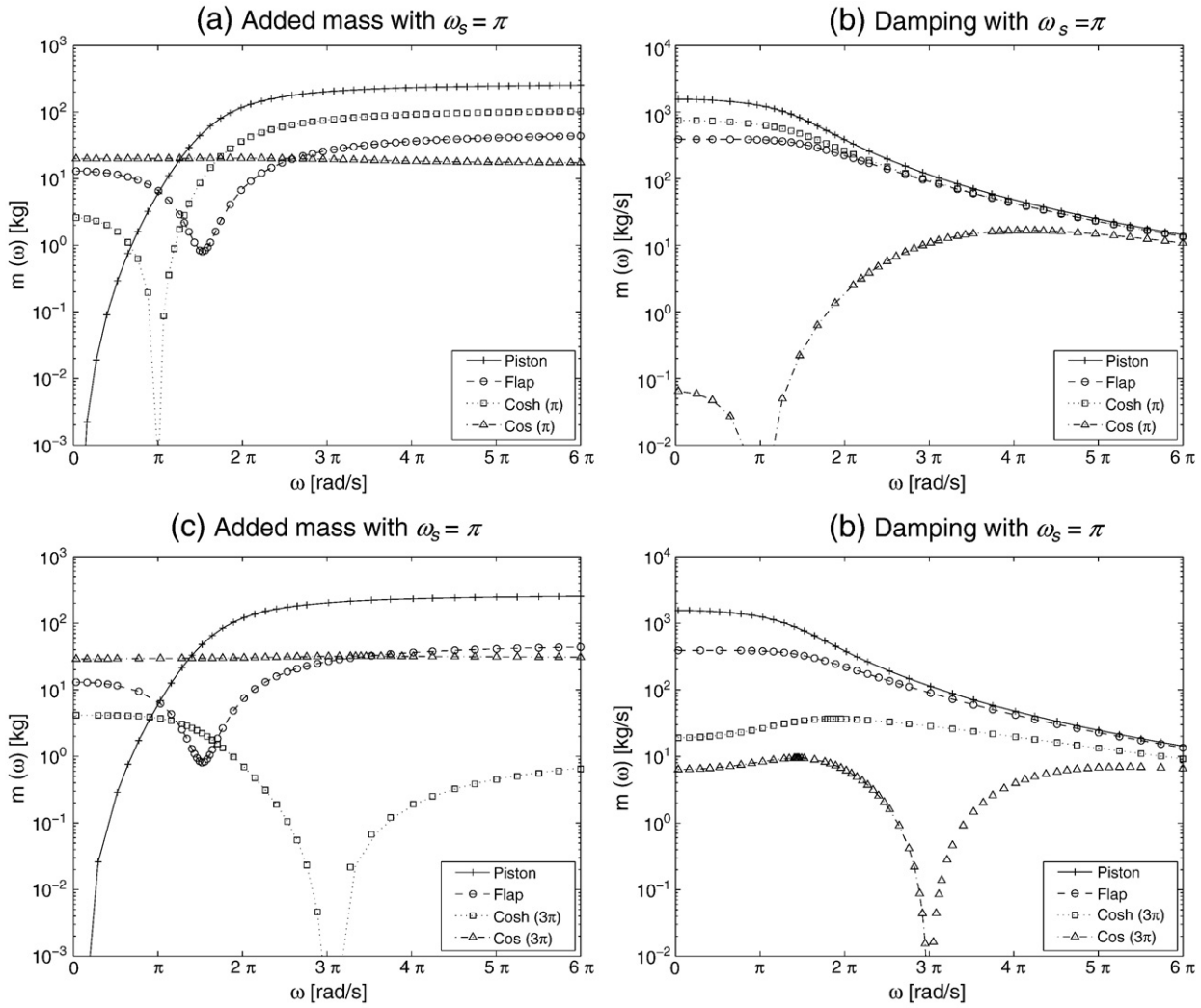

Fig. 2. Hydrodynamic coefficients for the four different shaped wavemakers; Piston, Bottom hinged flap, $cosh(\omega_s)$, $cos(\omega_s)$. Fig. 2a and b are for paddles with $\omega_s = \pi$, and Fig. 2c and d with $\omega_s = 3\pi$.

The corresponding expressions for added mass and damping for such a wavemaker are

$$m(\omega) = 4\rho \sum_{n=1}^{\infty} \frac{(-k_{3s}\sin(k_{3s}h)\cos(k_n h) + k_n \cos(k_{3s}h)\sin(k_n h))^2}{(2k_n h + \sin(2k_n h))(\cos(k_{3s}h))^2(-k_{3s}^2 + k_n^2)^2} \tag{32}$$

and

$$R(\omega) = \omega\rho \times \left(\frac{(-k_0 e^{a+b} + k_0 e^b - k_0 e^a + k_0 - ik_{3s}}{4(a + \sinh(a))\left(\cosh\left(\frac{b}{2}\right)\right)^2} \frac{+ ik_{3s}e^b - ik_{3s}e^a + ik_{3s}e^{a+b})^2 e^{-a-b}}{(k_0^2 + k_{3s}^2)^2} \right) \tag{33}$$

where, $a = 2k_0h$ and $b = 2ik_{3s}h$.

Obviously, a wavemaker operating in a manner that does not create any progressive waves would have little practical value. The hydrodynamic coefficients have been derived out of academic curiosity and to show that it is possible to have a paddle that will have zero damping and no progressive waves.

Fig. 2b and d show that such a wavemaker has zero damping at the design frequency of ω_s, but only at this frequency, at all other frequencies the damping is non-zero.

3. Absorption efficiency

This section applies control strategies for a wave energy converter, discussed by Price (2009), to absorbing wavemakers. The wavemaker shapes discussed in Sections 2.1.1, 2.1.2 and 2.1.3 are compared using absorption efficiency, similar to that used by Naito (2006) and Spinneken and Swan (2009b). Herein, the absorption efficiency is the ratio of absorbed power to maximum absorbed power and is plotted over discretised monochromatic waves.

3.1. Control strategies

According to Falnes (2002) the intrinsic impedance, Z_i, can be represented as

$$Z_i(\omega) = R(\omega) + i\left(\omega[M + m(\omega)] - \frac{c}{\omega}\right) \tag{34}$$

where, M is the mass of the paddle, c is the spring stiffness, $m(\omega)$ and $R(\omega)$ are added mass and damping respectively.

The optimum control force occurs when the control impedance, Z_u, equals the complex conjugate of the intrinsic impedance,

$$Z_u(\omega) = Z_i^*(\omega) = Z_{u,OPT}(\omega). \tag{35}$$

Thus,

$$Z_{u,OPT}(\omega) = R(\omega) - i\left(\omega[M + m(\omega)] - \frac{c}{\omega}\right) \tag{36}$$

and under a fixed coefficient system tuned to fixed frequency of $\omega = \omega_p$,

$$\begin{aligned} Z_{u,OPT}(\omega_p) &= R(\omega_p) - i\left(\left[\omega_p\left(M + m(\omega_p)\right) - \frac{c}{\omega_p}\right]\right) \\ &= R_p - i\left(\left[\omega_p\left(M + m_p\right) - \frac{c}{\omega_p}\right]\right) \end{aligned} \tag{37}$$

where, R_p and m_p denote fixed coefficients at a frequency of ω_p.

3.2. Spring-damping

There are a number of options available to implement this form of control; mass-spring-damper, spring-damping, mass-damping and pure damping. Each of these choices will lead to different absorption characteristics as shown by Price (2009). The following will present the derivation of absorption efficiency for a spring-damping control scheme with fixed control coefficients of r_u and c_u.

The control force in the time domain is represented as

$$f_u(t) = r_u u(t) + c_u x(t) \tag{38}$$

and thus the impedance in the frequency domain can be obtained as

$$Z_u(\omega) = r_u + \frac{c_u}{i\omega}. \tag{39}$$

Optimising Eq. (39) at a single frequency, ω_p, results in

$$Z_u(\omega_p) = r_u - \frac{ic_u}{\omega_p}. \tag{40}$$

Comparing Eqs. (37) and (40) gives the following control settings, which agree with those presented by Naito (2006)

$$r_u = R_p \tag{41}$$

$$c_u = \left(\omega_p^2\left(M + m_p\right) - c\right). \tag{42}$$

Substituting into Eq. (39), gives the tuned control impedance at ω_p, for a spring-damping system, over the full range of frequencies

$$Z_u(\omega) = R_p - \frac{i}{\omega}\left[\omega_p^2\left(M + m_p\right) - c\right]. \tag{43}$$

The maximum absorbed power, shown by Falnes (2002), can be represented as

$$\begin{aligned} P_u &= \frac{1}{2}\mathrm{Re}[Z_u(\omega)]\frac{|\hat{F}_{e,j}|^2}{|Z_i(\omega) + Z_u(\omega)|^2} \\ &= \frac{R_u(\omega)|\hat{F}_{e,j}|^2/2}{[R_i(\omega) + R_u(\omega)]^2 + [X_i(\omega) + X_u(\omega)]^2} \end{aligned} \tag{44}$$

where, F_e represents the excitation force.

Setting the control impedance, $Z_u(\omega)$ to the complex conjugate of the intrinsic impedance $\bar{Z}_i(\omega)$, namely setting the variables $R_u(\omega)$ and $X_u(\omega)$ to their optimum values of $R_i(\omega)$ and $-X_i(\omega)$ gives an expression for the maximum power

$$P_{u,\max} = \frac{|\hat{F}_{e,j}|^2}{8R_i}. \tag{45}$$

Combining Eqs. (44) and (45),which agrees with Spinneken and Swan (2009a), gives

$$\frac{P_u}{P_{u,\max}} = 4\frac{R_u(\omega)R_i(\omega)}{(R_i(\omega) + R_u(\omega))^2 + (X_i(\omega) + X_u(\omega))^2}. \tag{46}$$

Using radiation resistance and reactance expressions from Eqs. (34) and (43) and substituting into the power ratio Eq. (46), yields a power absorption ratio for a spring-damper controlled system,

$$\frac{P_u}{P_{u,\max}} = \frac{4R_pR(\omega)}{\left(R_p + R(\omega)\right)^2 + \left(\omega(M + m(\omega)) - \frac{\omega_p^2}{\omega}\left(M + m_p\right)\right)^2}. \tag{47}$$

Integrating Eq. (47) over the range of frequencies typical to a 1/100th scale wave tank (0.5 and 1.75 [Hz]) and normalising gives,

$$\xi = \frac{5}{2\pi}\int_{\pi}^{\frac{2\pi}{2}} \frac{P_u}{P_{u,\max}} d\omega \tag{48}$$

where, ξ is a measure of the efficiency of the wavemaker in absorbing discretised monochromatic waves of different frequencies to the tuned frequency, ω_p. Table 1 shows values of ξ for a mass-less, spring-damper controlled system for the various shaped wavemakers.

Construction of a mass-less paddle is physically impossible, but this could be implemented in a numerical code. This could provide an absorbing boundary condition to deal with wave reflections in a numerical wave tank. As can be seen from Table 1 very high levels of absorption, over the chosen integral range, could be achieved in conjunction with a $\cosh(3\pi)$ shaped wavemaker.

If the paddle has a finite mass, M, the absorption efficiency will decrease due to the second term in the denominator of Eq. (47). Table 2 shows ξ for a paddle with a mass of 1 kg. It can be seen that the introduction of mass decreases the absorption characteristics of the wavemaker.

3.3. Mass-damping

This section presents the absorption efficiency of a wavemaker using a mass-damping control system. The resulting absorption efficiency can be obtained as

$$\frac{P_u}{P_{u,\max}} = \frac{4R_pR(\omega)}{\left(R_p + R(\omega)\right)^2 + \left(\omega\left(m(\omega) - m_p\right) - \frac{c}{\omega}\left(1 - \frac{\omega^2}{\omega_p^2}\right)\right)^2}. \tag{49}$$

Implementing complex conjugate control at one tuned frequency, ω_p, will result in optimal control for all wavemakers at that specific

Table 1
Absorption efficiency, ξ, for a mass-less paddle controlled using spring-damper coefficients.

	Tuning frequency ω_p		
	π	2π	3π
Piston	0.628	0.652	0.312
Flap	0.876	0.904	0.775
$\cosh(\pi)$	0.699	0.735	0.430
$\cosh(2\pi)$	0.967	0.951	0.899
$\cosh(3\pi)$	0.990	0.991	0.986

Table 2
Absorption efficiency, ξ, for a paddle controlled using spring-damper coefficients.

	Tuning frequency ω_p		
	π	2π	3π
Piston	0.591	0.603	0.266
Flap	0.826	0.859	0.647
$cosh(\pi)$	0.662	0.690	0.372
$cosh(2\pi)$	0.875	0.904	0.736
$cosh(3\pi)$	0.709	0.852	0.680

frequency, $\omega=\omega_p$. It is important to note, that at this frequency, the absorption characteristics will be identical to that of a spring-damper system, but away from this frequency the absorption characteristics will differ to a system using spring-damping control coefficients. Thus resulting in different values of ξ over the chosen definite integral. This can be clearly seen in Table 3. The spring coefficient, which provides a restoring force against the hydrostatic force of the water, was chosen as $c=20$ N/m, based on the flap type wavemakers used at the University of Edinburgh.

3.4. Mass-spring-damper

For a mass-spring-damper controlled system, the ratio of absorbed power to maximum power is obtained as

$$\frac{P_u}{P_{u,\max}} = \frac{4R_pR(\omega)}{\left(R_p + R(\omega)\right)^2 + \left(\omega\left(m(\omega)-m_p\right)\right)^2}. \tag{50}$$

This is a case when both a mass term and a spring term are used to achieve complex conjugate control. Again, at the chosen control frequency, ω_p the absorption characteristics will be the same as the other control strategies using reactive control (i.e. full absorption) but differ greatly away from ω_p. The main difference using this kind of control scheme is that all wavemakers exhibit better levels of absorption across a broader bandwidth, than using any of the other control strategies. The best absorption, from Eq. (48), is obtained using a cosh(3π) paddle, tuned to $\omega_p=3\pi$. This results in 98.5% power absorption of incoming waves between frequencies of π to 3.5π rad/s (Table 4).

3.5. Damping

A purely real control system, using only a damping coefficient gives an absorption ratio of

$$\frac{P_u}{P_{u,\max}} = \frac{4R(\omega)\sqrt{R_p^2 + \left(\omega_p\left(M+m_p\right)-\frac{c}{\omega_p}\right)}}{\left(R(\omega) + \sqrt{R_p^2 + \left(\omega_p\left(M+m_p\right)-\frac{c}{\omega_p}\right)}\right)^2 + \left(\omega(M+m(\omega))-\frac{c}{\omega}\right)^2}. \tag{51}$$

This is the easiest form of control to implement physically and subsequently, the most widely used control strategy for power take off in wave energy converters. Table 5 shows how using a control strategy based upon damping alone affects the power absorption. An interesting result here is that for all wavemaker shapes, absorption efficiency is relatively insensitive to changes in tuning frequency. This suggests that the choice of control frequency, ω_p, is not a major contributor to absorption efficiency for these wavemakers between the chosen integral limits. The bottom hinged flap performs favourably compared to the three hyperbolic cosine shaped paddles, this could be due to there being a local minimum in the intrinsic reactance (added mass) of this paddle at a frequency of 1.7π[rad/s] (Fig. 2a) resulting in the real part of the power absorption Eq. (46) dominating over the imaginary part.

Table 4
Absorption efficiency, ξ, for a paddle controlled using mass-spring-damper coefficients.

	Tuning frequency ω_p		
	π	2π	3π
Piston	0.602	0.695	0.617
Flap	0.872	0.892	0.866
$cosh(\pi)$	0.677	0.761	0.712
$cosh(2\pi)$	0.941	0.951	0.936
$cosh(3\pi)$	0.883	0.982	0.985

3.6. Effect of control

In wave energy research, it has been long known that optimum absorption of incoming monochromatic waves can be achieved if the power take off (PTO) coefficients of the wave energy absorber are chosen such to achieve impedance matching. Mei (1976) showed that this could be implemented using two control coefficients; one proportional to acceleration and the other proportional to velocity. Evans (1981) arrived at the same results using a velocity-proportional damping force and a displacement-proportional spring force. Using either a mass-damping or a spring-damping approach will yield the same optimum absorption of incoming waves at that one specific tuned frequency, ω_p. Price (2009) showed that, for a point absorber acting in heave, both of these approaches differ when absorbing incoming monochromatic waves of a frequency $\omega\neq\omega_p$. Fig. 3 shows that this is true for absorbing devices acting in surge also.

Fig. 3 shows the absorption levels of four different wavemakers in discretised monochromatic waves using different control strategies, each tuned to $\omega_p=3\pi$. It is clear that the choice of control affects the absorption levels across the bandwith of frequencies. The difference between the various control strategies is most evident when considering just one wavemaker shape. For example, at a frequency of $\omega=3\pi$ in Fig. 3c the mass-damper, spring-damper and mass-spring-damper control strategies all achieve the same value of $P_u/P_{\max}=1$. Away from $\omega=3\pi$, the absorption levels of waves at frequencies different to that of the tuned frequency, $\omega\neq\omega_p$, differ greatly.

There is a notable difference in absorption levels between the mass-damper and the spring-damper methods of control in Fig. 3. This can be seen quantitatively comparing ξ in Tables 2 and 3, at a tuning frequency of $\omega_p=3\pi$. Control implemented using mass-damping

Table 3
Absorption efficiency, ξ, for a paddle controlled using mass-damper coefficients.

	Tuning frequency ω_p		
	π	2π	3π
Piston	0.585	0.689	0.609
Flap	0.815	0.879	0.856
$cosh(\pi)$	0.646	0.751	0.700
$cosh(2\pi)$	0.830	0.932	0.921
$cosh(3\pi)$	0.545	0.971	0.971

Table 5
Absorption efficiency, ξ, for a paddle controlled using just a damping coefficient.

	Tuning frequency ω_p		
	π	2π	3π
Piston	0.593	0.588	0.577
Flap	0.828	0.843	0.842
$cosh(\pi)$	0.665	0.664	0.667
$cosh(2\pi)$	0.881	0.885	0.884
$cosh(3\pi)$	0.770	0.808	0.795

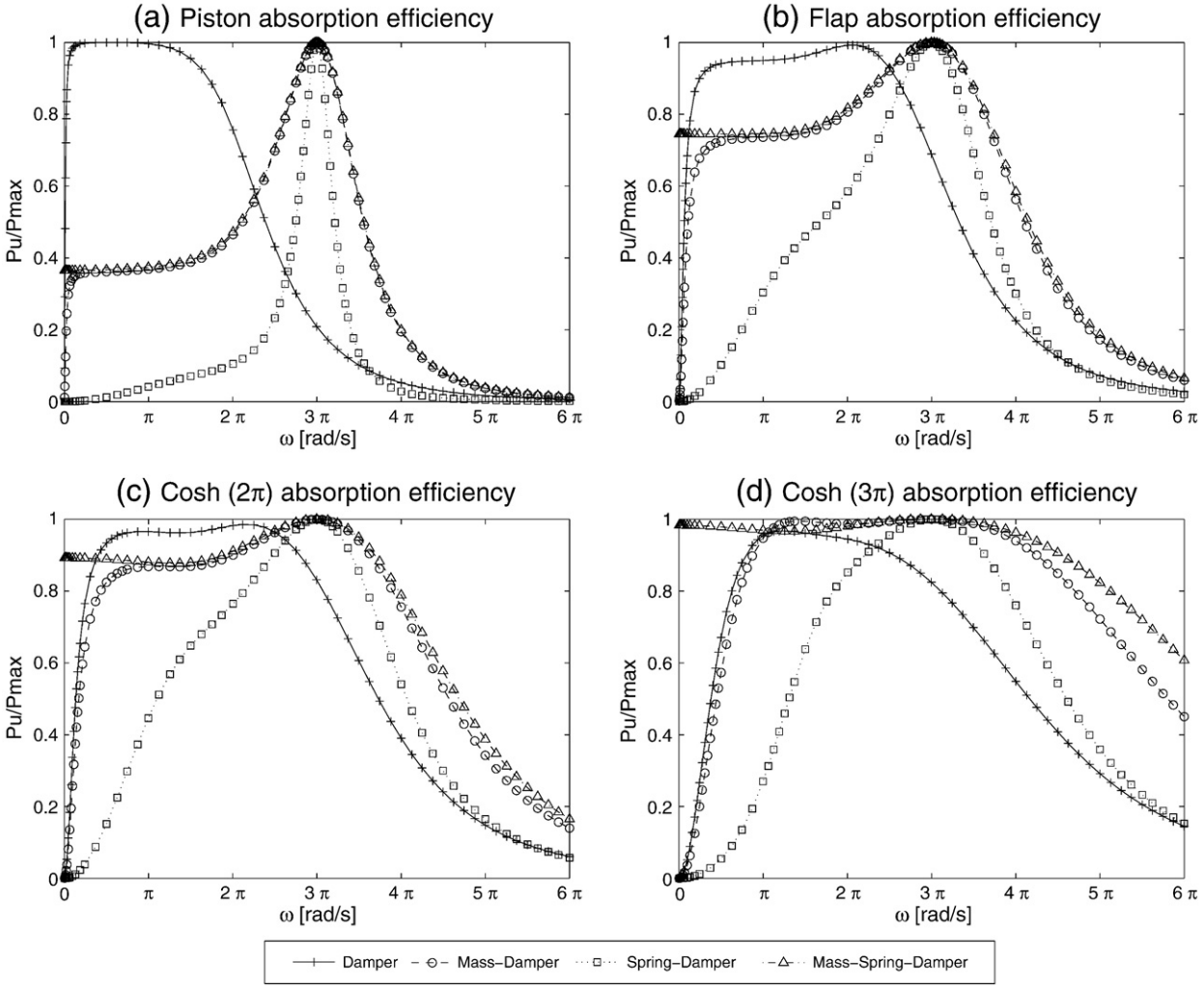

Fig. 3. Graphs showing the ratio of absorbed power to the maximum power theoretically achieveable, $\frac{P_u}{P_{\max}}$, for four paddle geometries, each using four different control configurations; Damping, Spring-damping, Mass-damping, Mass-spring-damping.

coefficients out performs that of spring-damping for every wavemaker shape. Interestingly, upon changing tuning frequency to $\omega_p = \pi$, the situation is reversed and control using spring-damping coefficients display better absorption characteristics than mass-damping.

When only a damping coefficient is used, complex conjugate control is not possible and optimal absorption, $P_u/P_{\max} = 1$, at ω_p is unachievable. When only real control is implemented for a piston wavemaker (Fig. 3a) optimal control is never achieved, but high levels of absorption are achieved at the lower bandwidth of frequencies. These lower frequencies will have longer wavelengths and once displacement limits are taken into consideration, these high levels of absorption would disappear.

The highest levels of absorption were obtained for a cosh(3π) paddle with a mass-spring-damper control strategy tuned to $\omega_p = 3\pi$. The construction of a cosh(3π) wavemaker would be difficult but this shape could be used in a numerical wave tank as an absorbing boundary condition instead of a computationally expensive damping region in the numerical domain.

In fact, the role of wavemaker geometry has an important influence on the absorption characteristics. This can be seen contrasting the graphs for the four different shaped wavemakers in Fig. 3. It can be seen that regardless of control strategy implemented, a cosh(3π) (Fig. 3d) wavemaker displays better absorption characteristics at frequencies of $\omega \neq \omega_p$, thus yielding much broader graphs.

4. Conclusions

This paper has shown that the absorption of incoming waves is sensitive to the shape of the absorbing wavemaker, the control strategy used to implement the absorption and also the choice of tuning frequency in the control strategy.

Three different shaped wavemakers were considered; a piston, a bottom hinged flap and a hyperbolic cosine paddle. The analytic solutions for the added mass and damping for each wavemaker were presented and it was shown that the added mass for the hyperbolic cosine paddle tended to be zero for a specific chosen frequency. The hydrodynamic coefficients were then used in the control strategies to absorb incoming waves.

The different control strategies considered were mass-spring-damping, spring-damping, mass-damping and damping. It was shown that the best absorption, of frequencies between π rad/s and 3.5π rad/s, was achieved with a hyperbolic cosine, cosh(ω_s), wavemaker with control coefficients tuned to a frequency of $\omega_p = 3\pi$ using a mass-spring-damper control system.

The authors are not suggesting building a *cosh*(ω_s) shaped wavemaker as it would prove difficult and in engineering terms result in only marginally better wave absorption compared to a bottom hinged flap over the typical frequency range of a wave tank. This shaped absorbing wavemaker could be used as a numerical boundary condition to deal with unwanted wave reflections in

numerical wave tanks, offering an alternative to other methods that can be computationally intensive.

For wave absorbers acting in surge, it has been shown that there are differences between using mass-damping, spring-daming and mass-spring-damping coefficients to implement complex conjugate control. All achieve optimal absorption of $P_u/P_{max}=1$, at ω_p but absorption levels differ at frequencies other than the tuned frequency. This highlights the importance in choosing what control strategy to choose and include in a wave absorbing device. All of the reactive control options are sensitive to the choice of tuning frequency ω_p adding another variable for consideration. This could have relevance to any surging wave energy converter that makes use of reactive control.

Furthermore, if the absorption of incoming waves is implemented using real control, there is little discernible difference in the absorption efficiency, ξ, upon changing the tuning frequency, ω_p, for all wavemaker shapes. A control strategy using just real control coefficients is insensitive to the tuning frequency. Better returns on absorption could be gained if design efforts concentrated on the shape optimisation as opposed to power take off optimisation.

There are limitations to this study. Displacement limits have not been considered and the amount of absorption reported in Fig. 3 would be an over estimation at the lower range of frequencies. The response times of the paddles was also neglected, this would have resulted in an over estimation of absorption at higher frequencies. The definite integrals chosen for absorption efficiency, ξ, were based upon frequency limits in the 1/100th scale tank at Edinburgh, so the concerns over displacement limits and motion response should be diminished. Future work will involve implementation of these wavemakers and the control strategies in a computational fluid dynamics code to investigate the performance of such novel paddles with the different control choices.

Acknowledgements

The authors wish to acknowledge funding for this project from the UK Engineering and Physical Sciences Research Council (EPSRC) as part of the Doctoral Training Programme of Phase 2 of SuperGen MARINE (EP/E040136/1).

Prof. Ingram acknowledges the support from the Scottish Funding Council of his position within the Joint Research Institute in Energy with the Heriot-Watt University which is a part of the Edinburgh Research Partnership in Engineering and Mathematics (ERPem).

Comments from Dr. David Forehand are greatly appreciated.

Appendix A. Derivation of added mass and damping of a bottom hinged paddle

Following Falnes' theory outlined in Section 2, the hydrodynamic coefficients for a bottom hinged flap ($c(z)=1+z/h$) can be derived. Using Eq. (13) and inserting orthogonality condition (16) yields

$$c_0 = -\frac{1}{ik_0h}N_0^{-1/2}\int_{-h}^{0}(1+z/h)\cosh(k_0(z+h))dz \tag{A.1}$$

$$= -\frac{1}{ik_0h}N_0^{-1/2}\frac{1+k_0h\sinh(k_0h)-\cosh(k_0h)}{k_0^2h}$$

$$= i(1+k_0h\sinh(k_0h)-\cosh(k_0h))k_0^{-3}h^{-2}$$

$$\left(\frac{1}{2}+\frac{1}{4}\frac{\sinh(2k_0h)}{k_0h}\right)^{-1/2}.$$

Thus, from Eq. (22) the damping for a bottom hinged paddle is

$$R(\omega) = 4\frac{\omega\rho(1+\sinh(k_0h)k_0h-\cosh(k_0h))^2}{k_0^4h^2(2k_0h+\sinh(2k_0h))}. \tag{A.2}$$

Similarly, combining Eq. (17) with Eq. (14) gives

$$c_n = -\frac{1}{k_nh}N_n^{-1/2}\int_{-h}^{0}(1+z/h)\cos(k_n(z+h))dz \tag{A.3}$$

$$= \frac{1}{k_nh}N_n^{-1/2}\frac{-1+\cos(k_nh)+k_nh\sin(k_nh)}{k_n^2h}$$

$$= (-1+\cos(k_nh)+k_nh\sin(k_nh))k_n^{-3}h^{-2}$$

$$\left(\frac{1}{2}+\frac{1}{4}\frac{\sin(2k_nh)}{k_nh}\right)^{-1/2}$$

and the resulting added mass (Eq. (23)) is

$$m(\omega) = 4\rho\sum_{n=1}^{\infty}\frac{(-1+\cos(k_nh)+\sin(k_nh)k_nh)^2}{k_n^4h^2(2k_nh+\sin(2k_nh))}. \tag{A.4}$$

Both of these coefficients for added mass and damping are in agreement with Newman (2008) who did not present the full derivation.

References

Biesel, F., Suquet, F., 1951. Laboratory wave-generating apparatus. La Houille Blanche 6, 147165.
Chatry, G., Clément, A., Gouraud, T., 1998. Self-adaptive control of a piston wave absorber. Proc. of 8th ISOPE Conference, pp. 127–133. Montreal, Canada.
Christensen, M., Frigaard, P., 1994. Design of absorbing wave maker based on digital filters. IAHR: Proc. International symposium: Waves — Physical and Numerical Modelling, pp. 100–109.
Dean, R., Dalrymple, R., 1991. Water Wave Mechanics for Engineers and Scientists. World Scientific Pub Co Inc.
Evans, D.V., 1981. Power from water waves. Annual Review of Fluid Mechanics 13 (1), 157–187.
Falnes, J., 2002. Ocean Waves and Oscillating Systems. Cambridge Univ Press.
Havelock, T., 1929. Forced surface waves on water. Philosophical Magazine 8 (7), 569–576.
Hughes, S., 1993. Physical Models and Laboratory Techniques in Coastal Engineering. World Scientific Pub Co Inc.
Maisondieu, C., Clément, A., 1993. A realizable force feedback–feedforward control loop for a piston wave absorber & Floating Bodies. Proc. 8th Int. Workshop Water Waves, vol. 82, pp. 79–82.
Mei, C., 1976. Power extraction from water waves. Journal of Ship Research 20, 63–66.
Milgram, J.H., 1970. Active water-wave absorbers. Journal of Fluid Mechanics 42 (04), 845 Mar.
Naito, S., 2006. Wave generation and absorption in wave basins: theory and application. International Journal of Offshore and Polar Engineering 16 (2), 81–89.
Nebel, P., 1992. Maximizing the efficiency of wave-energy plant using complex-conjugate control. Journal of Systems and Control 206 (4), 225–236.
Newman, J., 2008. Analysis of Wave Generators and Absorbers in Basins. http://wamit.com/Publications/Newman_AOR_submitted.pdf.
Price, A., 2009. New Perspectives on Wave Energy Converter Control. Ph.D. thesis, University of Edinburgh.
Salter, S., 1981. Absorbing wave-makers and wide tanks. Proceedings of ASCE & ECOR International Symposium on Directional Wave Spectra Applications, vol. 81, pp. 182–202. Berkley, California.
Salter, S., Jeffery, D., Taylor, J., 1976. The architecture of nodding duck wave power generators. The Naval Architect 21–24.
Schäffer, H., Stolborg, T., Hyllested, P., 1994. Simultaneous generation and active absorption of waves in flumes. Proc., waves-physical and numerical modelling. University of British Columbia, Vancouver, pp. 90–99.
Spinneken, J., Swan, C., 2009a. Second-order wave maker theory using force-feedback control. Part I: A new theory for regular wave generation. Ocean Engineering 36 (8), 539–548.
Spinneken, J., Swan, C., 2009b. Wave generation and absorption using force-controlled wave machines. Proceedings of the Nineteenth (2009) International Offshore and Polar Engineering Conference. Osaka, Japan.

Bibliography

AEA Technology. CFDS-Flow3D User Guide. Technical report, 1994.

Aeschliman, D., Oberkampf, W., and Blottner, F. A proposed methodology for computational fluid dynamics code verification, calibration, and validation. *ICIASF '95 Record. International Congress on Instrumentation in Aerospace Simulation Facilities*, pages 27.1–27.13, 1995. doi: 10.1109/ICIASF.1995.519133.

AIAA. Guide for the verification and validation of computational fluid dynamics simulations. *Am. Institute of Aeronautics and Astronautics*, 1998.

Anderson, J. *Computational fluid dynamics, the basics with application*, volume 206. McGraw-Hill, 1995.

ANSYS. Tech Support, 2008.

Apsley, D. and Hu, W. CFD simulation of two- and three-dimensional free-surface flow. *International Journal for Numerical Methods in Fluids*, 42(5):465–491, June 2003. ISSN 0271-2091. doi: 10.1002/fld.523.

Barkhudarov, M. Lagrangian VOF advection Method for FLOW-3DÂő. *Flow Science Inc., Technical Note, FSI-03-TN63-R*, (July):1–11, 2004.

Bergström, J. and Gebart, R. Estimation of numerical accuracy for the flow field in a draft tube. *International Journal of Numerical Methods for Heat & Fluid Flow*, 9(4):472–487, 1999. ISSN 0961-5539.

Bessho, M. Feasibility study of a Floating-type Wave Absorber. *34th JTTC*, 1973.

Bhinder, M., Mingham, C., Causon, D., Rahmati, M., Aggidis, G., and Chaplin, R. A joint numerical and experimental study of a surging point absorbing wave energy converter (WRASPA). In *Proceedings of ASME 28th International Conference on Ocean, Offshore and Arctic Engineering*, pages 1–7, 2009a.

Bhinder, M., Mingham, C., Causon, D., Rahmati, M., Aggidis, G., and Chaplin,

R. Numerical and Experimental Study of a Surging Point Absorber Wave Energy Converter. In *Proceedings of the 8th European Wave and Tidal Energy Conference*, Uppsala, Sweeden, 2009b.

Biesel, F. and Suquet, F. Laboratory Wave-generating Apparatus. *La Houille Blanche*, 6:147165, 1951.

Blottner, F. Accurate Navier-Stokes results for the hypersonic flow over a spherical nosetip. *AIAA Journal of Spacecraft and Rockets*, 27(2):113–122, 1989.

Bonnefoy, F., Touze, D., and Ferrant, P. A fully-spectral 3D time-domain model for second-order simulation of wavetank experiments. Part A: Formulation, implementation and numerical properties. *Applied Ocean Research*, 28(1):33–43, 2006. ISSN 01411187. doi: 10.1016/j.apor.2006.05.004.

Bullock, G. and Murton, G. Performance of a Wedge-Type Absorbing Wave Maker. *Journal of Waterway, Port, Coastal and Ocean Engineering*, 115:1–17, 1989.

Causon, D., Qian, L., Hu, Z. Z., and Mingham, C. CFD Modeling of Wave Loads on Offshore Wave Energy Devices. In *ISOPE-2008: Eighteenth(2008) International Offshore and Offshore and Polar Engineering Conference Proceedings*, volume 8, pages 137–142. International Society of Offshore and Polar Engineers, P. O. Box 189, Cupertino, CA, 95015-0189, USA„ 2008.

Celik, I. B., Ghia, U., Roache, P. J., Freitas, C. J., Coleman, H., and Raad, P. E. Procedure for Estimation and Reporting of Uncertainty Due to Discretization in CFD Applications. *Journal of Fluids Engineering*, 130(7):078001, 2008. ISSN 00982202. doi: 10.1115/1.2960953.

Chakrabarti, S. *Hydrodynamics of offshore structures: Mathematical theory and its applications in structures*. Springer-Verlag New York Inc., New York, NY, 1987.

Chatry, G., Clément, A., and Gouraud, T. Self-adaptive control of a piston wave absorber. In *Proc. of 8th ISOPE Conference*, pages 127–133, Montreal, Canada, 1998.

Christensen, M. and Frigaard, P. Design of absorbing wave maker based on digital filters. In *IAHR: Proc. International symposium: Waves - Physical and*

Numerical Modelling, pages 100–109, 1994.

Clément, A. Coupling of Two Absorbing Boundary Conditions for 2D Time-Domain Simulations of Free Surface Gravity Waves. *Journal of Computational Physics*, 126(1):139–151, June 1996. ISSN 00219991. doi: 10.1006/jcph.1996.0126.

Clément, A. and Mas, S. Hydrodynamic forces induced by solitary wave on a submerged circular cylinder. In *Proceedings of the Fifth International Offshore and Polar Engineering Conference, ISOPE, The Hague*, volume 3, pages 339–347, 1995.

Cruz, J. Ocean wave energy. *Springer, Berlin*, 10:978–3, 2008.

Cummins, W. The impulse response function and ship motions. *Schiffstechnik*, 9(1661):101–109, 1962.

Dean, R. and Dalrymple, R. *Water wave mechanics for engineers and scientists*. World Scientific Pub Co Inc, 1991.

Dong, C. and Huang, C. Generation and propagation of water waves in a two-dimensional numerical viscous wave flume. *Journal of Waterway, Port, Coastal, and Ocean Engineering*, 130(3):143, 2004. ISSN 0733950X. doi: 10.1061/(ASCE)0733-950X(2004)130:3(143).

Duclos, G., Clément, A., and Chatry, G. Absorption of outgoing waves in a numerical wave tank using a self-adaptive boundary condition. *International Journal of Offshore and Polar Engineering*, 11(3):168–175, 2001.

Elangovan, M. Simulation and Validation of Plunger Type Wave Maker by CFD. *IE Journal MR*, (I):10–16, 2010.

Elangovan, M. and Sahoo, G. Generation of Irregular Wave for Marine Application by Piston Type Wave Maker. In *Proceedings of the Twentieth International Offshore and Polar Engineering Conference*, volume 7, pages 566–571, Beijing, China, 2010. The International Society of Offshore and Polar Engineers.

ERCOFTAC. Quality and trust in industrial cfd-a european initiative. *Best practice guidelines, verion 1.0, EROCFTAC special interest group*, 2002.

European Union. DIRECTIVE 2009/28/EC OF EUROPEAN PARLIAMENT

AND OF THE COUNCIL of 23 April 2009 on the promotion of the use of energy from renewable sources and amending and subsequently repealing Directives 2001/77/EC and 2003/30/EC. *Official Journal of the European Union*, 2009.

Eurostat. Share of renewables in the EU27 energy supply almost doubled between 1999 and 2009, 2011.

Evans, D. V. A theory for wave-power absorption by oscillating bodies. *Journal of Fluid Mechanics*, 77(1):1–25, 1976.

Evans, D. V. Power from water waves. *Annual Review of Fluid Mechanics*, 13 (1):157–187, 1981.

Falnes, J. On non-causal impulse response functions related to propagating water waves. *Applied Ocean Research*, 17(6):379–389, 1995. ISSN 0141-1187.

Falnes, J. *Ocean waves and oscillating systems*. Cambridge Univ Press, 2002.

Falnes, J. A review of wave-energy extraction. *Marine Structures*, 20(4):185–201, October 2007. ISSN 09518339. doi: 10.1016/j.marstruc.2007.09.001.

Falnes, J. and Budal, K. Wave power conversion by point absorbers. *Norwegian Maritime Research*, 6(4):2–11, 1978.

Ferziger, J. and Peric, M. *Computational methods for fluid dynamics*. Springer Berlin, 1999.

Ferziger, J. and Perić, M. Computational methods for fluid dynamics. 2002.

FLOW3D. Email support from FLOW3D, 2010.

Freitas, C. J. The issue of numerical uncertainty. *Applied Mathematical Modelling*, 26(2):237–248, February 2002. ISSN 0307904X. doi: 10.1016/S0307-904X(01)00058-0.

Frigaard, P. and Brorsen, M. A time-domain method for separating incident and reflected irregular waves. *Coastal engineering*, 24(3-4):205–215, 1995. ISSN 0378-3839.

Galvin, C. Wave-height prediction for wave generators in shallow water. *Coastal*

Engineering research center, 1964.

Galvin Jr, C. Wave-height prediction for wave generators in shallow water. Technical report, COASTAL ENGINEERING RESEARCH CENTER VICKSBURG MS, 1964.

Gilbert, G., Thompson, D., and Brewer, A. Design curves for regular and random wave generators. *Journal of Hydraulic Research*, 9(2):163–196, 1971.

Givoli, D. Non-reflecting boundary conditions. *Journal of Computational Physics*, 94(1):1–29, 1991.

Gretton, G. *The hydrodynamic analysis of a vertical axis tidal current turbine*. Phd thesis, University of Edinburgh, 2009.

Gretton, G., Couch, S. J., Bryden, I. G., and Ingram, D. The CFD simulation of a lifting hydrofoil in close proximity to a free surface. In *Proceedings of the ASME 2010 29th International Conference on Ocean and Artic Engineering*, Shanghai, China, 2010.

Grilli, S. and Horrillo, J. Numerical generation and absorption of fully nonlinear periodic waves. *Journal of Engineering Mechanics*, 123(10):1060–1069, 1997.

Harlow, F. Numerical calculation of time-dependent viscous incompressible flow of fluid with free surface. *Physics of fluids*, 8:2182, 1965.

Hasselmann, S., Hasselmann, K., Bauer, E., Janssen, P., and Komen, G. The WAM Model. A Third Generation Ocean Wave Prediction Model. *Journal of Physical Oceanography*, 18(12):1775–1810, December 1988. ISSN 0022-3670. doi: 10.1175/1520-0485(1988)018<1775:TWMTGO>2.0.CO;2.

Havelock, T. Forced surface waves on water. *Philosophical Magazine*, 8(7):569–576, 1929.

Hirt, C. and Nichols, B. Volume of fluid (VOF) method for the dynamics of free boundaries. *Journal of computational physics*, 39(1):201–225, 1981.

Holmes, B. and Nielsen, K. Report T02-2.1 Guidelines for the Development & Testing of Wave Energy Systems. Technical report, OES-IEA, 2010.

House of Lords. House of Lords, Select Committee on the European Communities,

Alternative Energy Sources, 16th report. Technical report, House of Lords, 1988.

Hu, Z. Z., Causon, D., Mingham, C. G., and Qian, L. Numerical Wave Tank Study of a Wave Energy Converter in Heave. In *Proc. of 19th ISOPE Conference*, volume 1, pages 383–388, Osaka, Japan, 2009.

Huang, C., Zhang, E., and Lee, J. Numerical simulation of nonlinear viscous wavefields generated by piston-type wavemaker. *Journal of Engineering Mechanics*, 124:1110, 1998.

Hughes, S. *Physical models and laboratory techniques in coastal engineering*. World Scientific Pub Co Inc, 1993.

Israeli, M. and Orszag, S. Approximation of radiation boundary conditions. *Journal of Computational Physics*, 41:115–135, 1981.

Ito, K., Katsui, H., Mochizuki, M., and Isobe, M. Non-reflected multi directional wave maker theory and experiments of verification. In *Coastal Engineering (1996)*, pages 443–456, Orlando, Fla, 1996. ASCE.

Kim, C., Clément, A., and Tanizawa, K. Recent research and development of numerical wave tanks-a review. *International Journal of Offshore and Polar Engineering*, 9(4):241–256, 1999. ISSN 1053-5381.

Kim, M., Niedzwecki, J., Roesset, J., Park, J., Hong, S., and Tavassoli, A. Fully nonlinear multidirectional waves by a 3-D viscous numerical wave tank. *Journal of Offshore Mechanics and Arctic Engineering*, 123(3):124, 2001. ISSN 08927219. doi: 10.1115/1.1377598.

Kirby, J., Wei, G., Chen, Q., Kennedy, A., and Dalrymple, R. FUNWAVE 1.0. Fully nonlinear Boussinesq wave model. Documentation and userâĂŹs manual. Technical report, Center for Applied Coastal Research, University of Delaware, 1998.

Koo, W. and Kim, M. Numerical simulation of nonlinear wave and force generated by a wedge-shape wave maker. *Ocean Engineering*, 33:983–1006, November 2005. ISSN 00298018. doi: 10.1016/j.oceaneng.2005.09.002.

Lal, A. and Elangovan, M. CFD Simulation and Validation of Flap Type wave-

maker. *World academy of Science, Engineering and Technology*, 46:76–82, 2008.

Lin, P. and Liu, P. Internal wave-maker for Navier-Stokes equations models. *Journal of Waterway, Port, Coastal and Ocean Engineering*, 125(4):207–217, 1999.

Liu, S., Wang, X., Li, M., and Guo, M. Active Absorption Wave Maker System for Irregular Waves. *China Ocean Engineering*, 17(002):203–214, 2003. ISSN 0890-5487.

Longuet-Higgins, M. and Cokelet, E. The deformation of steep surface waves on water. I. A numerical method of computation. *Proceedings of the Royal Society of London. A. Mathematical and Physical Sciences*, 350(1660):1, 1976. ISSN 1364-5021.

Madsen, P., Fuhrman, D., and Wang, B. A Boussinesq-type method for fully nonlinear waves interacting with a rapidly varying bathymetry. *Coastal engineering*, 53(5-6):487–504, 2006. ISSN 0378-3839.

Maguire, A. and Ingram, D. Hydrodynamics and absorption efficiencies of wavemakers. In *Proceedings of the 8th European Wave and Tidal Energy Conference*, pages 859 – 868, Uppsala, Sweeden, 2009.

Maguire, A. and Ingram, D. Wavemaking in a commercial CFD code. In *Proceedings on the Third International Conference of the Application of Physical Modelling to Port and Coastal Protection*, number 1, 2010.

Maguire, A. and Ingram, D. On geometric design considerations and control methodologies for absorbing wavemakers. *Coastal Engineering*, 58(2):135–142, February 2011. ISSN 03783839. doi: 10.1016/j.coastaleng.2010.09.002.

Maisondieu, C. and Clément, A. A realizable force feedback-feedforward control loop for a piston wave absorber. In *Proc. 8th Int. Workshop Water Waves & Floating Bodies; pp79*, volume 82, 1993.

MARNET. Best practice guidelines for marine applications of computational fluid dynamics. Technical report, WS Atkins Consultants and Members of the NSC, MARNET-CFD Thernatic Network, 2002, 2002.

Mei, C. Power extraction from water waves. *Journal of Ship Research*, 20:63–66,

1976.

Milgram, J. H. Active water-wave absorbers. *Journal of Fluid Mechanics*, 42(04): 845, March 1970. ISSN 0022-1120. doi: 10.1017/S0022112070001635.

Mollison, D., Buneman, O., and Salter, S. Wave power availability in the NE Atlantic. *Nature*, 263(5574):223–226, 1976.

Moore, G. Cramming more components onto integrated circuits. *Electronics*, (1):114–117, September 1965. ISSN 0018-9219.

Naito, S. Wave generation and absorption in wave basins: theory and application. *International Journal of Offshore and Polar Engineering*, 16(2):81–89, 2006.

Naito, S. and Minoura, M. Research on element wavemakers and wave field generated by their combination. In *4th Proc. of ISOPE Conference*, volume 3, pages 8–16, 1994.

Naito, S. and Nakamura, S. Wave Energy Absorption in Irregular Waves by Feedforward control system. In *Imternatioal symposium on Hydrodynamics of ocean wave-energy utilization*, pages 269–280, 1985.

Nanri, E., Kihara, H., and Suzuki, K. On the Characteristics of an Absorbing Wavemaker with a Cross Section Having a Plumb Part near the Free Surface. *Journal of the Kansai Society of Naval Architects*, 238:63–69, 2002.

Nebel, P. Maximizing the efficiency of wave-energy plant using complex-conjugate control. *Journal of Systems and Control*, 206(4):225–236, 1992.

Newman, J. The interaction of stationary vessels with regular waves. In *Proc. 11th Symposium on Naval Hydrodynamics*, 1976.

Newman, J. Analysis of wave generators and absorbers in basins. *http://wamit.com/Publications/Newman_AOR_submitted.pdf*, 2008.

Nohara, B. T. An absorption algorithm and its implementation for irregular ocean waves in a test tank. *Journal of the Brazillain Socitey of Mechanical Sciences*, 20(4):553–563, 1998.

NPARC. NPARC Alliance CFD Verification and Validation, 2010.

Oberkampf, W. and Roy, C. *Verification and validation in scientific computing*. Cambridge Univ Pr, 2010. ISBN 0521113601.

Osher, S. and Sethian, J. Fronts propagating with curvature-dependent speed: algorithms based on Hamilton-Jacobi formulations. *Journal of computational physics*, 79:12–49, 1988.

Ouellet, Y. and Datta, I. A survey of wave absorbers. *Journal of Hydraulic Research*, 1986.

Pachauri, R. and Reisinger, A. Contribution of Working Groups I, II and III to the Fourth Assessment Report of the Intergovernmental Panel on Climate Change. Technical report, IPCC, Geneva, 2007.

Park, J. Numerical reproduction of fully nonlinear multi-directional waves by a viscous 3D numerical wave tank. *Ocean Engineering*, 31(11-12):1549–1565, 2004. ISSN 00298018. doi: 10.1016/j.oceaneng.2003.12.009.

Pengzhi, L. *Numerical modelling of water waves*. Spon Press, 2008. ISBN 0415415780.

Price, A. *New Perspectives on Wave Energy Converter Control*. PhD thesis, University of Edinburgh, 2009.

Richardson, L. The Approximate arithmetical solution by finite differences of physical problems involving differential equations, with an application to the stresses in a masonry dam. *Philosophical Transactions of the Royal Society of London. Series A, Containing Papers of a Mathematical or Physical Character*, 210(459-470):307–357, January 1910. ISSN 1364-503X. doi: 10.1098/rsta.1911.0009.

Ris, R. C., Holthuijsen, L. H., and Booij, N. A third-generation wave model for coastal regions 2. Verification. *Journal of Geophysical Research*, 104(C4): 7667–7681, 1999. ISSN 0148-0227. doi: 10.1029/1998JC900123.

Roache, P. J. Perspective: a method for uniform reporting of grid refinement studies. *Journal of Fluids Engineering*, 116(3):405–413, 1994.

Roache, P. J. Quantification of Uncertainty in Computational Fluid Dynamics. *Annual Review of Fluid Mechanics*, 29(1):123–160, January 1997. ISSN 0066-

4189. doi: 10.1146/annurev.fluid.29.1.123.

Roache, P. J. *Verification and validation in computational science and engineering*. Hermosa Publishers Albuquerque, NM, 1998.

Roache, P. J. Code Verification by the Method of Manufactured Solutions. *Journal of Fluids Engineering*, 124(1):4, 2002. ISSN 00982202. doi: 10.1115/1.1436090.

Roache, P. J. Building PDE codes to be verifiable and validatable. *Computing in Science & Engineering*, 6(5):30–38, 2004.

Romate, J. Absorbing boundary conditions for free surface waves. *Journal of computational Physics*, 99(1):145, March 1992. ISSN 00219991. doi: 10.1016/0021-9991(92)90281-3.

Salter, S. Absorbing wave-makers and wide tanks. In *Proceedings of ASCE & ECOR International Symposium on Directional Wave Spectra Applications*, volume 81, pages 182–202, Berkley, California, 1981.

Salter, S., Jeffery, D., and Taylor, J. The architecture of nodding duck wave power generators. *The Naval Architect*, pages 21–24, 1976.

Schäffer, H. Second-order wavemaker theory for irregular waves. *Ocean Engineering*, 23(1):47–88, January 1996. ISSN 00298018. doi: 10.1016/0029-8018(95)00013-B.

Schäffer, H. and Klopman, G. Review of multidirectional active wave absorption methods. *Journal of Waterway, Port, Coastal and*, 126(2):88–98, 2000.

Schäffer, H., Stolborg, T., and Hyllested, P. Simultaneous generation and active absorption of waves in flumes. In *Proc., waves-physical and numerical modelling.*, pages 90–99, University of British Columbia, Vancouver, 1994.

Silva, M. C., Vitola, M. d. A., Pinto, W. T. P., and Levi, C. A. Numerical Simulation of monochromatic wave generated in laboratory: Validation of a CFD code. In *23 Congresso Nacional de Transport Aquaviario Construcao Naval Offshore*, pages 1–12, Rio de Janeiro, 2010.

Smith, S. *The scientist and engineer's guide to digital signal processing*. California Technical Pub., 1997. ISBN 0966017633.

Spinneken, J. and Swan, C. Second-order wave maker theory using force-feedback control. Part I: A new theory for regular wave generation. *Ocean Engineering*, 36(8):539–548, 2009a. ISSN 00298018. doi: 10.1016/j.oceaneng.2009.01.019.

Spinneken, J. and Swan, C. Wave Generation and Absorption Using Force-controlled Wave Machines. In *Proceedings of the Nineteenth (2009) International Offshore and Polar Engineering Conference*, Osaka, Japan, 2009b.

Spinneken, J. and Swan, C. Theoretical Transfer Function of Force-controlled Wave Machines. In *Proceedings of the Twentieth International Offshore and Polar Engineering Conference*, volume 7, pages 409–417, Beijing, China, 2010.

Stern, N. *Stern Review: The economics of climate change*, volume 30. HM treasury London, London, 2006.

Sulisz, W. and Hudspeth, R. Complete second-order solution for water waves generated in wave flumes. *Journal of Fluids and Structures*, 7(2):253–268, 1993.

Tanizawa, K. and Naito, S. An application of fully nonlinear numerical wave tank to the study of chaotic roll motions. *International Journal of Offshore and Polar Engineering*, 9:90–95, 1999. ISSN 1053-5381.

Tanizawa, K. The state of the art on numerical wave tank. *Proc. 4th Osaka colloquium on seakeeping*, 2000.

Thomas, J. *Numerical Partial Differential Equations*. Springer, New York, 2 edition, 1995. ISBN 0387979999.

Tolman, H. User manual and system documentation of WAVEWATCH III TM version 3.14. *Technical note, MMAB Contribution*, 2009.

Ursell, F., Dean, R., and Yu, Y. Forced small-amplitude water waves: a comparison of theory and experiment. *Journal of Fluid Mechanics*, 7(01):33–52, 1960. ISSN 1469-7645.

Versteeg, H. and Malalasekera, W. *An introduction to computational fluid dynamics: the finite volume method*. Prentice Hall, 2007. ISBN 0131274988.

Wang, D.-l. and Zhao, Y.-h. Numerical Simulation of 2-D Nonlinear Wave. In *Proceedings of the Twentieth International Offshore and Polar Engineering*

Conference, volume 7, pages 586–589, Beijing, China, 2010. The International Society of Offshore and Polar Engineers.

Wang, H.-W., Huang, C.-J., and Wu, J. Simulation of a 3D Numerical Viscous Wave Tank. *Journal of Engineering Mechanics*, 133(7):761, 2007. ISSN 07339399. doi: 10.1061/(ASCE)0733-9399(2007)133:7(761).

Wehausen, J. Causality and the radiation condition. *Journal of Engineering Mathematics*, 26(1):153–158, 1992.

Westhuis, J. The numerical simulation of nonlinear waves in a hydrodynamic model test basin. *Doctor's thesis, University of Twente*, 2001.

Westphalen, J., Greaves, D. M., Williams, C., Zang, J., and Taylor, P. Numerical Simulation of Extreme Free Surface Waves. In *ISOPE-2008: Eighteenth(2008) International Offshore and Offshore and Polar Engineering Conference Proceedings*, volume 8, pages 55–61. International Society of Offshore and Polar Engineers, P. O. Box 189, Cupertino, CA, 95015-0189, USA,, 2008.

Westphalen, J., Greaves, D., Williams, C., Taylor, P., Causon, D., Mingham, C., Hu, Z. Z., Stansby, P., Rogers, B., and Omidvar, P. Extreme wave loading on offshore wave energy devices using CFD: a Hierarchical Team Approach. In *Eighth European Wave and Tidal Energy Conference, Sweden*, pages 500–508, 2009.

Woltering, S. and Karl-Friedrich, D. Mass transport and orbital velocities with Lagrangeian frame of reference. In *Proc. 24th International Conference on Coastal Engineering*, pages 2828–2842, Kobe, Japan, 1994.

Zhang, H., Schäffer, H., and Jakobsen, K. Deterministic combination of numerical and physical coastal wave models. *Coastal engineering*, 54(2):171–186, 2007. ISSN 0378-3839. doi: 10.1016/j.coastaleng.2006.08.009.